

UNIVERSITY OF BIRMINGHAM

Use of tailored hydrodynamic conditions to control reactions for AgNPs synthesis in microfluidic devices

by

Konstantia Nathanael

A thesis submitted to

The University of Birmingham

for the degree of

DOCTOR OF PHILOSOPHY

School of Chemical Engineering

College of Engineering and Physical Sciences

The University of Birmingham

B15 2TT, UK

August 2024

UNIVERSITY OF
BIRMINGHAM

University of Birmingham Research Archive

e-theses repository

This unpublished thesis/dissertation is copyright of the author and/or third parties. The intellectual property rights of the author or third parties in respect of this work are as defined by The Copyright Designs and Patents Act 1988 or as modified by any successor legislation.

Any use made of information contained in this thesis/dissertation must be in accordance with that legislation and must be properly acknowledged. Further distribution or reproduction in any format is prohibited without the permission of the copyright holder.

ABSTRACT

This thesis examines the impact of synthesis conditions on the formation of silver nanoparticles (AgNPs), focusing on system chemistry, hydrodynamics, and storage temperature. The study uses T-junction continuous single-phase flow and droplet microfluidic reactors with 500 μm width channels as well as a batch reactor (beaker). The microfluidic reactors were evaluated under identical conditions, revealing that continuous flow reactors produced AgNPs comparable in size to those from droplet reactors. Consequently, the study focused on the former design with optimization of AgNP formation initially carried out using a predictive regression model with response surface methodology, employing tannic acid (TA) and trisodium citrate (TC) as a reducing agent. Key factors affecting particle size, such as pH, stabilizer concentration, and reactor outlet curvature, were identified. However, limitations due to the complexity of the multi-step reaction scheme were noted, with response surface models being effective only within specific operating ranges and unable to provide detailed microscopic insights. To better understand AgNP reaction kinetics, the Finke-Watzky two-stage kinetic model was fitted to experiments carried out in a well-mixed reactor using two distinct chemical protocols. Incorporating these kinetics into a regression model allowed particle size distribution (PSD) predictions with an average error of 4.9%. Experimental validation of a more sophisticated coupled PBM-CFD simulation was then used to interpret hydrodynamic and kinetic effects on AgNP size distribution in the T-junction device and a well-mixed reactor, showing consistency with experimental trends, particularly regarding pH, stabilizer concentration, and average PSD in a well-mixed reactor. Specifically, the experimental

and Finke-Watzky based PBM predictions in the well-mixed reactor obtained at pH = 7 showed a maximum deviation of 10.1% and 31.2% for average particle diameter and standard deviation, respectively. PBM-CFD simulations for the continuous flow device showed that operating conditions, especially inlet flow rates, significantly impact precursor consumption rates and PSD. Helical channels posed additional challenges for precursor consumption, suggesting areas for further research. Machine learning and data science approaches were then used to further optimize AgNP synthesis in continuous reactors and generalize the regression model. A decision tree-guided design of experiments predicted AgNP size using generic parameters, reducing computational costs and enhancing model performance. Factors such as Reynolds number and the Dean number to Reynolds number ratio were used to assess hydrodynamics and mixing. Nucleation and growth constants derived from the independent set of experiments with TA and TC using the Finke-Watzky model examined the system's chemistry, while storage temperature ensured particle stability. The decision tree approach, validated by experimental data, proved effective, indicating that well-designed experiments could substantially reduce mean squared error (MSE) in models like XGBoost (-26%) and Random Forest (-38%). Additionally, in the context of data science, inverse modeling, employing polynomial functions and data assimilation, facilitated nanoparticle design with desired sizes, demonstrating consistency and accuracy, with an average percentage error of 11.99% between predicted and experimental sizes. This approach provided valuable insights for decision-making in nanoparticle manufacturing under uncertainty.

ACKNOWLEDGEMENTS

I would like to express my gratitude to all those who have supported me throughout my PhD journey. Without their encouragement, guidance, and assistance, this research would not have been possible. First and foremost, I am deeply thankful to my supervisors, Prof. Mark Simmons, and Dr. Nina M. Kovalchuk, for their continuous support, insightful guidance, and invaluable feedback throughout every stage of this project. Their expertise and mentorship have been fundamental in shaping the direction of my research and have served as a source of inspiration and motivation. I am truly grateful for the opportunity to undertake this research and for all the knowledge and experience I gained along the way. I also owe a debt of gratitude to the partners on my project at Imperial College London and University College London, particularly to Dr. Sibo Cheng, Dr. Rosella Arcucci, Dr. Alessio Lavino, Dr. Federico Galvanin, and Prof. Omar Matar. Their valuable assistance, and guidance have been important in advancing this project. A special mention goes to Paula Pico from Imperial College for her collaboration on our review paper and later on, our research paper, combining our experimental and numerical works. The PREMIERE team has been exceptional in their support and collaboration. A very big thank you to PREMIERE and University of Birmingham for the funding. In conclusion, I want to express a very big thank you to all those who directly and indirectly contributed to my thesis, including my family and friends. To my mum Rodothea, my dad Nathanael, and my brother George, as well as to my dear friends Myrofora, Christina, Maria, and Hazal in Cyprus and the UK. Your endless patience and love helped me get through my doctorate.

TABLE OF CONTENTS

CHAPTER 1: INTRODUCTION **23**

1.1 BACKGROUND AND MOTIVATION 23

1.2 SCOPE OF STUDY 25

1.3 THESIS AIMS & OBJECTIVES 26

1.4 STRUCTURE AND CONTENT OF THE THESIS 27

1.5 LIST OF JOURNAL PUBLICATIONS AND CONFERENCES ATTENDED 30

CHAPTER 2: LITERATURE REVIEW **33**

2.1 PROPERTIES AND APPLICATIONS OF SILVER NANOPARTICLES 33

2.2 METHODS OF SYNTHESIS AND CHARACTERISATION OF SILVER NANOPARTICLES 35

2.3 MICROFLUIDIC PRODUCTION OF SILVER NANOPARTICLES 50

2.4 MODELS USED TO DESCRIBE SILVER NANOPARTICLES FORMATION. 57

2.5 PARAMETERS AFFECTING THE PHYSICOCHEMICAL PROPERTIES OF AgNPs 64

2.6 SYNTHESIS AND PROPERTIES OF SILVER NANOPARTICLES: PHYSICS-BASED MODELS 71

2.7 DESIGN OF EXPERIMENTS AND RESPONSE SURFACE METHODOLOGY 74

2.8 DATA SCIENCE APPROACHES FOR THE OPTIMIZATION OF NANOPARTICLE'S SYNTHESIS 77

2.9 CONCLUSIONS.....85

CHAPTER 3: MATERIALS AND METHODS.....87

3.1 CHEMICAL REAGENTS AND PROPERTIES.....87

3.2 T-JUNCTION CONTINUOUS FLOW-DEVICE.....89

3.3 DROPLET MICROFLUIDIC DEVICE.....91

3.4 BATCH REACTOR AND KINETICS MEASUREMENTS.....97

3.5 CHARACTERISATION METHODS OF THE SAMPLES.....99

CHAPTER 4: CHARACTERISATION OF A DROPLET AND A CONTINUOUS FLOW MICROREACTOR FOR AgNP FORMATION.....102

4.1 INTRODUCTION.....102

4.2 DROPLET FLOW REACTOR.....103

4.3 COMPARISON OF CONTINUOUS FLOW AND DROPLET MICROREACTORS.....105

4.4 CONCLUSIONS.....111

CHAPTER 5: DEVELOPMENT OF A PREDICTIVE RESPONSE SURFACE MODEL FOR SIZE OF SILVER NANOPARTICLES SYNTHESIZED IN A T-JUNCTION MICROFLUIDIC DEVICE 112

5.1 INTRODUCTION.....112

5.2 PROCESS OPTIMIZATION USING DoE OVERVIEW......113

5.3 DEVELOPMENT OF THE MODEL AND STATISTICAL ANALYSIS.....115

5.4 RESPONSE SURFACE METHODOLOGY RESULTS.....123

5.5 EFFECT OF TRISODIUM CITRATE CONCENTRATION, PH AND STORAGE TEMPERATURE 125

5.6 EFFECT OF CURVATURE AND FLOW RATES 131

5.7 EXPERIMENTAL VALIDATION OF THE MODEL 134

5.8 CONCLUSIONS 138

CHAPTER 6: ANALYSIS ON REACTION KINETICS OF SILVER NANOPARTICLES SYNTHESIS 140

6.1 INTRODUCTION 140

6.2 KINETIC CONSTANTS OF TANNIC ACID AND TRISODIUM CITRATE 141

6.3 KINETIC CONSTANTS OF DMAB AND SDS AND COMPARISON WITH THE KINETICS OF TANNIC ACID AND TRISODIUM CITRATE 145

6.4 CORRELATION OF KINETICS AND INITIAL CONCENTRATIONS FOR BOTH SET OF CHEMICALS 151

6.5 CONCLUSIONS 154

CHAPTER 7: EXPERIMENTAL VALIDATIONS OF PBM-CFD SIMULATIONS ON SYNTHESIS OF SILVER NANOPARTICLES IN MICROFLUIDIC CHANNELS 155

7.1 INTRODUCTION 155

7.2 EXPERIMENTAL VALIDATION OF PBM: EFFECT OF pH AND [TC] ON THE SYNTHESIS OF AgNPs IN A WELL-MIXED REACTOR 157

7.3 PRECURSOR CONSUMPTION DYNAMICS IN THE T-JUNCTION MICROCHANNEL-EXPERIMENTAL VALIDATION OF PBM-CFD SIMULATIONS 162

7.4 CONCLUSIONS.....169

CHAPTER 8: OPTIMIZATION OF MICROFLUIDIC SYNTHESIS OF SILVER NANOPARTICLES USING MACHINE LEARNING AND INVERSE MODELLING 171

8.1 INTRODUCTION.....171

8.2 DECISION TREE GUIDED DESIGN OF EXPERIMENTS.....172

8.3 PEARSON CORRELATION AND THE EFFECT OF INPUT PARAMETERS.....176

8.4 PREDICTION RESULTS WITH DT-GUIDED EXPERIMENTS.....178

8.5 INVERSE MODELLING.....184

8.6 CONCLUSIONS.....200

CHAPTER 9: CONCLUSIONS & FUTURE WORK 203

9.1 CONCLUSIONS.....203

9.2 FUTURE WORK 207

REFERENCES 210

APPENDIX A: STATISTICAL ANALYSIS.....251

APPENDIX B: PARTICLES SIZES OF SILVER NANOPARTICLES AS A FUNCTION OF PH, CONCENTRATION OF TRISODIUM CITRATE, STORAGE TEMPERATURE, CURVATURE AND FLOW RATES.....254

APPENDIX C: NUCLEATION AND GROWTH CONSTANTS OF SILVER NANOPARTICLES ALONG WITH PARTICLES SIZES IN A WELL-MIXED REACTOR FOR TWO SET OF CHEMICALS.....256

APPENDIX D: PARTICLES SIZES OF SILVER NANOPARTICLES AS A FUNCTION OF NUCLEATION AND GROWTH CONSTANTS, STORAGE TEMPERATURE, REYNOLDS NUMBER AND DEAN NUMBER/REYNOLDS NUMBER FOR THE FIRST SET OF CHEMICALS 257

APPENDIX E: TRANSMISSION ELECTRON MICROSCOPE IMAGES. 259

APPENDIX F: UV MEASUREMENTS FOR BOTH SET OF CHEMICALS. 260

APPENDIX G: PBM MODEL IN A WELL-MIXED REACTOR FOR 2ND SET OF CHEMICALS 262

APPENDIX H: ALGORITHM 1 ITERATIVE MINIMISATION OF 3D-VAR COST FUNCTION VIA QUASI-NEWTON METHODS 264

LIST OF FIGURES

Chapter 2: Literature review

Figure 2.1 Summary of the main applications of AgNPs (Nathanael et al, 2022)……34

Figure 2.2 Steps of synthesis of AgNPs (Nathanael et al, 2022)……...38

Figure 2.3 Different configurations of microchannels such as A) continuous flow operation, droplet-based operation in B) T-junction geometry, C) co-axial geometry D) flow focusing geometry Reproduced from Shembekar et al (2016) ……53

Chapter 3: Materials and Methods

Figure 3.1 Chemical structures of the reagents employed for the synthesis of AgNPs. A) First chemical synthesis protocol B) Second chemical synthesis protocol…….89

Figure 3.2 A) Experimental set up using two-syringe pumps (depicted as two one-syringe pumps in the schematic for better visualization of the fluid injection), B) Schematic diagram of T-junction microfluidic device……90

Figure 3.3 Flow focusing microfluidic device showing the formation of droplets inside the microfluidic channels where the chemicals react to form AgNPs. Silicone oil was used as a continuous phase while the aqueous solutions of chemical reagents were utilised as the dispersed phase…….. 96

Figure 3.4 UV-silver ions measurements in a well-mixed reactor……98

Chapter 4: Characterisation of a drop and a continuous flow microreactor for AgNP formation

Figure 4.1 A) pH 12, TC 1.91 mM, 15 µL/min, B) pH 12, TC 1.91 mM, 30 µL/min, C) pH 7, TC 1.91 mM, 15 µL/min, D) pH 7, TC 1.91 mM, 30 µL/min, E) pH 7, TC 2.87 mM, 30 µL/min, F) pH 7, TC 3.82 mM, 30 µL/min……110

Chapter 5: Development of a predictive response surface model for size of silver nanoparticles synthesized in a T-junction microfluidic device

Figure 5.1 Residual plots for the size of AgNPs A) probability and B) histogram of residuals. The data set follows a basic normal (Gaussian) distribution (Nathanael et al, 2023b)……118

Figure 5.2 Pareto chart (Nathanael et al, 2023b)……122

Figure 5.3 Contour plots predicting the size of AgNPs. The pH, ST, TC, CR and FR were kept constant at 12, 0℃, 1.91 mM, 33.3 dm^{-1}, 1×10^{-5} dm^3/min respectively (Nathanael et al, 2023b) ……...124

Figure 5.4 A) Dissociation species of citrate, B) Production of dicarboxyacetone (DCA) as a by-product of the decarboxylation of citrate during silver reduction and C) Dissociation species of DCA. Reproduced from Gao & Torrente-Murciano (2020) and Marciniak et al (2020)……..128

Figure.5.5 A) Dependence of zeta potential of AgNPs on pH at different concentrations of trisodium citrate and B) Zeta potential of AgNPs at pH 12 for different concentrations of trisodium citrate (Nathanael et al, 2023b)……..130

Figure 5.6 AgNPs size distribution from TEM and zeta-sizer. AgNPs at 2×10^{-5} dm^3/ min, pH 12, TC 1.91 mM, CR 33.3 dm^{-1} and ST 0 ^oC (Nathanael et al, 2023b)……136

Figure 5.7 Predicted and true particle size of the A) training data (162 experiments including replications) and B) testing data (45 experiments including replications) using Eq. (5.3). The confidence intervals (CI) and prediction intervals (PI) for the predicted responses were estimated with error 95%. Note, that black and red dots represent the average of three experimental observations with corresponding error bars (Nathanael et al, 2023b)……138

Chapter 6: Analysis on reaction kinetics of silver nanoparticles synthesis

Figure 6.1 Application of the F-W mechanism for the analysis of AgNPs formation kinetics for the first set of chemicals. Time evolution of $[B]$ at 400 nm for A) pH 7 and B) pH 12 and different concentrations of the stabilising agent: symbols represent experimental data; lines are fitting of full model Eq. (2.6) with kinetic constants found from linear fitting; Fitting of experimental data using linear form of Finke-Watzky model as shown in Eq. (2.7) for C) pH 7 and D) for pH 12 (Nathanael et al, 2023a)……144

Figure 6.2 Time evolution of $[B]$ for second set of chemicals at 400 nm for A) 0.2 mM DMAD and B) 0.4 mM DMAB and different concentrations of the SDS: symbols represent

experimental data; lines are fitting of full model Eq. (2.6) with kinetic constants found from linear fitting……147

Figure 6.3 Linear fitting of F-W two step mechanism for the second set of chemicals using 0.2 mM DMAB (A) and 0.4 mM DMAB (B) for 60 mM and 80 mM SDS……148

Figure 6.4 A) Training and B) Testing data for the correlation for both set of chemicals..153

Chapter 7: Experimental validation of PBM-CFD simulations on synthesis of silver nanoparticles in microfluidic channels

Figure 7.1 PBM model in a well-mixed reactor for 1st set of chemicals. The graphs (A) and (C) show the temporal evolution of [B] between the experimental measurements (pink dots) and F-W based PBM predictions (blue line) while graphs (B) and (D) the PSD for AgNPs in a well-mixed reactor using 1.91 mM TC at pH 7 and pH 12 respectively……..161

Figure 7.2 Effect of flow rates and residence times on the steady-state concentration of silver ions along the T-junction microchannel. Experimental (A) results versus CFD mixing reaction model (B)……163

Figure 7.3 Experimental PSD of AgNPs at 50 (A), 100 (B) and 200 (C) $\mu\mathrm{L}/\mathrm{min}$ at different lengths of outlet channel……...166

Figure 7.4 Experimental (A) versus PBM results (B) at 0.25 m length and different flow rates……167

Chapter 8: Optimization of microfluidic synthesis of silver nanoparticles using machine learning and inverse modelling

Figure 8.1 Workflow chart and description of methods used in the building of machine learning-guided design of experiment based on the decision tree method (Nathanael et al, 2023a)……176

Figure 8.2 Pearson correlation between input variables and the size of AgNPs (Nathanael et al, 2023a)……177

Figure 8.3 Decision tree which examines the size of synthesized AgNPs as a function of five parameters where x_o, x_1, x_2, x_3, x_4, are nucleation constant k_1, growth constant k_2, storage temperature, Dean number/Reynolds number De/Re and Reynolds number (Re) respectively. Orange boxes are showing where there is a high MSE (Nathanael et al, 2023a)……182

Figure 8.4 Predicted versus real measurements for the size of AgNPs using DT. A) Original training data (20 initial conditions, 60 training samples in total including replications), B) Random extra experiments (10 experiments, 30 validation samples in total including replications) and C) Designed extra experiments (10 experiments, 30 validation samples in total including replications). The conditions that have been used for training, random extra experiments and designed extra experiments are described in detail in Appendix D. The average size of AgNPs on X, Y axes is given in nm (Nathanael et al, 2023a)……183

Figure 8.5 The actual versus predicted sizes were plotted for the polynomial function used for the Inverse modelling approach. It was built using k_1, k_2, T, Re and De/Re……187

Figure 8.6 Flowchart of data assimilation process in the inverse modelling approach employing LHS…….. 190

Figure 8.7 Steps to build the forward model, using the LHS and DA for the inverse model and how the inverse model was validated……..193

Figure 8.8 Inverse modelling sizes versus direct model sizes……194

Figure 8.9 Inverse modelling sizes versus experimental sizes……195

LIST OF TABLES

Chapter 2: Literature review

Table 2.1 Examples of chemical synthesis methods of AgNPs (Nathanael et al, 2022)…41

Table 2.2 Experimental investigations on microfluidic fabrication of AgNPs (Nathanael et al, 2022)…… 54

Table 2.3 Examples of nucleation (k_1) and growth (k_2) constants of Finke-Watzky model for synthesis of AgNPs using different methods and reagents. All the rate constants k_1 and k_2 were converted into min^{-1} and $M^{-1}min^{-,1}$ respectively from the original publications (Nathanael et al, 2022)……62

Chapter 3: Materials and Methods

No tables.

Chapter 4: Characterisation of a drop and a continuous flow microreactor for AgNP formation

Table 4.1: Size distribution of AgNPs at different flow rates and chemical conditions in the droplet reactor……105

Chapter 5: Development of a predictive response surface model for size of silver nanoparticles synthesized in a T-junction microfluidic device

Table 5.1 Factors and levels for D-optimal design (Nathanael et al, 2023b)……115

Table 5.2 Values of R^2 , R^2 Adj, AIC and BIC for each model (Nathanael et al, 2023b)…117

Table 5.3 A) Parameters and B) analysis of variance for the fitted polynomial model (Eq. (5.3)) of AgNPs optimization (Nathanael et al, 2023b)……120

Chapter 6: Analysis on reaction kinetics of silver nanoparticles synthesis

Table 6.1: Nucleation and growth constants for varied pH and concentrations of trisodium citrate…….. 145

Table 6.2: Kinetic constants of second set of chemicals involving DMAB and SDS and the experimental sizes under the investigated cases……..150

Table 6.3: Features and range investigated for the correlation between the kinetics and initial concentrations for both set of chemicals……..151

Chapter 7: Experimental validation of PBM-CFD simulations on synthesis of silver nanoparticles in microfluidic channels

Table 7.1: Comparison of experimental measurements of d, σ and $\mathrm{PDI} = (\sigma/\mathrm{d})^2$ with F-W based PBM predictions and normal distribution fitting (see § 3.5, Eq. (3.2)) for AgNPs in a well-mixed reactor under different pH and [TC] after full precursor consumption……..160

Chapter 8: Optimization of microfluidic synthesis of silver nanoparticles using machine learning and inverse modelling

Table 8.1: Input parameters and their investigated range (Nathanael et al, 2023a)…….174

Table 8.2: Decision tree (DT), Extreme Gradient boosting (XGBoost) and Random Forest (RF) results for original, random and designed experiments (Nathanael et al, 2023a)…184

Table 8.3: Assimilated values of De/Re and Re for different experimental conditions. Comparison of size of AgNPs requested by Inverse modelling and size predicted by direct model…….. 197

Table 8.4: Assimilated values of De/Re and Re for different experimental conditions. Comparison of size of AgNPs requested by Inverse modelling and size found experimentally……198

Table 8.5: Assimilated values of Re for different experimental conditions. Comparison of size of AgNPs requested by Inverse modelling and size predicted by direct model…….200

LIST OF ABBREVIATIONS

4-nitrophenol	4-NP
Akaike Information Criterion	AIC
Analysis of variance	ANOVA
Artificial intelligence	AI
Atomic force microscopy	AFM
Bayesian Information Criterion	BIC
Bayesian optimisation	BO
Bis(2-ethylhexyl) sulfosuccinate	AOT
Cetyltrimethylammonium bromide	CTAB
Computational fluid dynamics	CFD
Data Assimilation	DA
Dean number	De
Decision tree	DT

Deep neural network	DNN
Design of experiment	DoE
Dicarboxyacetone	DCA
Dimethylamine borane	DMAB
Direct blue	DB24
Dodecanoic acid	DDA
Dynamic light scattering	DLS
Ethylene glycol	EG
Extreme Gradient Boosting	XGBoost
Finke-Watzky	F-W
Four-Dimensional Variational Data Assimilation	4DVAR
Fourier transform infrared spectroscopy	FTIR
Gold nanoparticles	AuNPs
Iridium Nanoparticles	IrNPs
Machine learning	ML

Mean absolute error	MAE
Mean squared error	MSE
Methyl orange	MO
Methylene blue	MB
Micrometres	μm
Molecular dynamics	MD
Nanometres	nm
Nanoparticle	NP
Number density function	NDF
One-factor-at-a-time	OFAT
Particle size distribution	PSD
Phenol red	PR
Poly (ethylene glycol)	PEG
Poly(vinylpyrrolidone)	PVP
Polydispersity index	PDI

Polytetrafluoroethylene	PTFE
Polyvinyl alcohol	PVA
Population balance equation	PBE
Population balance model	PBM
Random Forest	RF
Reynolds number	Re
Root Relative Square Error	RRSE
Scanning electron microscopy	SEM
Silver nanoparticles	AgNPs
Silver nitrate	SN
Sodium dodecyl sulfate	SDS
Tannic acid	TA
Three-Dimensional Variational Data Assimilation	3DVAR
Transmission electron microscopy	TEM
Trisodium citrate	TC

Ultraviolet visible spectroscopy	UV-vis spectroscopy
Volume of fluid	VOF
X-ray diffractometry	XRD
X-ray photoelectron spectroscopy	XPS

CHAPTER 1: INTRODUCTION

1.1 BACKGROUND AND MOTIVATION

Silver nanoparticles (AgNPs) are well-known for their unique properties, making them particularly useful across various industries. However, different applications require specific properties, demanding precise control over the size, shape and distribution of AgNPs. This precise control is challenging to achieve, and its effective utilization in industry is further complicated by a combination of technical, economic and health and environmental reasons. For example, the synthesis of AgNPs involves a diverse array of reagents and methods developed over the years, varying independent experimental conditions as well as an incomplete understanding of some of the physicochemical processes involved. Additionally, the synthesis of AgNPs can be expensive, particularly when considering the cost of raw materials, synthesis methods and purification processes. Furthermore, there are ongoing concerns about the potential toxicity of AgNPs to humans and the environment leading to strict regulations that can also prevent industrial utilization. By improving current understanding and control of critical parameters in the synthesis of AgNPs, nanoparticles with enhanced properties tailored for specific applications can be produced. Research on AgNPs synthesis in microfluidics can provide insights into the mechanism of nanoparticle formation and growth but also foster the development of more efficient and innovative synthesis strategies. Microfluidic systems offer the potential for precise control over the reaction enabling the synthesis of AgNPs with precise size, shape and surface properties. Moreover, microfluidics can contribute to a more sustainable approach to nanomaterial discovery and production, minimising the environmental impact

through reduced waste and resource consumption compared to traditional bulk synthesis methods when used at small scale production. Scaling up the production of microfluidics devices can be complex and is beyond the scope of this thesis. The integration of machine learning and predictive models can also play a crucial role in advancing research on AgNPs synthesis. Models can optimize reaction conditions to achieve desired AgNP properties while minimising the need for trial and error, thus saving valuable time and resources. Predictive models can also be used to elucidate the complex mechanisms underlying nanoparticle formation and growth, enhancing the overall understanding of these processes.

The objective of this research project was thus to develop predictive models to forecast temporal evolution and physicochemical characteristics of AgNPs synthesized in both well-mixed reactors and microfluidic devices, employing different chemical synthesis protocols to further optimise their synthesis. The key components of this study include changing synthesis conditions, predictive modelling and optimization of synthesis.

The research described in this thesis was carried out as part of an Engineering and Physical Sciences Research Council (EPSRC) Programme Grant (EP/T000414/1), “PREMIERE”. PREMIERE stands for PREdictive Modelling with QuantIfication of UncERtainty for MultiphasE Systems and is a multidisciplinary collaboration between Imperial College London, the University of Birmingham, the University of Cambridge, University College London, and the Alan Turing Institute. The program has developed algorithms to solve energy, manufacturing, and healthcare problems using high fidelity physical modelling, artificial intelligence, and machine learning.

1.2 SCOPE OF STUDY

The scope of this study includes a comprehensive investigation into the synthesis of AgNPs using both well-mixed reactors and microfluidic devices. The research focuses on examining the synthesis processes and evaluating how different synthesis protocols impact the properties of AgNPs, such as size and size distribution.

The study involves comparing the performance of continuous flow and droplet microfluidic approaches for AgNP synthesis. As a result of this comparison, further work focused on using a simple T-junction microfluidic device made of polytetrafluoroethylene (PTFE) where the continuous flow of silver nitrate solution meets the continuous flow of tannic acid/trisodium citrate. Various parameters were investigated, including the flow rates of reagents, pH of the solution, concentration of stabilising agent, storage temperature and curvature of the outlet channel. The potential for enhancing mixing of fluids in the system and control AgNP properties was explored by coiling the outlet tube on a 3D-printed helical device. The purpose of this simple device was to provide data to validate physical and data-driven models describing AgNP synthesis in microreactors and further optimise the overall process. In addition, the thesis evaluates the predictability of AgNP sizes in well-mixed reactors under different chemical protocols, utilizing the Finke-Watzky mechanism to describe synthesis and estimate nucleation and growth constants. This thesis also integrates physical and data-driven models to provide insights into AgNP synthesis in continuous flow reactor, focusing on the interaction between hydrodynamics, reaction kinetics, and PSD. Data science and machine learning techniques are employed to further

optimize synthesis protocols, generalize the approach and improve control over AgNP properties.

Apart from the experimental part, a comprehensive literature review was conducted to gather previous studies relating to synthesis of AgNPs and investigate the different methods developed over the years, the parameters that affect the physicochemical properties of AgNPs, available kinetic models, methods and techniques for optimization and prediction of nanoparticle properties including physics-based models, DoE and data science approaches, and the areas requiring further study.

This thesis aims to contribute to the field by providing a framework for the efficient and controlled synthesis of AgNPs, using advanced predictive and optimization techniques. The results will be applicable to various industrial uses of AgNPs, enhancing their implementation across different sectors.

1.3 THESIS AIMS & OBJECTIVES

This research project has the overall aim of the control of reactions in microfluidic devices as a route to the formation of nano-scale particles, focussed on the nucleation and growth of silver nanoparticles. More specifically, the objectives can be outlined as follows:

- Identification of the optimal microfluidic experimental setup for efficiently gathering experimental data through comparison of a continuous flow reactor with a droplet-based reactor under identical chemical and hydrodynamic conditions for synthesizing AgNPs (Chapter 4).

- Identify experimental conditions which produce the minimum size of nanoparticles through application of a response surface methodology and design of experiments (DoE) to optimize microfluidic synthesis of silver nanoparticles (Chapter 5).
- Investigation of kinetics for two different set of chemicals in a well-mixed reactor and correlation development between kinetics and initial concentrations (Chapter 6).
- Experimental validation of PBM-CFD simulations on synthesis of AgNPs in T-junction continuous microfluidic and well-mixed reactors (Chapter 7).
- Optimization of microfluidic synthesis of silver nanoparticles using machine learning and data science approaches focusing on decision tree guided design of experiments and inverse modelling (Chapter 8).

1.4 STRUCTURE AND CONTENT OF THE THESIS

The thesis is structured as follows. Chapter 2 presents a literature review on properties and applications of AgNPs. Different experimental methods, the parameters influencing the physicochemical properties of AgNPs, available kinetic models, methods and techniques for optimizing and predicting nanoparticle properties, including physics-based models, DoE and data science approaches described in the literature are explored.

A comprehensive description of the chemical reagents used, and the experimental methods employed throughout this research is given in Chapter 3.

The results from this research project are recorded in Chapters 4 - 8. A comparison between AgNPs synthesized in T-junction continuous flow and droplet (multiphase flow) reactors under identical experimental conditions, including chemical protocol and

operating parameters is given in Chapter 4. This comparison includes an analysis of operating parameters, highlighting the differences and similarities in the synthesis outcomes.

The focus of Chapter 5 is on the application of a response surface methodology to optimize synthesis of silver nanoparticles in a microfluidic device. This work involved the synthesis of AgNPs in T-junction tubing device by a chemical route through the reduction of silver nitrate (SN). Tannic acid (TA) was used as a reducing agent while trisodium citrate (TC) was used as both stabilising and reducing agent. A DoE strategy based on the D-optimal approach was employed to build a model for optimization of the overall process. This study explored not only the adjustments of reagents used but also examined the control of hydrodynamic conditions. Particularly, DoE and microfluidics-based synthesis were combined to examine the effects of pH of the solution, collection and storage temperature, helical curvature of the outlet channel, flow rates and relative concentration of trisodium citrate on the size of AgNPs. It aimed to decrease the limitations of traditional approaches reliant on one-factor-at-a-time (OFAT) and batch-style chemical reactors contributing to a more sustainable and controlled AgNPs synthesis route. The kinetics of formation of AgNPs obtained from two different chemical protocols are explored in Chapter 6 using a well-mixed reactor. The kinetics from both chemical sets are combined with the initial concentrations of precursors to establish a correlation, investigating the possibility of predicting the size of AgNPs using these distinct chemical protocols. Chapter 7 presents the experimental validation of PBM-CFD simulations for the synthesis of AgNPs in microfluidic channels and well-mixed reactor. By combining Finke-Watzky reaction kinetics of AgNPs with computational fluid dynamics (CFD) and population

balance model (PBM), this investigation examined the effect of different operating conditions on the final particle size distribution in a T-junction microfluidic device, aiming to reduce material and energy demand. While numerical simulations were performed by Paula Pico at Imperial College London, the focus of this thesis was on experimental validation of PBM-CFD results.

Chapter 8 focuses on the optimization of microfluidic synthesis of silver nanoparticles using machine learning modelling based on decision tree guided design of experiments and data science approaches such as Inverse modelling. The properties of AgNPs are affected by various parameters, making optimisation of their synthesis a challenging task. This chapter discusses optimization facilitated by concurrent use of a T-junction microfluidic system and machine learning approach. AgNPs are synthesized by reducing silver nitrate with tannic acid in the presence of trisodium citrate. A decision tree-guided design of experiment and inverse modelling approaches are employed for AgNPs size. The developed approaches use kinetic nucleation and growth constants (see Chapter 6) derived from an independent set of experiments to account for chemistry of synthesis, the Reynolds number, and the ratio of Dean number to Reynolds number to reveal effect of hydrodynamics and mixing within device and storage temperature to account for particle stability after collection. The obtained DT model was used to define a parameter space for additional experiments carried out to improve the model further. The inverse model was used to identify the experimental conditions for different sizes of AgNPs. Chapter 9, provides the final conclusions of the thesis, reflecting on the overall aims and objectives of the project and offering recommendations for future work. Lastly, Chapter 10 contains

appendices, providing supplementary information and detailed data supporting this research project.

1.5 LIST OF JOURNAL PUBLICATIONS AND CONFERENCES ATTENDED

Journal Publications

1. Nathanael, K., Pico, P., Kovalchuk, N. M., Lavino, A. D., Simmons, M. J. H. & Matar, O. K. (2022) Computational modelling and microfluidics as emerging approaches to synthesis of silver nanoparticles – A review. *Chemical Engineering Journal*, **436**, 135178.
2. Nathanael, K., Cheng, S., Kovalchuk, N. M., Arcucci, R. & Simmons, M. J. H. (2023) Optimization of microfluidic synthesis of silver nanoparticles: A generic approach using machine learning. *Chemical Engineering Research and Design*, **193**, 65-74.
3. Nathanael, K., Galvanin, F., Kovalchuk, N. M. & Simmons, M. J. H. (2023) Development of a predictive response surface model for size of silver nanoparticles synthesized in a T-junction microfluidic device. *Chemical Engineering Science*, **279**, 118907.
4. Pico, P., Nathanael, K., Lavino, A. D., Kovalchuk, N. M., Simmons, M. J. H. & Matar, O. K. (2023) Silver nanoparticles synthesis in microfluidic and well-mixed reactors: A combined experimental and PBM-CFD study. *Chemical Engineering Journal*, **474**, 145692.
5. Basha, N., Arcucci, R., Angeli, P., Anastasiou, C., Abadie, T., Quilodran Casa, C., Chen, J., Cheng, S., Chagot, L., Galvanin, F., Heaney, C., Hossein, F., Kovalchuk,

N.M., Kalli, M., Kahouadi, L., Kerhouant, M., Lavino, A., Liang, F., Nathanael, K., Magrihi, L., Materazzi, M., Erigo, M. Pico, P., Pain, C., Shamsa, M., Simmons, M.J.H., Traversohi, T., Pablo Valdesa, J., Wolffs, Z., Zhu, K., Zhang, Y., Matar, O.K. (2024) Machine Learning and Physics-Driven Modelling and Simulation of Multiphase Systems, *Int. J. Multiphase Flow*, **179**, 104936.

Conferences attended

1. Nathanael, K., Kovalchuk, N.M., Simmons, M.J.H, Synthesis of silver nanoparticles (AgNPs) in a microfluidic device, 35th Conference of the European Colloid and Interface Society, Athens, Greece, 5- 10 September 2021.
2. Nathanael, K., Galvanin, F., Kovalchuk, N.M., Simmons, M.J.H, "Using design of experiments to optimise microfluidic synthesis of AgNPs". UK Chem Eng Day, London, UK, 2022.
3. Nathanael, K., Galvanin, F., Kovalchuk, N.M, Simmons, M.J.H, "Design of experiments to model the size of AgNPs in microfluidic synthesis". 36th ECIS conference, Chania, Crete, Greece, 2022.
4. Pico, P., Nathanael, K., Lavino, A.D, Kovalchuk, N.M, Matar, O.K, Simmons, M.J.H, "PBM-CFD simulations of microfluidic synthesis of AgNPs". 36th ECIS conference, Chania, Crete, Greece, 2022.

5. Pico, P., Nathanael, K., Lavino, A.D, Kovalchuk, N.M, Matar, O.K, Simmons, M.J.H, “Microfluidic assisted synthesis of silver nanoparticles: coupled PBM-CFD simulations and experimental study”. 75th APS-DFD meeting, Indianapolis, USA, 2022.

6. Nathanael, K., Pico, P., Cheng, S., Kovalchuk, N.M, Lavino, A.D, Arcucci, R., Matar, O.K, Simmons, M.J.H, “Optimization of microfluidic synthesis of silver nanoparticles by coupled experiments and modelling”. ICMF, Kobe, Japan, 2023.

7. Nathanael, K., Pico, P., Kovalchuk, N.M, Lavino, A.D, Matar, O.K, Simmons, M.J,H, “Predicting the particle size distribution of silver nanoparticles”, UK Colloids, Liverpool, UK, 2023.

8. Nathanael, K., Pico, P., Kovalchuk, N.M, Lavino, A.D, Matar, O.K, Simmons, M.J.H, “PBM-CFD simulations for the formation of AgNPs based on Finke-Watzky two step mechanism”. 37th ECIS conference, Naples, Italy, 2023.

9. Nathanael, K., Pico, P., Kovalchuk, N.M, Lavino, A.D, Matar, O.K, Simmons, M.J.H, “Predicting the particle size distribution of silver nanoparticles: coupled PBM-CFD simulations and experimental study”. 76th APS-DFD meeting, Washington DC, USA, 2023.

CHAPTER 2: LITERATURE REVIEW [1]

2.1 PROPERTIES AND APPLICATIONS OF SILVER NANOPARTICLES

According to the Allied Market Research report released by Newswire (2020) the global market of AgNPs was valued at $1.8 billion in 2019 and it is projected to reach $4.1 billion by 2027. During this forecast period, it is expected that the application of AgNPs in pharmaceutical sector will increase at the fastest growth rate in terms of volume and revenue due to their antibacterial and antiviral activity. AgNPs possess some unique properties which have enabled their application in multiple areas, as shown in Figure 2.1. AgNPs are effective against many bacteria including some antibiotic-resistant strains (Vazquez-Muñoz et al, 2019) and viruses (Lu et al, 2008), (Elechiguerra et al, 2005). The enhanced antibacterial properties of silver at the nanoscale are valuable for applications in filters for water disinfection (Wei et al, 2018), food packaging and preservation (Wu et al, 2019), sterile textiles (Ballottin et al, 2017), the health care sector as skin products (Szczepańska et al, 2020), wound dressings (Parveen et al, 2018), catheters (Chutrakulwong et al, 2020) and dental materials (Parveen et al, 2018). In skin products, these nanoparticles are employed as cleansers to kill harmful bacteria and treat acne or seborrheic dermatitis (Szczepańska et al, 2020). AgNPs can also be embedded into finger or toenail paints to treat fungal infections (Dantas et al, 2021). Other medical

[1] Sections 2.1-2.5 of the literature review are adapted from Nathanael, K., Pico, P., Kovalchuk, N.M., Lavino, A.D., Simmons, M.J.H., Matar, O.K. (2022) Computational modelling and microfluidics as emerging approaches to synthesis of silver nanoparticles – A review. *Chem. Eng. J.,* **436**, 135178.

applications of AgNPs include diagnostics and bioimaging (Noronha et al, 2017), drug delivery systems (Paul et al, 2020), and cancer treatment (Loiseau et al, 2019).

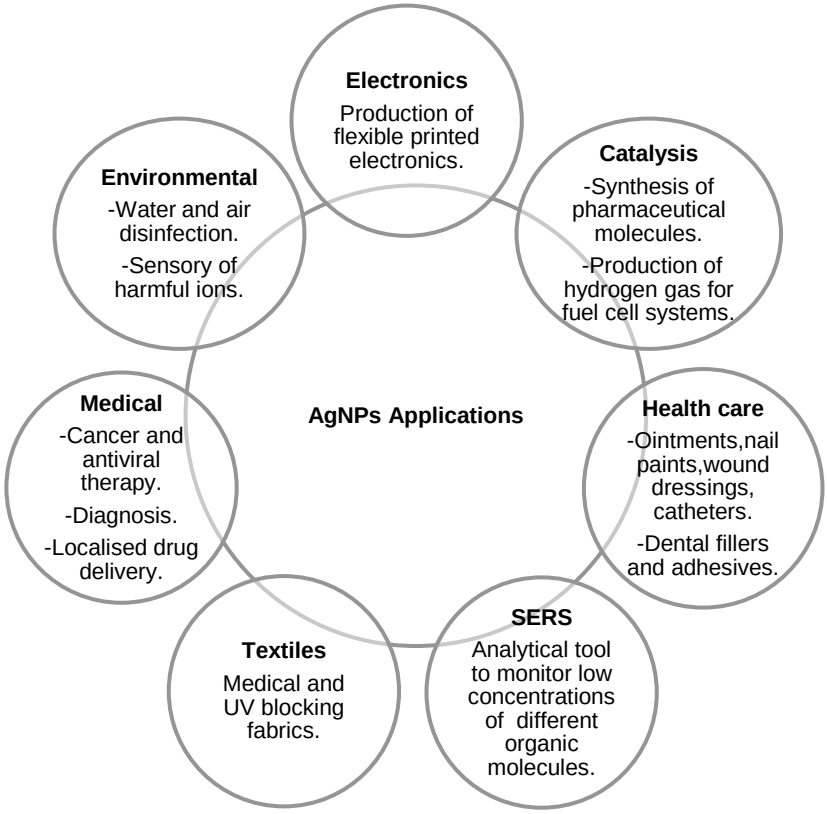


Figure 2.1 Summary of the main applications of AgNPs (Nathanael et al, 2022).

Silver is the most electrically conductive element. For nanoparticles, the melting temperature decreases with size because of increased surface energy. Thus, coalescence and sintering of nanoparticles within a deposited film can be chemically induced at room temperature, resulting in a highly conductive thin silver film (Magdassi et al, 2010). For this reason, conductive inks and silver films are among the most used materials in printed and flexible electronics (Rao, 2015).

AgNP-catalysts are highly effective given their large surface area to volume ratio and high selectivity. They find applications for general organic reactions (Dong et al, 2015) and degradation of various organic dyes, including 4-nitrophenol (4-NP), methylene blue (MB), methyl orange (MO), phenol red (PR), and direct blue (DB24) (Bogireddy et al, 2016). AgNPs are also very promising catalysts for the production of hydrogen for fuel cells (Huff et al, 2020). When electromagnetic radiation interacts with AgNPs, it induces a collective oscillation of surface conduction electrons called surface plasmons. Existence of surface plasmons during their interaction with light is also responsible for the strong interaction of Ag colloids in UV-Vis spectral region (Krajczewski et al, 2017). This allows the application of AgNPs in colorimetric probes for the selective sensing of different molecules in the food industry (Song et al, 2015), water quality control (Alzahrani, 2020), and medical diagnostics (Yen et al, 2015).

2.2 METHODS OF SYNTHESIS AND CHARACTERISATION OF SILVER NANOPARTICLES

The properties of nanoparticles, including AgNPs, are strongly dependent on their size and shape, which in turn are influenced by the fabrication method. There are various routes for AgNPs synthesis which can be divided into top-down and bottom-up methods. Top-down processes start from the bulk material and decrease the size of the particles to the desired values. Bottom-up methods use atomic, molecular, or ionic components to generate the more complex nanoscale structures (Lee & Jun, 2019). Top-down approaches mainly utilise physical methods (Reverberi et al, 2020) while bottom-up routes

exploit different chemical (Quintero-Quiroz et al, 2019), physical (El-Khatib et al, 2018), and biological (Siddiqi et al, 2018) processes. The most common physical methods include vapor condensation (Jung et al, 2006), arc-discharge (El-Khatib et al, 2018), laser ablation (Chen & Yeh, 2002) and ball milling method (Reverberi et al, 2020). All of these techniques provide quick processing time and decrease use of toxic chemicals. However, they have high energy consumption (Yusuf, 2019), (Siddiqi et al, 2018). Biological synthesis is based on microorganisms such as simple prokaryotic bacterial cells (Singh et al, 2018), yeast (Fernández et al, 2016), and eukaryotic fungi (Elamawi et al, 2018). This method have less control in AgNP size with main disadvantage being the mandatory stage of purification which may cause the generation of pathogenic bacteria and consequently a possible contamination if cleaning and quality protocols are not followed (Ge et al, 2014). Recent and comprehensive reviews of the available methods for the formation of AgNPs are given by Zahoor et al (2021) and Yaqoob et al (2020).

The fabrication of AgNPs via chemical methods, which comprise most of the literature, is characterised by various approaches including photochemical (Manikprabhu & Lingappa, 2013) and electrochemical (Roldán et al, 2013) techniques. Photochemical techniques use electromagnetic radiation to influence chemical reactions, while electrochemical techniques utilise electricity to force the movement of electrons causing chemical changes. The chemical reduction may occur in solid-state (Hosseinpour-Mashkani & Ramezani, 2014) and in a flow of inert gas such as N_2 (Nakano et al, 2016). Chemical reduction in liquid phase is one of the most common approaches to produce AgNPs as it requires simple equipment which allows for large-scale production (Quintero-Quiroz et al,

2019). Thermal decomposition of different silver precursors such as silver acetate (Nakano et al, 2016) and silver oxalate (Navaladian et al, 2006) is another possible way to produce AgNPs.

Reactions in liquid phase are usually carried out in macroscale reactors, but microreactors employing microfluidics or microemulsions are of growing interest. A microemulsion is a thermodynamically stable dispersion of surfactants, oil, and water (Wani et al, 2013), where the droplets are of 10-100 nm in size and can act as reactors to perform chemical reactions. More specifically, in aqueous droplets, silver salts are reduced to generate AgNPs. Different surfactants can be used for the microemulsion technique, such as sodium dodecyl sulphate (SDS) (Zhang et al, 2008), cetyltrimethylammonium bromide (CTAB) (Al-Thabaiti et al, 2008) and Triton X-100 (Wani et al, 2013).

Chemical reduction consists of three steps which are described as follow: i) the reduction of silver ions (Ag^{+}) to silver atoms (Ag^{0}) using reducing agents such as borohydrides (Lee et al, 2006), hydrazine compounds (Li et al, 2012), polyols (Kim et al, 2006), and sugars (Wang et al, 2005), ii) the nucleation and iii) the stabilisation of growing particles using surfactants like CTAB (Khan et al, 2011), or polymers like poly(vinylpyrrolidone) (PVP) (Kim et al, 2006) and poly (ethylene glycol) (PEG) (Roldán et al, 2013) (see Figure 2.2). Thiols (Aktara et al, 2019) and citrates (La Spina et al, 2020) are also widely used as stabilisers in the formation of AgNPs. Borohydrides (Lee et al, 2006), boranes (Rivero et al, 2013), hydrazine hydrate (Li et al, 2012) and aniline (Khan et al, 2011) are examples of strong reducing agents while ethylene glycol (Kim et al, 2006), glucose (Wang et al, 2005) and tannic acid (Ranoszek-Soliwoda et al, 2017) are weak reducing agents.

Homogenous nucleation takes place when a nucleus begins to form within a parent phase. This process can be described thermodynamically by the total free energy of a NP, which is determined as the sum of the surface free energy and the volume free energy. As the surface free energy is always positive and the volume energy is always negative, there is a maximum free energy where a stable nucleus with a given critical radius can be formed. The critical radius is the minimum size of a nucleus which can be formed in a solution without being redissolved.

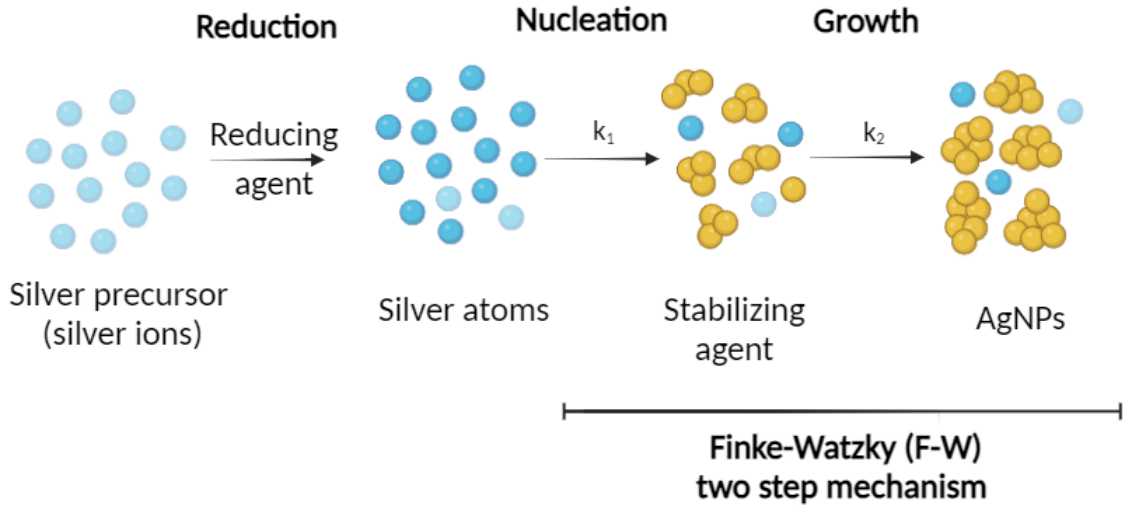


Figure 2.2 Steps of synthesis of AgNPs (Nathanael et al, 2022).

In general, the formed nuclei then serve as templates for crystal growth to give colloidal AgNPs with varied diameters (Thanh et al, 2014). The use of stabilising or capping agents, which adsorb or bind onto the surfaces of the NPs, prevents the further growth and aggregation of NPs and makes the colloidal system kinetically stable (Nagarajan, 2008).

Silver salts including $AgCl_4$ (Van Hyning & Zukoski, 1998), (Wuithschick et al, 2013), $AgCF_3COO$ (Glushko et al, 2015), $AgNO_3$ (Halder et al, 2021), $AgCH_3COO$ (Jana & Peng, 2003), (Dung et al, 2014), or $(PPh_3)_3$Ag-R (R=NO3 or Cl) (Andrieux-Ledier et al, 2013) can be used as silver precursors (Andrieux-Ledier et al, 2013). However, silver nitrate is the most common precursor due to its low cost and chemical stability (Ge et al, 2014). A growing list of viable chemicals for synthesis has been developing over the past few years and is summarized in Table 2.1.

Green chemistry has received a lot of attention in recent years in line with the increasing demands of more environmentally friendly, non-toxic, and clean approaches to the production of AgNPs and other materials. The use of toxic chemicals and solvents can be avoided using reducing and capping agents generated by plant systems such as *Melia dubia* (Kathiravan et al, 2014)*, Melia azedarach* (Jebril et al, 2020) or fruit extracts and fruit peels such as *Sterculia acuminata* (Bogireddy et al, 2016). For instance, *C.camphora* (Huang et al, 2007), *Lippia citriodora* (Cruz et al, 2010) coffee and tea extracts (Nadagouda & Varma, 2008) have been used to synthesize AgNPs as they contain alkaloids, flavonoids and carbohydrate compounds which were reported as reducing agents (Ahmad et al, 2019). Examples of green chemistry methods are also provided in Table 2.1.

The most common analytical techniques that have been used to characterize size distributions, morphology, stability, interactions and surface properties of nanoparticles including AgNPs are ultraviolet visible spectroscopy (UV-vis spectroscopy), X-ray diffractometry (XRD), Fourier transform infrared spectroscopy (FTIR), X-ray photoelectron

spectroscopy (XPS), dynamic light scattering (DLS), scanning electron microscopy (SEM), transmission electron microscopy (TEM) and atomic force microscopy (AFM).

SEM and TEM (Inkson, 2016) offer high resolution images of the nanoparticle (NP) morphology while XPS (Krishna & Philip, 2022) provide insights into the elemental composition and chemical state of the elements found on the NP surface. FTIR (Eid, 2022) is also useful to identify functional groups and chemical bonds on the NP surface. XRD (Epp, 2016) can provide information about the material's structure properties and DLS (Ross Hallett, 1999) is a rapid and accurate method for measurements about the particle size distribution and stability of NPs in a suspension. AFM (Bellotti et al, 2022) enables measurements for surface roughness, particle size and mechanical properties. UV-Vis Spectroscopy (Rizwan & Gwenin, 2021) is ideal for monitoring the optical properties and estimating the size of NPs based on their absorption spectra. For example, in the case of AgNPs, small particles (around 10-50 nm) generally have an absorption peak around 400 nm, while larger particles (approximately 100 nm) exhibit a peak that shifts toward longer wavelengths, close to 500 nm (De Leersnyder et al, 2019).

A very comprehensive comparison of the different analytical methods is described by Fissan et al (2014) who highlights the strengths and applications of each technique, providing a deeper understanding of their roles in nanoparticle characterisation. Each method can provide complementary information while their combined use can offer a thorough understanding of nanoparticle characteristics.

Table 2.1 Examples of chemical synthesis methods of AgNPs in batch reactors (Nathanael et al, 2022).

Method	Silver precursor	Reducing agent	Stabilising agent or surfactant	Particle size (nm)	Particle Shape	Activity/Application	References
Chemical reduction	$AgNO_3$	$NaBH_4$	Dodecanoic acid (DDA)	appr.7 nm	Spherical	Application as electrodes in printed circuit boards.	(Lee et al, 2006)
Chemical reduction	$AgNO_3$	$NaBH_4$	PVP	9.0 ± 2.1 nm	Spherical	Application as building blocks for the fabrication of NPs-based thin films.	(Li et al, 2012)
Chemical reduction	$AgCH_3COO$	$NaBH_4$	PVP	Not stated.	Not stated.	The prepared AgNPs functionalized with 4-ATP were combined with Fe_3O_4 NPs in order to apply in biomedicine.	(Dung et al, 2014)

Chemical reduction	$AgNO_3$	$NaBH_4$	Trisodium citrate	Appr.9.94 nm	Spherical and hemispherical	Antimicrobial activity against *Staphylococcus aureus*, *Escherichia coli*, *Escherichia coli* AmpC resistant and *Candida albicans.*	(Quintero-Quiroz et al, 2019)
Chemical reduction (micro emulsion)	$AgNO_3$	$NaBH_4$	Triton X-100	appr. 8 nm	Disc shaped	Antimicrobial activity against *Escherichia coli* and *Candida albicans.*	(Wani et al, 2013)
Chemical reduction	$AgClO_4$	$NaBH_4$	Without any stabilising agent.	Radius 5-8 nm. 20-30% polydispersity.	Spherical	Not stated.	(Polte et al, 2012)

Chemical reduction	$AgClO_4$	$NaBH_4$	PVP	Radius 5-7 nm. 15-20% polydispersity.	Spherical	Not stated.	(Polte et al, 2012)
Chemical reduction (microemulsion)	$AgNO_3$	$NaBH_4$	Natural biosurfactant, rhamnolipid and n-butanol as co-surfactant	6-15 nm	Spherical	Not stated.	(Xie et al, 2006)
Chemical reduction (microemulsion)	$AgNO_3$	$NaBH_4$	CTAB	Appr.40 nm	Cube shaped	Antimicrobial activity against *Escherichia coli* and *Candida albicans.*	(Wani et al, 2013)

Chemical reduction	(PPh_3) Ag-NO_3	Tert-butylamine borane (TBAB)	1-dodecanethiol	2.5 nm	Spherical	Not stated.	(Andrieux-Ledier et al, 2013)
Chemical reduction	(PPh_3) Ag-Cl	TBAB	1-dodecanethiol	4.8 nm	Spherical	Not stated.	(Andrieux-Ledier et al, 2013)
Chemical reduction	(Pph_3) Ag-Br	TBAB	1-dodecanethiol	3.4 nm	Spherical	Not stated.	(Andrieux-Ledier et al, 2013)
Chemical reduction	$AgNO_3$	$N_2H_4 \cdot H_20$	PVP	50-200 nm	Triangular	Application in surface-enhanced Raman scattering (SERS).	(Li et al, 2012)

Chemical reduction (microemulsion)	$AgNO_3$	$N_2H_4{\cdot}H_20$	Sodium bis (2-ethylhexyl) sulfosuccinate (AOT)	2-5 nm	Spherical	Antibacterial sector.	(Zhang et al, 2007)
Chemical reduction (microemulsion)	$AgNO_3$	$N_2H_4{\cdot}H_20$	SDS and isoamylalchohol as the co-surfactant	6.5-12.1 nm	Spherical	Not stated.	(Zhang et al, 2008)
Chemical reduction	$AgNO_3$	Aniline	CTAB	10-30 nm	Spherical	Not stated.	(Khan et al, 2011)
Chemical reduction	$AgNO_3$	Tannic acid	Sodium citrate	Appr.46 nm	Spherical	Not stated.	(Ranoszek-Soliwoda et al, 2017)

Chemical reduction	$AgNO_3$	Glucose	PVP. NaOH enhanced the speed of reaction.	20-80 nm	Spherical	Not stated.	(Wang et al, 2005)
Chemical reduction (polyol process)	$AgNO_3$	Ethylene glycol	PVP	17 ± 2 nm	Spherical	Not stated.	(Kim et al, 2006)
Thermal reduction	$AgCF_3COO$	Isoamyl ether	Oleic acid	7-11 nm	Spherical	Not stated.	(Lin et al, 2003)
Green chemistry (seed extract)	$AgNO_3$	Jack fruit seeds extract		22.12±1.05 nm	Not stated	Antibacterial activities against *Escherichia coli*, *salmonella Enterica Typhimurium*	(Chandhru et al, 2019)

Green chemistry (peel extract)	$AgNO_3$	Citrus sinensis peel extract	~35 nm	Spherical	Antibacterial activity against *Escherichia coli,* *Pseudomonas aeruginosa* and *Staphylococcus aureus*	(Kaviya et al, 2011)
Green Chemisty (leaf extract)	$AgNO_3$	*Melia dubia* leaf extract	~7.3 nm	Spherical	Anticancer activity against human breast cancer (KB) cell line.	(Kathiravan et al, 2014)
Green Chemisty (fruit extract)	$AgNO_3$	Fruit extract *Sterculia acuminata*	~10 nm	Spherical	Catalysis activity	(Bogireddy et al, 2016)

Green Chemisty (fruit extract)	$AgNO_3$	Fruit extract of *Phyllanthus emblica*	~39 nm	Spherical	Antimicrobial activity *in vitro* against the pathogen *Acidovorax oryzae* strain RS-2 of rice bacterial brown stripe	(Masum et al, 2019)
Green chemistry (seed extract)	$AgNO_3$	Seed extract of *Alpinia katsumadai*	~12.6 nm	Quasi-spherical	Cytotoxic effect against human gastric carcinoma SGC-7901 and antibacterial activity against Gram-positive bacterium *Streptococcus aureus* and the Gram-negative bacteria *Escherichia coli* and *Pseudomonas aeruginosa.*	(He et al, 2017)

Green Chemisty (leaf extract)	$AgNO_3$	*Moringa oleifera* leaf extract	~50 nm	Spherical and rectangular	Drug Delivery.	(Paul et al, 2020)

2.3 MICROFLUIDIC PRODUCTION OF SILVER NANOPARTICLES

Microfluidic devices offer numerous advantages compared to conventionally systems. According to a 2022 report released by the Allied Market Research, (Deshmukh, 2022) the global market of microfluidics is estimated to reach $158.1 billion by 2031.

These systems offer precise control over fluid behaviour and enable various applications such as chemical synthesis, diagnostics, drug discovery and DNA analysis (Niculescu et al, 2021). The most common fabrication routes of microfluidic devices involve photolithography, soft lithography, micromachining and 3D printing where microchannels and structures are created on substrates like glass, silicon or polymers (Scott & Ali, 2021).

Scaling down the reactor dimensions provides better control of the process of AgNPs synthesis and enables a low consumption and a high conversion of the reagents. Hence, the formation of undesired by-products and the waste produced are minimised, and the environmental impact is reduced (Badilescu & Packirisamy, 2012). By adjusting the supply of reagents for nucleation and growth, as well as varying the flow configuration, the size, shape and dispersity of particles can be controlled (Baber et al, 2017). Specifically for the synthesis of AgNPs, the reduction stage is fast (less than 200ms, according to Polte et al (2012) and mixing of silver precursor and other reactants is a critical stage to establish uniform reaction conditions.

Continuous-flow (Makgwane & Ray, 2014) and droplet-based production (Shembekar et al, 2016) are two of the main operational settings reported for microfluidic synthesis. Microfluidic flows are laminar, enabling a precise control of hydrodynamic conditions, with

slow mixing being balanced by reduced path lengths of diffusion. Continuous-flow production involves a monophasic liquid system comprised of the reactants (i.e., the precursor, the reducing agent, and the stabilisers) in aqueous solutions, as depicted in Figure 2.3A. Some of the main disadvantages of continuous flow microfluidic reactors are related to the classic laminar parabolic flow profile formed in the channel. The velocity distribution thus formed consequently causes a distribution of fluid residence times and the no-slip condition at the channel wall can lead to particle deposition and fouling or blockage of the channel. Performance of continuous flow reactors can be improved by employing channels with twists and turns to promote mixing (Wu et al, 2017) or by droplet-based operations.

In droplet microfluidics, discrete droplets are produced and manipulated using immiscible segmented liquid-liquid multiphase flows inside the microchannels. One of the liquid phases corresponds to an aqueous solution of the reactants and the other to an inert oil phase that carries the droplets through the channel, as shown in Figure 2.3 (B-D). A summary of relevant experimental studies on synthesis of AgNPs using microfluidic technology is presented in Table 2.2. Drop-based synthesis is usually comprised of three general stages: droplet formation, mixing of the reactants within the droplet, and chemical reactions resulting in the formation of AgNPs. Two primary operational settings for droplet-based synthesis are identified in the literature, one in which the reactants are brought together during the droplet formation step (e.g., Figure 2.3), and one in which the reactants are initially in separate droplets that collide and merge in the channel to initiate the mixing process and trigger the reactions. Various techniques such as crossflow

(commonly seen in T-junction setups), flow-focusing, and co-flow geometries (Anna, 2016) (see Figure 2.3) are utilised for droplet formation across the primary regimes: squeezing/dripping and jetting (Kovalchuk et al, 2019). It is noted that the majority of monodisperse droplets are formed within the dripping regime (Kovalchuk et al, 2018), suggesting its suitability for droplet production in microfluidic reactors. The size of the droplets is influenced by factors like interfacial tension during droplet formation and the viscosity ratio between the continuous and dispersed phases. Manipulating the flow rates of these phases allows for easy adjustment of droplet size. Determining the range of flow rates for the continuous and dispersed phases, ensuring reliable drop formation withing the dripping regime while achieving the desired drop size, can be accomplished through experimental investigation. Several parameters determine the successful coalescence of droplets as well, including the balance between the viscous, capillary, and inertial forces, the geometry of the channel, and the presence of surfactants (Shen et al, 2015). Experimental aspects of these topics have been discussed in numerous review papers (see for example Seemann et al (2012)).

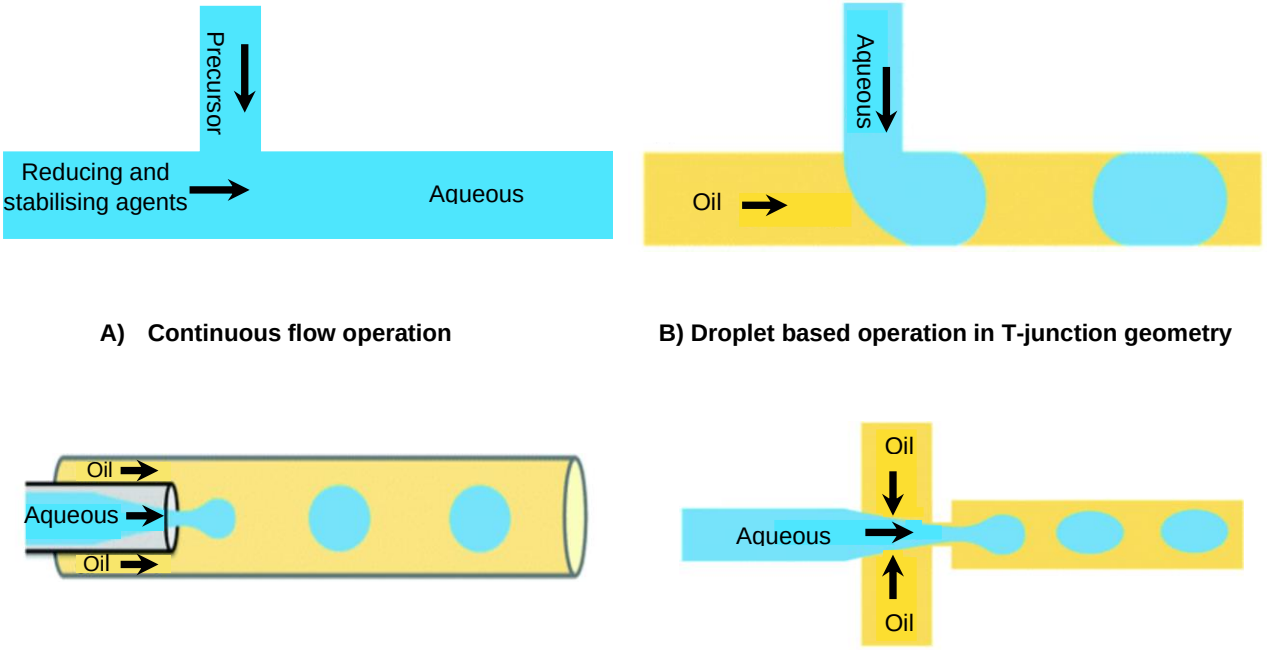


Figure 2.3 Different configurations of microchannels such as A) continuous flow operation, droplet based operation in B) T-junction geometry, C) co-axial geometry D) flow focusing geometry Reproduced from Shembekar et al (2016).

Table 2.2 Experimental investigations on microfluidic fabrication of AgNPs (Nathanael et al, 2022).

Silver Precursor	Reducing and stabilising agent or other reagents	Microfluidic type	Flow rates of continuous and dispersed phases	Size (nm)	References
$AgNO_3$	Borane dimethylamine (DMAB)/PVA and tween 80	Droplet-based microfluidics: Two phase flow system	Continuous phase/ oil flow rate: 5 mL/h Dispersed phase/water or reagent flow rate: 1mL/h	2.5±0.5 nm	(Wojnicki et al, 2019)
$AgNO_3$	Tannic acid/trisodium citrate	Droplet-based microfluidics: Y junction with straight and serpentines channels	Continuous phase/oil flow rate:60 and 80 µL/h. Dispersed phase/ reactant flow:16 and 32µL/h.	16/60 µL/h→~16.3 nm 16/80 µL/h→ ~12.8 nm 32/60 µL/h→~20.7 nm 32/80 µL/h→~22.3 nm	(Kašpar et al, 2019)

$C_3AgF_5O_2$ (silver pentafluoro propionate)	Trioctylamine and isoamyl ether at 100-140 ℃	Continuous flow tubular microreactor	0.08-0.7 mL/min	0.08 mL/min→8.7±0.9 nm 0.6 mL/min→ NPs varied between 3 and 12 nm	(Lin et al, 2004)
$AgNO_3$	$NaBH_4$/trisodium citrate	Co-axial microfluidic reactor	1, 2, 8 and 14 mL/min	1mL/min →3.1±1.6 nm, 2mL/min →3.3±2.2 nm, 8mL/min →5.6±2.7 nm and 14 mL/min →5.4±3.4 nm	(Baber et al, 2015)
$AgBF_4$	1-Butyl-3-methylimidazolium borohydride (BMIM-BH_4)	Droplet-based microfluidics: Multiple inlet T-junction device	Continuous phase/oil flow rate: 10 mL/h Dispersed phase/ reagent flow rates: 0.5 mL/h	3.73±0.77 nm	(Lazarus et al, 2012)

$AgNO_3$	Glucose/PVP	Piezoelectric actuated three phase flow pulsating mixing device	Inlets flow rate: 3.5 mL/min	29.11±3.98 nm	(Liu et al, 2018a)
$AgNO_3$	$NaBH_4$/PVP and EDTA as complexing agent	Droplet-based microfluidics: T-junction device	10-30 mL/h for both continuous phase/oil stream and dispersed phase/aqueous stream	10 mL/h→4.9±1.2 nm 30 mL/h→7.6±1.8 nm	(Xu et al, 2016a)

2.4 MODELS USED TO DESCRIBE SILVER NANOPARTICLES FORMATION.

Chemical synthesis of AgNPs is a dynamic process, thus, kinetic information, such as rate constants and mechanisms, is required to achieve the desired size and dispersity of particles. A brief description of LaMer model and Ostwald ripening mechanism is provided in this section, followed by detailed discussion of the Finke-Watzky two-step mechanism which was identified as the most suitable model to describe the autocatalytic synthesis of different metal-NPs like silver, gold and palladium (Özkar & Finke, 2017), (Luty-Błocho et al, 2017), (Wojnicki et al, 2016).

The first mechanism used to describe NPs synthesis was developed by LaMer & Dinegar (1950), who examined the synthesis of sulphur sols from the decomposition of sodium thiosulfate. According to LaMer model, synthesis starts with a single instantaneous nucleation process. After that, nucleation ceases to occur because of low monomer concentration. Following nucleation, growth takes place by the diffusion. More specifically, this model suggests that a spherical volume with radius h has a concentric spherical nucleus with radius x where growth takes place on the surface of the spherical nucleus upon the arrival of a diffusing monomer. Eq. (2.1) shows the mathematical expression for the temporal evolution the radius x:

$$\frac{\mathrm{d}}{\mathrm{dt}}(\mathrm{x}^2) = [\mathrm{C_{ss}} - \mathrm{C_s(t)}]\frac{2\mathrm{D}}{\rho} - \frac{2\mathrm{D}}{\mathrm{h}^3}\mathrm{x}^3, \tag{2.1}$$

where $\mathrm{C_{ss}}$ is the supersaturation concentration of sulfur, $\mathrm{C_s(t)}$ is the concentration of the soluble “monomer” above the saturation concentration as a function of time, D is the

diffusion coefficient of soluble sulfur monomers in the solution, ρ (rho) is the bulk density of elemental sulfur, h the outer radius of the spherical region where diffusion is occurring. Note the concentration $\mathrm{C_{ss}} - \mathrm{C_s(t)}$ is in $^{\mathrm{kg}}/_{\mathrm{m^3}}$.The Ostwald ripening mechanism was expressed by Lifshitz & Slyozov (1961) and Wagner (1961) (LSW theory). The mathematical theory of this growth model is based on the high solubility and the surface energy of smaller particles in a solution, which redissolve, thus allowing the larger particles to grow further. Piwoński et al (2016) and Shukla et al (2009) discussed Ostwald ripening mechanism in the growth of silver and silver halide particles, respectively. In this model, the radius r of the particle varies with time, as described in Eq. (2.2):

$$\frac{\mathrm{dr}}{\mathrm{dt}} = \frac{\mathrm{D}}{\mathrm{r}}\left(\Delta - \frac{\mathrm{a}}{\mathrm{r}}\right), \tag{2.2}$$

where $\Delta = \mathrm{c} - \mathrm{c}_\infty$, is the difference of current concentration (c) and saturated concentration (c_∞) of a solution, D is the diffusion constant, and $\mathrm{a} = {}^{2\sigma \mathrm{u c}_\infty}/_{\mathrm{RT}}$ is defined by the surface tension σ, solubility c_∞, atomic volume u of the solute, gas constant R, and temperature T.

The autocatalytic behaviour of transition metals like silver and gold cannot be described through LaMer model. This model requires super saturation conditions to initiate burst nucleation while the autocatalytic mechanism where the product of reaction acts as a catalyst for the same reaction takes place for reactions far below supersaturation conditions (Ashley et al, 2017).

The Finke-Watzky two-step model (Watzky & Finke, 1997) assumes a slow continuous nucleation followed by an autocatalytic growth step. The concentration of precursor A (e.g., Ag^{+}) remains almost constant for a long time and then a quick sigmoidal decrease is observed. During the first step, there is a direct formation of nuclei from precursor A through a pseudo-first order reaction, illustrated in Eq. (2.3). The nucleation step includes all processes leading up to the appearance of first nucleus, including the chemical reduction of precursor A using a reducing agent.

$$\text{Nucleation: } A \xrightarrow{k_1} B \quad ; \quad n_0 = k_1[A], \tag{2.3}$$

In Eq. (2.3), k_1, n_0, and $[A]$ correspond to the nucleation kinetic constant, the nucleation rate, and the molar concentration of the precursor, respectively. After nucleation, an autocatalytic growth of B nuclei and the formation of B particles follows, as shown in Eq. (2.4):

$$\text{Growth: } A + B \xrightarrow{k_2} 2B \quad ; \quad G = k_2[A][B], \tag{2.4}$$

where k_2, G, and $[B]$ correspond to the growth kinetic constant, the growth rate, and the molar concentration of the silver in nuclei and NPs, respectively. Usually, a stabilising agent is used in this step to stabilise particles and avoid aggregation. The overall reaction rate can be expressed as shown in Eq. (2.5):

$$-\frac{d[A]}{dt} = \frac{d[B]}{dt} = k_1[A] + k_2[A][B] \tag{2.5}$$

Assuming that the concentration of silver in nuclei and NPs [B] changes with time t as $[B](t) = [A]_0 - [A](t)$, where [A](t) is the concentration of silver in precursor, including silver atoms and particles of prenuclear size at time t and $[A]_0$ is the initial concentration of the silver precursor, [A] depends on time as shown in Eq. (2.6):

$$[A](t) = \frac{\frac{k_1}{k_2} + [A]_0}{1 + \frac{k_1}{k_2[A]_0} * \exp(k_1 + k_2[A]_0)\, t}. \quad (2.6)$$

Values of rate constants k_1 and k_2 can be obtained from fitting experimental data to Eq. (2.6) or from its linearized form (Eq. (2.7)):

$$\ln\left(\frac{[A]_0 - [A]}{[A]}\right) = \ln\left(\frac{k_1}{k_2[A_0]}\right) + k_2[A]_0 t, \quad (2.7)$$

obtained under assumptions $k_2[A]_0/k_1 \gg 1 \text{ and } [A] < [A]_0$ (Amirjani & Haghshenas, 2018).

The Finke-Watzky mechanism has been widely used to describe the kinetics of AgNPs synthesis. Various methods have been employed to determine the rate constants for nucleation (k_1) and growth (k_2). Some relevant examples are described below and summarized in Table 2.3. Kytsya et al (2015) studied the kinetics of the synthesis of AgNPs using the method of direct potentiometry. AgNPs were obtained by the reduction of silver nitrate with hydrazine at basic pH and using sodium citrate as stabilising agent. The authors verified the use of the Finke-Watzky two-step mechanism in AgNP formation

and reported that the nucleation of AgNPs is limited by the reduction of silver ions to silver atoms. For this reason, they proposed a surface-dependent model for AgNP growth based on Finke-Watzky model, which leads to equations that describe the total reaction rate. A similar study is described by Sandoe et al (2019), who measured the change in AgNP surface plasmon resonance and change in silver ion concentration, during citrate method for the synthesis of AgNPs using UV-visible spectroscopy (indirect method), ion-selective electrode potentiometry and atomic absorption spectroscopy (AAS) (direct method). The sigmoidal kinetic curves obtained were described by Finke-Watzky model and the rate constants for nucleation (k_1) and growth (k_2) were estimated for each method separately. Sandoe et al (2019) showed that the average values of k_1 and k_2 overlapped within experimental error between the different methods. Amirjani & Haghshenas (2018) also indicated that the nucleation and growth of AgNPs is very similar to the Finke-Watzky mechanism. The authors used three different approaches to model the kinetics of the synthesis process including linear fitting, non-linear fitting and a modified Finke-Watzky mechanism by considering a reversible pseudo-first order reaction for the nucleation step. Their kinetic data were obtained by borohydride reduction with PVP and showed significant differences between the three different approaches. In the case of 0.0008 g PVP and linear Finke-Watzky mechanism, k_1 and k_2 were estimated to be 0.034 ± 0.0001 min^{-1} and 911 ± 6 $M^{-1}min^{-1}$, respectively. For the same conditions but non-linear fitting, k_1 and k_2 were calculated to be 0.031 ± 0.01 min^{-1} and 574 ± 5 $M^{-1}min^{-1}$, respectively. By using a modified Finke-Watzky mechanism, the authors developed a kinetic model closer to the synthesis system with k_1 and k_2 equal to 1.025 ± 0.003 min^{-1} and 107.7 ± 5 $M^{-1}min^{-}$

^{1}, respectively. By estimating k_1 and k_2 at different concentrations of PVP, they also showed that PVP can hinder both the nucleation and growth stages.

The improvement and development of kinetic models for AgNPs synthesis is still an open field of research. Specifically, there is a need to develop a kinetic model suitable for using in numerical simulations which simultaneously account for the process of hydrodynamics, as will be described in detail in the upcoming sections.

Table 2.3: Examples of nucleation (k_1) and growth (k_2) constants of Finke-Watzky model for synthesis of AgNPs using different methods and reagents. All the rate constants k_1 and k_2 were converted into min^{-1} and $M^{-1}min^{-,1}$ respectively from the original publications (Nathanael et al, 2022).

Method/Reagents	k_1 (min^{-1})	k_2 ($M^{-1}min^{-1}$)	References
Chemical reduction/Silver nitrate, sodium hydroxide, hydrazine hydrate, sodium citrate dihydrate at 20°C.	9×10^{-6} min^{-1}	959 M^{-1} min^{-1}	(Kytsya et al, 2015)

Chemical reduction/Silver nitrate (0.2mM), sodium citrate (1 mM), (UV-visible spectroscopy).	$(2.2\pm0.4) \times 10^{-5}$ min^{-1}	(0.53 ± 0.01) $M^{-1}min^{-1}$	(Sandoe et al, 2019)
Microwave technique/ Silver nitrate, ethylene glycol, PVP at 130-180^{0}C	$(1.3\pm0.6) \times 10^{-8}$ min^{-1} at 180^{o}C $(2\pm0.2) \times 10^{-5}$ min^{-1} at 130^{o}C	$(24.1\pm0.6) \times 10^{-2}$ $M^{-1}min^{-1}$ at 180 ^{o}C $(1.65\pm0.02) \times 10^{-2}$ $M^{-1}min^{-1}$ at 130^{o}C	(Özkar & Finke, 2017)
Chemical reduction/Silver nitrate (2.5mM), trisodium citrate dihydrate (0.1 M), sodium borohydride (1.25mM, PVP (7.2×10^{-6} mole) (non-linear fitting).	0.031 ± 0.01 min^{-1}	574 ± 5 $M^{-1}min^{-1}$	(Amirjani & Haghshenas, 2018)

Photoreduction of silver perchlorate in water/AOT/benzene water in oil(w/o) microemulsions.	9×10^{-3} min^{-1}	71×10^{-2} $M^{-1}min^{-1}$	(Harada et al, 2010)
Reduction of silver nitrate (0.012M) by hydrazine (0.66 M) in the reverse micelles of oxyethylated surfactant Triton N-42 at 25°C.	9.59×10^{-3} min^{-1}	1.848×10^{4} $M^{-1}min^{-1}$	(Tatarchuk et al, 2013)

2.5 PARAMETERS AFFECTING THE PHYSICOCHEMICAL PROPERTIES OF AgNPs

Since well-defined properties of AgNPs are necessary for many industrial applications, the selection and control of the reaction conditions to achieve a reproducible synthesis process is critical. Some experimental parameters can be tuned to control AgNPs size, shape, and stability, including reagents concentration, reaction temperature, pH of the solution, use of a complexing agent, and mixing rate, among others.

Firstly, the size and shape of AgNPs can be controlled by adjusting the type and concentration of the reducing agent and silver precursor (Calderón-Jiménez et al, 2017), (Siddiqi et al, 2018). Sobczak-Kupiec et al (2011) found that the increase in the concentration of the precursor used (silver nitrate) leads to larger particles because of an increased collision frequency. By preparing AgNPs using different silver phosphine precursors, such as RAg (PPH_3)n (R=Cl, Br, or NO_3 and n=1 or 3), with tert-butylamine borane (TBAB) in the presence of dodecanethiols (C_{12}), Andrieux-Ledier et al (2013) showed that the nature of the functional group in the silver precursor affects the AgNPs size as well. The authors assumed that the small raise of the redox potential (NO_3Ag (PPH_3) > BrAg (PPH_3) > ClAg (PPH_3)) results in a significant rise of the nucleation rate and hence a reduction in the size of AgNPs from Cl to Br and Cl to NO_3, respectively.

Regarding the type of reducing agent, Demchenko et al (2020) showed that decreasing redox potentials of reducing agents results in larger NPs. Specifically, use of sodium borohydride ($NaBH_4$) as a strong reducing agent can facilitate instant nuclei generation, leading to the formation of smaller NPs, while a weaker reducing agent, such as ascorbic acid, produces bigger NPs. When using weak reductants, the reaction rate can be raised by raising the temperature (Ge et al, 2014). Skrabalak et al (2008) presented a study on how the polyol synthesis can be used to produce AgNPs with different shapes, such as nanowires and nanocubes. They showed that heating ethylene glycol in air results in its oxidation to glycolaldehyde (GA), a powerful reducing agent. The temperature of reaction strongly affects the amount of GA produced and hence the reduction rate.

A very comprehensive review about the different approaches that can be used for the synthesis of AgNPs of a desired size and shape is provided by Mukherji et al (2019). As another example of the temperature effect, Kaviya et al (2011) prepared spherical AgNPs at room temperature (25 ℃) and 60 ℃ using citrus sinensis peel extract as the reducing and capping agent. The sizes of AgNPs were 35 nm and 10 nm at 25 ℃ and 60 ℃, respectively. Similarly, Liu et al (2020) examined the effect of temperature on the nucleation and growth kinetic constants. They showed that the nucleation rate constant increases sharply at high temperatures, while the growth rate constant rises linearly with the reaction temperature. The authors concluded that the decrease of particle size at high temperatures can be attributed to the sharp rise in the nucleation constant instead of the reduced growth rate constant. For microfluidic synthesis, glass-based microreactors enable broad temperature control due to the thermal stability of borosilicate glass, which remains stable at temperatures up to 1500°C (Tang et al, 2021). In contrast, PDMS devices allow for temperature control only within a limited range, typically up to 70 ℃.

As mentioned previously, the morphology and size of AgNPs can be controlled by the addition of complexing agents. Some common complexing agents include ammonia (NH_3) (Zhao et al, 2010) and ethylenediaminetetraacetic acid (EDTA) (Feng et al, 2011). V. Goia & Matijević (1998) demonstrated the changes in redox potentials of Ag^+ as a consequence of complex formation. For example, NH_3 reacts with Ag^+ to form the complex [$Ag(NH_3)_2^+$] (Peard & Pflaum, 1958). This complex is more stable and more difficult to reduce to Ag^o compared to Ag^+, as indicated by its lower redox potential of 0.38 V versus 0.799 V for Ag^+/Ag^o. When the reaction occurs in the presence of $Ag(NH_3)_2$, ethylene glycol and

PVP, the growth of silver grains is supressed resulting in smaller size of AgNPs, as investigated by Zhao et al (2010). The presence of ammonia can reduce the concentration of free silver ions in the solution, thus influencing the equilibrium between AgNPs/Ag+ (Kostigen Mumper et al, 2013). This controlled environment facilitates the formation of smaller and more uniform AgNPs. An interesting example in the literature is also described by Feng et al (2011), reported that Ag/EDTA complex significantly reduces the reaction speed of AgNPs and thus provides good selectivity during crystalline growth.

Another factor that affects reaction chemistry and thus kinetic constants, particle size, shape and AgNPs' aggregation due to change of zeta potential, is pH. Alqadi et al (2014) studied the effect of pH on the aggregation of AgNPs synthesized by chemical reduction and showed that the size decreases with an increase in pH. They also suggested that this difference can be attributed to the difference in the reduction rate of silver precursor.

Marciniak et al (2020) studied the effect of pH on the size of AgNPs using citric acid, as reducing agent. At alkaline conditions, they observed that the charges of citrate (pka =6.4) change and dicarboxyacetone (DCA) is produced as a by-product of the decarboxylation of citrate during silver reduction. At a pH value of 12, there is a completely hydrolysed DCA^{2-} and Cit^{3-} species, and a higher reducing ability leading to faster reduction of the silver ions during the growth stage. Similarly, Qin et al (2010) presented that high pH improves the reducing power of ascorbic acid and smaller size particles can be obtained. The influence of pH on the shape of AgNPs has been discussed in detail by Dong et al (2009). The authors used citrate reduction of silver nitrate under high and low pH (from 5.7 to 11.1) and developed a stepwise reduction method to have a better control over the

shape of AgNPs. At high pH, AgNPs were both spherical- and rod-like due to fast reduction rates of silver nitrate, while at low pH AgNPs were triangle- and polygon-shaped as a result of slow reduction rate of silver precursor. They proposed a fast nucleation stage at high pH followed by a slow growth stage in lower pH to improve the balance between the nucleation and growth processes.

The effect of mixing on AgNPs size has also been investigated. Ng et al (2012) synthesized AgNPs through a green chemistry method using a rotating packed bed reactor. The intense mixing and high mass transfer rates led to more uniform and smaller-sized AgNPs. Similarly, Kisyelova et al (2016) used a stirred tank reactor (STR) with a turbine impeller and a spinning disc reactor (SDR). They showed that these reactor configurations can intensify the mixing process and reduce the average size of AgNPs from 31 to 16 nm.

Generally, AgNPs tend to agglomerate and gradually grow into larger particles to reduce their overall surface energy. Therefore, to preserve the targeted mean size and particle size distribution of synthesized AgNPs, it is important to use a stabilising agent. Multiple mechanisms of AgNPs stabilisation by capping agents are found in the literature, including steric, electrostatic, or electro steric stabilisation. Ionic stabilisers (e.g., citrate) generate a charged layer around particles that serves as an electrostatic barrier to agglomeration. More specifically, repulsive forces are created between NPs and, provided the electric potential related to the double layer is high enough, the electrostatic repulsion will inhibit aggregation (Roucoux et al, 2002). According to Badawy et al (2010), uncoated AgNPs at pH 8.9 have Z-potential -22 mV, while AgNPs stabilised electrostatically through the

ionization of the carboxyl groups of citrate have -40mV. The electrostatic stabilisation can be influenced by pH, temperature, and concentration of stabilising agent.

On the other hand, non-ionic compounds can be adsorbed onto the surface of the NPs and provide a steric protective layer which can limit the free motion of NPs in the solution (Roucoux et al, 2002), (Manojkumar et al, 2016). The thickness of this protective layer depends on the nature and length of the stabilising agent. The incorporation process of non-ionic molecules depends on surface properties of NP. For example, noble metals such as silver are well bonded with thiols, amines, and cyanides (Guerrini et al, 2018). Examples of non-ionic stabilisers are PVP and PEG. It has been reported that AgNPs sterically stabilised by PVP and PEG are more stable than citrate-coated AgNPs, which weakly interact with the Ag core and stabilise AgNPs through charge repulsion (Tejamaya et al, 2012). However, the main advantage of citrate in AgNPs synthesis is the opportunity of further functionalisation of NPs as citrate can be easily replaced by other compounds. This is a consequence of the weak interactions of citrate molecules with metal surfaces.

An interesting study that combined the two mentioned protective mechanisms was conducted by Wang et al (2020). They used the steric hindrance effect of PVP and the charge repulsion effect of sodium tripolyphosphate (STPP) to observe differences in dispersity, stability, and redox process of AgNPs synthesis. The synergistic effect of both PVP and STPP limited the reaction rate of silver ions preventing by this way the polydispersity of NPs.

Aside from the parameters directly involved in AgNPs synthesis, storage conditions, storage time, and the stabilisation mechanism can also affect the temporal evolution of

the AgNPs properties. According to Izak-Nau et al (2015), AgNPs dispersion can age during storage and the most significant factors affecting ageing are temperature, exposure to daylight, and the nature of the stabilising agent. The changes that can be seen during ageing are related to processes of agglomeration, dissolution, or oxidation. In the case of dispersions stored at room temperature and exposed to daylight, an increase in particle size was observed. An increase of temperature results in an increase of NP collision rate, which causes agglomeration, while the exposure to daylight induces the photo-reduction of already dissolved Ag ions and the generation of new AgNPs increasing the sample's dispersity. Regarding the nature of the stabilising agent, it was found that AgNPs coated by neutral stabilisers demonstrate better stability over time compared to the AgNPs stabilised electrostatically. Particularly, Izak-Nau et al (2015) showed that negative and positive capping agents may cause agglomeration at room temperature. Other observed effects during ageing are related to dissolution and oxidation of AgNPs, which may change the composition of samples and modulate their toxicity. For example, in the case of negatively charged AgNPs samples, it was shown that longer storage time leads to an increase in the amount of Ag ions. Similarly, positively charged AgNPs exhibited a similar trend being the most toxic, causing damage to cell membranes and cell death. In contrast, neutral AgNPs showed the least impact on cell viability measures. An explanation for this behaviour could be related to the stabilisation mechanism as neutral AgNPs were stabilised sterically, while positively and negatively charged AgNPs were stabilised electrostatically (Izak-Nau et al, 2015).

2.6 SYNTHESIS AND PROPERTIES OF SILVER NANOPARTICLES: PHYSICS-BASED MODELS

Numerical simulations using physics-based models have become a valuable tool for optimizing the synthesis of AgNPs. By conducting computational simulations at various levels, significant operational parameters influencing the final properties of AgNPs have been identified (Yoneya & Sugisawa, 2019), (Liu et al, 2018b), (Kyrychenko et al, 2017). Over the years, extensive investigations have been conducted at different scales, including molecular dynamics (MD) simulations at molecular level and population balance modelling (PBM) and CFD at the meso- and macroscale. These studies aim to predict the behavior of the reacting system during NPs synthesis and elucidate the final properties of AgNPs, along with understanding their molecular interactions with other components.

For instance, Zeng et al (2007) examined the growth mechanisms of AgNPs when various surfactants were employed as capping agents using MD simulations. The aim was to achieve enhanced control over particle morphology, which is crucial for diverse applications. The growth mechanisms were investigated by assessing the interaction energies between the surfactants and different Ag crystalline planes (100,110,111). The surfactants tested included bis(2-ethylhexyl) sulfosuccinate (AOT), 1-dodecanethiol ($C_{12}SH$), and cetyltrimethylammonium bromide (CTAB). Results revealed that all surfactants exhibited a preference for absorption on the (111) plane, characterized by the lowest interaction energy. This preference was found to hinder crystal growth in that direction, thereby influencing the final shape of the nanoparticles. Balankura et al (2020) conducting molecular scale investigations contributed insights into the synthesis and

aggregation mechanism of PVP-coated triangular Ag nanoplates under vacuum conditions and in the presence of ethylene glycol (EG) solvent. Their findings suggest that PVP molecules continuously diffuse or desorb, around the aggregate to create vacant spaces between particles. Additionally, they observed that the free energy barrier required for attachment is considerably higher for face-to-face aggregation compared to lateral aggregation. Milek & Zahn (2014) also conducted MD simulations to investigate the formation of AgNPs from silver nitrate in EG solution. This study focused on examining the association of Ag^{+} ions and the dynamic evolution of Ag clusters' structure under varying redox potential conditions. The simulation outcomes conclusively demonstrated the pivotal influence of redox potential on both the overall shape and the internal structure of the cluster.

The studies outlined above underline the significance of MD simulations in understanding how diverse particle sizes and shapes can be achieved through the use of different stabilising agents. This knowledge is crucial for guiding the design of novel stabilising agents and synthesis pathways, facilitating the selection of reactants to achieve specific nanoparticle properties.

However, to incorporate additional phenomena such as hydrodynamics, models operating at meso- and macro scales studies are needed. Efforts have been made in multiscale computational modelling to describe synthesis processes in microfluidic continuous and droplet-flow reactors, further advancing the understanding of nanoparticles synthesis such as the works of Liu et al (2014b) and Kašpar et al (2019).

Liu et al (2014b) utilised a combined approach involving PBM and CFD with reactive kinetics to forecast the PSD of AgNPs produced in a continuous flow microchannel. The PBM framework is based on a mesoscale depiction of a collection of discrete sub-entities, with their PSD evolution described by a population balance equation (PBE). The PBE represents a kinetic transport equation in terms of the number density function (NDF), which quantifies the number of particles possessing a specific property or internal variable per unit volume. The PBE version introduced by Liu et al (2014b) is based on the assumption that the AgNPs population displays polydispersity solely in particle size, thus making NDF univariate. Additionally, the transport of the NDF via molecular diffusion was neglected, along with terms representing discrete events such as particle agglomeration or de-agglomeration.

The combined experimental and CFD investgation by Kašpar et al (2019) explored mixing phenomena within serpentine channels for the synthesis of AgNPs. In this study, AgNPs were synthesized via the reduction reaction involving silver nitrate and tannic acid in the presence of trisodium citrate as stabilising agent. Reactants and continuous phase (mineral oil) flows meet at a junction where aqueous droplets with reactants were formed and then traversed through a meandering channel.

Unlike typical approaches (Sarrazin et al, 2006),(Madadelahi & Shamloo, 2017) CFD simulations in this study did not employ a volume of fluid (VOF) method. They utilised a field-based level set approach incorporating a conservation equation for the level set function. Computational modelling incorporated tracer particles to monitor the mixing process within the droplet, aligning with the aforementioned methodology.

The findings form the experimental and CFD analyses provided valuable insights into droplet formation and mixing processes. Notably, the mixing analyses confirmed earlier observations regarding the impact of channel bends on droplet mixing efficiency. Simulation results revealed that, after 40 milliseconds of operation, droplets passing through straight channels achieved only 67% mixing efficiency, whereas those navigating meandering channels achieved approximately 88% mixing efficiency at equivalent flow rates.

2.7 DESIGN OF EXPERIMENTS AND RESPONSE SURFACE METHODOLOGY

The design and optimisation of synthesis of AgNPs is an inherently complex process which involves many variables. For example, the degree of mixing of reagents (Kisyelova et al, 2016), redox potentials of reducing agents (Demchenko et al, 2020), reaction temperature (Kaviya et al, 2011) and pH of the solution (Alqadi et al, 2014) are key parameters which can be tuned to control the reduction rate of silver ions and therefore the physicochemical characteristics of nanoparticles. Employment of one factor at time (OFAT) experimentation (Eckert & Trinh, 2016) to elucidate the effect of these variables individually whilst the others are held constant is a time and resource intensive process which ignores the effect of interactions between variables and results in the development of a poor prediction.

To overcome these limitations, design of experiments (DoE) methods can be exploited (Mason et al, 2003). DoE methodology (Durakovic, 2017) is a statistical tool used to find the relationship between a set of independent variables (input variables) and a dependent

variable (measured response variable) where factors are the input experimental parameters which can be quantitative or qualitative and levels are the different values that factors can take.

The most commonly used designs in scientific and engineering disciplines include full and fractional factorial (Altayb et al, 2021), (Kania et al, 2021), (Echeverría et al, 2021) and response surface designs (Nourafkan et al, 2017), (Ayyubi et al, 2022), (Ho et al, 2022). Full factorial design (FFD) (Antony, 2014a) contains all possible combinations of selected factors and levels. Although it provides the best insight into a system, FFD might generate a large set of experiments and be very expensive in terms of cost and time if the number of factors and levels are high. Conversely, fractional factorial design (Antony, 2014b) focusses on the main variables that affect the response (interactions are usually confounded) with the minimum possible number of runs (Mason et al, 2003).

Designs associated with response surface methodology (RSM) include central composite design (CCD), Box-Behnken design (BBD) and non-standard designs such as D-optimal design.

These designs are used to provide an understanding of the system and the relationship between factors and responses and also to enable system optimization using minimum required experimental runs (Montgomery, 2013) . CCD (Wagner et al, 2014) is based on factorial designs where the centre points are augmented with a group of axial points called star points to estimate the curvature, while in BBD (Das & Dewanjee, 2018), there are no axial points and the possible combinations of experimental points are placed at the centre points of the edges of experimental domain. D-optimal design (Montgomery, 2013) is an

alternative to consider in cases where there is an irregular experimental region, a non-standard model that deviates from the usual first or second order ones or an unusual sample size requirement.

The application of DoE has been expanded to many industry sectors including pharmaceutical, (Ho et al, 2022), (Baghaei et al, 2021), (Baroutaji et al, 2019) and food (Encina-Zelada et al, 2019),(Santos et al, 2018) as a part of design, development and optimisation of products and processes. There are a few studies to optimize AgNPs formulations using a systematic experimental design with main focus on the control of reactants used.

Prema et al (2022) optimized batch synthesis of AgNPs using a central composite design (CCD) with three independent variables ($AgN0_3$ concentration, green tea extract concentration and temperature) at three different levels. The dependent variables were the size of AgNPs using their UV absorbance, zeta potential and polydispersity index. A second order polynomial quadratic equation was used to describe the relationship between the different factors across each response and used to find the optimised conditions (1 mM $AgN0_3$, 0.5% green tea extract and 80 ^oC).

Sarkar et al (2021) optimized the yield of AgNPs produced from Eucalyptus globulus fruit extract using a batch process. The authors used factorial design to identify the significant parameters and a CCD with three factors ($AgN0_3$ concentration, dose of the extract, time) at two levels. They found that the optimal conditions for maximum yield of AgNPs are $AgN0_3$ 1.8 mM, 10% fruit extract and 12 h.

2.8 DATA SCIENCE APPROACHES FOR THE OPTIMIZATION OF NANOPARTICLE'S SYNTHESIS

Machine learning (ML) combined with microfluidic synthesis offers a promising approach to tackle the repeated and extensive experimental tests and accelerate the development of efficient protocols (Chen & Lv, 2022).

Recently, artificial intelligence (AI) has become a valuable aid for many scientific and engineering fields, including nanotechnology, due to its contribution in data acquisition and processing improvements (Hrvat et al, 2021), (Zhang et al, 2021),(Adir et al, 2020). ML algorithms which are a subset of AI have been employed specifically in the synthesis of AgNPs to predict their characteristics (Sun et al, 2017), (shafaei & Khayati, 2020), (Findlay et al, 2018) or perform other kinds of decision making under uncertainty (Liu et al, 2021). Mekki-Berrada et al (2021) combined a deep neural network (DNN) and Gaussian process-based Bayesian optimization (BO) to synthesize AgNPs with a desired absorbance spectrum in a droplet microfluidic device. They used the flow rates of silver seeds ($\mathrm{Q_{seed}}$), of silver nitrate, SN ($\mathrm{Q_{AgNO_3}}$), of trisodium citrate, TC ($\mathrm{Q_{TC}}$) and polyvinyl alcohol, PVA ($\mathrm{Q_{PVA}}$) as input parameters and efficiently predicted the desired plasmon resonance for the reaction synthesis. Sattari & Khayati (2020) applied a Gene Expression Programming (GEP) to predict the size of AgNPs prepared by a green synthesis route. The proposed predictive model with coefficient of determination, $\mathrm{R^2}$= 0.9961, mean absolute error, MAE = 0.2545, and root relative square error, RSME= 0.0668 showed that the initial concentration of silver precursor and plant extract were the most influential parameters for the final particle size. Other relevant work used to predict the final particle

size of AgNPs is shown in Shabanzadeh et al (2013). In general, it is important to mention that the accuracy of models is strongly dependent on the quality and quantity of data used for training, testing and validation.

Decision trees (DT) are an established keystone in ML literature (Myles et al, 2004) as a powerful tool for prediction, interpretation and data manipulation. More specifically, a decision tree is a supervised learning algorithm which sorts a population into segments. This approach looks like an inverted tree with a root node, some internal nodes and leaf nodes. The root node, always positioned at the top of the tree structure, represents the variable that effectively divides or splits the data into subsets based on certain criteria (Aaboub et al, 2023). For example, these criteria could be Chi-square (Song & Lu, 2015) which finds statistically significant splits, or entropy, (Aning & Przybyła-Kasperek, 2022) that measures how disordered the data is. As you move down the tree, each internal node continues to split the data further based on additional variables or conditions. Eventually, at the bottom of the tree, the leaf nodes present the final outcomes or predictions resulting from a combination of these decisions. A decision pathway is presented by a line connecting the root node with one of the leaf nodes (Song & Lu, 2015). Compared with deep learning approaches (LeCun et al, 2015), the advantages of a tree-based algorithm are the good interpretability of the constructed models and the low computational cost. It can identify, in a linear way, information and relationships that can be used to design future experiments and analyse data (Myles et al, 2004). A limitation is that it can display overfitting or underfitting within a small data set (Song & Lu, 2015).

Data science algorithms have been applied not only to forward problems but also to inverse modelling methods (Hassan, 2020), (Vallone et al, 2023),(Wang et al, 2021). Inverse design that predicts conditions enabling required size of nanoparticles has a critical role in industry. Typically, the required properties for a specific application are known, and the goal is to determine the protocol to make this possible. For example, by providing the chemical synthesis protocol and the desired size, inverse modelling can identify the parametric space for the hydrodynamic conditions. The studies mentioned below are based on simulation data rather than experiments. It is important to note that, to the best of current knowledge, there is no experimental validation for inverse design of nanoparticles. For instance, Ma et al (2018) examined the application of deep-learning model in design and optimization of three-dimensional chiral nanoparticles. These nanoparticles exhibit chiroptical responses, meaning they have the ability to interact differently with left- and right-circularly polarized light at specific wavelengths. This unique property makes them highly useful in advanced optical and photonic applications, including sensors, and technologies designed for precise control and manipulation of light. The study utilized a deep-learning framework consisting of two bidirectional neural networks combined through a partial stacking strategy. These networks were trained on a large dataset derived from simulated optical responses of various metamaterial structures. The design parameters focused on five geometrical features of the metamaterial, such as the size and thickness of its components and the twisted angle between layers. Additionally, the training data included reflection spectra under three polarization states: left-circular polarized (LCP), right-circular polarized (RCP), and cross-polarized components, as well as circular dichroism (CD), which quantifies the difference

in absorption between LCP and RCP light. This method can give forward predictions of optical performance (e.g., reflection spectra and CD) of chiral structures under different polarization conditions but also inversely find designs needed to achieve a desired optical response. Ma et al (2021) combined the Monte Carlo, Mie scattering simulations and bidirectional neural network (BNN) model to optimize the design of structural colours of gold nanoparticles (AuNPs). Their study focused on effect of particle size, volume fraction, and layer thickness on the structural colours of AuNP systems. Datasets for the colour and geometric properties of the AuNPs, generated from simulations, were used to train the BNN. This model was applied to directly predict the structural colours of AuNPs and inversely design the geometric parameters required for achieving specific colours. Using the human chromatic discrimination ability as criterion, the proposed method showed 99.83% and 98.5% accuracy on the predicted colours and designed geometric parameters respectively.

While traditional data science methods for inverse design have their strengths as described in the studies above, they may have limitations when compared to data assimilation (DA) techniques (Cheng et al, 2023) , particularly in handling dynamic systems (where the state of the system evolves over time), accounting for uncertainty and optimizing model parameters. To be more specific, variational DA is a technique that is used to combine observations with numerical models to generate the best estimate of the state of a system (Carrassi et al, 2018), (Arcucci et al, 2017). This technique has been widely applied in meteorology and oceanography (Ghil & Malanotte-Rizzoli, 1991), but its application is also useful in other fields such as engineering and agriculture (Pandya et al,

2022). Stochastic and variational data assimilation are two different approaches widely used based on the nature of the uncertainties and the available observational data. Variational data assimilation approaches aim to identify the model that best fit the observations to minimise the cost function while stochastic data assimilation examines uncertainties in both the observations and the model to estimate the probability distribution of the model state based on the observations (Vetra-Carvalho et al, 2018), (Bannister, 2017).

3DVAR (Three-Dimensional Variational Data Assimilation) and 4DVAR (Four-Dimensional Variational Data Assimilation) are two common variational approaches to data assimilation that differ primarily in their temporal aim. For example, 3DVAR aims to find the model state that minimises the difference between the observational and model's output data at a single time frame while 4DVAR optimizes the model state within a continuous time window (Cushman-Roisin & Beckers, 2011), (Shutyaev et al, 2023).

The transformation operator that connects the state space to the observable space is represented by H. Both the background state and the observations are uncertain quantities, with the error in the background state denoted by $\in_{\mathrm{b}}$ and the error in the observations denoted by $\in_{\mathrm{y}}$. The background state (initial estimate) and the true state (actual state) are represented as $\mathbf{x}_{\mathrm{b}}$ and $\mathbf{x}_{\mathrm{t}}$ respectively in Eq. (2.8) while Eq. (2.9) shows the difference between the observed values (y) and the model-generated observations $(\mathrm{H}(\mathbf{x}_{\mathrm{t}}))$. $\mathrm{H}(\mathbf{x}_{\mathrm{t}})$ gives the model's prediction of the observable data, based on the true state.

$$\epsilon_b = \mathbf{x}_b - \mathbf{x}_t \tag{2.8}$$

$$\epsilon_y = y - H(\mathbf{x}_t) \tag{2.9}$$

In data assimilation, the fundamental concept is to combine the model's background information with observational data in a way that balances the two. The background vector represents the initial estimates or predictions, which could be a physical field e.g. temperature, pressure, or velocity or a set of parameters like coefficients in a model. The loss function can be expressed as:

$$J(\mathbf{x}) = \frac{1}{2}(\mathbf{x} - \mathbf{x}_b)^T B^{-1}(\mathbf{x} - \mathbf{x}_b) + \frac{1}{2}(y - H(\mathbf{x}))^T R^{-1}(y - H(\mathbf{x})) \tag{2.10}$$

Alternatively, using norm notation,

$$= \frac{1}{2}||\mathbf{x} - \mathbf{x}_b||^2_{B-1} + \frac{1}{2}||y - H(\mathbf{x})||^2_{R-1}. \tag{2.11}$$

The x represents the vector of model parameters that are being optimized in the data assimilation process (the vector of the unknown model parameters). The y is the vector of observed values. The point of minimum in Eq. (2.10) is the analysis state, $\mathbf{x}_a$,

$$\mathbf{x}_a = \text{argmin}(J(\mathbf{x})) \tag{2.12}$$

When H is non-linear, approximate iterative methods are commonly used to solve the optimization problem through variational data assimilation. Specifically, the gradient $\nabla J(\mathbf{x})$ can be approximated by the following:

$$\nabla J(\mathbf{x}) \approx 2B-1(\mathbf{x} - \mathbf{x}_{b,t}) - 2HT\ R-1(y - H(\mathbf{x})) \tag{2.13}$$

The x in $\nabla J(\mathbf{x})$ should be bold to indicate that it represents a vector of parameters to distinguish them from scalar quantities.

Quasi-Newton methods (e.g, BFGS approaches (Gong et al, 2020)) can then be applied iteratively:

$$\mathbf{x}_{k+1} = \mathbf{x}_k - L_{Var}\,[\mathrm{Hess}(J)(\mathbf{x}_k)]^{-1}\nabla J(\mathbf{x}_k) \tag{2.14}$$

where k is the current iteration, and $L_{Var} > 0$ is the learning rate of the descent algorithm, and

$$\mathrm{Hess}\,(J(\mathbf{x} = [x_0,\ldots,x_{n-1}]))_{i,j} = \frac{\partial^2 J}{\partial x_i\,\partial x_j} \tag{2.15}$$

represents the Hessian matrix of the cost function J. Eq. (2.15) is iterated until the optimization criteria is satisfied. The variational data assimilation with iterative minimisations is summarized in Algorithm 1 as it can be seen in Appendix H.

The objective of data assimilation process, described through Eqs. (2.10) - (2.15) is to adjust the background state using the available observations. This adjustment is achieved by balancing the influence of the background and the observations, with the relative weighting determined by the covariance matrices B and R. The covariance matrices B and R that are shown in Eqs. (2.10)-(2.13) not only depict the variation of measurement errors but also their spatial correlation (Fisher et al, 2005),(Cheng et al, 2022b). The R matrix represents the covariance of observation errors, capturing the uncertainties associated with measurement inaccuracies. Meanwhile, the B matrix represents the uncertainties in the initial model predictions, reflecting the variability or confidence in the model's starting estimates.

DA enables ongoing adjustments to model forecasts, accounting for both model and observation errors or uncertainties exhibiting higher interpretability, reliability, and adeptness in managing prior error knowledge compared to typical data science methods for inverse modelling focusing on ML algorithms. DA techniques offer several advantages in the synthesis of AgNPs, yet their application in this domain remains largely unexplored.

Zhuang et al (2022) developed a novel image-based data driven model to predict droplet interactions within a microfluidic device employing experimental data. They built an algorithm scheme that combines surrogate modelling and Ensemble-type learning algorithms (LA) in reduced-order latent spaces. Results suggested that the proposed data-driven model can predict the coalescence probability within microfluidics and guide the choice of experimental parameters. It can predict five out of eight outcomes correctly for a correction interval of 60 frames. Achieving 62.5% accuracy by correctly predicting five out of eight outcomes within a correction interval of 60 frames is considered a good result, especially given the limited data sets used in this analysis. Notably, the model's performance can be further improved by conducting additional experiments, which may yield even better results.

The literature review revealed that previous ML studies for the synthesis of AgNPs focused on input parameters which are related to specific chemical compositions and process conditions. This means that a model which is derived for a certain experimental configuration cannot be applied for another set of reagents or for a different reactor design and a generalised workflow to design experiments for the synthesis of AgNPs is needed.

2.9 CONCLUSIONS

This literature review examined the formation mechanisms of AgNPs, exploring their nucleation and growth processes, and properties, with a particular focus on the important role of microfluidic technology, computational modelling and data-driven approaches.

The existing experimental literature revealed chemical reduction as the predominant method for AgNPs synthesis. Microfluidic devices, offering various operational configurations such as droplet-based and continuous flow systems, provide precise control over reaction conditions, thereby reducing the polydispersity of AgNPs. Operating conditions, including reagent type and concentration, pH of the solution, temperature control, and mixing dynamics, significantly influence the size of the nanoparticles.

The ability to regulate the size and morphological attributes of AgNPs is of great significance for their catalytic, optical, and electrical properties paving the way for innovative applications. Whilst the Finke-Watzky two-step model sheds light on kinetic aspects and mechanisms, incorporating hydrodynamic processes into models is crucial for a more comprehensive mechanistic understanding.

Regarding the physics-based models, MD simulations have been shown to be particularly significant in elucidating the intricate interactions between NPs and capping agents or other structure directing agents. These insights pave the way for the precise tailoring of NP shapes to suit specific applications. Furthermore, exploring numerical investigations of meso- and macroscopic phenomena showed that they have mainly utilised coupled PBM-CFD simulations within microfluidic channels. This approach allows the consideration of nucleation, growth, and hydrodynamic aspects like mixing through CFD

and representing the particle population though PBM allowing a comprehensive understanding of PSD and average particle size.

Further evaluations such as particle-particle interactions are considered essential for future research. This assessment can determine whether phenomena such as agglomeration should be integrated into the PBE.

In addition, it was shown that design of experiments/response surface methodology along with data-driven models can offer cost-effective means to explore various aspects for AgNP research. Much attention has been focused on finding the relationships between operational conditions and final product characteristics, but also to obtain AgNPs with novel properties. However, despite recent progress, these methods have primarily focused on batch synthesis of NPs. Current data-driven models are limited in their ability to elucidate the underlying physics of the synthesis process and lack the generalizability needed to be applied to other similar systems.

The potential integration and analyses produced from physics based on data-driven models (DoE, DT and inverse modelling) alongside experimental methodologies such as microfluidic synthesis have strong potential for advancing AgNP synthesis and also for reducing the ecological footprint.

CHAPTER 3: MATERIALS AND METHODS

3.1 CHEMICAL REAGENTS AND PROPERTIES

The synthesis of AgNPs was conducted using two different chemical protocols:

1. utilizing tannic acid, $C_{76}H_{52}O_{46}$, (TA) which is a weak reducing agent in combination with trisodium citrate, $Na_3C_6H_5O_7 \cdot 2H_2O$, (TC) which served in the reaction as both a reducing and stabilising agent.
2. using dimethylamine borane (DMAB), a strong reducing agent along with sodium dodecyl sulfate (SDS), an anionic surfactant.

For the first protocol, the concentrations of silver nitrate, $AgN0_3$, (SN) and TA were 0.92 mM and 0.123 mM, respectively, while the concentration of TC ranged from 1.91 to 3.82 mM. In § 6.4 half the concentration of the precursor (0.41 mM) and double the amount of reducing agent (0.246 mM) were utilised to explore the correlation between kinetics and the initial concentrations of precursors for the two investigated set of chemicals. This experimental procedure was adopted from the work of Kašpar et al (2019) with adjustments made to the concentrations of TA and TC.

Although the concentration of TA was smaller than that of SN, an excess of TA was chosen due to its reducing ability. Each molecule of TA can effectively reduce up to 20 molecules of SN, whereas trisodium citrate can only reduce 4 silver ions (Sivaraman et al, 2009), (Rashid et al, 2013). For example, the molar ratio of TA to SN is 0.05 based on the stoichiometry but in the investigated experimental case is 0.13, indicating that TA is set in excess. The pH of the aqueous solution of tannic acid and trisodium citrate was set

to either 7 or 12 using 0.1 M NaOH. Silver nitrate, 99+% ($AgNO_3$), tannic acid ($C_{76}H_{52}O_{46}$), trisodium citrate dihydrate ($Na_3C_6H_5O_7 \cdot 2H_2O$) and sodium hydroxide (NaOH) were purchased from Alfa Aesar.

Regarding the second chemical protocol, the concentration for the SN used was 0.08 mM while the concentrations of DMAB, (Sigma Aldrich) and SDS, (Sigma Aldrich) varied from 0.1 to 0.4 mM and from 60 to 100 mM respectively. Dimethylamine borane has the capability to reduce up to 6 silver ions (KoÇak Ç et al, 2020),(Sithole & Ntuli, 2022) (see the Figure 3.1 below for the structures of chemicals).

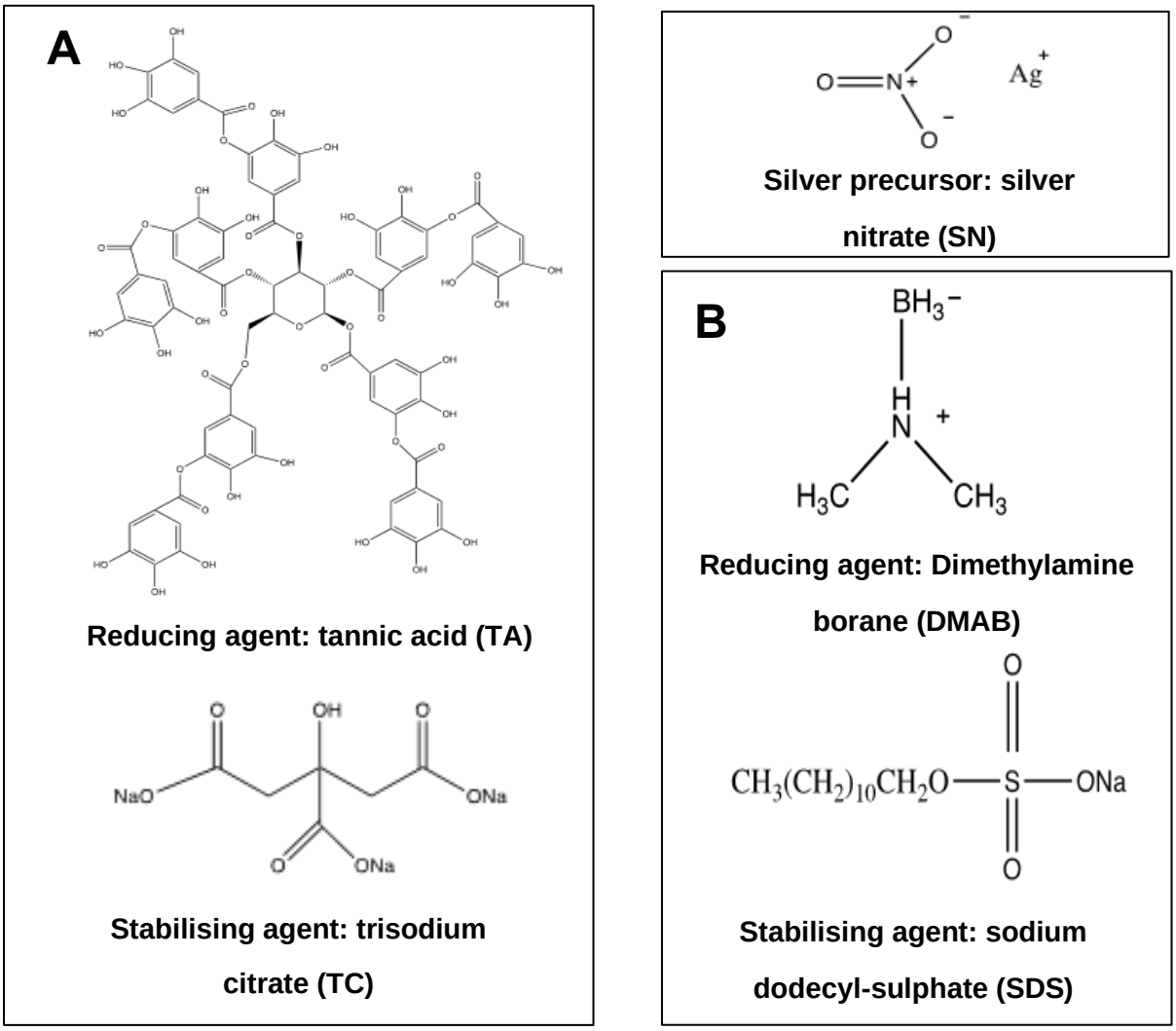


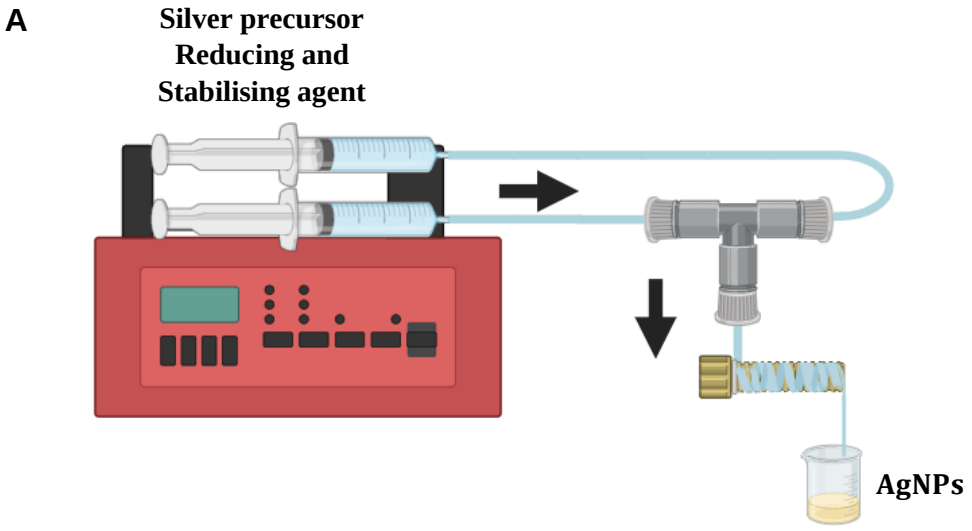
Figure 3.1 Chemical structures of the reagents employed for the synthesis of AgNPs. A) First chemical synthesis protocol B) Second chemical synthesis protocol.

3.2 T-JUNCTION CONTINUOUS FLOW-DEVICE

The T-junction continuous flow device (Figure 3.2) was composed of two inlets (length of 0.6 m each) of 500 μm inner diameter (ID) polytetrafluoroethylene (PTFE) cylindrical

tubing from Cole-Palmer. The aqueous solutions of reagents were supplied by two separate inlet channels meeting at a Tee tubing junction (0.020" Thru-Hole) (Upchurch Scientific), whereas the reaction was carried out in the outlet channel of 2 m length (ID=500 $\mu\mathrm{m}$). The inlet flow rates were controlled using syringe pump from World Precision Instrument-AL-4000 equipped with two 5 mL plastic syringes (Fisher).

Using a two-syringe pump ensured identical flow rates for both inlets. The flow rate referred to in the below discussion is defined as the flow rate for one inlet. Hence, Q denotes the flow rate of each individual inlet and the total, $\mathrm{Q_{total}} = 2 \times \mathrm{Q}$. The outlet tubing was either straight or coiled using 3D printed helix devices with a diameter of 3 mm and 5 mm (pitch=2 mm) to improve the mixing of the reagents. Other helical devices with 9.46 mm and 12.5 mm diameters were bought from TERF® and Amazon UK respectively.



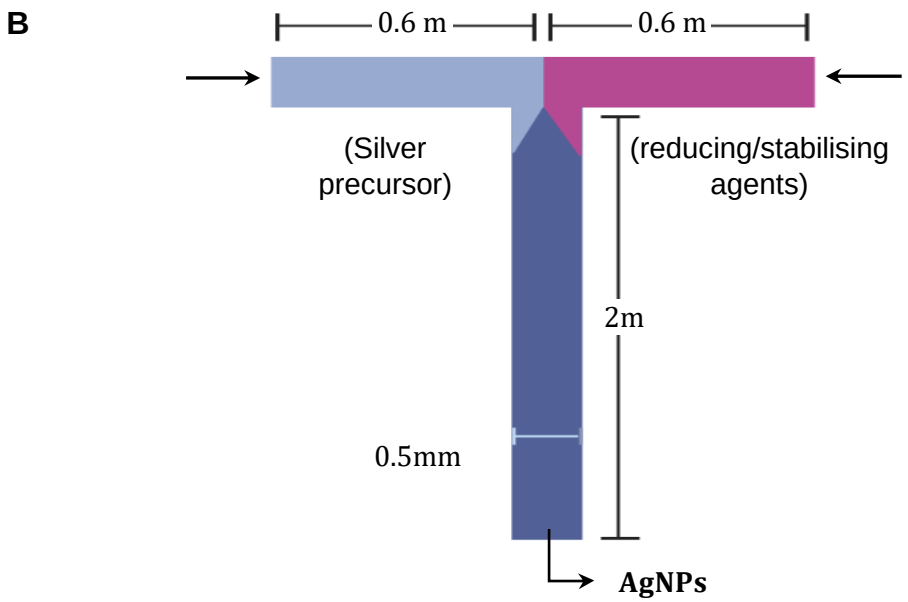


Figure 3.2 A) Experimental set up using two-syringe pumps (depicted as two one-syringe pumps in the schematic for better visualization of the fluid injection), B) Schematic diagram of T-junction microfluidic device.

3.3 DROPLET MICROFLUIDIC DEVICE

The microfluidic device consisted of two main components, a glass 75 $\mathrm{mm} \times 50\ \mathrm{mm}$ plain micro-slide from Corning® coated with a layer of PDMS and a tightly attached geometry made from PDMS. The PDMS channels were connected to $500\ \mu\mathrm{m}$ inner diameter Tygon® microbore tubing from Cole-Parmer and 5 mL syringes (Fisherbrand) were used to load the solutions. The flow rates were controlled with a World Precision Instrument syringe pump. The width and height of the channel, respectively, measured as 418.5 $\mu\mathrm{m}$ and 107.5 $\mu\mathrm{m}$ for the investigated channels. The flow direction was periodically reversed

by using turnings with radius of curvature of 688 μm. The exit tube of 1.47 m length was attached to the exit of droplet device and coiled on the helix device with diameter 3 mm to promote further mixing of the reagents.

Discrete droplets were generated using a liquid-liquid two phase flow within a flow-focusing microfluidic device where the continuous phase consisted of oil and the dispersed phase comprised the reagents. For the droplet microfluidic device (see Figure 3.3), two separate solutions were utilised as disperse phases (one containing SN and the other TA and TC), while the continuous phase was supplied through two side inlets of silicone oil to form droplets by hydrodynamic flow focusing. The reactants were supplied by two separate channels merging close to flow focusing junction.

Droplets with reagents were formed within the oil phase and were carried along the microchannel. Droplet formation was observed using a microscope Nikon Eclipse Ti2-U set to 20× magnification with resolution of $1\mu m/pixel$ to be sure that there is no blockage of the microfluidic channels, backflow in the inlet channels, channelling, droplets sticking to walls or droplet coalescence. Backflow, in the inlets channels refers to the undesired reverse flow of fluid often caused by pressure fluctuations while channelling occur when the fluid flow to certain paths within microchannels, neglecting other areas.

Preliminary experiments were conducted to eliminate any potential issues such as channelling or back flow, and to determine the optimal continuous phase for the investigated case. Vegetable and silicone oil were investigated for their ability to form stable droplets. While vegetable oil had a good performance in producing stable droplets, its surfactant content raised concerns regarding potential interaction with other chemicals

and the risk of non-uniform particle distribution. Specifically, vegetable oils are complex mixtures that include fatty acid chains (Orsavova et al, 2015). These fatty acids can be polar (Liang & Wen, 2014) allowing them to dissolve in the aqueous phase and interact with other reagents present. Silicone oils, by contrast, have non-polar characteristics, making them more stable and less reactive (Brook, 2023).

Consequently, silicone oil with a kinematic viscosity of 20 cSt (SIGMA-ALDRICH) (0.95 $\mathrm{g/mL}$) was used as the continuous phase, which led to the formation of more stable droplets in the dispersed phase due to its higher viscosity. However, to facilitate the separation of AgNPs from the oil phase during characterisation, silicone oil of 5 cSt from SIGMA-ALDRICH (0.91 $\mathrm{g/mL}$) was used as the continuous phase due to its larger density difference from water (0.999 $\mathrm{g/mL}$).

The PDMS components, including glass coating and the geometry structure, were prepared using a silicone elastomer base and silicone elastomer curing agent from SYLGARD^{TM} in a ratio of 10:1. The mixture was blended in a plastic cup and then it was place in the vacuum chamber to create a vacuum using a vacuum pump. The coated glass plate is prepared by adding a small quantity of PDMS onto the centre of the micro-slide, followed by even distribution using a POLOS^{TM} spin-coater (1000 rpm) to form a uniform PDMS coating. Subsequently, the plate was heated on a hot plate at 80℃ for 20 minutes and left to cool.

The device's geometric template was designed using AUTOCAD, and then was utilised to make a mould on silicon wafer through photolithography. Photolithography is a process used to create geometric patterns on a photoresist layer attached to a silicon wafer

(Martinez-Duarte & Madou, 2010). It begins with designing the geometry in AutoCAD. The silicon wafer is first cleaned, dried, and coated with a photoresist (SU-8 2075 resist used in this study) using spin coating. After coating, the photoresist is soft baked to remove solvent and solidify the film. A photomask, created from the AutoCAD design, is aligned with the wafer. The wafer is then exposed to UV light through the photomask, transferring the pattern onto the photoresist. The photomask allows UV light to pass through the areas corresponding to the pattern (transparent), while blocking light in other areas (which are black). After exposure, a post-exposure bake is performed to stabilize the photoresist. The wafer is subsequently developed, dissolving the photoresist in the unexposed regions and revealing the desired pattern. Finally, the wafer is rinsed and dried, and ready to be used.

Winding channels were designed for the microfluidic device as it was found in previous studies, they can promote mixing (Tung et al, 2009), (Wang et al, 2015). The wafer was coated with photoresist SU-8, soft baked and exposed to UV light. After post-exposure baking the untreated photoresist was dissolved. PDMS prepared as described above was then poured onto these wafers and put in vacuum to remove bubbles. After this, PDMS was cured in a furnace at 70℃ for 2 hours.

The resulting geometry was precisely cut out, holes were punched for the inlet and exit tubes and attached to the plate using corona discharge technology from OPlasma. The PDMS channels and the substrate were treated both with corona discharge to facilitate bonding between the PDMS and the glass slide. This treatment temporarily enhanced the hydrophilicity of the PDMS surface by lowering its contact angle (this effect gradually weakens over time). Once bonded, the device was placed on a hot plate for 20 minutes

at 90℃. Novec (3M) was flushed through the device via the exit channel to hydrophobise the channels, followed by purging with air and silicone oil 5cst (SIGMA-ALDRICH) to remove any residuals of Novec from the microchannels. No wetting issues were observed, and the droplets flowed smoothly through the channels without sticking to the walls.

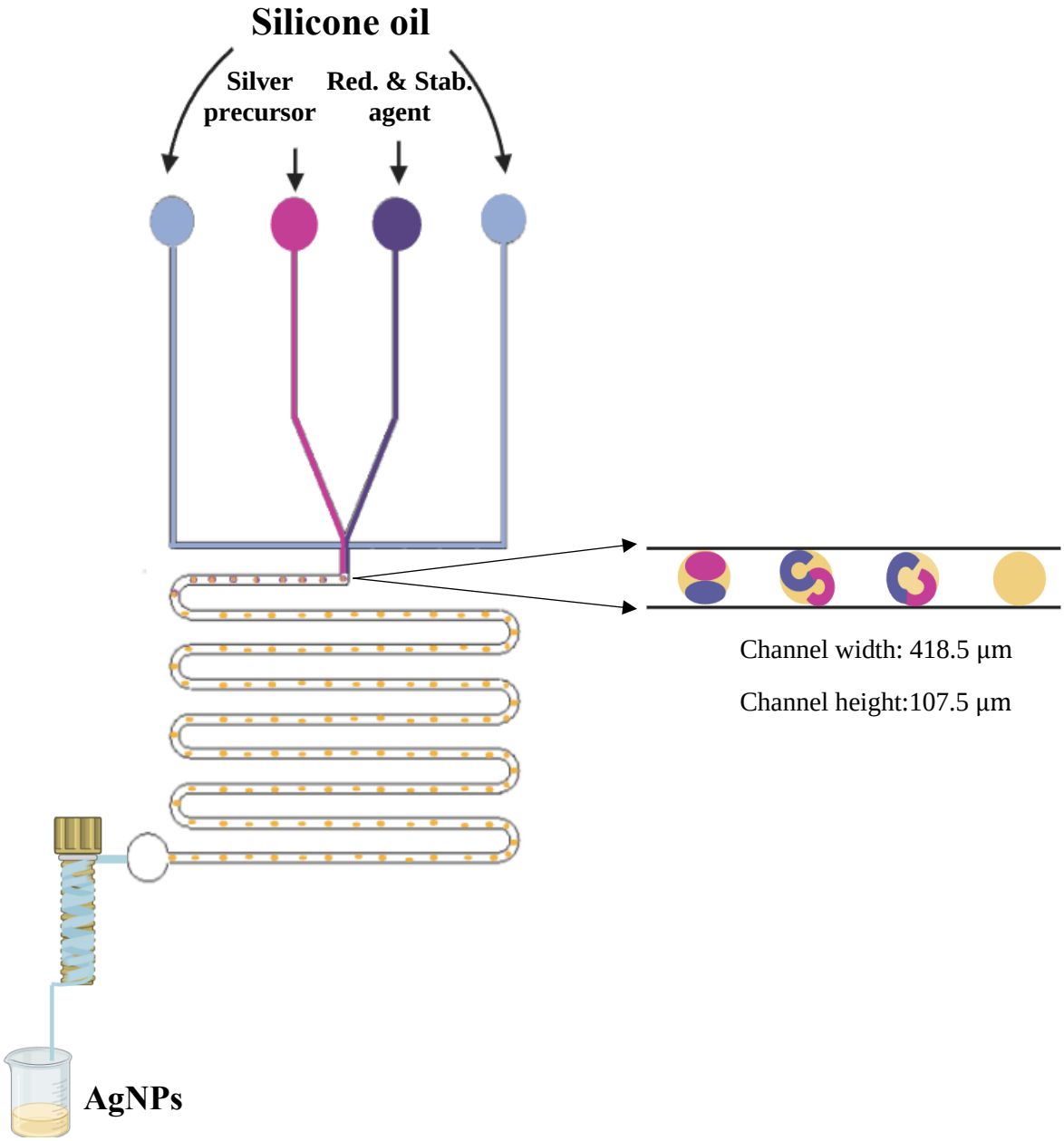


Figure 3.3 Flow focusing microfluidic device showing the formation of droplets inside the microfluidic channels where the chemicals react to form AgNPs. Silicone oil was used as a continuous phase while the aqueous solutions of chemical reagents were utilised as the dispersed phase.

3.4 BATCH REACTOR AND KINETICS MEASUREMENTS

Chemical reactions in the batch reactor were carried out by mixing precursor and reducing / stabilising agent solutions for each chemical protocol using a magnetic stirrer (Stuard CB302) (see Figure 3.4). The reactions were conducted in a 500 mL glass beaker using a magnetic stir bar 6×20 mm (VELP SCIENTIFICA, Italy) and mixing was set at a point where the AgNPs formation was independent of mass transfer. The synthesis of AgNPs was conducted at different rotation velocities while keeping all the other parameters constant. When the final PSD didn't change significantly with varying rotation velocities, it indicated that mass transfer was not a limiting factor. The rotation speed was thus set to 1500 rpm for both set of chemicals. The pH of the solution of reducing / stabilising agent for the first set of chemicals was regulated at pH 7 or 12 before mixing. The nucleation, k_1 and growth k_2, rate constants describing the synthesis of AgNPs under the different chemical synthesis protocols were determined from the time dependence of absorbance intensity at 400 nm (characteristic for AgNPs) based on the F-W two step mechanism (see Appendix F). Note, the absorption peak of silver nitrate solution is around 310 nm (Nakamura et al, 2011). The time dependence of AgNPs' absorbance was measured by UV-vis spectrophotometer (Jenway-6300, Figure 3.4) and recorded every 5 mins. The values of k_1 and k_2 were estimated for both set of chemicals using the linear form of F-W model, as expressed in Eq. (2.7).

$$([\mathrm{A_o}] - [\mathrm{A}])/[\mathrm{A}] = \mathrm{a}/(1 - \mathrm{a}) \tag{3.1}$$

In the Eq. (3.1) above, a is $([A_0]-[A])/[A_0]$, A_0 refers to the initial concentration of reactant A and A refers to its concentration at any time t (Amirjani & Haghshenas, 2018). The definition of a is the ratio of intensity due to silver in NPs at time t to the intensity at ∞ when all silver is in NPs. The derivation of this equation relies solely on the assumption that intensity is directly proportional to the silver concentration, allowing intensities to be substituted with concentrations. When all the silver is incorporated into nanoparticles, its concentration becomes $[B]_\infty=[A]_0$. At any given time t, the concentration is expressed as $[A_o]-[A]$. Thus, $a=([A]_0-[A])/[A]_0$. By using this definition and computing $a/(1-a)$, equation (3.1) is obtained. By plotting, $\ln(a/1-a)$ versus t, a straight line is obtained. The slope and intercept of this line can then be used to determine the rate constants $k_1$and k_2 . To be more specific in Eq. (2.7), $\ln\left(\frac{k_1}{k_2[A_0]}\right)$ is equal to the intercept and $k_2[A]_0$ to the slope.Regarding the first chemical synthesis protocol, the values of rate constants were found by varying pH of reducing solution at two levels, pH 7 and pH 12. At each value of pH, three different concentrations of TC were employed: 1.91, 2.87 and 3.82 mM. This provided six different pairs of nucleation and growth constants to be used in the predictive models later. Regarding the second set of chemicals four different pairs of nucleation and growth constants were obtained by varying concentrations of reducing agent at 0.2 mM and 0.4 mM and concentrations of stabilising at 60 mM and 80 mM respectively.

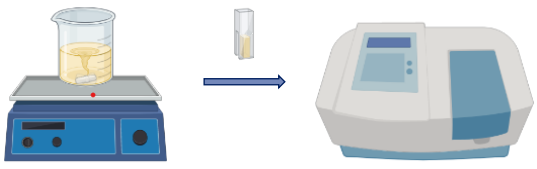


Figure 3.4 UV-silver ions measurements in a well-mixed reactor.

3.5 CHARACTERISATION METHODS OF THE SAMPLES

Particle size and zeta-potential of samples obtained from well mixed reactor and microfluidic devices were measured in triplicate from three independent experiments using Zetasizer Nano series, (Malvern Panalytical, Malvern, UK) with the refractive index of AgNPs set to 0.135 (Zwar et al, 2023).

Zetasizer measures the intensity fluctuations of scattered laser light caused by the Brownian motion of particles in a suspension. By analysing these fluctuations, it determines the velocity of Brownian motion, which is directly related to the size of the particles. It is capable of measuring particle sizes ranging from approximately 0.3 nm to 10 $\mu\mathrm{m}$, making it suitable for analysing a wide range of nanoparticles and colloidal systems. DLS measures the hydrodynamic diameter of particles in suspension, not their actual physical diameter, especially for non-spherical particles. Hydrodynamic diameter which refers to the effective diameter of a particle as it moves through the liquid. Non-spherical particles (e.g., rods, discs, or irregular shapes) may exhibit different diffusion characteristics compared to spherical ones, which DLS assumes for its measurements.

UV-vis spectroscopy measurements (Carry 50) have been performed to indicate the presence of material obtained. Figures in Appendix F showed that all the samples obtained under the different experimental conditions have a peak at 400 nm which is characteristic for AgNPs (Shaikhaldein et al, 2020), (Njagi et al, 2011) indicating the formation of AgNPs. It is worthy to mention here that in the range of particle sizes approximately between 3 and 20 nm, the absorption spectra exhibit a relatively weak dependence on particle size (Henglein, 1993).

The results from dynamic light scattering (DLS) were confirmed using transmission electron microscopy (TEM) (JEOL JEM-1400). One drop of the sample was placed onto formvar/carbon 400 mesh copper grids (Agar scientific), followed by air-drying at room temperature for a few minutes. Particle size distribution was measured from the TEM images using Image J. The fitted values of particle size (Exp. (fit)) were calculated using the probability density function of a normal distribution given by:

$$f(L) = \frac{1}{\sigma\sqrt{2\pi}} e^{-\frac{(L-\mu)^2}{2\sigma^2}} \tag{3.2}$$

In Eq. (3.2), L is the particle size of AgNPs, μ and σ are the mean and standard deviation of the observed NP size from the experimental data while $\sqrt{2\pi}$ is a fundamental part of the normalization factor for the Gaussian distribution to make it a valid probability density function. More specifically, it ensures the proper scaling of the normal distribution so that it satisfies the total probability condition: $\int_{-\infty}^{\infty} f(L)dL = 1$.

The concentration of silver ions was measured using a silver electrode (EDT direction) connected to a mV meter (Mettler Toledo-FP20) calibrated by a series of standard solutions (0.1,1,5,10,100 ppm). The standard solutions were prepared by the dilution of the stock solution, corresponding to 1000 ppm (EDT direction). For measurements above 50 ppm, 1 mL of 5 M ionic strength adjustment buffer (ISAB) (EDT direction) was added. Using the electric potential mV values on linear axis and the concentration of silver ions on the log scale a calibration curve was made. Each of the samples was measured in triplicate. The experimental setup did not allow for real-time in situ measurements for the concentration of silver ions in the microchannels. For this reason, different inlet flow rates

(Q=200,100,67 and 50 $\mu L/min$) and channel outlet lengths (0.1,0.5, and 1 m) were employed to find the concentration of silver ions. The samples were collected in triplicate after ~240 sec of operation for each of the outlet tube lengths and inlet flow rates. The actual measurement was carried out after a certain period of time (around 1 min) that corresponds to the transportation of the sample. The calibration curve obtained from the standard solutions was employed to determine the unknown sample concentrations at different outlet tube lengths and inlet flow rates.

The PSD measurements were conducted under similar conditions as silver ions concentrations, Q=200,100, and 50 $\mu L/min$ at 0.25, 0.5, 1 and 2 m along the reaction outlet channel. The samples were collected in ice to quench further reactions. The final concentration of silver ions was tested to determine the reaction yield.

CHAPTER 4: CHARACTERISATION OF A DROPLET AND A CONTINUOUS FLOW MICROREACTOR FOR AgNP FORMATION

4.1 INTRODUCTION

While many prior studies documented in the literature have mainly focused on comparing batch reactors with microfluidics devices (Wojnicki et al, 2019), (Gioria et al, 2020), (Tsachouridis et al, 2024) in the synthesis of nanoparticles, there has been limited exploration of single-phase versus two-phase reactors (Xu et al, 2016b). Batch reactors typically handle larger volumes of reactants compared to microfluidic systems, which operate at micro- or nano level scales and require fewer reagents and less energy. Mixing in batch reactors relies on mechanical agitation or stirring, whereas microfluidics systems exploit laminar flow, enabling mixing through passive diffusion or active methods such as acoustic or electric (Agha et al, 2023). Passive mixing in microfluidics relies on the channel design and geometric structure of the microfluidic channels to enhance fluid mixing without requiring external energy sources. Different studies have placed obstacles within the channel to disrupt the laminar flow and induce vortices that enhance mixing (Wang & Hu, 2010), (Mondal et al, 2019). Utilizing a winding, snake-like pattern channels induces continuous formation of Dean vortices , facilitating efficient mixing through repeated folding of fluid streams (Wang et al, 2015), (Madadelahi & Shamloo, 2017), (Tung et al, 2009).

Microfluidic systems are characterised by their superior precision in fluid manipulation and reactions control, they can operate under varied settings as elaborated in § 2.3, resulting in the production of nanoparticles with different properties. Continuous flow microfluidics

involve the continuous flow of fluids through channels, while droplet-based microfluidics generate discrete droplets within another immiscible phase. In this chapter, a droplet flow reactor and a continuous microfluidic reactor are compared under identical hydrodynamic and chemical conditions in terms of the size distributions of AgNPs generated in both devices. A comparison between continuous flow and droplet based microfluidic device under identical hydrodynamic and chemical conditions (TA, TC) is important to provide a comprehensive understanding of the advantages and limitations of each approach, specifically to determine if performance differences are due to the design of the microfluidic systems rather than variations in experimental operating conditions.

4.2 DROPLET FLOW REACTOR

The droplet reactor utilised in this study operates through the generation of discrete droplets containing reactants within continuous silicone oil phase using flow focusing. A detailed description of the experimental setup can be found in § 3.3. As these droplets flow through the reactor, chemical reactions occur within them (see Figure 3.3). The internal flow dynamics within each droplet significantly improves the mass transfer because of the recirculatory flow patterns caused by the radial and axial velocity gradients that develop inside the droplets, which continuously move the reactants around and enhance their contact. This internal circulation facilitates mixing as discussed by Morales & Zahn (2010) who compared the protein partitioning efficiency in droplet flow and stratified flow conditions. Their results showed that the droplet flow provides a higher extraction of proteins with minimal loss of DNA in the aqueous phase due to the convective transport improvement produced by the inner circulation of the droplets. Lu et al (2020)

analysed the fluids dynamics of droplet internal circulation through experiments and numerical simulations. They concluded that the droplet viscosity predominantly influences the strength of the internal circulation, whereas factors such as the interfacial tension and droplet volume have minimal effect. Additionally, they identified that a large velocity slip between the adhered droplet and the external flow induces the internal flow, leading to vortex formation inside the droplet. This velocity slip enhances the mixing efficiency, as it generates shear forces that promote better fluid circulation within the droplet.

As it can be seen in Table 4.1, the size of AgNPs synthesized in the droplet-based reactor was mainly influenced by the pH of the solution, the concentration of TC and the total flow rate. The size of AgNPs is seen to decrease as the pH of the solution, concentration of TC and total flow rate increase. These results agree with previous studies which examined the effect of pH (Alqadi et al, 2014), stabilising agent (El Badawy et al, 2012), and residence time (Ling et al, 2022). For example, for lower concentrations of stabilising agent, the surface coverage was probably incomplete enabling further particle growth. Also, further growth of particles can happen at lower flow rates of reactor operation as a result of higher residence time in the reaction channel. Under alkaline conditions, the reducing ability of citrate is improved leading to a faster reduction and smaller particles (Marciniak et al, 2020),(Dong et al, 2009).

pH	[TC], mM	Total flow rate, $\mu L/min$	Average $d \pm \sigma$ / nm
7	1.91	30	6.86 ± 1.67
7	1.91	15	6.91 ± 1.77
12	1.91	30	3.997 ± 0.73
12	1.91	15	4.51 ± 1.76
7	2.87	30	6.44 ± 0.99
7	3.82	30	6.14 ± 1.02

Table 4.1 Size distribution of AgNPs obtained by DLS at different flow rates and chemical conditions in the droplet reactor. The pH refers to the pH of the aqueous phase after TA and TC are mixed. TC represents the total concentrations in the aqueous phase after mixing.

4.3 COMPARISON OF CONTINUOUS FLOW AND DROPLET MICROREACTORS

To compare the outcomes of a single-phase and two-phase systems such as the one of T-junction microfluidic device described in § 3.2 and droplet reactor detailed in § 3.3 same hydrodynamic and chemical conditions should be achieved. The continuous flow device employed (see Figure 3.2) operates with homogeneous streams, where enhancing mixing efficiency relies primarily on processes such as coiling the outlet tube around a helical device as described in § 3.2.

The same concentrations of reagents and same pH of the solutions were used while flow rates and curvatures were adjusted to get the same Dean (De) numbers and residences times.

$$De = Re\sqrt{d/2R_c} = \frac{pud}{\mu}\sqrt{d/2R_c} \tag{4.1}$$

where d is the inner diameter of the microchannel, R_c is the radius of helix curvature and Re is the Reynolds number where ρ is the fluid density, u is the average velocity of the fluid, and μ is the viscosity of the fluid.

For the continuous flow device using a 3 mm helix device and 2 m outlet tube, operating at a total flow rate of 20 $\mu L/min$, the De was found to be 0.34. The calculation of the hydraulic diameter was essential for the droplet microfluidic device due to the utilization of non-cylindrical channels, specifically rectangular channels but also to find the velocity and thus the flow rates needed to have the same conditions as in the continuous flow device. The hydraulic diameter (Curd et al, 2001) was estimated using the equation provided below:

$$D_h = 4\frac{A}{P} = 2\frac{WH}{W+H} \tag{4.2}$$

where A represents the area of the channel, P denotes the perimeter of the channel and W and H are the width and height of the channel, respectively, measured as 418.5 μm and 107.5 μm for the investigated channels. Subsequently, the total flow rate for the droplet device was determined to be 15.24 $\mu L/min$.

Preliminary experiments indicated that a 2:1 ratio of the continuous and dispersed phases was effective for controlling droplet size and distance between droplets. The size of droplets is determined by the balance between surface tension and shear stress, while droplet spacing depends primarily on the ratio between flow rates of the dispersed and continuous phases, consistent with mass balance principles. When the shear stress remains constant, the droplet size does not change, but the distance between the droplets should be smaller. However, an increase in the dispersed phase flow rate reduces the velocity difference between the two phases, thereby decreasing shear stress, which can lead to larger droplet sizes. A higher ratio of continuous to dispersed phase flow rates increases droplet spacing, while a lower ratio decreases it. Thus, the flow rates for the continuous and dispersed phases were set to 10.16 $\mu L/min$ and 5.08 $\mu L/min$, respectively.

The residence time in the continuous flow reactor at a total flow rate of 20 µL/min was calculated to be 19.63 minutes. To achieve the same residence time, an exit tube measuring 1.47 m in length was attached to the outlet of the droplet device and coiled in the same helix configuration as the continuous flow reactor. The residence time within the PDMS droplet device itself was determined to be 0.56 minutes. Subtracting this from the continuous reactor's residence time of 19.63 minutes yielded a difference of 19.07 minutes. This difference was used to calculate the required length of the droplet device's outlet tube, which was determined to be 1.47 m. The cross-sectional area of the output tube was larger than that for the channel in the drop device, thus the Dean number in the output tube was also smaller. To understand the impact of the variation of the Dean

number on NP size, a total flow rate of 30 $\mu L/min$ was also examined for the droplet reactor and found to be negligible (Table 4.1). Upon analysing the data, it was found that using the same De (0.34 and 0.67) for both the continuous flow device and drop flow reactor revealed no significant difference in the sizes of synthesized AgNPs, as shown in Figure 4.1. The data show that at the same chemistry, residence time and Dean number, the size of AgNPs and PSD is the same.

The data show that when there is the same mixing effect the size of AgNPs is the same. Given no advantage of the more cumbersome droplet microreactor could be demonstrated, the more practical continuous flow device was chosen for further experimentation. However, it is important to mention that the there are some disadvantages in the use of the continuous flow device such as particle deposition or fouling within the channels which can result in a decrease in particle concentration compared to batch (beaker) methods. In the PTFE tubing used in the continuous flow reactor deposition of dark material on the tubing surface was clearly seen after the synthesis, obviously leading to a decrease in AgNPs concentration. To ensure that fouling did not affect the results, the outlet tube of the continuous flow reactor was periodically replaced whenever dark material was observed on the tubing surface. This step helped prevent fouling from causing blockages that could impact the flow rate or reaction efficiency. Three runs of the experiment were performed for each case, and the consistency of results confirmed that fouling did not impact the reaction efficiency. Additionally, the comparison between the drop device and the continuous flow device, conducted under the same hydrodynamic and chemical conditions, showed similar

particle sizes. To reduce the fouling in the continuous flow reactor, coating the inner surfaces of the device with anti-fouling materials can be highly effective. Materials such as polyethylene glycol (PEG) (Zhang & Chiao, 2015) can help minimize the adhesion of NPs to the surfaces. Additionally, optimizing flow conditions, such as adjusting the residence time within the channels, can also contribute to reducing fouling and improving reactor performance. However, an advantage of continuous flow devices is that NPs do not require downstream separation from the continuous oil phase.

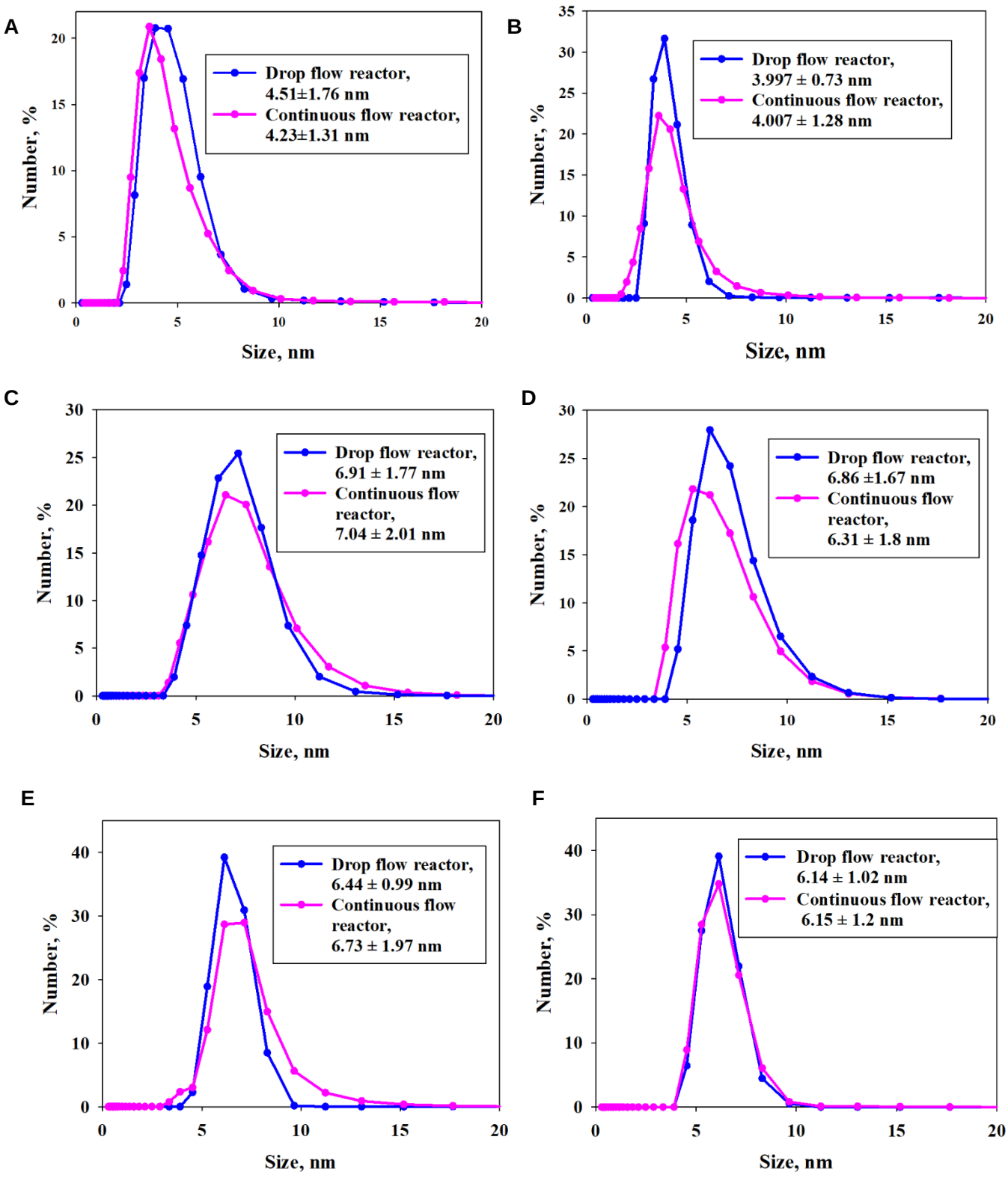

A
Number, %
Size, nm
Drop flow reactor, 4.51±1.76 nm
Continuous flow reactor, 4.23±1.31 nm
B
Number, %
Size, nm
Drop flow reactor, 3.997 ± 0.73 nm
Continuous flow reactor, 4.007 ± 1.28 nm
C
Number, %
Size, nm
Drop flow reactor, 6.91 ± 1.77 nm
Continuous flow reactor, 7.04 ± 2.01 nm
D
Number, %
Size, nm
Drop flow reactor, 6.86 ±1.67 nm
Continuous flow reactor, 6.31 ± 1.8 nm
E
Number, %
Size, nm
Drop flow reactor, 6.44 ± 0.99 nm
Continuous flow reactor, 6.73 ± 1.97 nm
F
Number, %
Size, nm
Drop flow reactor, 6.14 ± 1.02 nm
Continuous flow reactor, 6.15 ± 1.2 nm

Figure 4.1 Comparison of the PSD of AgNPs produced in droplet-based and continuous flow devices at: A) pH 12, TC 1.91 mM, 15µL/min and De = 0.34 B) pH 12, TC 1.91 mM, 30µL/min and De = 0.67 C) pH 7, TC 1.91 mM, 15µL/min and De = 0.34 D) pH 7, TC 1.91 mM, 30µL/min and De = 0.67 E) pH 7, TC 2.87 mM, 30µL/min and De = 0.67 F) pH 7, TC 3.82 mM, 30µL/min and De = 0.67.

4.4 CONCLUSIONS

The comparison between continuous flow and droplet-based microfluidic devices under identical hydrodynamic and chemical conditions, showed that both approaches exhibit comparable performance in synthesizing AgNPs of similar sizes. This indicates that under equivalent mixing efficiencies (characterized by consistent Dean numbers and residence times), the choice between these microfluidic systems does not significantly impact nanoparticle size.

Despite drawbacks such as particle concentration reduction due to deposition or fouling within channels, the continuous flow device was selected for further experimentation. This choice was mainly based on considerations of effectiveness and convenience for further research. This type of device simplifies measurements as nanoparticles do not need to be separated from the oil phase. Compared to a droplet device, which requires additional steps to construct the PDMS device, operating the entire process is also simplified.

Future research could explore strategies to reduce deposition of particles within the channels of continuous flow systems, aiming to optimize nanoparticle production efficiency in microfluidic environments.

CHAPTER 5: DEVELOPMENT OF A PREDICTIVE RESPONSE SURFACE MODEL FOR SIZE OF SILVER NANOPARTICLES SYNTHESIZED IN A T-JUNCTION MICROFLUIDIC DEVICE [2]

5.1 INTRODUCTION

Whilst batch processes to produce AgNPs have been extensively optimised using DoE approaches, continuous microfluidic approaches have not received equivalent attention despite their several benefits. Microreactors are a valuable high-throughput experimental tool for technology optimisation enabling the use of less volume of reagents and thereby reducing the ecological footprint. DoE optimization is useful for microfluidic synthesis of AgNPs because it is an emerging approach where datasets are limited. This study investigates the application of an experimental design strategy based on the D-optimal approach to build a model to predict the size of AgNPs synthesized in a T-junction microfluidic device. The effect of chemical parameters (solution pH, relative concentration of stabilising agent), collection storage temperature and also parameters affecting the hydrodynamics (curvature of the outlet channel and reagent flow rates) on the size of AgNPs are investigated. The aim of the study is to tackle the limitations of traditional OFAT and batch-style chemical reactors approaches. OFAT, characterized by testing one factor at a time, often results in high energy and material consumption and limits the ability to account for interactions between factors. Similarly, batch-style chemical reactors are

[2] Sections 5.1-5.7 of this chapter are adapted from Nathanael, K., Galvanin, F., Kovalchuk, N.M., Simmons, M.J.H. (2023) Development of a predictive response surface model for size of silver nanoparticles synthesized in a T-junction microfluidic device. *Chem. Eng. Sci.*, **279**, 118907.

known for the need of larger volumes of reagents and solvents. This study seeks to deliver a more sustainable and controlled route for AgNPs synthesis by overcoming these limitations.

5.2 PROCESS OPTIMIZATION USING DoE OVERVIEW.

The preliminary experiments along with analysis of literature data from Marciniak et al (2020), Wu et al (2017), Das et al (2021), Izak-Nau et al (2015) were used to determine the factors and levels for the experimental design. The optimal conditions for the minimum particle size for synthesis of AgNPs in microfluidic reactor were determined by response surface methodology and particularly, a D-optimal design (Montgomery, 2013) formed by five factors. Trisodium citrate concentration, flow rates, pH of the solution, curvature of outlet tubing, and storage temperature (numeric variables) were set at different levels, as shown in Table 5.1, while the size of AgNPs from DLS was investigated as the response. Note, in the experimental design, some parameters were kept constant to ensure that any observed changes were solely due to the manipulation of the experimental factors. Temperature was maintained at 25°C throughout all experiments to eliminate its influence on reactions. Residence time was maintained by using the same length of outlet tube in all experiments. A D-optimal design was selected to limit the number of runs with a specific goal to minimise the variance of model parameters. It was preferred over other designs because there are multiple levels of factors, and the mid-point of levels is not exactly the central one. The final composite matrix was constituted of 162 experiments including

three replications. The large number of experiments contributed to a higher accuracy in the predictions.

After the selection of representative runs for the experiment, regression-analysis was performed using Minitab and MATLAB. A quantitative dependence of the response on factors and interactions in the form of a regression equation was obtained using the least squares method. Analysis of variance (ANOVA) and lack-of-fit test were conducted to determine the statistical significance and quality of fit of the regression model at a confidence interval (CI) of 95% (Eq. (A10) in Appendix A). The goodness of fit for the model was expressed through the coefficient of determination (R^2), (Eq. (A4) in Appendix A) and the adjusted coefficient of determination (R^2 Adj), (Eq. (A5) in Appendix A). Both terms were used to measure the performance of the model while R^2 Adj provided more precision and reliability by considering the number of independent variables in the model (Cheng et al, 2014),(Cho et al, 2019). Response surface plots were also used to visualise the relationship between the independent and dependent variables. A p-value ≤ 0.05 was considered statistically significant. Additional details may be found in the Appendix A at the end of this thesis.

Table 5.1 Factors and levels for D-optimal design (Nathanael et al, 2023b).

Factors	Levels		
pH	7	/	12
Concentration of trisodium citrate [TC] (mM)	1.91	2.87	3.82
Curvature, CR (dm^{-1})	0	/	33.3
Storage temperature, ST (℃)	0	/	20
Flow rates, FR (dm^3/ min)	1×10^{-6}	1×10^{-5}	4×10^{-5}

5.3 DEVELOPMENT OF THE MODEL AND STATISTICAL ANALYSIS

The experimental data (see Table A1 in Appendix B) collected through the D-optimal design, were fitted to a number of polynomial functions to predict the size of AgNPs (y) in nm, where x_1 is pH, x_2 is ST, x_3 is [TC], x_4 is CR and x_5 is FR.

Model 1:

$$y = 59.0 - 2.61x_1 + 1.651\,x_2 - 13.34x_3 - 1.56\,x_4 - 28\,262\,x_5 - 0.49\,{x_3}^2 - 0.12\,x_1x_2 - 0.55\,x_2x_3 - 0.011\,x_2x_4 - 7\,730\,x_2x_5 - 0.66\,x_1x_3 + 0.09\,x_1x_4 + 33\,089\,x_1x_5 + 0.57\,x_3x_4 - 186\,782\,x_3x_5 + 6\,806\,x_4x_5 + 0.039\,x_1x_2x_3 + 0.0005\,x_1x_2x_4 - 109\,x_1x_2x_5 + 0.024\,x_2{x_3}^2 + 0.00098\,x_2x_3x_4 + 2\,575\,x_2x_3x_5 + 69.4\,x_2x_4x_5 + 0.45\,x_1{x_3}^2 - 0.019x_1x_3x_4 - 8\,301\,x_1x_3x_5 - 299\,x_1x_4x_5 - 0.06\,x_4{x_3}^2 + 49\,298\,x_5{x_3}^2 - 1\,361\,x_3x_4x_5 \quad (5.1)$$

Model 2:

$$y = 92.27 - 5.9x_1 + 0.18\,x_2 - 39.08\,x_3 - 0.58\,x_4 - 174\,254\,x_5 + 4.015\,{x_3}^2 - 0.006\,x_1x_2 + 0.02\,x_2x_3 - 0.003\,x_2x_4 - 377\,x_2x_5 + 1.9\,x_1x_3 + 0.04\,x_1x_4 + 3\,531x_1x_5 + 0.05\,x_3x_4 + 33\,099\,x_3x_5 + 1\,057\,x_4x_5 \quad (5.2)$$

Model 3:

$$y = 88.70 - 5.66x_1 + 1.14\,x_2 - 37.9x_3 - 1.16\,x_4 - 43\,634\,x_5 + 3.97\,{x_3}^2 + 1.85\,x_1x_3 - 0.11\,x_1x_2 - 0.002\,x_2x_4 - 0.33\,x_2x_3 + 0.097\,x_1x_4 + 0.26\,x_3x_4 + 0.036\,x_1x_2x_3 - 0.022x_1x_3x_4 \quad (5.3)$$

Different model structures were considered, however, examples of only three models are presented here by Eqs. (5.1) – (5.3). Specifically, Eq. (5.1) shows all possible squared and cubic terms, Eq. (5.2) includes only all squared interactions, whilst Eq. (5.3) presents only some of the possible square and cubic terms such as ${x_3}^2$, x_1x_3, x_1x_2, x_2x_4, x_2x_3, x_1x_4, x_3x_4, $x_1x_2x_3$, $x_1x_3x_4$.

The coefficient of determination (R^2), Eq. (A4) and the adjusted determination coefficient (R^2 Adj), Eq. (A5), for the models Eqs (5.1) – (5.3) (Table 5.2) are very close to 1 indicating that models provide a good fit to the data. However, R^2 and R^2 Adj are not reliable indicators for the formation of a good regression model. The value of R^2 increases as a new variable is added, even if it is not statistically significant. The R^2 Adj includes the

number of parameters but it gives only the variation of independent variables which affect the dependent variable. The selection of the relevant factors in a regression model and consequently the number of model parameters, affects the complexity of the model and ultimately the Akaike Information Criterion (AIC) (Akaike, 1974) and Bayesian Information Criterion (BIC). Both AIC and BIC are widely applied in the area of machine learning and data science to discriminate between the accuracy of models by the number of parameters involved and thus identify those that best describe a system. In BIC, the penalty term is larger than that in AIC. Therefore, BIC generally results in choosing models with less parameters while AIC has larger chances of choosing a model with too many parameters (Claeskens & Hjort, 2008). The expressions of the statistical approaches used to select model are as follows (Akaike, 1974),(Schwarz, 1978), (Bhattacharya & Burman, 2016):

$$\mathrm{AIC} = \mathrm{n}\log\left({}^{\mathrm{SSE}}/_{\mathrm{n}}\right) + 2\mathrm{k} \tag{5.4}$$

$$\mathrm{BIC} = \mathrm{n}\log\left({}^{\mathrm{SSE}}/_{\mathrm{n}}\right) + \mathrm{k}\log(\mathrm{n}) \tag{5.5}$$

where n is the number of experiments, k the number of parameters (or coefficients) in the regression model and SSE is the sum of squared errors, (Eq. (A3)). The model with smallest AIC and BIC is thus the optimal one.

Table 5.2 Values of $\mathbf{R^2}$, $\mathbf{R^2}$ Adj, AIC and BIC for each model (Nathanael et al, 2023b)

Model	R^2	R^2 Adj	AIC	BIC
Model 1	0.9360	0.9214	117.06	123.56
Model 2	0.8895	0.8773	127.52	131.08
Model 3	0.910	0.9015	109.07	112.21

On the basis of the above criteria, Eq. (5.3) was selected over the others because it had the smallest values for both AIC and BIC (Table 5.2). This model can predict the size of AgNPs within the limits of the experimental factors with a minimum standard error equal to 1.84 nm. Note, the model (Eq. (5.1)) includes all variables and their interactions and therefore has the highest values of R^2 and $R^2\ \mathrm{Adj}$, but has larger values of AIC and BIC than model (Eq. (5.3)) because of larger k.

The normal probability plot is a tool to determine if a data set follows a hypothesized distribution (vertical axis is adapted for normal distribution). The probability plot in Figure 5.1A revealed that the plotted points lie on a straight line while histogram plot in Figure 5.1B showed that variation is normally distributed. Both residual plots indicated that there is no deviation from normality, so the errors appear to be independent.

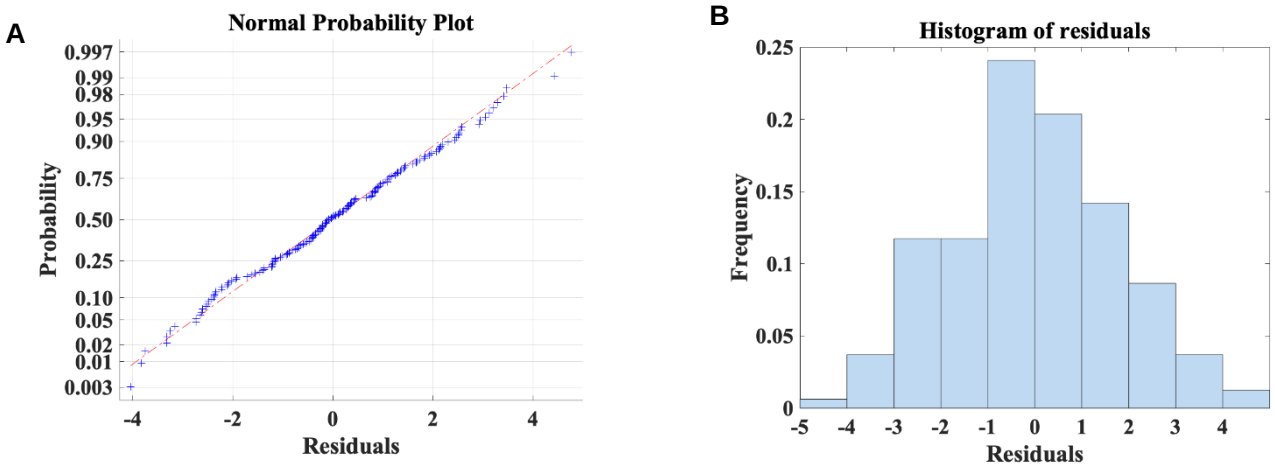


Figure 5.1 Residual plots for the size of AgNPs A) probability and B) histogram of residuals. The data set follows a basic normal (Gaussian) distribution (Nathanael et al, 2023b).

ANOVA (King, 2010) and luck-of-fit test (Fisher, 1922) were performed on the regression model (Eq. (5.3)) for the size of AgNPs to determine the statistical significance and the quality of fit of the model to the dataset. ANOVA uses the sum of squares Eqs. (A1) – (A3) to compare response and error data, the mean square Eqs. A6, A7 to provide an estimate of population variance and the F-test (Eq. (A8)) to show the significant effects at a given probability level based on the sample variance (Wagner et al, 2014). The high F-values along with p-values smaller than 0.05 obtained in the ANOVA test for the model showed the significance of the correlations between the experimental set of data and the fitted polynomial model. The results of the ANOVA and lack-of-fit tests are reported in detail in Table 5.3B. As the assumptions on the normality and variance of residuals were met, confidence intervals (CI) (Eq. (A10)) for regression parameters (Table 5.3A) were calculated. These upper and lower bounds for the CI showed the uncertainty for the parameters (or coefficients) with a confidence of 95%. The t-values (Eq. (A9)) which are also shown in Table 5.3A are used to establish the uncertainty associated with the estimates. A critical t-value (tcrit) equal to 1.98 was used to show how well each parameter was estimated (t > tcrit means that the factor is statistically significant) assuming the parameters are normally distributed.

Table 5.3 A) Parameters and B) analysis of variance for the fitted polynomial model (Eq. (5.3)) of AgNPs optimization (Nathanael et al, 2023b). To link the parameters with the symbols used in the model in Eq. (5.3), y, is the size of AgNPs in nm, x_1 is pH, x_2 is ST, x_3 is [TC], x_4 is CR and x_5 is FR.

A)

Term	Parameter	T-value (A9)	95% Confidence interval for Parameters (A10)	
			Lower Bound	Upper Bound
Variable	88.7	19.54	80	98
pH	-5.66	-13.58	-6	-5
[TC]	-37.9	-16.40	-42	-33
ST	-1.14	5.11	-1	-2
CR	-1.16	-8.58	-1.18	-1
FR	-43 634	-4.79	-61 686	-25 835
$[TS]^2$	3.97	11.66	3.31	4.65
ST.CR	-0.002	-2.21	-0.004	-0.00019
pH. [TC]	1.85	13.56	1.58	2.11
ST. pH	-0.11	-4.52	-0.15	-0.06
ST.[TC]	-0.33	-4.38	-0.48	-0.18
CR. pH	0.097	6.79	0.068	0.12
CR.[TC]	0.26	5.85	0.17	0.35
ST.pH. [TC]	0.036	4.63	0.021	0.052
CR.pH. [TC]	-0.022	-4.61	-0.03	-0.0123

B)

Source	Sum of squares (S1), (A2), (A3)	F-Value (A8)	p-value
Regression	5041.7 (Eq. (A1))	106.21	2.00×10^{-17}
pH	625.61 (Eq. (A2))	184.50	1.00×10^{-17}
[TC]	911.52	268.82	1.00×10^{-06}
ST	88.4	26.07	1.00×10^{-17}
CR	249.62	73.62	1.23×10^{-14}
FR	77.82	22.95	4.02×10^{-06}
$[TS]^2$	461.07	135.98	1.00×10^{-17}
ST.CR	16.51	4.87	1.27×10^{-05}
pH. [TC]	623.81	183.97	1.00×10^{-17}
ST. pH	69.23	20.42	2.53×10^{-10}
ST.[TC]	64.92	19.15	2.28×10^{-05}
CR. pH	156.5	46.16	2.89×10^{-02}
CR.[TC]	115.86	34.17	3.14×10^{-08}
ST.pH. [TC]	72.65	21.42	8.02×10^{-06}
CR.pH. [TC]	72.05	21.25	8.69×10^{-06}
Error	498.45 (Eq. (A3))	/	/

The Pareto chart in Figure 5.2 shows the standardized effects of factors, from the largest to the smallest, with a reference line to note which are statistically significant (Ramachandran & Tsokos, 2021). This chart was built based on t-values (Eq. (A9)) with the threshold calculated using the Student's t-distribution (Student, 1908) with N-Ntheta degrees of freedom (N is the overall number of points used in calibration, Ntheta is the number of parameters or coefficients). Using a pareto chart, the importance and

magnitude of the factors on the size of AgNPs can be determined. Particularly, the most significant factors of the model (Eq. (5.3)) include the pH of the solution, the concentration of trisodium citrate, the interaction of pH and trisodium citrate concentration and the curvature of the output channel. All the experimental factors cross the reference line that is at 1.98 which means all of them are statistically significant at the 0.05 level with current model terms.

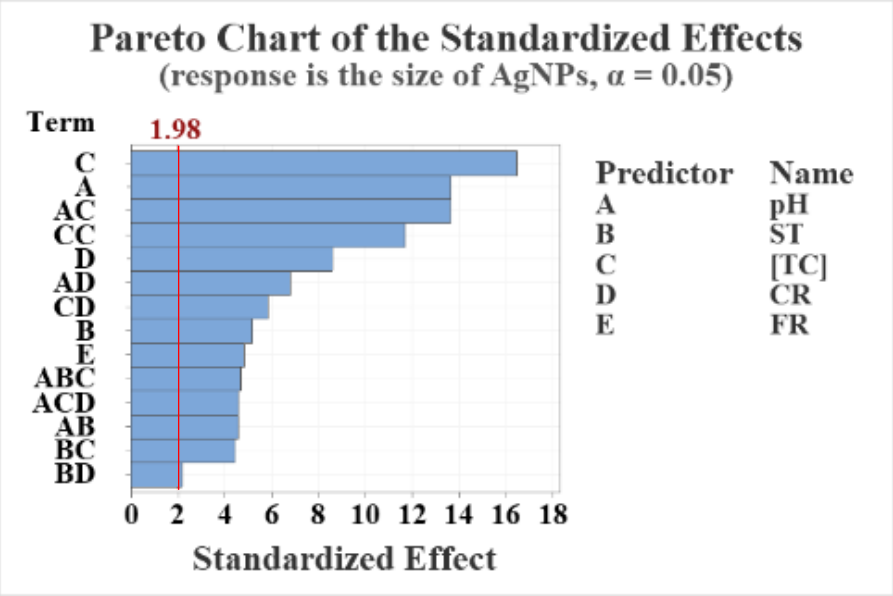


Figure 5.2: Pareto chart (Nathanael et al, 2023b)

Since all parameters are statistically significant, each term meaningfully contributes to the model's predictive power. The inclusion of higher-order terms and interactions prevents the model from oversimplifying or overlooking real-world complexities, ensuring a comprehensive interpretation of the system. For example, the pH and TC concentration interaction (term x_1x_3) is particularly important. Based on the experiments, it was observed that the concentration of TC exhibits a non-linear behaviour at higher pH values, where

increasing pH generally decreases the NP size, but only at certain concentrations of TC. This suggests that the relationship between pH and TC concentration is not a simple linear one, especially for larger values of TC. The quadratic term $3.97x_3^2$ for $[TC]^2$ indicates a non-linear relationship between the concentration of TC (x_3x_3) and the size of AgNPs (y). Non-linearities like this suggest that the effect of TC concentration on the size may not be proportional across different levels of x_3.

5.4 RESPONSE SURFACE METHODOLOGY RESULTS

A graphical representation of the regression model obtained (Eq. (5.3)) is shown via the two-dimensional contour plots in Figure 5.3. The plots were used to study the combined effect between the formulation parameters and the size of AgNPs and to define the optimum condition of each factor to deliver a minimum size of AgNPs.

The plot of storage temperature versus trisodium citrate concentration (Figure 5.3B), shows that the size of the AgNPs is virtually independent of storage temperature for a trisodium citrate concentration below 3 mM. The AgNPs produced are also small under these conditions.

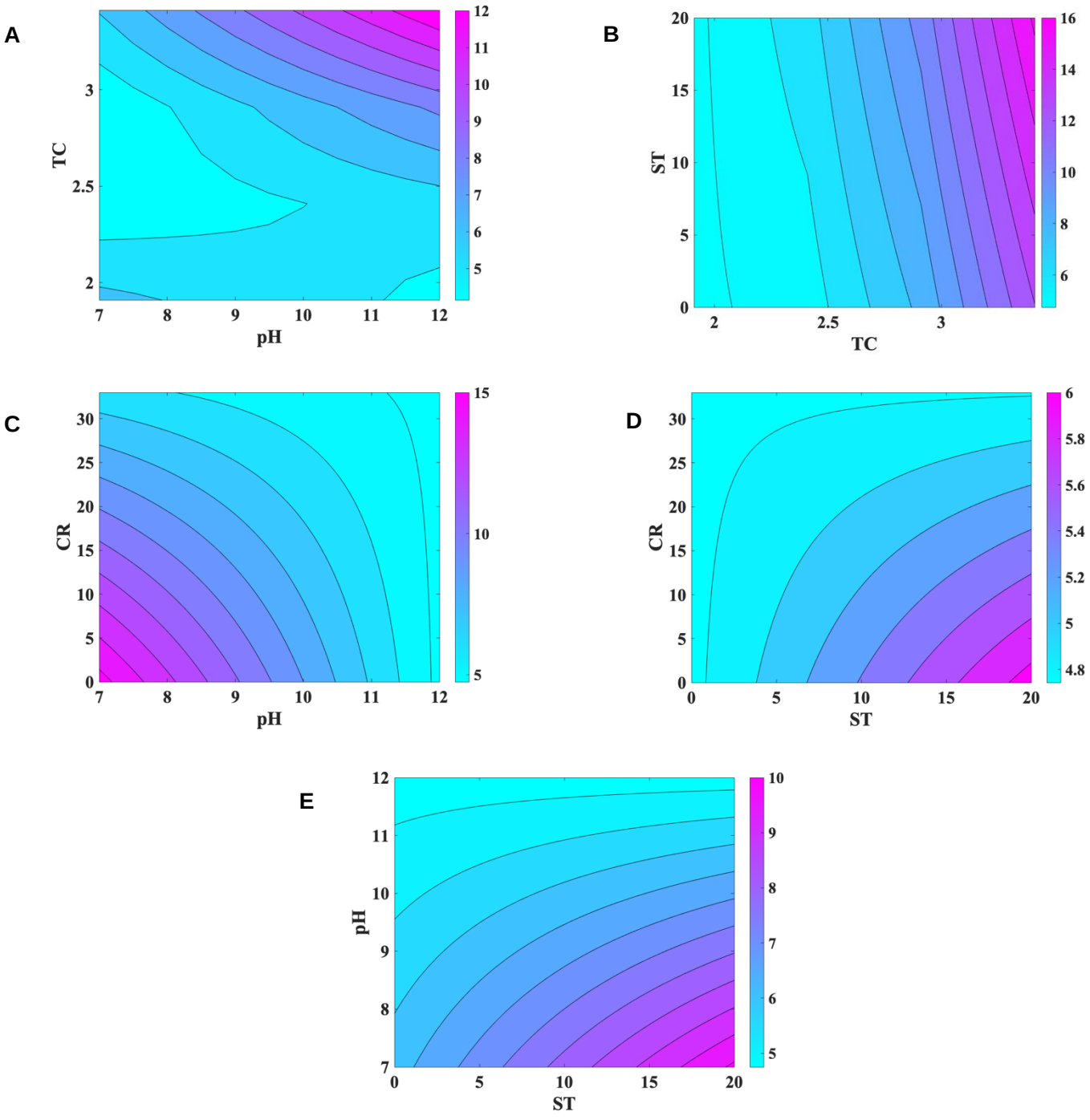


Figure 5.3 Contour plots predicting the size of AgNPs. The pH, ST, TC, CR and FR were kept constant at 12, 0℃, 1.91 mM, 33.3 dm^{-1}, 1×10^{-5} dm^3/min respectively.

Note the units for curvature expressed in dm^{-1} , flow rates in dm^3/min, storage temperature in ℃, and concentrations in mM (Nathanael et al, 2023b).

There is an effect of storage temperature and concentration of TC on the size of particles above TC = 3 mM. The plot of curvature of the outlet channel versus storage temperature (Figure 5.3D) shows that there is a strong effect on the size of particles at higher storage temperatures and smaller curvature of the outlet channel. According to the plot of storage temperature versus pH in Figure 5.3E, the interaction of pH and storage temperature strongly influences the size of particles only at smaller pH. Similarly, the plot of curvature of the channel versus pH (Figure 5.3C) of the solution shows a significant effect of curvature of the channel at a value of pH below 11. The effect of different factors on the size of AgNPs, in particular Figure 5.3A, will be discussed in more detail in the next sub-sections.

5.5 EFFECT OF TRISODIUM CITRATE CONCENTRATION, PH AND STORAGE TEMPERATURE

Trisodium citrate acts as both reducing and stabilising agent in the synthesis of AgNPs. Citrate ions can reduce silver ions at elevated temperatures (Khatoon et al, 2017) or under alkaline conditions (Marciniak et al, 2020), but they can also weakly interact with silver generating a charged layer that works as an electrostatic barrier to aggregation (El Badawy et al, 2012). The effect of trisodium citrate concentration was investigated over a range from 1.91 mM to 3.82 mM. Figure 5.3A shows that there is an optimal range of concentration of TC for the minimum size of AgNPs between 2.3 mM and 3.1 mM at pH

7. It may be assumed that trisodium citrate within this concentration range fully covers the surface of the AgNPs and thus prevents further particle growth. At lower concentrations, the surface coverage is incomplete enabling the particle growth. An increase of concentration above 3.1 mM can result in a decrease of Debye length due to an increase of ionic strength of the solution, below a certain critical point aggregation may occur. Henglein & Giersig (1999) investigated the formation of AgNPs through γ-irradiation of $\mathrm{AgClO_4}$ which contains 2-propanol and a range of citrate concentrations from 0.05 to 1.5 mM. In this system, citrate did not participate in silver reduction and so is present solely to stabilise the AgNPs. It was found in Henglein & Giersig (1999) that the small particles with a narrow size distribution were obtained at 0.1 mM $\mathrm{AgClO_4}$ solutions for a range of citrate concentrations between 0.1-0.5 mM (silver concentration in this work is considerably higher while TC concentrations comparable). At smaller concentrations, large particles with a broad size distribution were formed. This was ascribed to a rather loose citrate layer on the surface of Ag clusters which was unable to prevent their growth first via condensation and later via coalescence. At concentrations larger than the optimum, larger particles were formed via coalescence due to high ionic strength of the solution. The Ag concentration in this work is considerably higher than in the Henglein & Giersig (1999) study, while the TC concentrations used were comparable and a bit higher. Das et al (2021) also showed that there is an optimal concentration of trisodium citrate in AgNPs synthesis. Their study investigated the effect of TC concentration on AgNP size and distribution using DLS. Low TC concentrations resulted in larger, more variable particles (~51 nm) due to inadequate coverage, allowing continued growth. The optimal

TC concentration produced the smallest particles (~7 nm) with a narrow distribution, as it effectively coated the nanoparticle surfaces and restricted growth. Excess TC raised the pH of the solution, promoting aggregation and growth, which reduced its stabilizing effect. These results were explained by the LaMer model, which suggests low monomer concentrations favor larger particles due to limited nucleation.

It is well-known that the pH of the solution influences the chemistry of a reaction mixture. Here, the effect of pH on the reaction was examined by adjusting the pH at two levels of 7 and 12. The nanoparticles formed at pH 12 and a concentration of TC of 1.91 mM were smaller compared to those produced at pH 7 and a concentration of TC of 1.91 mM, indicating that a basic pH altered the kinetics of reaction (Figure 5.3A). Under alkaline conditions, the dissociation of citrate and dicarboxyacetone (DCA), which is produced as a by-product of the decarboxylation of citrate during silver reduction, is shown in Figure 5.4. The completely hydrolysed DCA^{2-} (Marciniak et al, 2020) and Cit^{3-} species (Dong et al, 2009) at pH 12 have a higher reducing ability, leading to faster reduction of the silver ions to silver atoms and thus smaller particles.

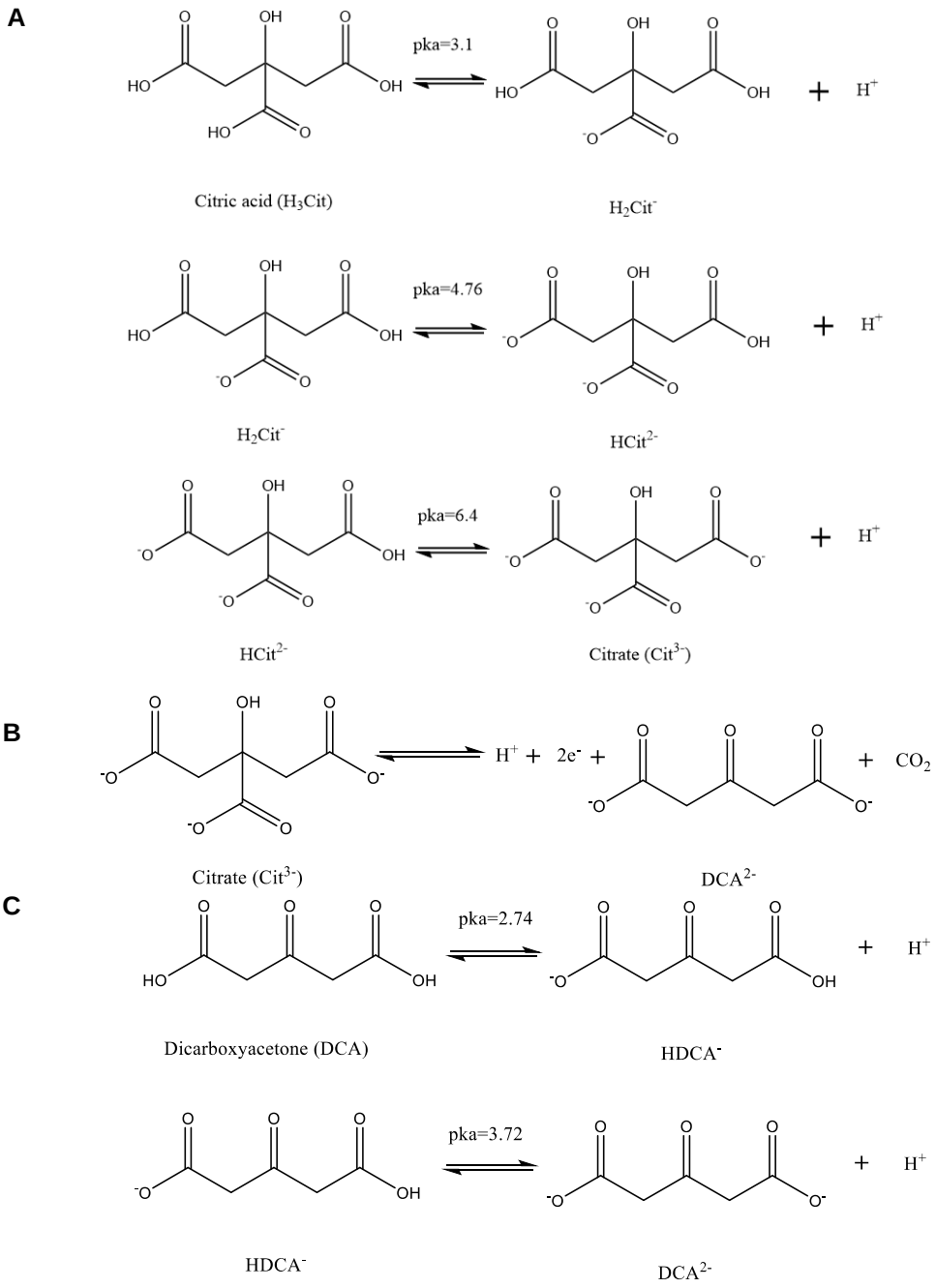


Figure 5.4 A) Dissociation species of citrate, B) Production of dicarboxyacetone (DCA) as a by-product of the decarboxylation of citrate during silver reduction and C) Dissociation species of DCA. Reproduced from Gao & Torrente-Murciano (2020) and Marciniak et al (2020).

Furthermore, at basic pH, tannic acid can be hydrolysed into gallic acid and glucose (Osawa & Walsh, 1993) where the former is a good reducing agent and the latter is a good stabilizer. Hence, the chemical rearrangement in the structure of tannic acid when exposed to alkaline pH promotes the formation of smaller particles (La Spina et al, 2020). However, when the pH of the solution was increased alongside a trisodium citrate concentration above 2.87 mM, the size of particles increased (Figure 5.3A). The balance between attractive van der Waals and repulsive electrostatic forces which governed the stability of colloidal dispersion can be manipulated by changes in pH, ionic strength and temperature (Chhabra & Basavaraj, 2019). In general, as the ionic strength of a solution increases, the thickness of double layer associated with the AgNPs is reduced, resulting in weaker electrostatic repulsions between the AgNPs (Phan & Haes, 2019). This can be the reason for an increase in particle size at high concentration of trisodium citrate.

The surface charge of AgNPs is governed by the ionization of carboxyl-groups, ($-\mathrm{COOH}$), of the citrate molecules, which is dependent on the pH and ionic strength of surrounding aqueous phase (Badawy et al, 2010). AgNPs obtained at concentrations of TC less than 2.87 mM were smaller for both values of pH studied, when compared to AgNPs prepared at larger concentrations (3.82 mM) (Figure 5.3A). At higher concentrations of TC, particles of smaller size were observed only at smaller pH. In Figure 5.5A, it can be seen that the zeta-potential of AgNPs prepared at pH 7 and TC = 2.87 mM is approximately the same as the AgNPs obtained at pH 12 and TC = 1.91 mM, indicating that higher concentration

of stabilising agent increases the stability of AgNPs in the same way as alkaline pH. By increasing the pH, the carboxyl-groups ($-\mathrm{COOH}$) on the AgNP surface reach a higher degree of deprotonation and the value of negative surface charge increases. Thus, the electrostatic repulsion between particles is improved causing smaller AgNP diameters.

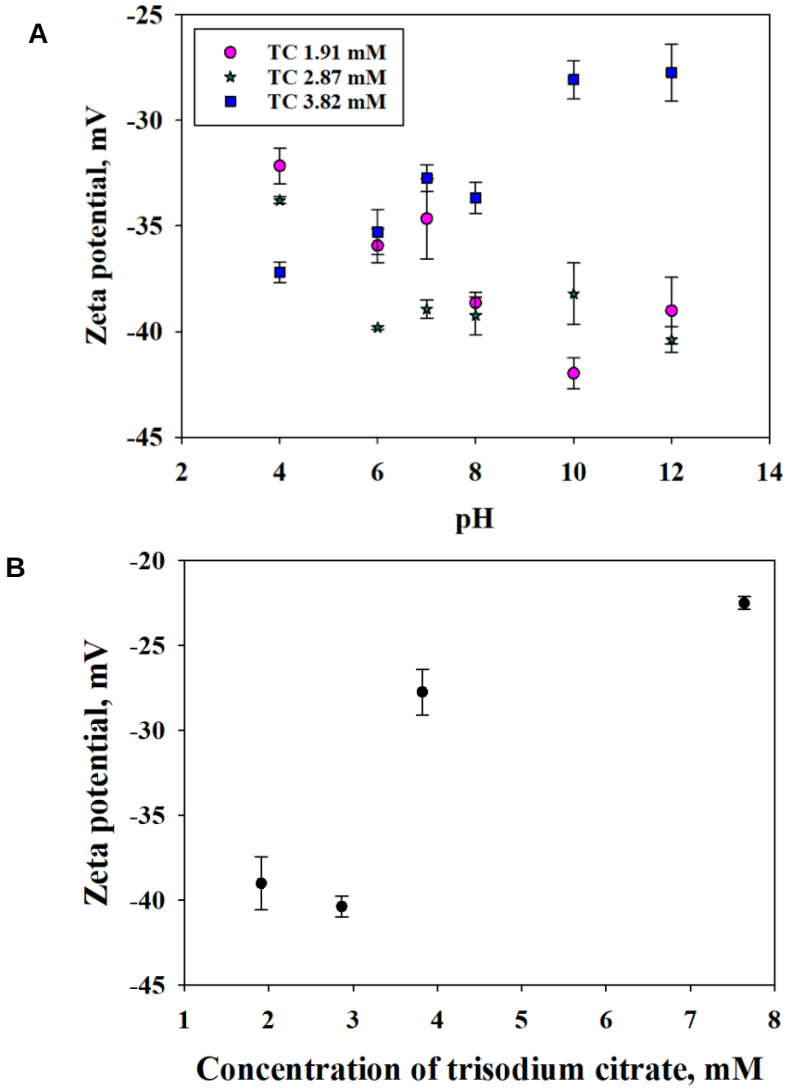


Figure.5.5 A) Dependence of zeta potential of AgNPs on pH at different concentrations of trisodium citrate and B) Zeta potential of AgNPs at pH 12 for different concentrations of trisodium citrate (Nathanael et al, 2023b).

On the other hand, AgNPs prepared at 3.82 mM TC showed a small gradual increase in diameter and a decrease in zeta potential absolute values with an increase in pH (Figure 5.5A), indicating reduction in electrostatic repulsion due to decrease of surface potential and probably due to decrease of Debye length. Figure 5.5B also shows that as the concentration of trisodium citrate increases at pH 12, the surface-potential decreases. In line with this suggestion, Liu et al (2014a) examined the effect of pH and ionic strength on the growth of tannic acid-poly(N-vinylpyrrolidone) (TA-PVPON) multilayers, and found that the thicker multilayers are obtained at alkaline pH in the presence of high salt concentrations. They claimed that these conditions cause thicker multilayers due to screening of the negatively charged tannic acid.

The ageing of AgNPs dispersions can be also affected by storage temperature since chemical reaction rate increases with temperature. As it can be seen in Figures 5.3E and 5.3D, the collection of samples at T = 0 ℃ quenched the reduction reaction or aggregation and led to the production of smaller particles. Many previous studies reported changes in nanoparticles samples kept at room temperature such as Velgosova et al (2017) and Peng et al (2010).

5.6 EFFECT OF CURVATURE AND FLOW RATES

In microreactors, variation in the flow rates of reagents and the flow configurations changes the residence times and mixing conditions, thus influencing the overall reaction of AgNPs including nucleation and growth steps (Baber et al, 2017), (Ravi Kumar et al, 2012). The formation of AgNPs requires uniform reaction conditions because the reduction of silver ions to silver atoms is very fast. For example, uniform mixing is essential

to distribute reactants evenly and prevent local variations in concentration. Non-uniform conditions can result in incomplete reduction of the silver precursor leading to wide variations in sizes and shapes of NPs. It has been reported that reduction stage can be carried out in less than 200 ms (Polte et al, 2012). In the present study, the flow rates of reagents varied from 1×10^{-6} dm^3/min to 4×10^{-5} dm^3/min and mixing was intensified by coiling the outlet tube on a 3D-printed helical design. The Dean number (De) (Eq. (4.1)), which represents the Dean force due to secondary flow in curved channels (Nivedita et al, 2017) was calculated to be 0.033, 0.34 and 1.39 respectively for the three different flow rates used in the experiments, see Table 5.1. The Dean numbers observed in this study are relatively low when compared to the thresholds reported in the literature for significant curvature effects or enhanced mixing. The channel diameter used in this study (0.5 mm) is smaller than those employed in several other studies, which may influence the interpretation of these values. For instance, Mansour et al (2019) demonstrated that optimal mixing occurred at De=10 for cylindrical channels with diameters of 5–15 mm. In contrast, Wu et al (2017) observed significant effects on AgNP size and size distribution in microfluidic devices at De≥2, with narrow distributions emerging at De≥7 for helical tubular reactors with an inner diameter of 0.762 mm. Note, at the low De values used in this study, any secondary flows or vortices are weak compared to the dominant axial flow. However, even weak secondary flows can influence PSD. For example, De≤0.34 in coiled channels resulted in statistically significant reductions in AgNP size compared to straight channels (De=0). This suggests that while the strength of the vortices is relatively small at these De values, they still contribute to enhanced mixing and particle formation dynamics compared to purely axial flows in straight channels. Thus, while fully developed

Dean vortices are unlikely to form at the Dean numbers in this study, the minor secondary flow effects are sufficient to influence the system's behaviour.

The increase in the flow rate decreases the residence time in the outlet tube, but increases the mixing, especially in helical channel. To check for completeness of reaction, experiments (pH 7, TC 1.91, ST 0℃, CR 0 dm^{-1}) were performed at two different flow rates in straight channel (2×10^{-4} dm^3/min and 6.7×10^{-5} dm^3/min) with different outlet tube lengths (2 m and 0.667 m), so that residence time was the same for both cases. The concentration of silver nitrate was measured at the exit using the silver electrode. Results showed that mixing (even in straight output channel) and residence time are both significant. At conditions of 2×10^{-4} dm^3/min and 2 m length, the residual concentration of silver nitrate was 0.031 $\pm$ 0.0036 mM ($\sim$ 3% of initial concentration) but at the same residence time at 6.7×10^{-5} dm^3/min and 0.667 m length the silver nitrate concentration was 0.051 $\pm$ 0.0054 mM ($\sim$ 5% of initial concentration). The larger residual concentration of silver nitrate in the last case shows that at the smaller flow rate, the reaction was farther from completion. Considering that reagent transfer in a straight tube is mostly diffusional, the degree of mixing at the T-junction, which increases with an increase of flow rate, may be a significant factor. The characteristic diffusion times of $AgNO_3$, tannic acid and trisodium citrate were calculated as 36, 288 and 46 seconds respectively, for the diffusion length of 0.25 mm while the residence time in both devices was estimated as 117.75 seconds. Although the diffusion time of tannic acid suggests slower interaction with silver ions, this does not completely exclude its role in the reduction process. Factors such as its concentration and its potential interaction with trisodium citrate could influence the

reaction dynamics. It is also worthy mention that not only diffusion of tannic acid towards the silver nitrate is important for reduction but also diffusion of silver nitrate into tannic acid solution which is fast. Note, the diffusion constant of $AgNO_3$, tannic acid and trisodium citrate are 1.738 $\times 10^{-9}$ (Harned & Hildreth, 1951), 2.171 $\times 10^{-10}$ (Poling, 2001) and 1.351 $\times 10^{-9}$ m^2/s (Sadeghi & Ziamajidi, 2007) respectively.

At 6.7 $\times$ 10^{-5} dm^3/min with a 2 m outlet tube, the residual concentration of silver nitrate was around 0.017 $\pm$ 0.00053 mM (less than 2% of initial concentration). Therefore, the reduction of silver nitrate was practically complete when the residence time was increased from 117.75 sec to 353 sec. It was also observed that the size of AgNPs is greatly influenced by the curvature of the output channel (e.g., Figure 5.3C). In straight channels under laminar flow, there is a characteristic parabolic profile. The curvature of the outlet tube modified the flow pattern by the formation of secondary flows (Dean vortices) which improved the radial mixing in the channel (Wu et al, 2017). Sufficient mixing allowed fast mass transfer during reduction process and homogenous growth and hence led to the formation of smaller particles.

5.7 EXPERIMENTAL VALIDATION OF THE MODEL

The validation of the obtained model and verification of the optimization results was carried out according to the optimal synthesis conditions. Using (Eq.(5.3)), the model predicted the global minimum size to be 2.62 nm and a local minimum size of AgNPs to be 4.32 nm when the optimal conditions were set to pH 7, trisodium citrate 2.68 mM, curvature 33.3 dm^{-1}, storage temperature at 0^{o}C and flow rate 4×10^{-5} dm^3/min and to pH

12, trisodium citrate concentration 1.91 mM, curvature 33 dm^{-1}, flow rate 2×10^{-5} dm^3/min and storage of samples at 0 ^oC respectively. These predicted conditions for minimum size of AgNPs were confirmed experimentally with an error of 16.1% and 7.0% respectively, see Figure 5.6. The Figure 5.6 and Figure A1 in Appendix E show a comparison between the PSDs measured using dynamic light scattering (DLS) with zetasizer and transmission electron microscope (TEM) under different experimental conditions. The zetasizer instrument gives measurements of PSD based on the assumption that the particles are spherical. The measurements between these two characterisation methods presented a very good agreement supporting the assumption that particles are spherical. Previous studies such as Ranoszek-Soliwoda et al. [53] have also used TA and TC for the synthesis of AgNPs and reported the production of spherical particles under similar conditions. It is worth noting that in Figure 5.6, the tails differ slightly because DLS number distributions tend to emphasize smaller particles, which can mask the contribution of larger particles to the overall distribution. This results in the absence of a tail towards larger sizes in DLS data, whereas TEM data directly measures the physical size of particles and captures a broader range of sizes, including outlier particles. Intensity-based distributions from DLS often show broader size distributions not observed in TEM. Overall, number distributions are more representative of the sample than TEM measurements.

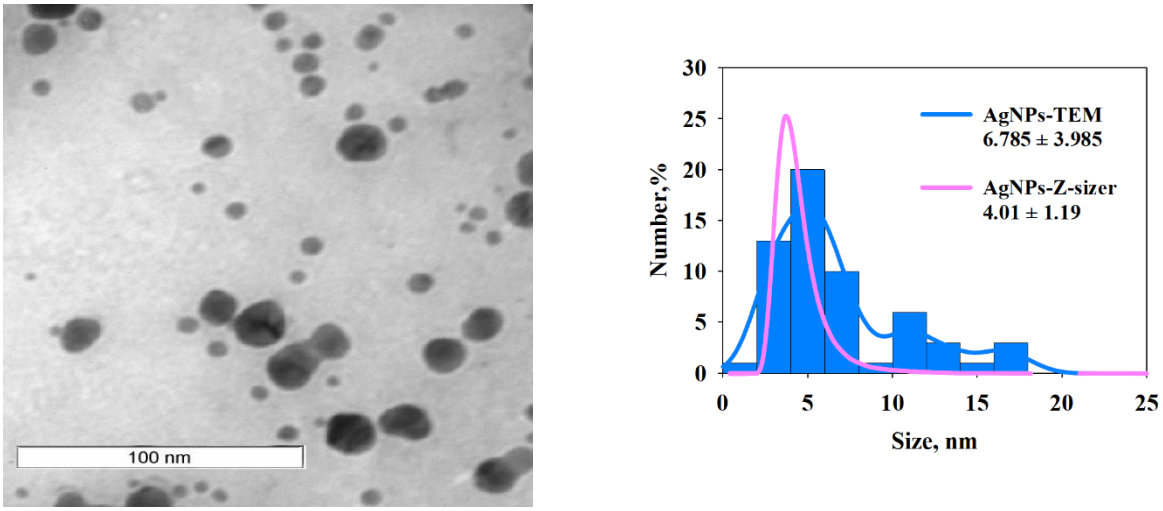


Figure 5.6 AgNPs size distribution from TEM and zeta-sizer. AgNPs at 2×10^{-5} $\mathbf{dm^3/min}$, pH 12, TC 1.91 mM, CR 33.3 $\mathbf{dm^{-1}}$ and ST 0 ℃ (Nathanael et al, 2023b).

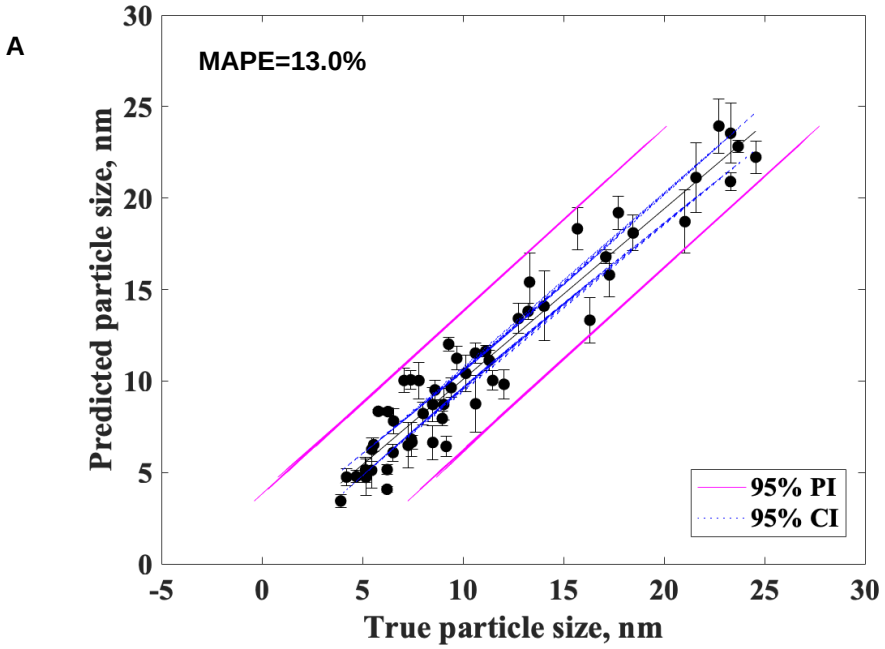
More subsequent experiments were performed in triplicate to validate the predicted model. The predicted versus experimental values of AgNPs size for the training data and testing data are presented in Figures 5.7A and 5.7B respectively. The mean absolute percentage error (MAPE) (Eq. (5.6)),(Dash & Dash, 2017) was calculated using the equation below where y_k is the measured response and $\widehat{y_k}$ is the predicted value:

$$\mathrm{MAPE} = \frac{1}{n}\sum_{k=1}^{n}\left|\frac{y_k-\widehat{y_k}}{y_k}\right| \times 100\,\% \qquad (5.6)$$

The training data contains 162 experiments, including replications, while testing data comprised of only 45 experiments including replications. The testing data were taken from independent experiments selected randomly within the limits of experimental factors.

These include experiments close to optimal conditions and beyond them. The optimal points are illustrated with red dots in Figure 5.7B. The confidence intervals (CI), Eq. (A10), and prediction intervals (PI), Eq. (A11), for the predicted responses were estimated to present the uncertainty with a probability of 95%. To be more precise, PI appears wider than CI because it shows the variability related to single observations, while CI reflects the variability associated with the uncertain estimates of parameters (or coefficients) (Lane & DuMouchel, 1994).

The predicted values are close to experimental responses of the testing data set and within the confidence and prediction intervals, suggesting that the model is successfully developed with correlation between the different factors and the size of AgNPs. The average prediction error of the training set was estimated around 13%, with 37% the maximum error while the average prediction error of the testing set was calculated to be 6.8% with 16.1% being the maximum error.



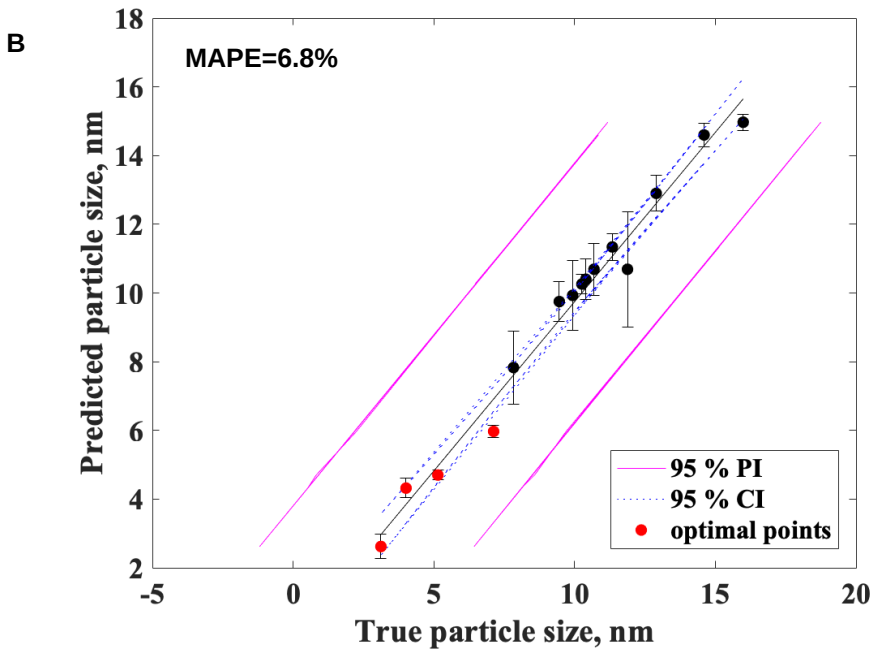


Figure 5.7: Predicted and true particle size of the A) training data (162 experiments including replications) and B) testing data (45 experiments including replications) using Eq. (5.3). The confidence intervals (CI) and prediction intervals (PI) for the predicted responses were estimated with error 95%. Note, that black and red dots represent the average of three experimental observations with corresponding error bars (Nathanael et al, 2023b).

5.8 CONCLUSIONS

A D-optimal experimental design was applied to build a predictive regression model using response surface methodology to optimize the formation of AgNPs in a microfluidic continuous flow reactor. The statistical analysis provided an insight into factors effects on the measured response as well as interaction effects between factors which are difficult

to identify using OFAT methods. Different response surface models were considered, and model discrimination was carried out to select the model using AIC and BIC. Through the investigation of five experimental factors including storage temperature, pH of the solution, concentration of stabilising agent (trisodium citrate), curvature of output channel and flow rates, it was shown that all factors are significant for the measured response while pH, concentration of trisodium citrate, curvature, and the interaction of trisodium citrate concentration and pH are the most vital. The resulting model equation was graphically represented as a response surface function and allowed identification of optimized hydrodynamic and reaction conditions. The optimal combinations (pH 7, TC 2.68 mM, CR 33.3 dm^{-1}, ST 0 ^{o}C and FR 4×10^{-5} dm^3/min) and (2×10^{-5} dm^3/ min, pH 12, TC 1.91 mM, CR 33.3 dm^{-1} and ST 0 ^{o}C) predicted AgNPs with an average size of 2.62 nm and 4.32 nm respectively. The average prediction error of testing data set was calculated as 6.8% confirming that a reliable model has been developed which correlates the effect of the different factors on the size of AgNPs.

CHAPTER 6: ANALYSIS ON REACTION KINETICS OF SILVER NANOPARTICLES SYNTHESIS [3]

6.1 INTRODUCTION

Understanding the kinetic constants governing the synthesis of silver nanoparticles is essential for advancing their industrial applications (Nathanael et al, 2022) and evaluating their environmental impact (Mbanga et al, 2022). This chapter aims to elucidate these constants for comparing two distinct chemical protocols using a well-mixed batch reactor. By investigating the kinetics of AgNP formation using these protocols, quantitative data will be derived to serve as inputs for numerical simulations and data-driven models.

The kinetics not only influence the rate of NP formation but also play a significant role in controlling their size, shape, and dispersity—critical factors for their performance in various industrial applications (Nathanael et al, 2022). A detailed understanding of the reaction mechanisms underlying AgNP synthesis can be obtained through these kinetic studies. Differences in reaction pathways between the two protocols can provide insights into the dominant steps and rate-limiting processes involved in NP formation.

As discussed in § 2.4, the Finke-Watzky two-step mechanism (Watzky & Finke, 1997) has been recognized as a suitable model for describing the autocatalytic synthesis of AgNPs.

[3] Sections 6.2, 8.2-8.4 and 8.6 of these chapters are adapted from Nathanael, K., Cheng, S., Kovalchuk, N.M., Arcucci, R., Simmons, M.J.H. (2023) Optimization of microfluidic synthesis of silver nanoparticles: a generic approach using machine learning, *Chem. Eng. Res. Des.*, **193**, 65-74.

Therefore, it will be employed to estimate the nucleation and growth constants of AgNPs derived from the two distinct chemical sets in a well-mixed reactor.

This investigation the kinetic constants of AgNPs using two different protocols represents a critical step towards enhancing the understanding of their synthesis dynamics and utilizing this knowledge for practical applications in nanotechnology and environmental science.

6.2 KINETIC CONSTANTS OF TANNIC ACID AND TRISODIUM CITRATE

The first chemical protocol for the synthesis of AgNPs in a well-mixed reactor involves tannic acid and trisodium citrate and is fully described in § 3.1.

The kinetic curves characterizing time dependence of concentration of silver included in nanoparticles are shown in Figures 6.1A and 6.1B. At pH 7, nucleation is rather slow, and the kinetic curves have a typical sigmoidal shape.

Table 6.1 reports the values of k_1 and k_2 for each case of conditions, found from the linear fitting of F-W, as well as the estimations of t_{ind}, t_{max} and $t_{plateau}$ using Eqs. (6.1) -(6.4).

$$t_{ind,j} = \frac{\ln\left(\left(2-\sqrt{3}\right)\frac{k_2[A]_0}{k_1}\right)}{k_1+k_2[A]_0} \tag{6.1}$$

$$t_{ind,p} = \frac{k_1+k_2[A]_0}{(k_1-k_2[A]_0)^2}\ln\left(\frac{k_2[A]_0}{k_1}\right) + \frac{2}{k_1-k_2[A]_0} \tag{6.2}$$

$$t_{max} = \frac{\ln\left(\frac{k_2[A]_0}{k_1}\right)}{k_1+k_2[A]_0} \tag{6.3}$$

$$t_{plateau} = \frac{\ln\left(\left(2+\sqrt{3}\right)\frac{k_2[A]_0}{k_1}\right)}{k_1+k_2[A]_0} \tag{6.4}$$

Where $t_{ind,j}$ and $t_{ind,p}$ represent different interpretations of the induction time, t_{max} reports the time at the maximum rate of consumption, and $t_{plateau}$ accounts the time at which fully consumption of precursor is achieved. Bentea et al (2017) derived these expressions from the overall F-W reaction rate of consumption as shown in Eq. (2.5). To be more specific the characteristic times (induction period, maximum slope, and time of maximum growth) are derived directly from the analytical expressions for the first, second, and third derivatives (rate, acceleration, and rate of change of acceleration) of the product concentration $[B]_t$ over time, which are based on the fundamental F-W model parameters (k_1, k_2, $[A]_0$). Notably, the time of maximum rate (t_{max}) corresponds to the inflection point of the sigmoidal curve, while the time of maximum acceleration (t_{ind}) marks the transition from the lag to the exponential growth phase.

Using the values for k_1 and k_2,shown in Table 6.1, it is easy to find that condition $k_1 \ll k_2[A]$ is valid for [A] >> 0.03 mM, which is only 3% of initial concentration of SN, 0.92 mM. The obtained values of rate constants are validated by recalculating the full kinetic curve using Eq. (2.6) with these constants.

Excellent agreement between the theoretical and experimental kinetic curves is shown in Figure 6.1A (pH 7). Multiple studies such as Anigol et al (2017), Jebakumar Immanuel Edison & Sethuraman (2013), and Dong et al (2009) have shown that pH changes the kinetics in the formation of AgNPs, using *Capparis Moonii* fruit extract, Pod Extract of *Acacia nilotica* and citrate as reducing agents, respectively. At moderate pH, there is a

slow reduction rate of the precursor while at high pH there is an improved reducing ability of the reducing agent that results in smaller size particles.

At pH 12, it was observed that the silver nuclei formation proceeded very fast, without a noticeable lag phase for all studied stabilising agent concentrations, in agreement with literature data (Iashchishyn et al, 2017). Only the right-hand side part of sigmoidal curve can thus be measured, which mostly accounts for particle growth.

It is important to note that t_{ind} and t_{max} using the fittings of k_1 and k_2 at pH 12 lead to negative values reported as '–' in Table 6.1. Although the linear fitting in Figure 6.1D (pH 12) gives a reasonable fit, using values of kinetic constants provided in Table 6.1 shows that this linear fitting is valid only for [A] >> 0.5 mM for [TC] = 3.82 mM and [A] >> 1 mM for [TC] = 1.91 mM. Using these constants with the full F-W model, Eq. (2.6), does not provide as good agreement with experimental data as for the lower value of pH, but it is still acceptable as can be seen from Figure 6.1D (pH 12). Note, non-linear fitting directly using Eq. (2.6) does not improve the fitting presented in Figure 6.1B (pH 12). Thus, the values of nucleation and growth constants presented in Table 6.1 were used as the best possible fitting.

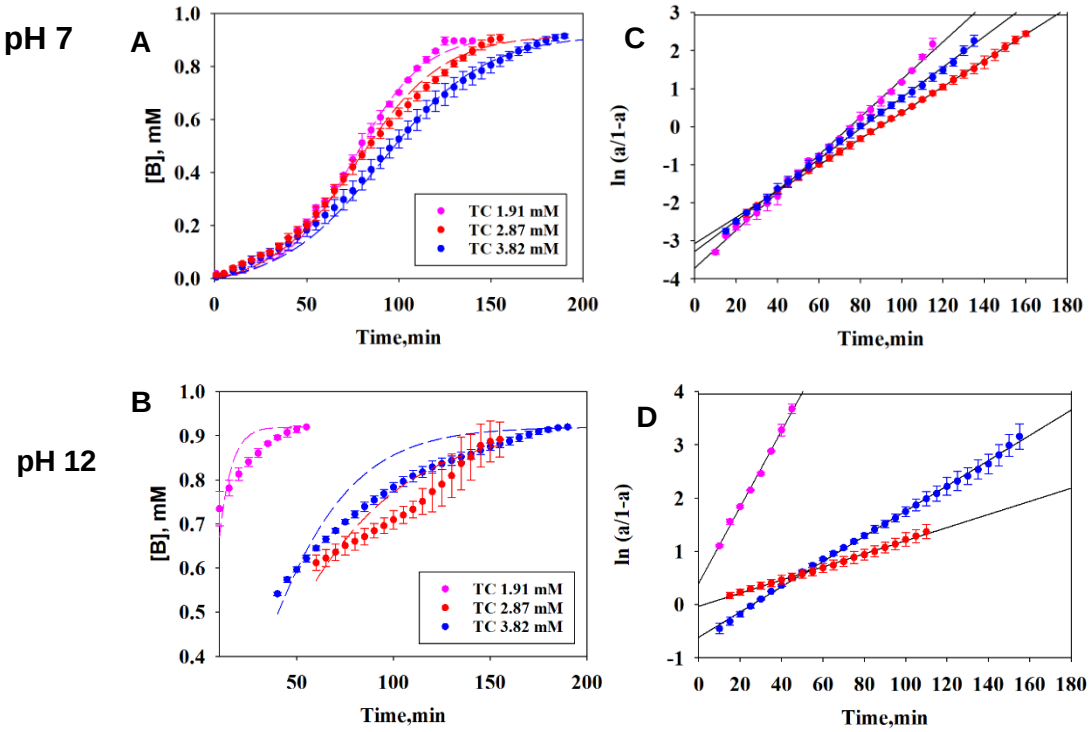


Figure 6.1 Application of the F-W model for the analysis of AgNPs formation kinetics for the first set of chemicals (TA and TC). Time evolution of $[B]$ found from absorption at 400 nm for A) pH 7 and B) pH 12 and different concentrations of the stabilising agent (TC): symbols represent experimental data; lines are fitting of full model Eq. (2.6) with kinetic constants found from linear fitting Eq. (2.7); Fitting of experimental data using linear form of Finke-Watzky model as shown in Eq. (2.7) for C) pH 7 and D) for pH 12 (Nathanael et al, 2023a). In plots C and D, a is $([A_0] - [A])/[A_0]$, A_0 refers to the initial concentration of reactant A, and [A] refers to its concentration at any time t.

For the investigated case, under alkaline pH, there is a full dissociation of citrate species (Dong et al, 2009) and dicarboxyacetone (DCA) (Marciniak et al, 2020), generated as a by-product of the decarboxylation of citrate during silver ions reduction, which makes the chemistry of the system more complex. Therefore, it is possible that several parallel processes are involved with different nucleation and growth constants making fitting of the kinetic curves much more challenging.

Table 6.1 Nucleation and growth constants for varied pH and concentrations of trisodium citrate. The silver nitrate concentration was 0.92 mM.

pH	[TC] (mM)	Nucleation constant,k_1 (min^{-1}) (average)	Growth constant, k_2 ($M^{-1}min^{-1}$) (average)	$k_2[A]_0/k_1$	$t_{ind,j}$ /min	$t_{ind,p}$ /min	t_{max} /min	$t_{plateau}$ /min
7	1.91	0.0011	55.51	46.43	48.32	40.16	73.57	98.81
7	2.87	0.0013	37.86	26.79	62.34	52.04	99.10	135.8
7	3.82	0.0015	44.81	27.48	46.73	39.37	77.56	108.4
12	1.91	0.1	77.97	0.72	-	-	-	5.73
12	2.87	0.012	13.66	1.05	-	0.63	1.88	55.48
12	3.82	0.0128	26.01	1.87	-	5.82	17.03	52.89

6.3 KINETIC CONSTANTS OF DMAB AND SDS AND COMPARISON WITH THE KINETICS OF TANNIC ACID AND TRISODIUM CITRATE

A second set of chemicals was investigated for the synthesis of AgNPs in a well-mixed reactor. This chemical protocol fully described in § 3.1 involved DMAB and SDS. The nucleation and growth constants were estimated experimentally in the same way (linear fitting of F-W mechanism, see Figures 6.2 and 6.3) as first set of chemicals based on F-

W mechanism (Watzky & Finke, 1997) described in detail in § 2.4. Previous studies such as Rivero et al (2013) and Wojnicki et al (2019) investigated DMAB as reducing agent in the synthesis of AgNPs, while studies such Kora et al (2009), Parrey et al (2021) and Shah et al (2019), explored the effects of SDS. However, the combined effect of DMAB and SDS have not been previously investigated.

Rivero et al (2013) investigated the effect of DMAB in AgNPs synthesis and they observed that as the concentration of DMAB increased, the maximum absorption bands shifted towards shorter wavelengths, leading to a change in the colours formed during the synthesis process, transitioning from violet to orange. This phenomenon is often observed when the size or shape of the NPs changes, or when there is a change in the local environment of the nanoparticles. In general, a shift of the absorption peak towards shorter wavelengths, indicates a decrease in NP size (Chicea et al, 2023).

Al-Thabaiti et al (2008) examined the formation and characterisation of surfactant stabilized AgNPs using SDS in the reduction of silver nitrate by ascorbic acid. They suggested that the behaviour of SDS in the stabilization of AgNPs may be due to several factors, including the solubilization or incorporation of reactant species and AgNPs into the micellar phase, as well as the adsorption of AgNPs onto the anionic head group of SDS micelles through electrostatic interactions. Additionally, they suggested that the

positive charge on Ag^{+} forms an ion pair with the negative group of SDS micelles ($-SO^{-}{}_{3}Ag^{+}$).

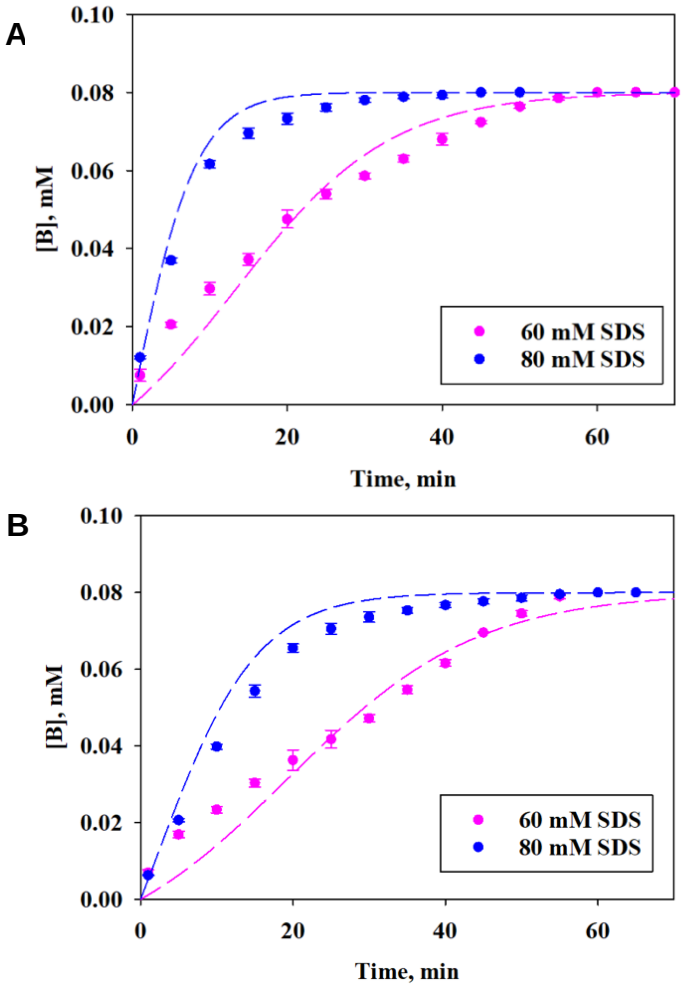


Figure 6.2 Time evolution of $[B]$ for second set of chemicals found from absorption at 400 nm for A) 0.2 mM DMAD and B) 0.4 mM DMAB and different concentrations of the SDS: symbols represent experimental data; lines are fitting of full model Eq. (2.6) with kinetic constants found from linear fitting.

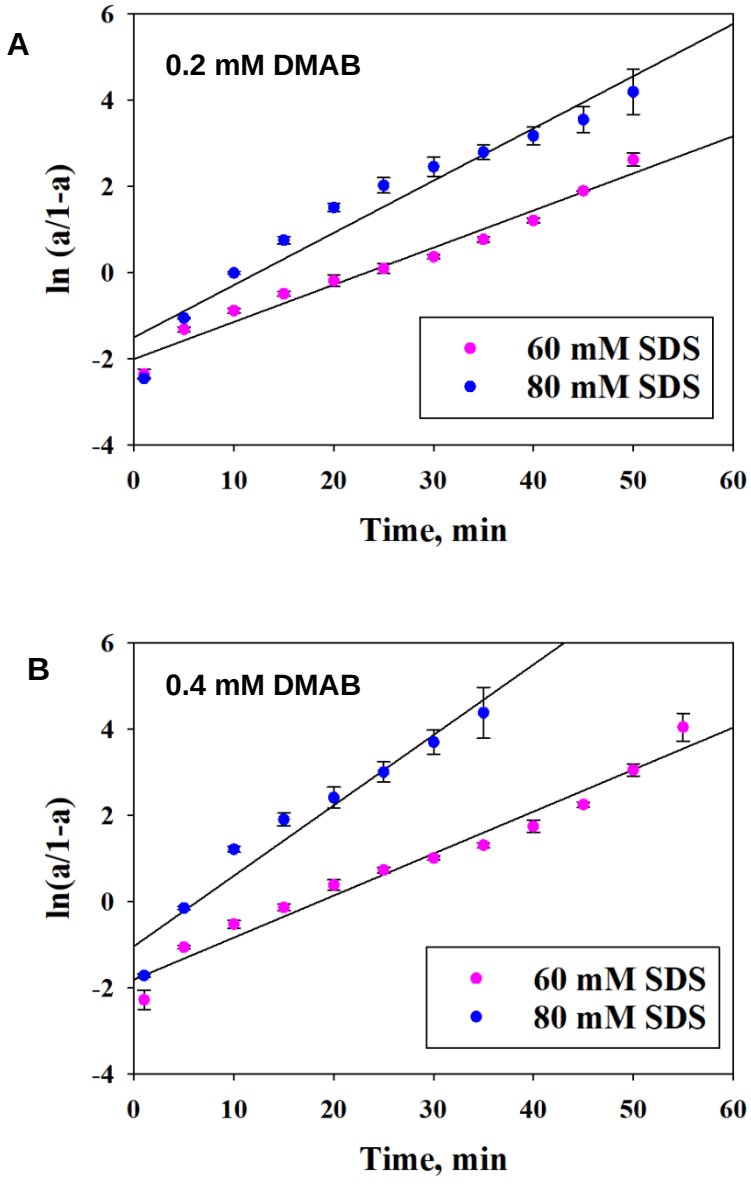


Figure 6.3 Linear fitting of F-W two step mechanism for the second set of chemicals using 0.2 mM DMAB (A) and 0.4 mM DMAB (B) for 60 mM and 80 mM SDS.

Patil et al (2012) explored the synthesis of AgNPs using sodium borohydride and SDS. Their investigation revealed an optimal concentration of SDS for monodispersed AgNPs.

By keeping precursor ($AgNO_3$) concentration at 0.001 M and $NaBH_4$ at 0.003 M, they observed an increase in λ_{max} with increasing the SDS concentration, followed by a decrease at higher SDS concentrations. They proposed that the negative charge of SDS molecules played a significant role in preventing agglomeration of AgNPs. Furthermore, they suggested that the higher SDS concentration led to more nuclei formation, resulting in smaller PSD. Higher concentrations of SDS enhance the nucleation process by stabilising nuclei and preventing their aggregation into larger particles.

In this chapter, the combined effect of DMAB and SDS is firstly investigated. At lower concentrations of the reagents, nucleation progresses at a slower rate compared to higher concentrations. The kinetic curves (Figure 6.2) differ from the typical sigmoidal shape observed in the first chemical protocol at pH 7, likely due to the strong reducing agent DMAB. It behaves similarly to the conditions in the first set of chemicals at pH 12. With DMAB, silver nuclei formation proceeded rapidly across all studied SDS concentrations, without a noticeable lag phase.

As the concentrations of the reducing agent or/and stabilising agent increased, the sizes of AgNPs decreased. For example, at 0.2 mM DMAB and 60 mM SDS, the size was 3.82 ± 0.8 nm whereas at 0.4 mM DMAB and 80 mM SDS, the size reduced to 2.73 ± 0.4 nm (see Table 6.2).

In the same context, the inductions times of their synthesis, denoted as $t_{ind,j}$ and $t_{ind,p}$ decreased with the concentrations of the reagents. This indicates that reduction occurs more rapidly with higher concentrations of the reagents, leading to the formation of smaller AgNPs, as illustrated in Table 6.2. Moreover, the induction times. $t_{ind,j}$ and $t_{ind,p}$ for the

second set of chemicals are comparable to those for the first set of chemicals at pH 12 (refer to Table 6.1).

Table 6.2 reports the values of k_1 and k_2 for each case of conditions, found from the linear fitting of F-W, as well as the estimations of t_{ind}, t_{max} and $t_{plateau}$ using Eqs. (6.1) -(6.4). The nucleation and growth constants from the second set of chemicals were also integrated into numerical simulations described in Pico et al (2023) and results can be found in the Appendix G.

Table 6.2 Kinetic constants of second set of chemicals involving DMAB and SDS and the experimental sizes found from DLS under the investigated cases.

$[DMAB]$, mM	$[SDS]$, mM	k_1, min^{-1}	k_2, $M^{-1}min^{-1}$	$k_2[A]_0/k_1$	$t_{ind,j}$ /min	$t_{ind,p}$ /min	t_{max} /min	$t_{plateau}$ /min	$d \pm \sigma$, nm (PDI)
									Exp.
0.2	60	0.014	831.25	4.75	2.996	7.41	19.36	35.72	3.82 ± 0.8 (0.05)
0.2	80	0.064	1120	1.40	-	0.74	2.19	10.76	2.92 ± 0.5 (0.026)
0.4	60	0.021	989.58	3.77	0.1	4.88	13.25	26.4	3.08 ± 0.56 (0.033)
0.4	80	0.125	1500	0.96	-	-	-	5.21	2.73 ± 0.4 (0.021)

6.4 CORRELATION OF KINETICS AND INITIAL CONCENTRATIONS FOR BOTH SET OF CHEMICALS

Building on the investigations of two distinct chemical protocols and comparing a second set of chemicals with the first, there is potential to identify a correlation between the kinetics and initial concentrations of these two different sets of chemicals.

Table 6.3 Features and range investigated for the correlation between the kinetics and initial concentrations for both set of chemicals.

Feature	Range investigated
Initial concentration of precursor, $\mathrm{A_o}$, (M)	0.00008-0.00092
Nucleation constant, $\mathrm{k_1}$ ($\mathrm{min^{-1}}$)	0.0011 - 0.125
Growth constant, $\mathrm{k_2}$ ($\mathrm{M^{-1}min^{-1}}$)	13.66-1500

The experimental data (see Table A2 in Appendix C) from both set of chemicals were fitted to polynomial function using 2 poly degree and 3 variables to predict the size of AgNPs (y) in nm , where $\mathrm{x_1}$ is $\mathrm{A_o}$ $\mathrm{x_2}$ is $\mathrm{k_1}$ and $\mathrm{x_3}$ is $\mathrm{k_2}$. This analysis focused on exploring a comprehensive model that accounts a variety of terms that imply dependencies on $\mathrm{A_o}$, $\mathrm{k_1}$, $\mathrm{k_2}$, individually and in combinations, rather than exclusively through direct correlations.

$$\mathrm{y} = 1.76 - 538.9\mathrm{x_1} - 41.73\mathrm{x_2} + 0.0028\mathrm{x_3} - 0.7413{\mathrm{x_1}}^2 + 4.00386\mathrm{x_1x_2} + 44.0225\mathrm{x_1x_3} - 5.4148\,{\mathrm{x_2}}^2 + 0.0433\mathrm{x_2x_3} - 0.000005{\mathrm{x_3}}^2 \quad (6.5)$$

The value of R^2, (Eq. (A4)) was found to be 0.987 indicating that the model provided a good fit to the data. This model can predict the size of AgNPs within the limits of the experimental features with a minimum standard error equal to 0.296 nm.

The validation of the obtained model was carried out using different and random synthesis conditions for the two investigated set of chemicals. Using (Eq. (6.5)), the model predicted the size of AgNPs in nm while the sizes of AgNPs were confirmed experimentally using DLS.

Experiments for all the investigated cases were performed in triplicate to validate the predicted model. The predicted versus experimental values of AgNPs size for the training data and testing data are presented in Figure 6.4.

The training data contains 33 experiments, including replications, while testing data comprised of only 18 experiments including replications. The testing data were taken from independent experiments selected randomly.

The predicted values as shown in the Figures 6.4A and 6.4B closely align with the experimental responses of the testing dataset and fall within the confidence and prediction intervals (Eq. (A10) and Eq. (A11) in Appendix A). This indicates the successful development of the model, demonstrating a strong correlation between the various features of both sets of chemicals and the resulting size of AgNPs. The average prediction error of the training set was estimated around 2.93%, with 9.9% the maximum error while the average prediction error of the testing set was calculated to be 4.9% with 11.9% being the maximum error.

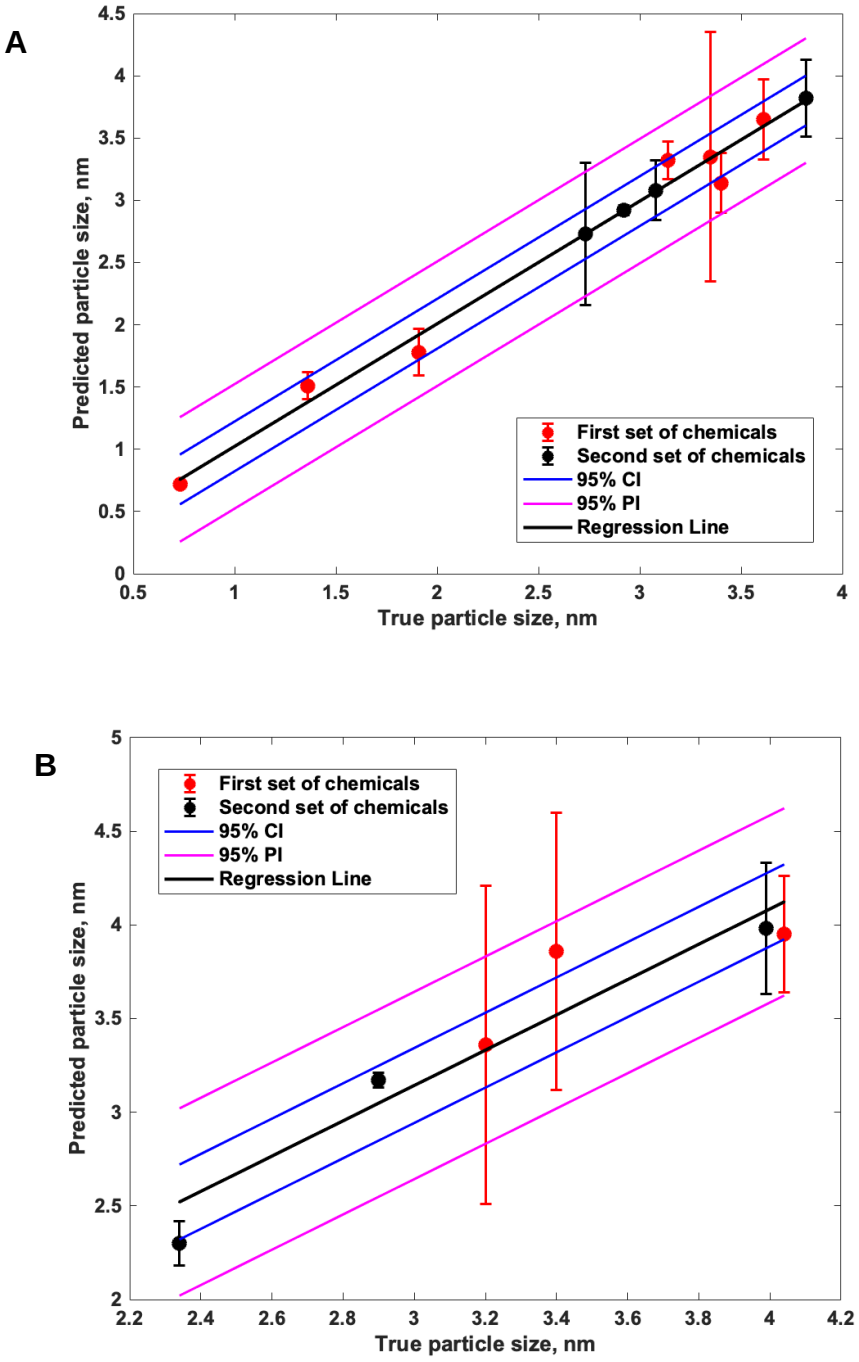


Figure 6.4 A) Training and B) Testing data for the correlation for both set of chemicals. The first set of chemicals involve TA and TC and the second set of chemicals include DMAB and SDS.

6.5 CONCLUSIONS

The kinetics investigations conducted in well mixed reactors for both set of chemicals, demonstrated the influence of different types of reducing and stabilising agents. For example, in the first chemical protocol, it was shown that pH plays a significant role on the PSD of AgNPs. At alkaline pH, silver nuclei formation proceeded very quickly, without a noticeable lag phase for all the studied stabilising agent concentrations. At pH 7, the kinetic curves followed the typical sigmoidal shape, indicating that nucleation is relatively slow. Regarding the second chemical set, the combined effect of DMAB and SDS was firstly investigated. It was shown that as the concentrations of reducing and stabilising agent increased, the sizes of AgNPs decreased. The kinetic curves were similar to the conditions of the first chemical protocol at pH 12 due to the strong reducing behaviour of DMAB.

Building on the findings of kinetics investigations conducted on both sets of chemicals, a regression model on the kinetics and their respective initial concentrations for the two different sets of chemicals was constructed for the first time to predict the PSD. The average prediction error of the testing dataset was calculated as 4.9%. The close alignment between the predicted PSD values and the experimental PSD confirms the reliability of the model, indicating a strong correlation between the different features of the two sets of chemicals and the size of AgNPs

CHAPTER 7: EXPERIMENTAL VALIDATIONS OF PBM-CFD SIMULATIONS ON SYNTHESIS OF SILVER NANOPARTICLES IN MICROFLUIDIC CHANNELS[4]

7.1 INTRODUCTION

The review paper by Nathanael et al (2022), concluded that integrating microfluidics with numerical modelling offers a promising approach for optimizing nanoparticle formation. Literature has demonstrated that employing computational modelling alongside microfluidics as a high-throughput experimental method can yield valuable insights about the system, that are otherwise inaccessible experimentally. This integrated approach not only allows a comprehensive understanding of processes of nano-particles formation and growth but also reduces the number of experiments required, as well as the necessary reagents and energy, benefitting sustainability. Many experimental and computational investigations, as detailed in § 2.2, § 2.3 and § 2.6 have been undertaken over the years to uncover the correlations between operating synthesis parameters and the final properties of AgNPs for a range of applications. However, despite all these extensive efforts, the comprehension of the underlying phenomena leading to specific outcomes remains incomplete and elusive.

For instance, prior mechanisms described by Watzky & Finke (1997), Perala & Kumar (2014) and Mozaffari et al (2017) are tailored specifically for batch reactions under

[4] Sections 7.1-7.4 of this chapter are based on the data from Pico, P., Nathanael, K., Lavino, A.D., Kovalchuk, N.M., Simmons, M.J.H., Matar, O.K. (2023) Silver nanoparticles synthesis in microfluidic and well-mixed reactors: A combined experimental and PBM-CFD study. *Chem. Eng. J.*, **474**, 145692.

condition of ideal mixing. In continuous flow systems, such as the one outlined in § 3.2, the reactants are initially in separate states, and the degree of mixing, plays a significant role in the entire process. Additionally, the existing computational literature concerning various NPs formation in microfluidic systems, such as SiO_2 (Bal & Bandyopadhyaya, 2019) and $CdSe$ (Kumar & Ganesan, 2017) primarily based on precipitation and supersaturation-driven crystallization processes. There is a lack of focus on reduction-based and low saturation models, which are better suited for describing the synthesis of AgNPs.

A computational model that couples mixing dynamics, reduction kinetics, nucleation and growth, particle agglomeration and diffusion to predict the PSD and its variations under different operating conditions within microchannels was developed by Pico et al (2023). The experimental validation of this computational model will be elaborated upon in this chapter. As fully described in Pico et al (2023), this computation framework lays the groundwork for a more comprehensive modelling approach towards the production of reduction-based NPs in both well-mixed and continuous flow reactors. The research paper Pico et al (2023) introduced a PBM-CFD modelling framework, implemented in an open-source code, to extend the kinetic model of F-W to continuous flow reactors, enabling prediction of the PSD for the AgNPs. Note, in the well mixed batch system of this thesis, reaction kinetics are the rate-controlling step. When transitioning from a well-mixed batch system to a flow system, it is assumed that the reaction kinetics remain the same because the chemical process is unchanged and the key difference in flow systems is the additional contribution of mass transfer that plays a significant role in influencing the

overall reaction rate. Additionally, the F-W mechanism assumes there is no separate reduction step and therefore does not explicitly involve reactants for CFD modelling, CFD simulations can be adapted to include a separate reduction step. This flexibility allows CFD to provide a more comprehensive analysis of systems where reduction dynamics play a role.The PBM modelling including details on how kernels are determined is discussed in Pico et al (2023).The limitations and advantages of the suggested approach are discussed.

7.2 EXPERIMENTAL VALIDATION OF PBM: EFFECT OF pH AND [TC] ON THE SYNTHESIS OF AgNPs IN A WELL-MIXED REACTOR

The nucleation and growth constants integrated in numerical simulations were estimated experimentally (see § 6.2) based on F-W model (Watzky & Finke, 1997) described in detail in § 2.4. Data for the average particle size, d, standard deviation, σ, polydispersity index (PDI) and experimental conditions for each investigated case for the well-mixed reactor are presented in Table 7.1. PDI is defined as the distribution of particle sizes within a sample.

$$\mathrm{PDI} = (\sigma/\mathrm{d})^2 \tag{7.1}$$

The experimental and F-W based PBM predictions are in good agreement for pH 7 (Figure 7.1), showing a maximum deviation of 10.1% and 31.2% for d and σ respectively. Regarding the fitted experimental data, the maximum deviations reach 7.2% and 13.6% for d and σ respectively. Perala & Kumar (2014) examined the performance of F-W for IrNPs though a PBM framework and found that standard deviation of the PSD is over-predicted up to 150%. At pH 12, an expansion of discrepancies was observed for σ that

comes in alignment with the work of Perala & Kumar (2014) who focused on IrNPs. As mentioned in Pico et al (2023), the significant deviation of ~150% in σ observed by Perala & Kumar (2014) is related to the selection of representing the mean diameter by lower-order moments. It is important to note that the overall framework of nucleation followed by autocatalytic growth is applicable to both IrNPs and AgNPs.

Smaller particle sizes of AgNPs were achieved with higher concentrations of TC. This, coupled with the reaction kinetics and characterisation times detailed in Tables 7.1 and 6.1, respectively, illustrates the stabilising effects of TC. These findings are consistent with the results of Bastús et al (2014), who observed smaller AgNPs by reducing the ratio of TA to TC.

At pH 12, the deviations of experimental measurements of σ against PBM based on F-W predictions are particularly significant. The errors are between 5.9 to 13.0% and 78.0 to 85.5% for d and σ respectively. It is important to note that deviations of σ for pH 12 are under predicted for all the investigated concentrations of TC. The source of these discrepancies of σ are linked to the rapid nucleation at pH 12 but also to the assumptions of F-W about the uncoupled nucleation and growth steps (see § 2.4).

The PBM results from the well-mixed reactor showed the crucial importance of the ratio $\mathrm{k_2[A]_0/k_1}$ to predict the d, σ and PDI in the context of F-W two step mechanism. Further investigations, as presented in the paper of Pico et al (2023), suggested that this ratio is the sole predictor of d, σ and PDI after the plateau stage when $\mathrm{A_o}$ is constant. For instance, smaller AgNPs observed at high pH can be attributed to enhanced nucleation,

$(k_2[A]_0/k_1 < 1)$ leading to the formation of numerous small nuclei instead of significant growth events, resulting in limited precursor availability, restricted growth, and ultimately smaller particle sizes. Conversely, opposite arguments $(k_2[A]_0/k_1 > 1)$ apply to cases characterized by lower pH values. Use of this ratio is a simplification; however, Eq. (6.5) in § 6.4 includes significant interaction and quadratic terms which highlight the presence of non-linear effects and interactions not accounted for by the PBM model. This emphasizes the importance of integrating experimental data with theoretical models to achieve a comprehensive understanding of when simplifying assumptions can be made and ensure accurate predictions. The same PBM framework for well-mixed reactors was applied to the second chemical protocol using DMAB and SDS, and good agreement was found between experiments and simulations (see Appendix G).

The results from the PBM model for the well-mixed reactor from the second set of chemicals have shown there is an influence of dcrit or "critical diameter". This term represents the critical size above which particles are stable and can grow further, while below this size, particles may tend to dissolve (Pelegrina & Guillermet, 2018). There are different silver nanoclusters with diameters of 0.92, 0.95, 1.08, 1.10, 1.37, 1.49, 1.60, and 2.60 nm for Ag_{25}, Ag_{43}, Ag_{44}, Ag_{63}, Ag_{141}, Ag_{78}, Ag_{136}, and Ag_{374}, respectively (Feng et al, 2022). It may be a fitting parameter that needs to be adjusted based on the chemical protocol.

A length-based number density function assuming spherical particles was used. The function is given by $G(L, y_i) = G(V, y_i)/3L^2$, where $G(V, y_j)$ is a volume-based growth rate. This expression assumes that particle growth in length (diameter) is proportional to

particle size. This approach is consistent with the F-W assumption that all atoms in a nanoparticle contribute to particle growth, not just those located at the surface.

Table 7.1 Comparison of experimental measurements of $\mathbf{d}$, $\boldsymbol{\sigma}$ and $\mathbf{PDI} = (\boldsymbol{\sigma}/\mathbf{d})^2$ with F-W based PBM predictions and normal distribution fitting (see § 3.5, Eq. (3.2)) for AgNPs in a well-mixed reactor under different pH and [TC] after full precursor consumption.

pH	[TC] (mM)	$\mathbf{k_1}$ $(\mathbf{min^{-1}})$	$\mathbf{k_2}$ $(\mathbf{M^{-1}min^{-1}})$	$\mathbf{k_2[A]_0/k_1}$	$\mathbf{d \pm \sigma\ (nm)}$ $(\mathbf{PDI})$		
					PBM	**Exp.**	**Exp.(fit)**
7	1.91	0.0011	55.51	46.43	3.60 ± 0.91 (0.064)	3.61 ± 1.30 (0.13)	3.74 ± 1.02 (0.07)
7	2.87	0.0013	37.86	26.79	3.03 ± 0.66 (0.048)	3.37 ± 0.96 (0.08)	3.26 ± 0.76 (0.05)
7	3.82	0.0015	44.81	27.48	3.12 ± 0.69 (0.049)	3.14 ± 0.94 (0.09)	3.00 ± 0.67 (0.05)
12	1.91	0.1	77.97	0.72	0.77 ± 0.04 (0.003)	0.73 ± 0.18 (0.06)	0.68 ± 0.10 (0.02)
12	2.87	0.012	13.66	1.05	1.54 ± 0.10 (0.004)	1.36 ± 0.57 (0.18)	1.48 ± 0.54 (0.13)
12	3.82	0.0128	26.01	1.87	1.66 ± 0.16 (0.009)	1.91 ± 1.10 (0.33)	1.87 ± 0.50 (0.07)

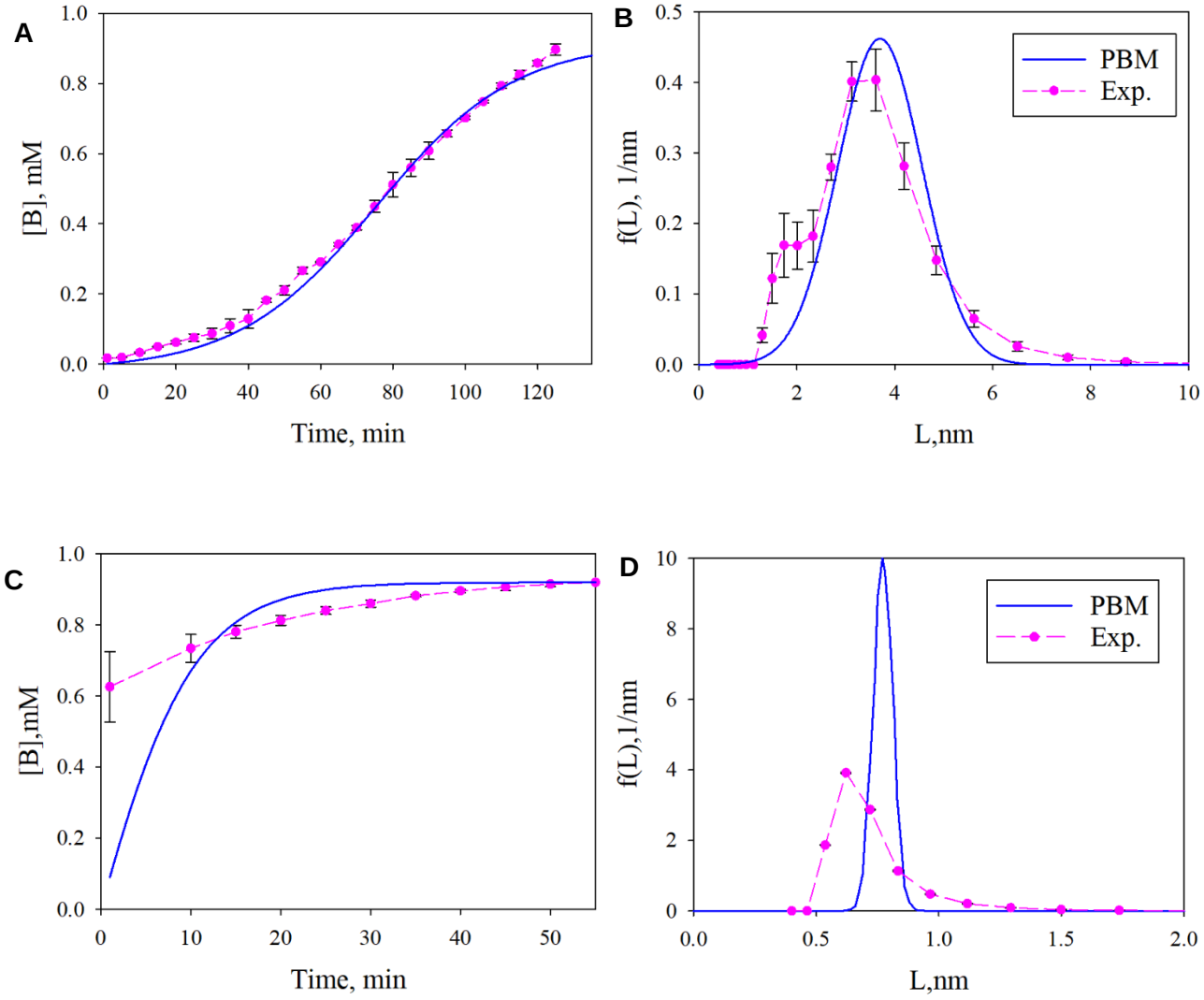


Figure 7.1 PBM model in a well-mixed reactor for 1st set of chemicals. The graphs (A) and (C) show the temporal evolution of [B] between the experimental measurements (pink dots) and F-W based PBM predictions (blue line) while graphs (B) and (D) the PSD for AgNPs in a well-mixed reactor using 1.91 mM TC at pH 7 and pH 12 respectively.

7.3 PRECURSOR CONSUMPTION DYNAMICS IN THE T-JUNCTION MICROCHANNEL-EXPERIMENTAL VALIDATION OF PBM-CFD SIMULATIONS

Figure 7.2A shows the experimentally measured steady-state concentration of silver ions along the channel length at different inlet flow rate for pH 7 and TC 1.91 mM. The experimental spatial profiles of the continuous flow reactor illustrate a rapid consumption of silver ions within the first ~0.125 m, followed by a much slower consumption. At a distance of 2 m along the outlet channel, small but non-negligible traces of silver ions were detected ([SN]=0.031 $\pm$ 0.0036 and [SN]=0.013 $\pm$ 0.0013 mM for 200 $\mu\mathrm{L/min}$ and 50 $\mu\mathrm{L/min}$ respectively).

The straight outlet channel design used in this study removes any potential for transversal flow development, typically induced by coiled or helical reactors even at low Re (Kašpar et al, 2019), (Wu et al, 2017). As shown in Figures 7.2 A and B, there is a fast precursor consumption along the channel with lower flow rates in both numerical and experimental results. Lower flow rates result in longer residence times, which enhance reagents consumption through the reduction reaction.

As observed in the experimental concentration profiles, the areas of interest predominantly occur within the first metre of the outlet channel. Consequently, the simulation results were limited to a total length of 1 m instead of 2 m to minimise the computational time. The increase in silver precursor consumption per channel length at lower flow rates impacts the generation of silver atoms, thereby influencing PSD. For example, previous studies on similar NPs like AuNPs (Yoo et al, 2022), (Iwamoto et al,

2005) showed that the rate of reduction reaction has a crucial effect on the evolution of subsequent reactions and the final PSD.

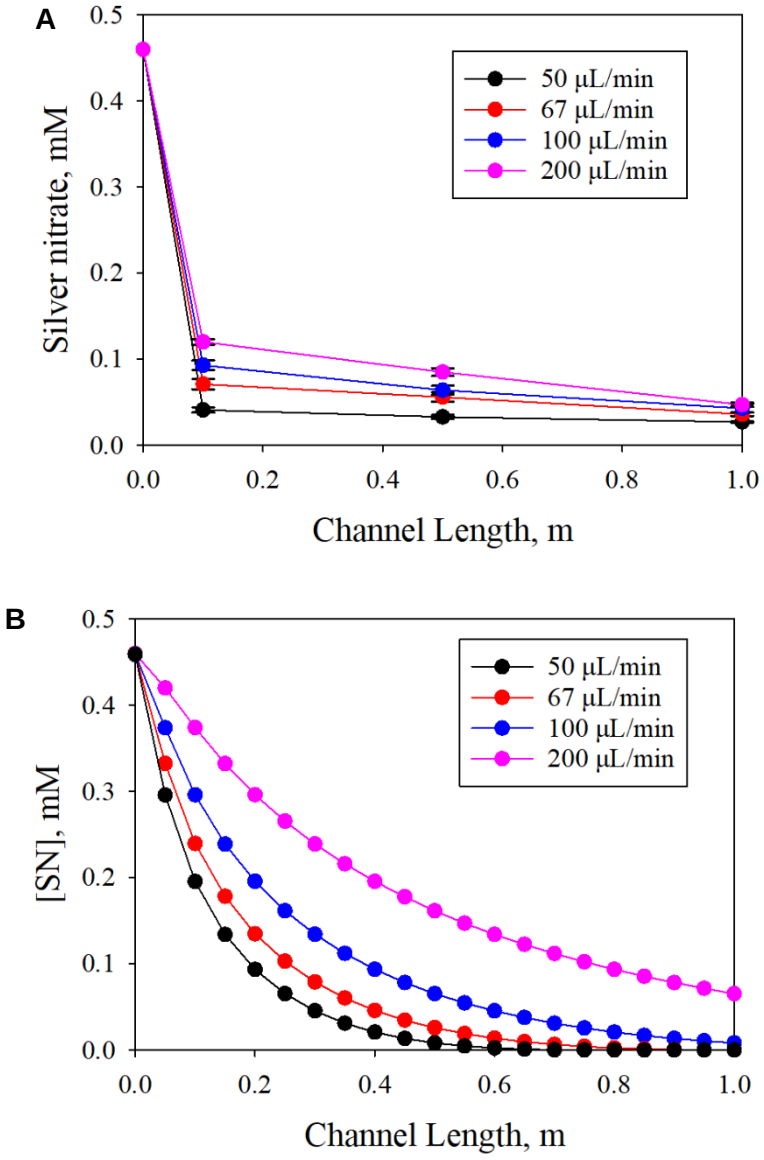


Figure 7.2 Effect of flow rates and residence times on the steady-state concentration of silver ions along the T-junction microchannel. Experimental (A) results versus CFD mixing reaction model (B).

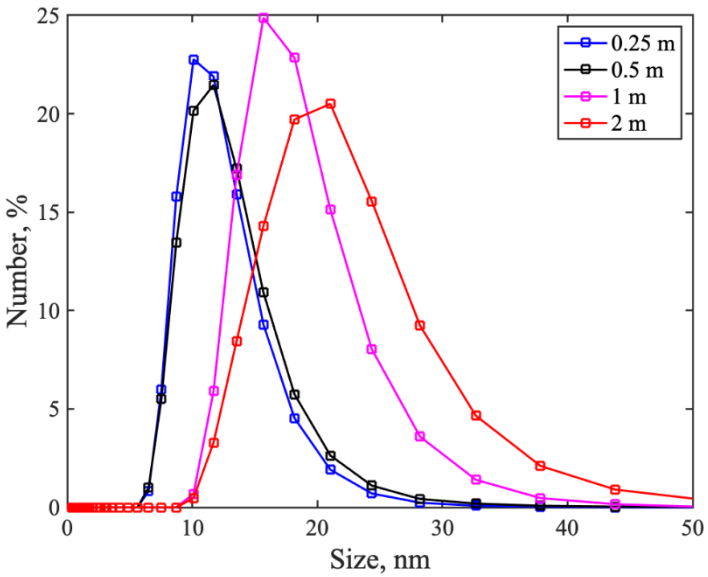
Building on the prior discussion of hydrodynamic and kinetic time-scale phenomena and their influence on reactant consumption during AgNP synthesis in the T-junction microchannel, this section will delve into the experimental and simulation outcomes regarding PSD. Figures 7.3 (A-C) present experimentally measured steady-state PSD along various channel lengths for different inlet flow rates, accompanied by detailed results. These findings show the significant relationship between hydrodynamics and PSD. Specifically, the results reveal a consistent trend wherein both the average PSD and their standard deviation decrease monotonically with increasing flow rate across all channel lengths. Unexpectedly, the PDI (Eq. (7.1)) does not exhibit a monotonic behaviour in response to changes in channel length and flow rates.

A low PDI (e.g., 0.1) indicates uniform sizes while high PDI (e.g. 0.5) suggests a wide range of particle sizes. However, it's noteworthy that in all cases, a PDI of $\leq$0.10 corresponds to monodisperse samples.

The simulation results (depicted in Figure 7.4B) follow the observed trend of flow rates and PSD evolution, consistent with the experimental findings. These simulation outcomes are presented for channel length of 0.25 m, chosen to reduce the computational demands. The experimental and numerical findings align with prior studies explored the impact of hydrodynamics in microreactors on PSD (Khan et al, 2004),(Kim et al, 2012),(Ling et al, 2022),(Aljarrah et al, 2022). These studies have noted that shorter residences times result in a reduction in particle size. The differences in both d and σ when transitioning from a well-mixed reactor to a continuous flow reactor under identical chemical conditions, as shown in Figure 7.1 (sizes in beaker) and Figure 7.4 (sizes in T-junction) are

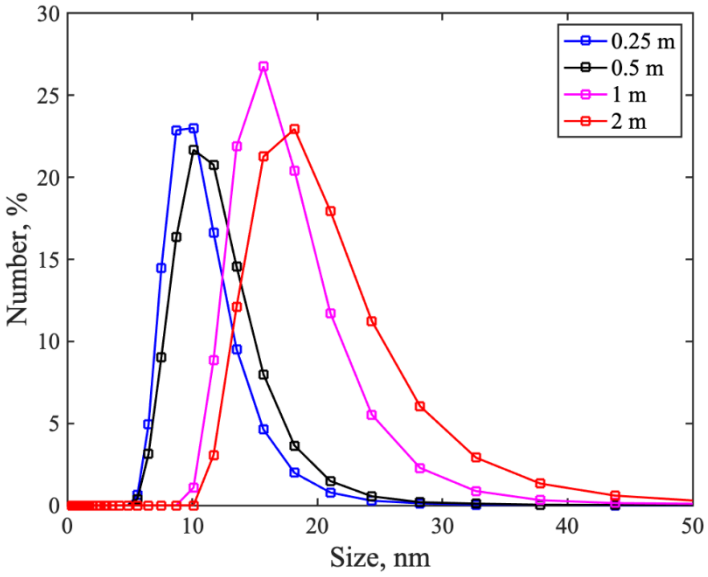
approximately tenfold. The utilization of the T-junction continuous flow device yields larger AgNPs, accompanied by comparable or slightly elevated PDI values.

A

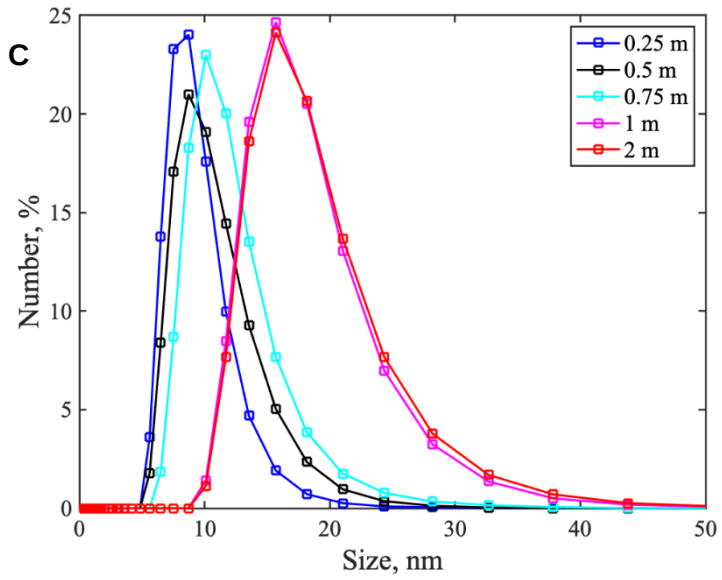


Channel length / m	d ± σ / nm (PDI)
0.25	11.85 ± 3.34 (0.08)
0.5	12.34 ± 3.81 (0.10)
1	17.96 ± 4.69 (0.07)
2	21.27 ± 7.03 (0.11)

B



Channel length / m	d ± σ / nm (PDI)
0.25	10.37 ± 2.95 (0.08)
0.5	11.40 ± 3.39 (0.09)
1	17.01 ± 4.54 (0.07)
2	19.69 ± 6.07 (0.10)



Channel length / m	$d \pm \sigma$ / nm (PDI)
0.25	9.04 ± 2.44 (0.07)
0.5	10.19 ± 3.36 (0.10)
0.75	11.50 ± 3.54 (0.09)
1	17.48 ± 4.83 (0.08)
2	17.86 ± 5.12 (0.08)

Figure 7.3 Experimental PSD of AgNPs at 50 (A), 100 (B) and 200 (C) $\mu L/min$ at different lengths of outlet channel.

In the well-mixed reactor, the consumption of silver precursor follows reaction kinetics without the influence of mass transfer, enabling the production of smaller particles sizes. Conversely, reactions in microchannels are governed by slow convective and diffusive dynamics ($\mathrm{Re} = 4.24 - 16.98$).

As a result, larger particles are formed compared to those in a well-mixed reactor, where delays in reaction due to mixing are minimised, and particles do not have sufficient time to aggregate significantly during the reaction completion phase.

This contrasts with situations where mixing is less effective or reactions proceed over extended periods, leading to increased particle aggregation over time. In microchannels, an inverse relationship between the final particle size and inlet flow rates was observed. While the reaction is complete even at higher flow rates by the end of microchannel, the consumption of silver precursor per reactor length decreases with shorter residence times.

This reduction in precursor availability limits the production of silver atoms which serve as the building blocks for nucleation and growth. Both of these factors contribute to the smaller particle size measured. Conversely, longer residence times in the microchannels at lower flow rates, could potentially promote particle agglomeration, leading to larger particle sizes.

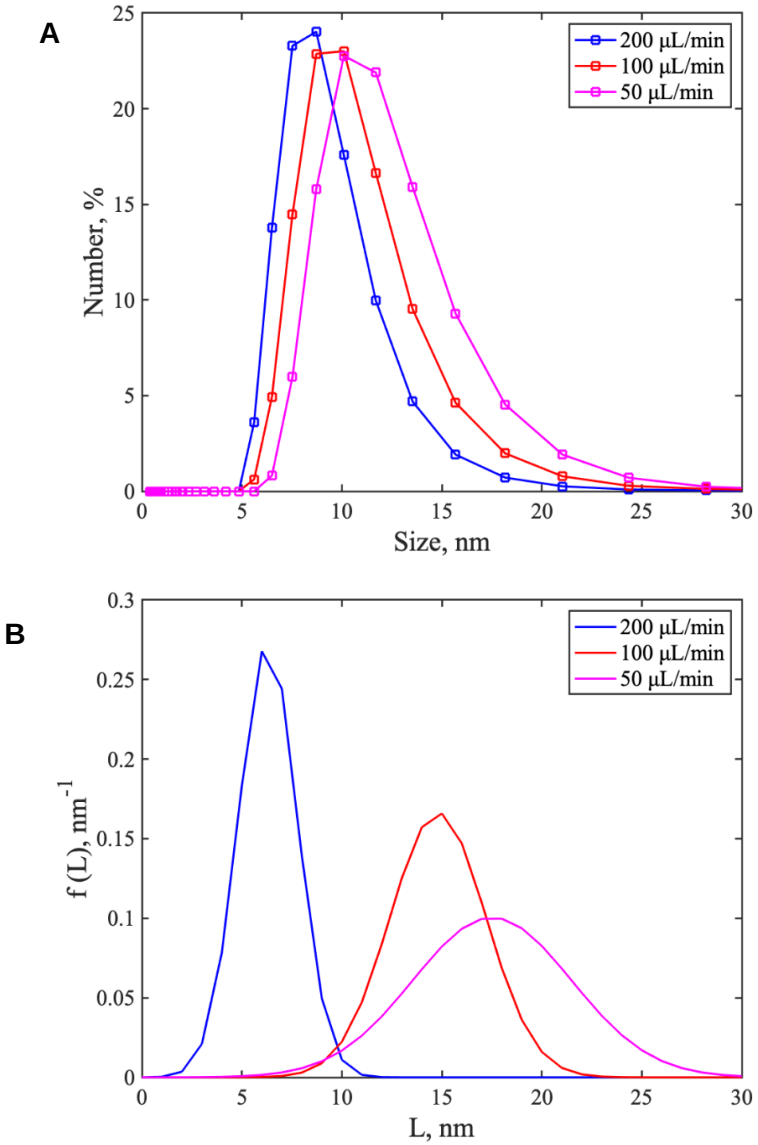


Figure 7.4 Experimental (A) versus PBM results (B) at 0.25 m length and different flow rates.

Wu et al (2017) investigated various microreactor geometries and observed smaller PSD in helical devices. This phenomenon was attributed to the development of transversal flows, that enhance reactant mixing and facilitate a rapid consumption of precursor and NP nucleation.

As elaborated in Appendix E, Figure A1 (B) and (C) compare the final PSD in the straight and coiled geometries of the T-junction continuous flow device, employing identical pH and flow rates. The coiled reactor facilitates convective mixing due to formation of Dean vortices, resulting in the formation of smaller AgNPs.

There are some quantitative deviations between the experimental results and the F-W based PBM-CFD simulations, primarily focused on three limitations of the model. Firstly, there is uncertainty regarding the reduction rate reaction, as it cannot be directly measured experimentally, along with uncertainties surrounding the properties of TA-TC complex. These parameters significantly influence the rate of silver precursor reduction and, consequently the PSD.

Secondly, the application of the F-W two step mechanism in the modelling of the T-junction continuous flow reactor, originally developed for a well-mixed system, may introduce some inconsistencies. The proposed model is elaborately described in Pico et al (2023) where the approach encompasses the diffusive and convective mixing effects and reduction rate reaction was modelled separately. The third factor relates to the simulation domain using a 2-D version of the channel, contrasting with the circular cross section geometry of the microchannel in the experimental setup. This can result in minor

but not insignificant differences in the mixing process, which has been identified as one the primary factors affecting the PSD.

7.4 CONCLUSIONS

PBM-CFD simulations integrated hydrodynamic and reactive kinetics, enabling predictions of AgNP size distribution in continuous flow microchannels, and batch reactors. Experimental results were compared with simulation results to unveil the interplay between hydrodynamics, reaction kinetics and PSD, offering valuable insights into AgNPs synthesis that involves multi-step reaction processes.

Despite some discrepancies, the F-W model effectively captures the overall dynamics and qualitative trends observed in experiments regarding pH, stabilizer concentration, and average PSD. Notably, the experimental results and F-W based PBM predictions in the well-mixed reactor exhibit good agreement for pH 7 conditions with only some deviations, particularly in σ. These discrepancies, observed also in previous studies highlight the challenges in accurately predicting the PSD, especially at higher pH values where nucleation and growth rate constants are accelerated. At pH 12, the substantial deviations in experimental measurements of σ against F-W based predictions are attributed to rapid nucleation and assumptions of the F-W model regarding uncoupled nucleation and growth steps.

Utilizing F-W-based simulations, the impact of pH and initial stabilizer concentration on size distribution were shown using a unique parameter that significantly influences final

particle size, σ, and PDI. This parameter, defined as, $k_2[A]_0/k_1$ can be directly linked to particle size.

In continuous flow microchannels variations in operating conditions, particularly the inlet flow rates, highlight the influence of residence time on precursor consumption rates and the subsequent PSD at the outlet channel. Lower flow rates result in longer residence times in the channel leading to bigger particle sizes. Despite the promising insights provided, there are notable differences between experiments and PBM-CFD simulations in the T-junction microfluidic device, attributed to uncertainties in reduction rate reaction, properties of TA-TC complex, and limitations in the simulation domain. Overall, the study shows the complexity of NP synthesis processes and the importance of integrate experimental and computational approaches to gain a comprehensive understanding, offering routes for refining nanoparticle design and manufacturing strategies in various industrial applications.

CHAPTER 8: OPTIMIZATION OF MICROFLUIDIC SYNTHESIS OF SILVER NANOPARTICLES USING MACHINE LEARNING AND INVERSE MODELLING [5]

8.1 INTRODUCTION

Data science provides powerful, robust methodologies for modelling, prediction, and optimization of various processes such as the synthesis of AgNPs. In this chapter, a machine learning-guided design of experiments based on the decision tree method and inverse modelling have been applied to the synthesis of AgNPs in a continuous flow microreactor.

The developed approaches for both ML and inverse modelling use kinetic nucleation and growth constants from the Finke-Watzky model to account for the chemistry of the system. Parameters such as the Reynolds number and the ratio of Dean number to Reynolds number are incorporated to reveal the effect of hydrodynamics and mixing within the device. Additionally, storage temperature is considered to account for particle stability after collection.

The nucleation and growth constants (see Tables 6.1) for both data science methods were derived from an independent set of experiments carried out in a beaker using the Finke-Watzky (F-W) two-step mechanism (Watzky & Finke, 1997) which has been applied previously to describe well a wide range of kinetic processes such as protein aggregation

[5] Sections 6.2, 8.2-8.4 and 8.6 of these chapters are adapted from Nathanael, K., Cheng, S., Kovalchuk, N.M., Arcucci, R., Simmons, M.J.H. (2023) Optimization of microfluidic synthesis of silver nanoparticles: a generic approach using machine learning, *Chem. Eng. Res. Des.*, **193**, 65-74.

(Iashchishyn et al, 2017), (Ohgita et al, 2022) and metal nanoparticle formation including silver (Sandoe et al, 2019), gold (Pestovsky & Srichana, 2022), palladium (Wojnicki et al, 2016) and rhodium (Yao et al, 2012). Only one set of chemicals with kinetic constants presented in Table 6.1 was used in this study providing several pairs of nucleation and growth constants. By integrating these data science approaches with AgNP synthesis, researchers can systematically explore the extensive parameter space of microfluidic synthesis, leading to a deeper understanding and enhanced control over the production of AgNPs. This chapter aims to elucidate the methodologies and advantages of employing decision tree algorithms and inverse modelling in achieving precision and efficiency in AgNP synthesis.

8.2 DECISION TREE GUIDED DESIGN OF EXPERIMENTS

The proposed strategy based on decision tree, which uses optimal and flexible experiment designs based on uncertainty analysis, can provide more flexibility compared to existing approaches such as design of experiments (Sethuramiah & Kumar, 2016), since the exact values of the initial parameters are not fixed and the training features could be parameters which have been calculated based on physical parameters, such as nucleation and growth constants. These kinetic constants were used as input parameters in the decision tree to build a ML model which combines parameters that can be applied in the future for different sets of chemicals.

By applying this strategy, a general model for the synthesis of AgNPs can be obtained in a more direct way by providing the region of interest for further experiments. The suggested approach can also enable a considerable reduction of ecological impact of

process optimization by using microfluidics, which manipulates small samples under well-controlled conditions resulting in a considerable reduction of materials and energy consumption.

The machine learning analysis was performed using Python programming language with the Scikit-learn package (Pedregosa, 2011). Tree-based algorithms, including Decision Tree (DT), Random Forest (RF), and Extreme Gradient Boosting (XGBoost) were applied to test the prediction performance for the sizes of AgNPs. These methods have been extensively used in a wide range of engineering problems (Natekin & Knoll, 2013), (Cheng et al, 2022a), (Gong et al, 2022). After implementation, all the proposed models were compared based on the accuracy of their predictions.

The DT algorithm used to guide the experiments was built based on 20 samples, each being repeated three times to obtain the averaged '(output quantity)' as model output. For fair comparison, 10 extra experiments (30 experiments in total, including three replications) were carried out either randomly or following the DT-guided design of experiments to enhance the performance of the predictive models. For each experiment, the average size was recorded. Each dataset was divided into five inputs and one predicted output. The training features (inputs) and their investigated range are summarized in Table 8.1.

Table 8.1 Input parameters and their investigated range (Nathanael et al, 2023a).

Feature	Range investigated
Nucleation constant (min^{-1})	0.0011 - 0.1
Growth constant ($\mathrm{M}^{-1}\mathrm{min}^{-1}$)	13.66-77.97
Storage temperature (℃)	0 - 20
$\mathrm{Dean\ number/Reynolds\ number}$	0 - 0.41
Reynolds number	0.0849-16.96

The effect of the chosen input parameters on the size of AgNPs was investigated through the Pearson correlation (Navlani et al, 2021) shown in Eq. (8.1) (Profillidis & Botzoris, 2019).

$$p_{XY} = \frac{\sum(x_i-\bar{x})(y_i-\bar{y})}{\sqrt{\sum(x_i-\bar{x})^2 \cdot \sum(y_i-\bar{y})^2}} \quad (8.1)$$

In Eq. (8.1) x_i is for the values of the independent variables, $\bar{x}$ is the mean of the values of x-variable, y_i is for the values of the dependent variables and $\bar{y}$ is the mean of the values of y-variable.

The iterative process of prediction and experiment design carried out is shown in Figure 8.1, with the key focus being to perform experiments where the predictive model has the highest uncertainties. In particular, DT is chosen to guide the experiments thanks to its good interpretability and computational efficiency (Gilpin et al, 2018). The first step in the proposed approach described previously was focused on obtaining the datasets required for the training of the algorithm, i.e., data collection based on experimental measurements.

The second and third steps included data sorting or any other required data processing and the development of the most appropriate algorithm. For example, during these steps, the independent and dependent variables were identified, and a DT based algorithm was built. To ensure a good explainability of the DT model for the uncertainty evaluation, the maximum tree depth for this stage was set to be 4.

The fourth step comprised carrying out additional experiments where the obtained DT algorithm has the highest mean squared error (MSE). The challenge of this step was to ensure that the developed DT model based on the designed experiments can improve the performance regarding different models.

As shown in Figure 8.1, once the experimental design is performed using the preliminary DT model, other ML classifiers such as RF and XGBoost can be applied to achieve a more accurate prediction based on the new experimental data.

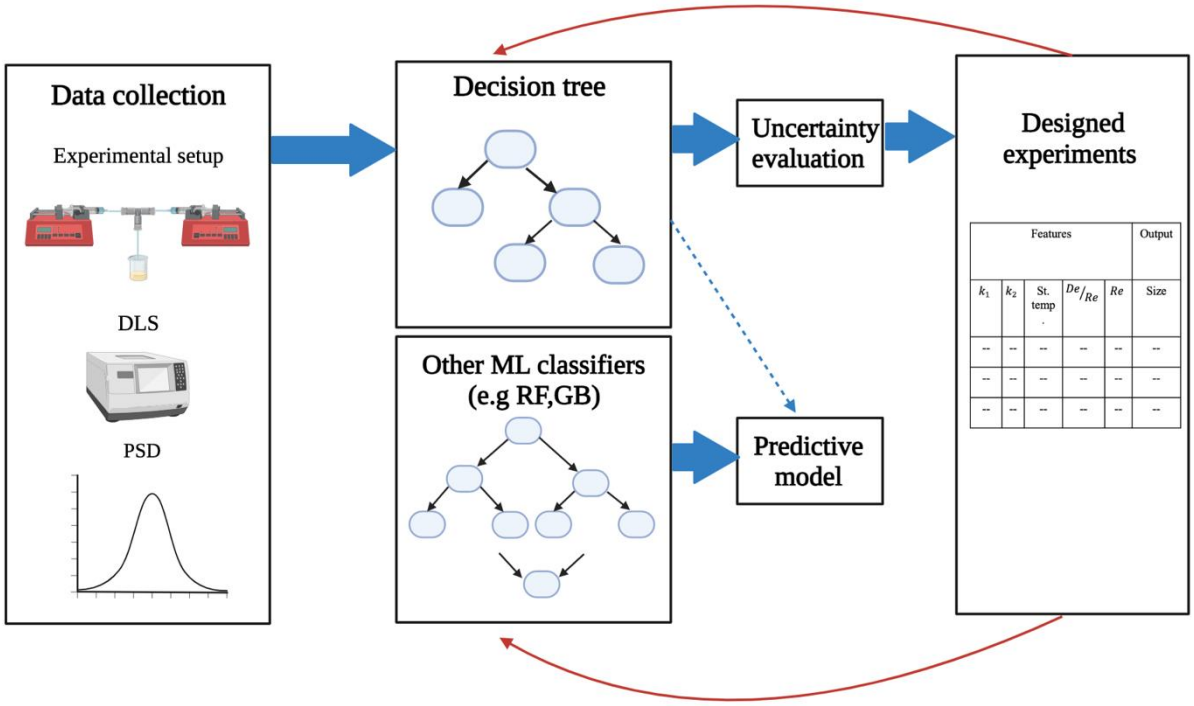


Figure 8.1 Workflow chart and description of methods used in the building of machine learning-guided design of experiment based on the decision tree method (Nathanael et al, 2023a).

8.3 PEARSON CORRELATION AND THE EFFECT OF INPUT PARAMETERS

The results of Pearson correlation calculations are presented in Figure 8.2 which shows that all input variables impact the particle size significantly with a correlation larger than 0.12 in absolute value. The estimation of the Pearson correlation value was obtained using all of the data generated in this study, which can be found in Appendix D. For

example, it was observed that the variables including k_1, k_2 and De/Re impact the particle size negatively, whilst the storage temperature and Re impact the size of particles positively. The Pearson correlation calculations showed that k_2 is less important compared to k_1 for the prediction of the size of AgNPs. In this study, the effect of kinetic constants was investigated for only one set of chemicals, so k_1 and k_2 cannot be considered as completely uncoupled. Therefore, it cannot be concluded that faster growth results in smaller particles, because for the chosen set of chemicals all growth constants are of the same order of magnitude, whereas nucleation constants vary over 2 orders of magnitude. Thus, the particle size is mostly defined by the nucleation constant. Similar studies, such as the works of Mansouri & Ghader (2009) and Liu et al (2020) showed that size of particles is a result of a significant effect of k_1 instead of k_2.

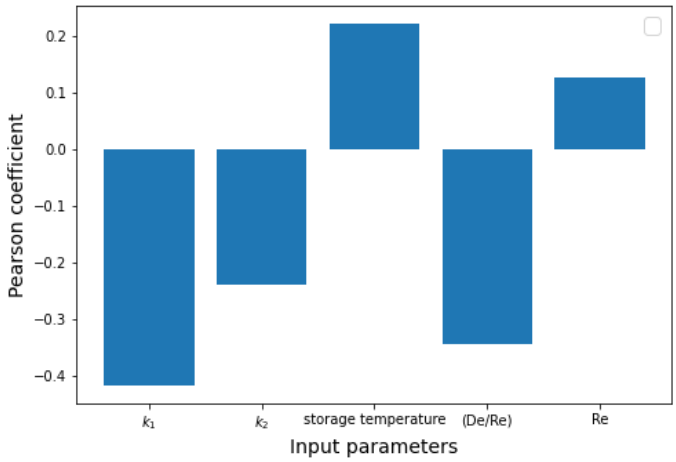


Figure 8.2 Pearson correlation between input variables and the size of AgNPs (Nathanael et al, 2023a).

The samples of AgNPs were kept at 20 ℃ and 0 ℃ and Figure 8.2 shows that the temperature has a positive effect on the particle size, i.e., that smaller particles were observed at low storage temperatures. The small residual concentrations of silver nitrate showed that the reaction was practically complete for all the investigated values of Re including the highest one where residence time was smallest. For example, at $\mathrm{Re} = 5.66$ with a 2 m outlet tube, the residual concentration of silver nitrate was around 0.017 $\pm$ 0.00053 mM (less than 2% of initial concentration) whilst at highest flow rate used, $\mathrm{Re} = 16.96$ and 2 m length, the residual concentration of silver nitrate was 0.031 ± 0.0036 mM ($\sim$ 3% of initial concentration). Izak-Nau et al (2015) and Peng et al (2010) have described in detail the ageing of AgNPs samples stored at room temperature, proposing that growth of the particle size is due to agglomeration or oxidation of silver.

When helical coils are employed, improved mixing due to the formation of Dean vortices leads to smaller particles, and this effect is one of the largest (Figure 8.2). It can be assumed that a decrease in particle size due to faster mixing is the result of more intensive nuclei formation at the initial stage of reaction. Of course, faster mixing results also in faster particle growth, but comparing the relative effect of nucleation and growth constant in Figure 8.2, it can be suggested that effect of faster nucleation is larger than the effect of faster growth. The effect of the Reynolds number is positive, yet the least significant.

8.4 PREDICTION RESULTS WITH DT-GUIDED EXPERIMENTS

The performance of the developed models (DT, RF, XGBoost) was described through MSE (A7), MAE (A12) and R^2 (A4) (see Appendix A). Both MSE and MAE are commonly

used to evaluate ML models, each offering unique insights into the model's performance. For example, MSE is more sensitive to outliers because it squares the errors, giving more weight to larger errors. In contrast, MAE measures the absolute errors, making it less sensitive to outliers compared to MSE.

The decision tree shown in Figure 8.3 examined the synthesis of AgNPs based on the combination of five conditions. The decision tree shows different routes from up to down for preparing AgNPs. Each box presents the value of the parameter, the estimated size, the MSE and the sample sizes. The tree showed that there is a high MSE (Eq. (A7) in Appendix A) in some synthesis routes e.g., when the growth constant, k_2 was smaller than 32 (Figure 8.3 on the first leaf node), the storage temperature was higher than 10 ℃, and the values of De/Re and Re were smaller and higher than 0.2 and 0.47 respectively.

To improve the performance of the DT developed, synthesis routes were designed under the conditions with high MSE (orange routes on DT). These designed experiments were used not only to improve the performance of the developed DT model but also of other models such us RF and XGBoost. Additionally, the designed synthesis routes (set of parameters identified in the DT with high MSE) were applied to confirm the validity of this approach.

The closer the value of R^2 is to 1 and the values of MAE and MSE are to zero, the better is the fit of the developed models. The statistical characteristics of the three appropriate models for the original (20 initial conditions used to build the DT model), random (10

random extra experiment conditions) and designed extra data sets (10 extra designed experiment conditions where high uncertainty was found) are given in detail in Table 8.2.

These results are obtained on the unseen test data. In particular, the designed data sets are obtained by uncertainty analysis (on the training data) of preliminary DT predictions as illustrated in Figure 8.3. As shown, the values of R^2 are always increasing with the designed experiments for all the models while MSE is always decreasing. MAE is always decreasing with random added experiments. The observed decrease in MAE for random added experiments indicates that even when experiments are not systematically designed, there is an improvement in model accuracy. However, the systematic approach of designed experiments based on DT predictions consistently results in both increased R^2 and decreased MSE, which are stronger indicators of model performance improvement.

The designed experiments specifically target areas of high uncertainty or poor prediction performance, leading to more efficient data collection and model refinement. This targeted approach ensures that each new experiment provides maximum informational value, thereby enhancing the model's predictive power more effectively than random experiments. Consequently, this method improves the final predictive models with less cost and time.

As shown in Figure 8.4 and Table 8.2, the computed predictive models, including DT, RF, and XGBoost, which were assisted by DT-based designed of experiments, outperform considerably the ones trained on random extra experiments. These results also confirmed

that the proposed DT-based on designed experiments can significantly enhance the performance of other machine learning algorithms with a considerable reduction (-26% for XGBoost and -38% for RF) of MSE compared to the original model. Note, this study consists of a 'proof of concept' of the proposed DT-guided design of experiments and more experimental data should be collected to obtain more reliable predictions.

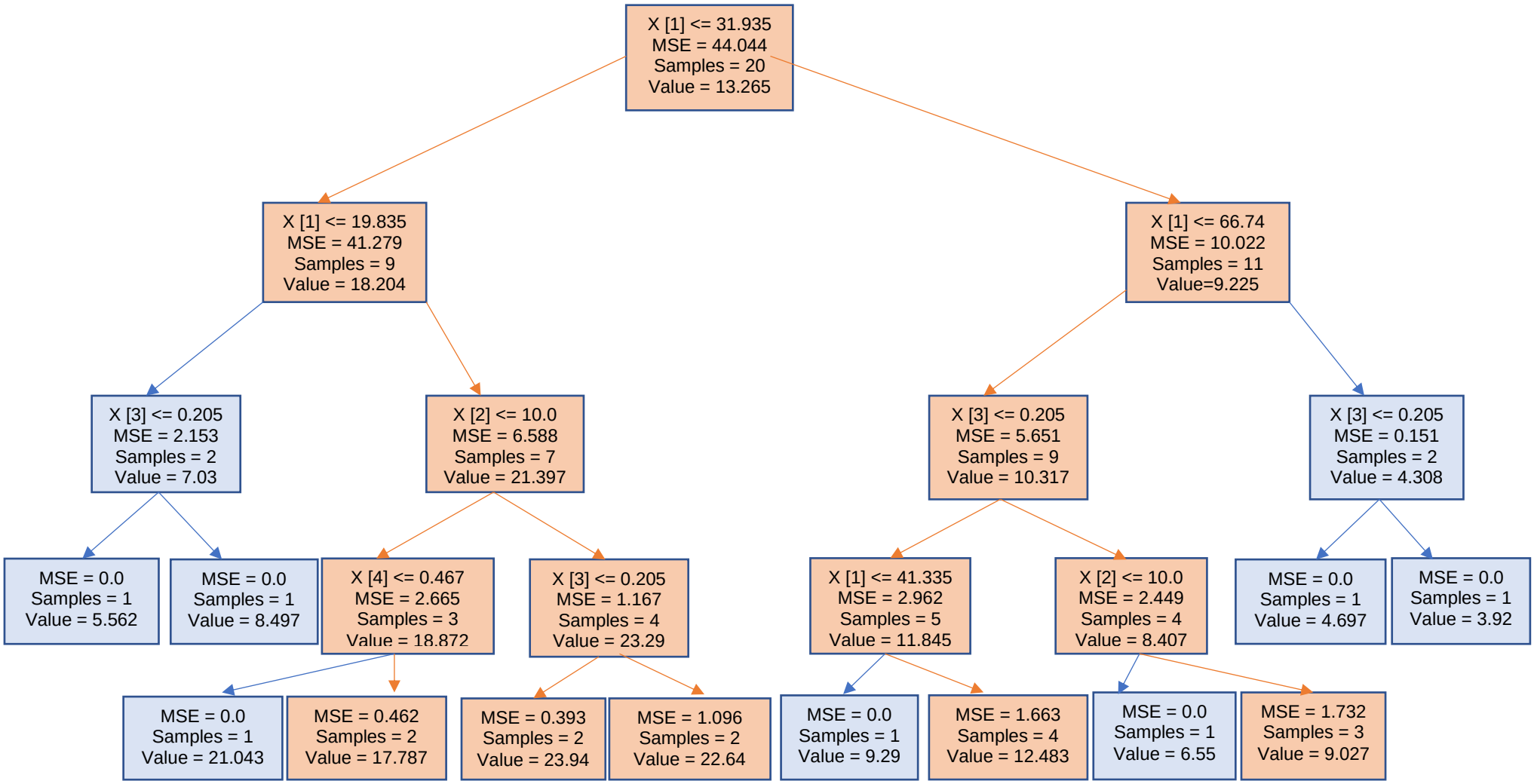


Figure 8.3 Decision tree which examines the size of synthesized AgNPs as a function of five parameters where x_o, x_1, x_2, x_3, x_4, are nucleation constant k_1, growth constant k_2, storage temperature, Dean number/Reynolds number De/Re and Reynolds number (Re) respectively. Orange boxes are showing where there is a high MSE (Nathanael et al, 2023a).

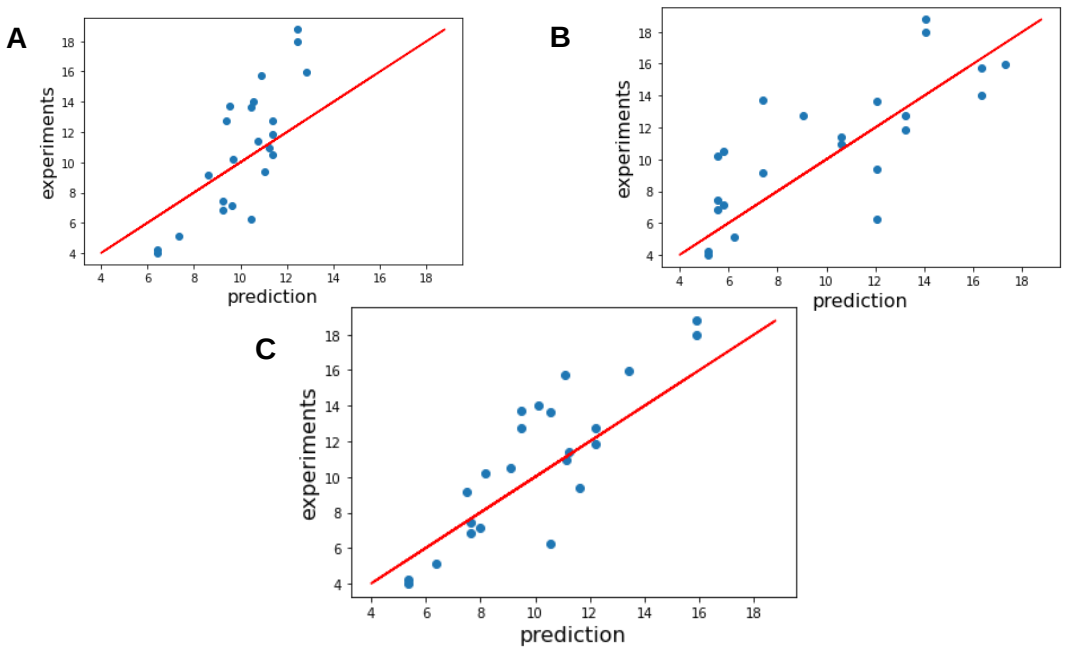


Figure 8.4 Predicted versus real measurements for the size of AgNPs using DT. A) Original training data (20 initial conditions, 60 training samples in total including replications), B) Random extra experiments (10 experiments, 30 validation samples in total including replications) and C) Designed extra experiments (10 experiments, 30 validation samples in total including replications). The conditions that have been used for training, random extra experiments and designed extra experiments are described in detail in Appendix D. The average size of AgNPs on X, Y axes is given in nm (Nathanael et al, 2023a).

Table 8.2 Decision tree (DT), Extreme Gradient boosting (XGBoost) and Random Forest (RF) results for original, random and designed experiments (Nathanael et al, 2023a).

A. Decision Tree

	MSE	MAE	R^2
Original	9.43	2.46	0.45
Random	8.65	2.24	0.49
Designed	6.41	2.01	0.62

B. Gradient Boosting

	MSE	MAE	R^2
Original	8.88	2.27	0.47
Random	7.26	2.01	0.57
Designed	6.56	2.16	0.61

C. Random Forest

	MSE	MAE	R^2
Original	9.42	2.52	0.44
Random	6.45	1.93	0.62
Designed	5.82	1.96	0.66

8.5 INVERSE MODELLING

Various data science methods as discussed in § 2.8, have been employed for inverse design, primarily focusing on ML algorithms, without exploring the potential advantages of Data Assimilation (DA) techniques. Previous ML models for nanoparticles such as those developed by Nathanael et al (2023a) have utilised tree based methods for predicting NP characteristics. While these models are good in predictive performance and capturing

complex interactions, their non-linear nature and high dimensionality pose significant difficulties for inverse modeling.

Designing nanoparticles through inverse modelling can be challenging due to the large design space involved. This includes a wide range of variables, including storage temperature, mixing of the reactants, pH of the solution, types of reducing and stabilising agents, each of which can significantly impact the properties and characteristics of the nanoparticles produced. The diversity within this design space means that multiple combinations must be explored to identify optimal designs. This complexity can make the process of inverse modelling for nanoparticle design intricate and demanding, requiring sophisticated algorithms and computational resources to navigate effectively.

Another notable challenge in inverse modelling is the construction of a differentiable forward model. This requires a thorough understanding of the fundamental physics or mechanisms governing the system, which can be complex and challenging to determine.

In this chapter, an inverse modelling approach for the synthesis of AgNPs in microfluidics will be examined, exploiting the benefits of using polynomial functions and DA techniques.

This chapter aims to enhance the precision in controlling the synthesis conditions of AgNPs in microfluidic devices. By employing advanced data assimilation techniques and inverse modelling, the proposed strategy seeks to provide a more sustainable and direct approach to obtaining AgNPs with desirable characteristics.

The goal is to significantly reduce the need for extensive trial-and-error experiments by implementing a systematic and efficient synthesis process. This approach demonstrates

the potential to create a reliable data-driven model that enables the prediction of synthesis conditions for producing AgNPs of varying sizes in microfluidic devices.

For the inverse modelling approach first, a polynomial function of degree 3 (Eq. (8.2)) for particle size was built using k_1, k_2, T, Re, De/Re. Then, T, k_1, k_2 were fixed as constant terms. Polynomial functions are chosen because they provide a mathematical representation that is easily differentiable, allowing the calculation of gradients (the slopes of the loss function), which simplifies the process of updating the model parameters step-by-step in the optimization process. This, in turn, allows the application of efficient optimization algorithms within the inverse modelling framework.

$$P(k_1, k_2, T, Re, De/Re) = \sum_{i=0}^{3} \sum_{j=0}^{3-i} \sum_{k=0}^{3-i-j} \sum_{l=0}^{3-i-j-k} \sum_{m=0}^{3-i-j-k-l} a_{ijklm} \cdot {k_1}^i \cdot {k_2}^j \cdot T^k \cdot Re^l \cdot De/Re^m \quad (8.2)$$

In the Eq. (8.2), a_{ijklm} are the coefficients that represent the weights for each term in the polynomial expansion while the indices i, j, k, l, m correspond to the powers of the respective variables k_1, k_2, T, Re, and De/Re. This summation captures all possible combinations of powers for these variables up to a total degree of 3, providing a flexible model for representing complex relationships between them. P represents the polynomial function used to predict the size of AgNPs in the system based on the influence of various input parameters (Figure 2). The high correlation between experimental and predicted sizes from direct model, with an R^2 score of 0.94, highlights the model's accuracy in representing the relationship between these parameters and particle size.

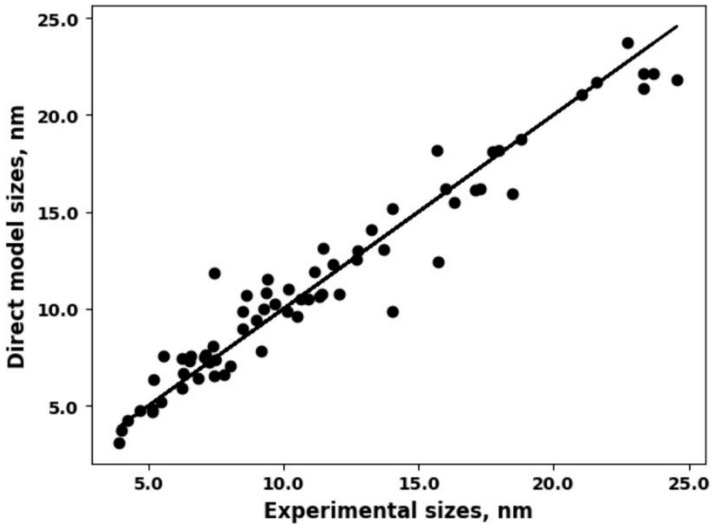


Figure 8.5 The experimental particle sizes obtained from the experimental setup were plotted against the sizes predicted by the direct model, developed using polynomial regression based on Eq. (8.2). This model was constructed using $\mathbf{k_1}$, $\mathbf{k_2}$, T, Re and De/Re. The $\mathbf{R^2}$ score was found 0.94.

After the fixing of parameters, Latin hypercube sampling was used to find initial guesses in the area of Re and $\mathrm{De/Re}$. Using these initial guesses of Re and $\mathrm{De/Re}$ as a background state ($\mathbf{x}_\mathrm{b}$) and size of AgNPs as observation data assimilation was performed. After this the best assimilated values for Re and $\mathrm{De/Re}$ were found. Re and $\mathrm{De/Re}$ were chosen for assimilation for the purpose of experiment validation due to challenges associated with obtaining specific kinetic constants.

Latin hypercube sampling (LHS) (McKay et al, 1979) is a powerful statistical technique that can be used to analyse and explore complex systems with multiple input variables and uncertain parameters. It is a method for generating samples from a given multidimensional probability distribution. The LHS initially divides the input space into

equally probable intervals along each variable of interest. Using LHS, in this study, 100 points were generated in the possible area of Re and $\mathrm{De/Re}$. The range for $\mathrm{De/Re}$ is from 0 to 0.41 while the range for Re is between 0.0849 and 16.96. The specific upper and lower bounds of Re and $\mathrm{De/Re}$ were selected to reflect the physical limits of the experimental data available and to guarantee that the LHS sampling covers the entire input space without redundancy. Then, Latin squares are constructed by randomly transposing the intervals along each variable, while ensuring that each interval turns up once in each row and column of the square. Once the Latin squares are constructed, samples are produced by randomly selecting one value from each interval in the Latin squares (Li & Yang, 2023). LHS guarantees that the samples are evenly distributed across the input space without unnecessary or overlapping representations, thus systematically covering the entire input space. It ensures the independence of samples along each variable, which is useful for uncertainty quantification but also higher accuracy compared to traditional random sampling techniques, requiring fewer samples (Huntington & Lyrintzis, 1998),(Deutsch & Deutsch, 2012). Additionally, and most importantly, LHS has the capability to cover the entire parameter space, ensuring that the global minimum is not missed when subsequently conducting DA.

After conducting LHS, data assimilation was employed to integrate initial guesses of Re and $\mathrm{De/Re}$ as background state ($\mathbf{x}_\mathrm{b}$) and experimental sizes of AgNPs (y) as observational data into the model. This integration not only led to improved predictions but also served to reduce the overall uncertainty in model forecasts. Together, these methodologies form a robust approach for comprehending complex systems and making decisions under

uncertainty. Subsequently, using the polynomial function (Eq. (8.2)), given the observed sizes of AgNPs, the best assimilated values of Re and De/Re were determined (see Figure 8.6). The goal in data assimilation is to minimize the loss function given in Eq. (2.10). In the investigated case, the parameters of interest are the Re and De/Re , both of which are represented as $\mathbf{x}_b$ the initial guesses obtained from a LHS approach. Since the model function H(**x**), which relates these parameters to the predictions, is non-linear, finding an exact solution to the loss function is not straightforward. Instead, the gradient of the loss function ∇J(**x**) (Eq. (2.13)) shows the direction in which the model parameters should change to reduce the error, guiding the iterative update of the model parameters to minimize the loss function. This gradient essentially informs how to adjust the parameters based on both the prior estimates x_b and the discrepancy between the model predictions H(**x**) and the observed experimental data y, which in this case represents the size of the AgNPs. In the iterative optimization process, a Quasi-Newton method, BFGS, is employed. This method uses the gradient ∇J(**x**) and an approximation of the Hessian matrix (second-order derivative of the loss function) to iteratively refine the parameter estimates. At each iteration, the parameters $\mathbf{x}_b$ are updated, and the model is run to obtain new predictions for the nanoparticle size y. The process continues until the algorithm reaches a point where the parameters stop changing significantly, meaning the optimal solution is found. The "best assimilated values", $\mathbf{x}_a$ are the parameter estimates that minimize the loss function J(**x**). These estimates balance the discrepancy between the model predictions and the observed nanoparticle size data, while also incorporating the prior knowledge of the parameters (represented by the initial guesses $\mathbf{x}_b$). Thus, the final

values $\mathbf{x}_a$ that represent the best estimates for the Re and the ratio of De/Re, derived by adjusting the model to better match the experimental data ((see Figure 8.6).

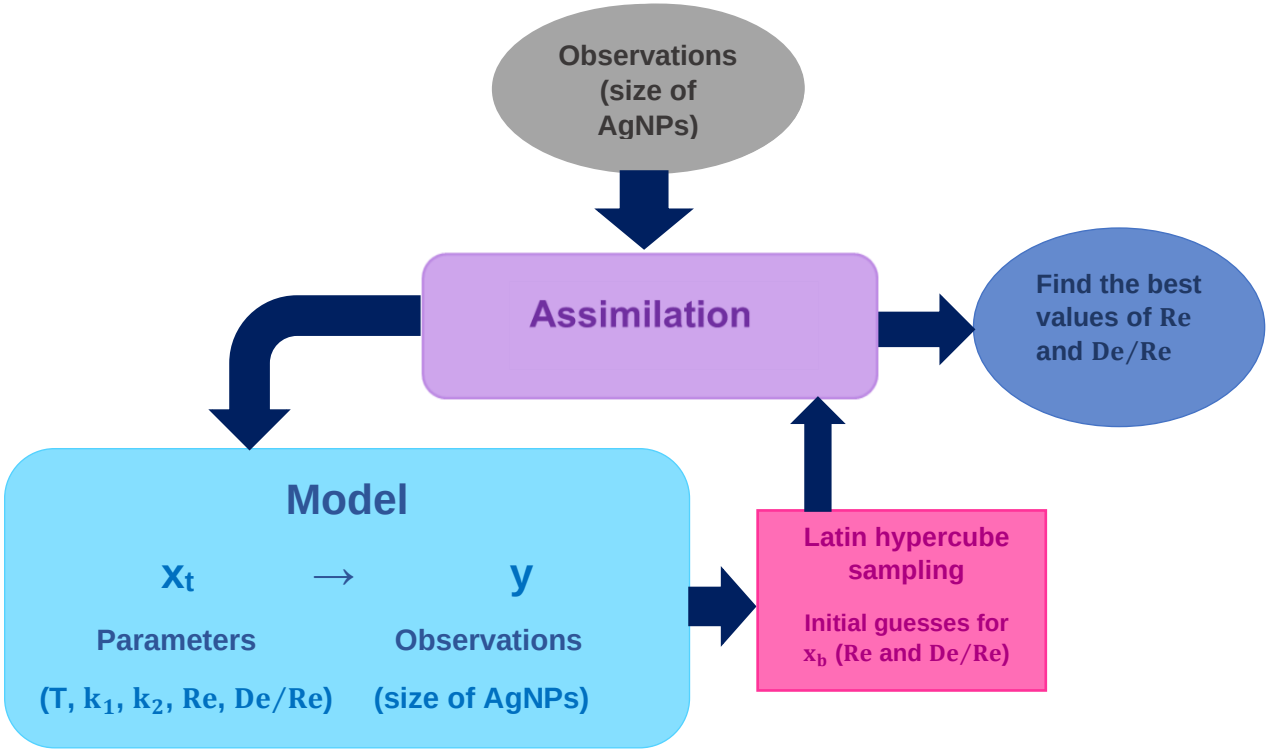


Figure 8.6 Flowchart of data assimilation process in the inverse modelling approach employing LHS.

In this study, the system state is represented by a vector of real parameters, denoted by $\mathbf{x}_t$, which contains the exact target values of these parameters at a given time t. In DA, by representing the state as x_t, allows for the continuous updating and refinement of the state vector as new data becomes available, thereby enhancing the accuracy of the model over time. These target values are always out of reach in real DA problems due to measurement errors (e.g., sensitivity of equipment), incomplete observations, and model imperfections. The goal of DA is to estimate these parameters as accurately as possible,

knowing that the true state can never be perfectly known. The DA system comprises two main components, an initial estimation of parameters $\mathbf{x}_b$ (also referred to as the background state) and observations of a physical field, y typically obtained through real-time sensors. In this study $\mathbf{x}_b$ are the initial guesses of Re and De/Re and y is the particle size of AgNPs in nm from the experiments in the microfluidic setup described in section 3.2.

In the 3D VAR assimilation process applied in this chapter, the background error covariance matrix B characterizes the uncertainty surrounding the system's initial state. Its diagonal elements were set to [1, 10], reflecting the uncertainties in the two input components De/Re and Re. The [1, 10] error covariance matrix reflects the assumption that the De/Re ratio has smaller uncertainty, as it is more directly tied to the specific design of the system compared to the broader factors influencing Re. These coefficients are chosen relative to De/Re and Re when the error covariance is calculated, ensuring they are proportional to their absolute values. Setting specific values like 1 and 10 in the background covariance matrix B is a standard practice in data assimilation to reflect varying levels of uncertainty in different parameters of the system. This practice ensures that the assimilation process appropriately weights the influence of prior information relative to new observations. In this case, the value 1 assigned to De/Re indicates relatively low uncertainty. This suggests that De/Re is a variable for which there exists more reliable prior information and therefore, there is a higher confidence in the initial estimate. Conversely, the value 10 assigned to Re shows higher uncertainty. Re represents a variable that is less constrained by prior information meaning there is less

confidence in its initial estimate. The R matrix on the other hand, represents the uncertainty associated with the experimental observations. It is important to note that B and R matrices are relative, which means the crucial factor is their ratio, and not their absolute values.

Subsequently, the background and analysis predictions were assessed to determine the posterior covariance. The resulting values [0.00783, 9.92] represent the estimated variances of De/Re and Re, respectively. These figures offer insights into the uncertainty associated with the estimated variables following the assimilation of observational data into the model. Lower values denote higher confidence in the estimates, whereas higher values signify increased uncertainty. Once the inverse modelling approach has been built, a set of unseen test data is utilised to evaluate the performance of the whole approach (see Figure 8.7).

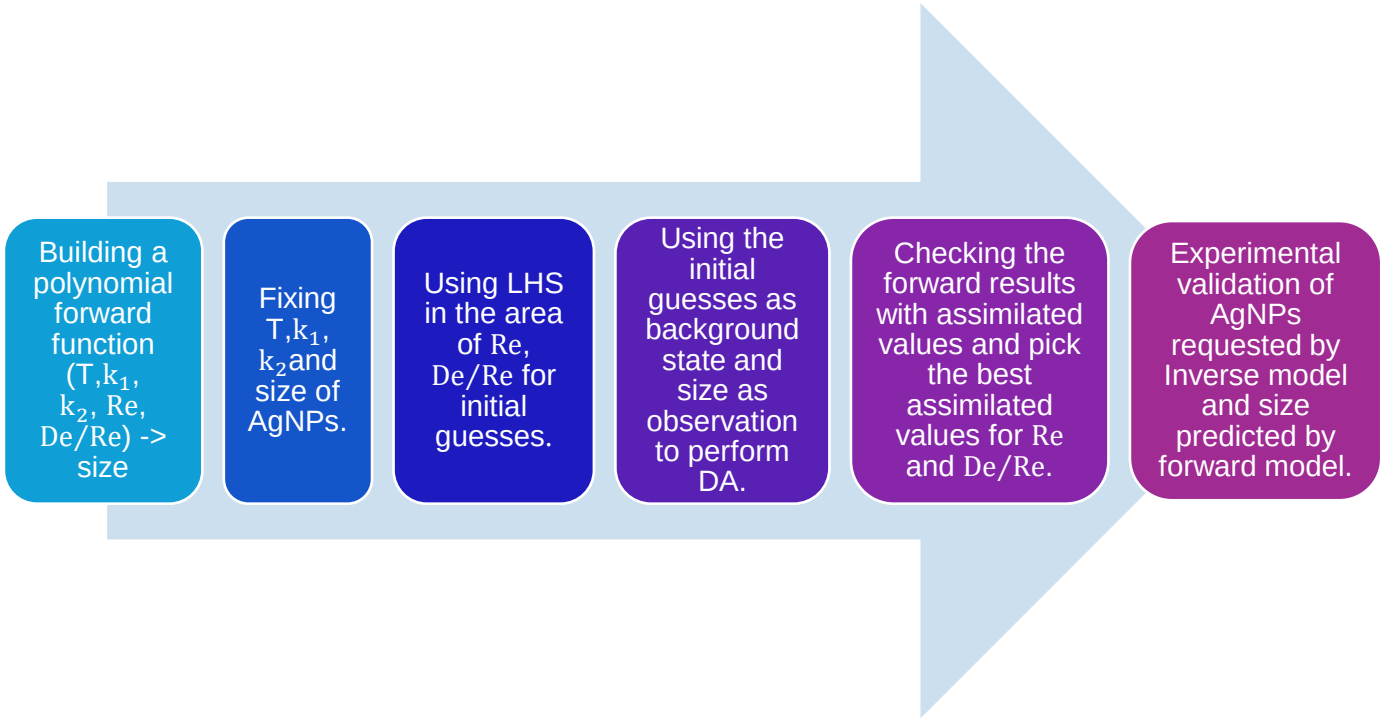


Figure 8.7 Steps to build the forward model, using the LHS and DA for the inverse model and how the inverse model was validated.

The results of these evaluations are presented in Figure 8.8 and Figure 8.9. Figure 8.8 shows the results from the forward prediction model for the size of AgNPs, where the predictions are based on parameters derived from inverse modelling. The test set used for this prediction involves applying the parameters such as the De/Re ratio and Re, which were previously assimilated through inverse modelling. These parameters, along with others from the model, serve as inputs to the forward prediction process. The forward prediction model is used to test how well the predicted parameters perform in determining the nanoparticle size. Figure 8.9 shows the comparison between experimental data and the design requirements set by inverse modelling. Unlike the forward prediction model,

which uses the assimilated values as input parameters for prediction, the experimental data presented in this figure were obtained by performing experiments using the De/Re ratio and Re values that were derived from inverse modelling. These parameters, along with other experimental conditions, were set according to the model's predictions and used to guide the experiments. The purpose of this figure is to demonstrate how the experimental results compare to the design targets established through the inverse modelling process, validating whether the experimental data meets the expected requirements.

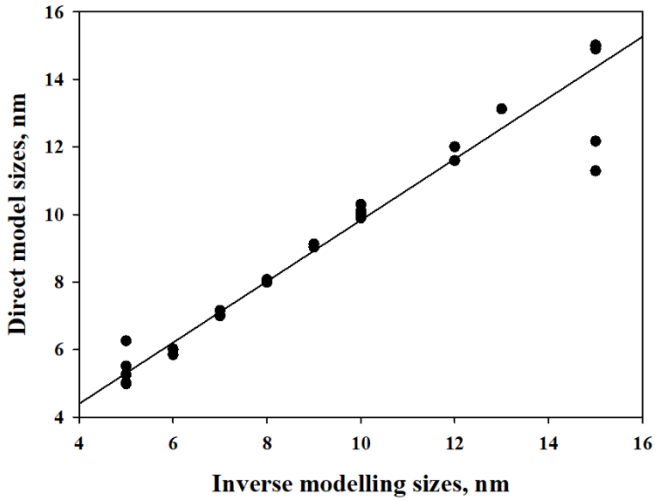


Figure 8.8 Inverse modelling sizes versus direct model sizes

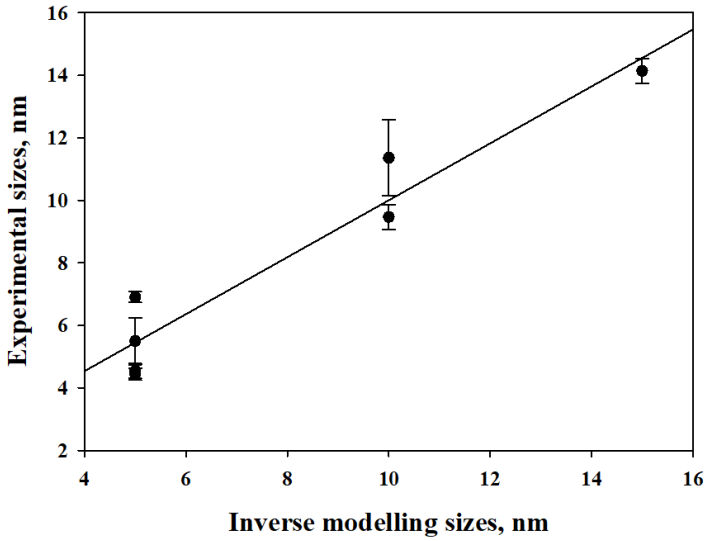


Figure 8.9 Inverse modelling sizes versus experimental sizes

It is important to mention that different polynomial degrees were investigated to get a good performance of the data but also avoid overfitting. For example, using polynomial function of degree 2, the sizes requested by inverse modelling with k_1= 0.0011 $1/\mathrm{min}$, k_2=55.51 $1/\mathrm{Mmin}$ and T=0 ℃ as constant terms, significantly differed from the sizes predicted by the forward model using the assimilate values of Re and De/Re, resulting in a percentage error of approximately 32%. However, when using polynomial function of degree 3, the average percentage error for the sizes predicted by direct model compared to the sizes requested by Inverse model reduced to 2.65% with a maximum error at 23.3%.

For a comprehensive understanding of the assimilated values of De/Re and Re under various experimental conditions, alongside the sizes of AgNPs required for inverse modelling, predicted by the direct model, and obtained experimentally, please refer to Tables 8.3, 8.4 and 8.5. These tables provide detailed insights into the relationship

between the model parameters and experimental outcomes, facilitating a thorough assessment of the inverse modelling process. As expected, the sizes of AgNPs were decreased with the increase in the of ratio of De/Re and Re. These findings align with previous studies (Wu et al, 2017), (Ling et al, 2022) investigating the effect of hydrodynamics on NP size. However, the results presented in the Tables 8.3, 8.4 and 8.5 indicate some discrepancies in the sizes of AgNPs, that may be attributed to uncertainties associated with Re rather than the ratio of De/Re, where confidence is higher. The resulting values [0.00783, 9.92] that represent the estimated variances of De/Re and Re showed that the uncertainty around the estimated values of De/Re provide more confidence than Re values.

The average percentage error for the sizes found experimentally and sizes requested by Inverse model is 11.99% with 28.07% the maximum error. The error variance is 1.2 with the biggest error observed at smaller particle sizes (Table 8.4). The average percentage error for the sizes predicted by direct model and size requested by Inverse model is 2.65% with maximum error at 23.3% and error variance 0.469 (Table 8.3). The maximum error of 23.3% is likely due to the uncertainty related to Re or the limits of Re, which are set between 0.0849-16.96.

The average error for the size of AgNPs requested by Inverse modelling and size predicted by direct model (Table 8.5) using only assimilated values of Re is very small (0.0009%).

Both forward and inverse paths for the size of AgNPs exhibit reasonably good consistency. The experimental data confirm the viability of this approach in designing AgNPs with different desired sizes.

Table 8.3 Assimilated values of De/Re and Re for different experimental conditions. Comparison of size of AgNPs requested by Inverse modelling and size predicted by direct model.

Fixing k_1= 0.0011 $1/min$, k_2=55.51 $1/Mmin$ and T=0 ℃ as constant terms for Inverse Modelling approach				
Assimilated value of De/Re	**Assimilated value of Re**	**Size requested by Inverse Modelling (nm)**	**Size predicted by Direct model (nm)**	**Percentage error (%)**
0.36	1.73	5	5.26	4.94
0.355	0.58	7	7.16	2.23
0.277	0.4	9	9.12	1.32
0.23	0.35	10	10.11	1.088
0.14	0.44	12	12.007	0.058
0.067	0.085	14	14.02	0.14
0.034	0.086	15	15.02	0.13

Fixing k_1= 0.0013 $1/min$, k_2=37.86 $1/Mmin$ and T=0 ℃ as constant terms for Inverse Modelling approach				
Assimilated value of De/Re	**Assimilated value of Re**	**Size requested by Inverse Modelling (nm)**	**Size predicted by Direct model (nm)**	**Percentage error (%)**
0.409	5.69	5	5.01	0.2
0.378	5.56	6	6.015	0.25
0.3907	0.88	8	8.073	0.9
0.375	0.54	10	10.3	2.91

0.2835	0.318	13	13.126	0.96
0.2	0.0849	15	12.17	23.25
Fixing k_1= 0.0015 $1/\mathrm{min}$, k_2=44.81 $1/\mathrm{Mmin}$ and T=0 ℃ as constant terms for Inverse Modelling approach				
Assimilated value of $\mathrm{De/Re}$	**Assimilated value of Re**	**Size requested by Inverse Modelling (nm)**	**Size predicted by Direct model (nm)**	**Percentage error (%)**
0.0405	11.16	7	7.0028	0.04
0.37	0.99999	9	9.036	0.4
0.27	0.0849	12	11.6	3.45
Fixing k_1= 0.1 $1/\mathrm{min}$, k_2=77.97 $1/\mathrm{Mmin}$ and T=20 ℃ as constant terms for Inverse Modelling approach				
Assimilated value of $\mathrm{De/Re}$	**Assimilated value of Re**	**Size requested by Inverse Modelling (nm)**	**Size predicted by Direct model (nm)**	**Percentage error (%)**
0.0028	1.24	6	5.85	2.56
0.0042	1.82	5	4.86	2.88

Table 8.4 Assimilated values of $\mathrm{De/Re}$ and Re for different experimental conditions. Comparison of size of AgNPs requested by Inverse modelling and size found experimentally.

Fixing k_1= 0.0011 $1/\mathrm{min}$, k_2=55.51 $1/\mathrm{Mmin}$ and T=0 ℃ as constant terms for Inverse Modelling approach				
Assimilated value of $\mathrm{De/Re}$	**Assimilated value of Re**	**Size requested by Inverse Modelling (nm)**	**Size found, experimentally (nm)**	**Percentage error (%)**
0.41	0.91	5	5.56 ± 1.08	10.07
0.32	2.49	5	6.95 ± 1.55	28.06

0.23	0.35	10	11.36 ± 3.19	11.97
Fixing k_1= 0.0013 $1/\mathrm{min}$, k_2=37.86 $1/\mathrm{Mmin}$ and T=0 $^{\circ}\mathrm{C}$ as constant terms for Inverse Modelling approach				
Assimilated value of De/Re	**Assimilated value of Re**	**Size requested by Inverse Modelling (nm)**	**Size found, experimentally (nm)**	**Percentage error (%)**
0.409	5.69	5	4.54 ± 0.85	10.13
0.32	6.34	10	9.47 ± 1.2	5.6
0.2	0.0849	15	14.14 ± 2.097	6.08

Table 8.5 Assimilated values of Re for different experimental conditions. Comparison of size of AgNPs requested by Inverse modelling and size predicted by direct model.

Fixing k_1= 0.0011 $1/\mathrm{min}$, k_2=55.51 $1/\mathrm{Mmin}$, De/Re = 0.41 and T=0 ℃ as constant terms for Inverse Modelling approach			
Assimilated value of Re	**Size requested by Inverse Modelling (nm)**	**Size predicted by Direct model (nm)**	**Percentage error (%)**
6.3	10	9.99	0.001
Fixing k_1= 0.1 $1/\mathrm{min}$, k_2=77.97 $1/\mathrm{Mmin}$, De/Re = 0.41 and T=20 ℃ as constant terms for Inverse Modelling approach			
5.014	10	9.99	0.001
Fixing k_1= 0.1 $1/\mathrm{min}$, k_2=77.97 $1/\mathrm{Mmin}$, De/Re = 0.32 and T=20 ℃ as constant terms for Inverse Modelling approach			
16.43	10	9.9	0.001
Fixing k_1= 0.0015 $1/\mathrm{min}$, k_2=44.81 $1/\mathrm{Mmin}$ De/Re = 0.32 and T=0 ℃ as constant terms for Inverse Modelling approach			
Assimilated value of Re	**Size requested by Inverse Modelling (nm)**	**Size predicted by Direct model (nm)**	**Percentage error (%)**
3.92	8	8.0008	0.0001
6.46	7	7.0001	0.00001
Fixing k_1= 0.0015 $1/\mathrm{min}$, k_2=44.81 $1/\mathrm{Mmin}$ De/Re = 0.41 and T=0 ℃ as constant terms for Inverse Modelling approach			
Assimilated value of Re	**Size requested by Inverse Modelling (nm)**	**Size predicted by Direct model (nm)**	**Percentage error (%)**
4.0035	6	5.99	0.00167
0.0849	8	7.99	0.00125

8.6 CONCLUSIONS

A machine learning-guided design of experiments based on the decision tree method for the size of AgNPs synthesized in a continuous flow T-junction device was implemented.

The parameters investigated were nucleation and growth constants derived from an independent set of experiments using F-W mechanism, as well as storage temperature and hydrodynamic parameters including Reynolds and Dean number.

The obtained model showed the areas of interest for further experiments (regions with high MSE) and numerical results showed that well designed synthesis routes can significantly improve the performance not only of DT itself but also of other regression methods such as RF and XGBoost compared to randomly chosen extra synthesis routes. In particular, considerable reduction of MSE compared to the original model, 26% for XGBoost and 38% for RF, was found. Additionally, the obtained model can be developed further in the future by data-assimilation from numerical simulations and additional experiments, including experiments with other chemicals and other device types.

In the inverse modeling approach described, a polynomial function was constructed using key parameters such as k_1, k_2, T, Re, De/Re. By keeping certain terms constant and employing LHS, initial guesses were explored in the area of Re and De/Re. Subsequently, data assimilation was employed to integrate observational data into the model, leading to improved predictions and reduced uncertainty. Evaluation of the inverse modeling approach involved testing against unseen data, demonstrating reasonably good consistency between forward and inverse paths for NP size prediction. The experimental data further validated the effectiveness of this approach in designing nanoparticles with desired sizes.

The combination of inverse modeling, LHS, and data assimilation has been shown to offer a robust framework for comprehending complex systems and making decisions under uncertainty, providing valuable insights into nanoparticle design and manufacturing processes. The existing inverse model can be tested for its general applicability by incorporating data from other chemical protocols. Adding data for smaller particle sizes or varying Re will enhance the model's accuracy and robustness. Other routes of future work would be developing novel data assimilation schemes that could integrate more advanced machine learning methods (such as neural networks) as forward functions to perform the inverse modelling.

CHAPTER 9: CONCLUSIONS & FUTURE WORK

9.1 CONCLUSIONS

This literature review of this thesis provided an in-depth exploration of the formation mechanisms, properties, and applications of AgNPs, with a particular emphasis on the role of microfluidic technology, computational modelling, and data-driven approaches. Chemical reduction emerged as the primary method for synthesis of AgNPs, with microfluidic devices offering precise control over reaction conditions and reducing the polydispersity of AgNPs. Operational parameters such as reagent type and concentration, pH, temperature, and mixing dynamics significantly impact nanoparticle size. The Finke-Watzky two-step mechanism was identified as the most suitable model to describe the autocatalytic synthesis of different metal-NPs like silver, but hydrodynamic processes need to be integrated to provide a more comprehensive understanding of AgNP synthesis. Numerical simulations, including coupled PBM-CFD simulations within microfluidic channels, were found significant to facilitate insights into particle size distribution and average size. DoE and response surface methodology, along with data science approaches, offer cost-effective means to explore various aspects of AgNP synthesis but also face challenges in generalization of systems and elucidating underlying physics.

As chemical reduction serves as the primary method for synthesizing AgNPs, the research presented in this thesis utilised two distinct sets of chemicals. The first set consisted of TA, a weak reducing agent, and TC, which functions as both a reducing and stabilising

agent. The second set comprised DMAB, a strong reducing agent, and SDS, an anionic surfactant, as stabilising agent. Additionally, this study employed various reactors, including a well-mixed reactor, a continuous flow reactor, and a droplet reactor, to investigate the hydrodynamic effects on the size of AgNPs. Although previous studies primarily focused on comparing batch reactors with microfluidic devices for nanoparticle synthesis, this thesis aimed to explore the comparison between single-phase and two-phase reactors, serving as one of the key objectives of this work. It was discovered that similar mixing conditions resulted in no significant differences in the sizes of AgNPs produced by these systems. Despite encountering challenges such as particle concentration reduction due to deposition or fouling within channels, the continuous flow device was selected for further investigation. This decision was primarily driven by its effectiveness and convenience, especially in simplifying measurements, as nanoparticles do not require separation from the oil phase.

A D-optimal experimental design was first utilised to build a predictive regression model via response surface methodology, to optimize AgNP formation in a T-junction microfluidic continuous flow reactor using first set of chemicals. This approach provided insights into the effects of various factors on the response, showing significant interaction effects often missed by traditional OFAT methods. By employing model discrimination techniques, such as AIC and BIC, the most appropriate model was identified. The investigation focused on five experimental factors, including storage temperature, pH, trisodium citrate concentration, curvature of the output channel, and flow rates, revealed their significant impacts on the response. Notably, pH, trisodium citrate concentration, curvature, and

their interaction emerged as particularly influential. The resulting model equation, depicted graphically as a response surface function, facilitated the identification of optimal hydrodynamic and reaction conditions. The predicted optimal parameter combinations gave AgNPs with average sizes of 2.62 nm and 4.32 nm, respectively. With an average prediction error of 6.8% for the testing dataset, the developed model demonstrated reliability in correlating various factors with AgNP size.

Through kinetics investigations on the two sets of chemicals in a well-mixed reactor, a correlation was established indicating that PSD can be predicted if the kinetic constants and initial concentrations are known. By incorporating these kinetics and concentrations into a regression model, the PSD for two different sets of chemicals could be predicted with an average error of 4.9%. The model's close agreement with experimental data shows its reliability and a strong connection between chemical features and AgNP size.

A novel approach developed by project partners, which integrated PBM with CFD to predict the PSD of AgNPs in both T-junction continuous flow microchannels and well-mixed reactors, was validated by comparison with experiments. This pioneering PBM-CFD approach provided deeper insights into the interplay between hydrodynamics, reaction kinetics, and PSD in multi-step synthesis processes compared to the predictive response surface model.

Whilst the Finke-Watzky (F-W) model effectively captured qualitative trends, discrepancies were noted, especially at higher pH values, attributed to rapid nucleation and assumptions of uncoupled nucleation and growth steps. F-W-based simulations demonstrated the impact of pH and initial stabilizer concentration on size distribution in

the well-mixed reactor. Variations in operating conditions in continuous flow microchannels highlighted the influence of residence time on precursor consumption rates and PSD. The small differences observed between experimental and simulation results in the T-junction device showed the complexity of NP synthesis processes. These differences may be attributed to uncertainties in reduction rate reaction, properties of TA-TC complex, and limitations in the simulation domain.

To enhance further the synthesis of AgNPs in a continuous flow T-junction device and broaden its applicability, data science approaches based on DT and inverse modelling were employed. A ML-guided approach utilizing DT methods and inverse modelling investigated various parameters, including nucleation and growth constants, storage temperature, and hydrodynamic factors. By analysing these parameters, the DT model effectively identified the areas for further experimentation, leading to optimized synthesis pathways. Notably, this approach significantly reduced MSE compared to random methods, demonstrating its effectiveness in improving performance. The potential of the model for future development through data assimilation and additional experiments using alternative sets of chemicals was emphasized, highlighting its role in tailoring NPs to meet specific application requirements. Inverse modelling, based on Latin hypercube sampling and data assimilation, offered significant insights in nanoparticle manufacturing, particularly in tailoring nanoparticles to meet specific application requirements. Assessing, this methodology included examining its performance with new data, demonstrating good consistency between predicting NP size both forwards and

backwards. Experimental results further confirmed the efficacy of this method in designing NPs of specific sizes as intended.

The work presented in this thesis demonstrates the potential of these combined approaches to reduce the ecological footprint in the screening of AgNP production methods, by minimising the use of large volumes of reagents, as well as reducing the need for repeated and extensive experimental tests. Returning to the scope of the study, this thesis provided a comprehensive analysis of the synthesis of AgNPs by investigating the nucleation and growth kinetics under two distinct chemical protocols. These protocols utilised both weak and strong reducing agents and different types of stabilising agents, such as surfactants and electrolytes, in a well-mixed batch reactor. Furthermore, this research examined AgNP synthesis, in two different microfluidic device operations: continuous flow and droplet reactors. It also investigated the impact of different chemical and hydrodynamic conditions on the final sizes of AgNPs. Advanced machine learning and data science techniques were employed not only to optimize and generalise the entire synthesis process but also to predict the size of AgNPs. The thesis also highlighted the importance of integrating kinetics with initial silver concentrations, hydrodynamic factors, and computational studies in predicting the PSD.

9.2 FUTURE WORK

The limitations and gaps of this thesis include the validation of machine learning and data science methods to other set of chemicals and other microfluidic set-ups. These approaches used generalised terms for the different synthesis conditions, but they were

validated for a single set of chemicals and a single microfluidic device. To further expand the application of these models, incorporating additional physicochemical characteristics such as the dispersity and shape of AgNPs is recommended.

Additionally, examining the correlation between the initial concentrations of the silver precursor with the observed kinetics for two chemical protocols with more sets of chemicals and more experimental data will validate and broaden its wide use.

In future work it would be beneficial to examine the DT and inverse models with alternative chemical protocols, such as DMAB and SDS or others, in both batch and microfluidic setups. Expanding the current models can aid in developing robust predictions for the sizes and other physicochemical characteristics of AgNPs (shape and dispersity) or other NPs more directly with much more accuracy.

Development of novel microfluidic channel geometries and configurations is significant to enhance mixing efficiency and reaction control in AgNPs synthesis. Investigations on the impact of different designs, channel materials and surface modifications are needed as well on the synthesis process to provide valuable insights.

Regarding the chemical aspect of this thesis, it is worth exploring the role of the tannic acid-trisodium citrate complex in the reduction of silver nitrate which remains unexplored. Further to that, experiments with different chemical reducing agents and stabilisers to improve the synthesis efficiency, stability but also biocompatibility is required. Environmental and safety considerations must be addressed by investigating the environmental impact and safety of the resulting AgNPs.

Further investigations should focus on the correlation identified for predicting the PSD for the two sets of chemicals. Combining the initial concentrations of the silver precursor with the observed kinetics has been found to play a crucial role in accurately predicting the PSD of AgNPs.

The accuracy of ML models is strongly dependent on the quality and quantity of data used for training, testing and validation. Therefore, extending the experimental database would significantly improve ML models even before integrating them with physics-based models. Furthermore, integrating physics-based models with experimental methodologies, such as microfluidic synthesis, to provide more data for data-driven models holds a significant promise for advancing NP synthesis and reducing the ecological footprint. Experimental work provides a solid foundation for model assumptions and parameter estimations, while simulations bridge experimental findings with intricate relationships, unveiling complex dynamics.

Finally, it is worthy to develop strategies to scale up the microfluidic synthesis process for industrial production while maintaining control over NP characteristics. The potential of parallelization of microfluidic channels to increase throughput is important to be explored.

By addressing these areas, future research can further advance the synthesis of AgNPs in microfluidic devices, enhancing their efficiency, scalability, and applicability in various industrial and scientific domains.

REFERENCES

Aaboub, F., Chamlal, H. & Ouaderhman, T. (2023) Statistical analysis of various splitting criteria for decision trees. *Journal of Algorithms & Computational Technology*, 17, 17483026231198181.

Adir, O., Poley, M., Chen, G., Froim, S., Krinsky, N., Shklover, J., Shainsky-Roitman, J., Lammers, T. & Schroeder, A. (2020) Integrating Artificial Intelligence and Nanotechnology for Precision Cancer Medicine. *Adv Mater*, 32(13), e1901989.

Agha, A., Waheed, W., Stiharu, I., Nerguizian, V., Destgeer, G., Abu-Nada, E. & Alazzam, A. (2023) A review on microfluidic-assisted nanoparticle synthesis, and their applications using multiscale simulation methods. *Discover Nano*, 18(1), 18.

Ahmad, S., Munir, S., Zeb, N., Ullah, A., Khan, B., Ali, J., Bilal, M., Omer, M., Alamzeb, M., Salman, S. M. & Ali, S. (2019) Green nanotechnology: a review on green synthesis of silver nanoparticles — an ecofriendly approach. *International Journal of Nanomedicine.* Dove Press.

Akaike, H. (1974) A new look at the statistical model identification. *IEEE Transactions on Automatic Control*, 19(6), 716-723.

Aktara, M. N., Nayim, S., Sahoo, N. K. & Hossain, M. (2019) The synthesis of thiol-stabilized silver nanoparticles and their application towards the nanomolar-level colorimetric recognition of glutathione. *New Journal of Chemistry*, 43(34), 13480-13490.

Al-Thabaiti, S. A., Al-Nowaiser, F. M., Obaid, A. Y., Al-Youbi, A. O. & Khan, Z. (2008) Formation and characterization of surfactant stabilized silver nanoparticles: A kinetic study. *Colloids and Surfaces B: Biointerfaces*, 67(2), 230-237.

Aljarrah, M. T., Alboull, A. a. M., Alharahsheh, M. S., Ashraf, A. & Khandakar, A. (2022) Parametric Study of Gold Nanoparticles Synthesis under Micro-Continuous Flow Conditions. *Molecules*, 27(24), 8651.

Alqadi, M. K., Abo Noqtah, O. A., Alzoubi, F. Y., Alzouby, J. & Aljarrah, K. (2014) pH effect on the aggregation of silver nanoparticles synthesized by chemical reduction. *Materials Science-Poland*, 32(1), 107-111.

Altayb, H. N., Kouidhi, B., Baothman, O. A. S., Abdulhakim, J. A., Ayed, L., Hager, M. & Chaieb, K. (2021) Mathematical modeling and optimization by the application of full factorial design and response surface methodology approach for decolourization of dyes by a newly isolated Photobacterium ganghwense. *Journal of Water Process Engineering*, 44, 102429.

Alzahrani, E. (2020) Colorimetric Detection Based on Localized Surface Plasmon Resonance Optical Characteristics for Sensing of Mercury Using Green-Synthesized Silver Nanoparticles. *Journal of Analytical Methods in Chemistry*, 2020, 6026312.

Amirjani, A. & Haghshenas, D. F. (2018) Modified Finke–Watzky mechanisms for the two-step nucleation and growth of silver nanoparticles. *Nanotechnology*, 29(50), 505602.

Andrieux-Ledier, A., Tremblay, B. & Courty, A. (2013) Synthesis of Silver Nanoparticles Using Different Silver Phosphine Precursors: Formation Mechanism and Size Control. *The Journal of Physical Chemistry C*, 117(28), 14850-14857.

Anigol, L. B., Charantimath, J. S. & Gurubasavaraj, P. M. (2017) Effect of Concentration and pH on the Size of Silver Nanoparticles Synthesized by Green Chemistry.

Aning, S. & Przybyła-Kasperek, M. (2022) Comparative Study of Twoing and Entropy Criterion for Decision Tree Classification of Dispersed Data. *Procedia Computer Science*, 207, 2434-2443.

Anna, S. L. (2016) Droplets and Bubbles in Microfluidic Devices. *Annual Review of Fluid Mechanics*, 48(Volume 48, 2016), 285-309.

Antony, J. (2014a) 6 - Full Factorial Designs, in Antony, J. (ed), *Design of Experiments for Engineers and Scientists (Second Edition)*. Oxford: Elsevier, 63-85.

Antony, J. (2014b) 7 - Fractional Factorial Designs, in Antony, J. (ed), *Design of Experiments for Engineers and Scientists (Second Edition)*. Oxford: Elsevier, 87-112.

Arcucci, R., D'Amore, L., Pistoia, J., Toumi, R. & Murli, A. (2017) On the variational data assimilation problem solving and sensitivity analysis. *Journal of Computational Physics*, 335, 311-326.

Ashley, B., Vakil, P. N., Lynch, B. B., Dyer, C. M., Tracy, J. B., Owens, J. & Strouse, G. F. (2017) Microwave Enhancement of Autocatalytic Growth of Nanometals. *ACS Nano*, 11(10), 9957-9967.

Ayyubi, S. N., Purbasari, A. & Kusmiyati (2022) The effect of composition on mechanical properties of biodegradable plastic based on chitosan/cassava starch/PVA/crude glycerol: Optimization of the composition using Box Behnken Design. *Materials Today: Proceedings*.

Baber, R., Mazzei, L., Thanh, N. T. K. & Gavriilidis, A. (2015) Synthesis of silver nanoparticles in a microfluidic coaxial flow reactor. *RSC Advances*, 5(116), 95585-95591.

Baber, R., Mazzei, L., Thanh, N. T. K. & Gavriilidis, A. (2017) An engineering approach to synthesis of gold and silver nanoparticles by controlling hydrodynamics and mixing based on a coaxial flow reactor. *Nanoscale*, 9(37), 14149-14161.

Badawy, A. M. E., Luxton, T. P., Silva, R. G., Scheckel, K. G., Suidan, M. T. & Tolaymat, T. M. (2010) Impact of Environmental Conditions (pH, Ionic Strength, and Electrolyte Type) on the Surface Charge and Aggregation of Silver Nanoparticles Suspensions. *Environmental Science & Technology*, 44(4), 1260-1266.

Badilescu, S. & Packirisamy, M. (2012) Microfluidics-Nano-Integration for Synthesis and Sensing. *Polymers*, 4(2), 1278-1310.

Baghaei, M., Tekie, F. S. M., Khoshayand, M. R., Varshochian, R., Hajiramezanali, M., Kachousangi, M. J., Dinarvand, R. & Atyabi, F. (2021) Optimization of chitosan-based polyelectrolyte nanoparticles for gene delivery, using design of experiment: in vitro and in vivo study. *Materials Science and Engineering: C*, 118, 111036.

Bal, V. & Bandyopadhyaya, R. (2019) Mechanistic aspects in the formation of nano- and submicron particles in a batch and a continuous microfluidic reactor: Experiment, modeling and simulation. *Chemical Engineering Journal*, 371, 43-54.

Balankura, T., Yan, T., Jahanmahin, O., Narukatpichai, J., Ng, A., Fichthorn, K. A. & Fichthorn, K. A. (2020) Oriented attachment mechanism of triangular Ag nanoplates: A molecular dynamics study. *Nanoscale Advances*, 2, 2265-2270.

Ballottin, D., Fulaz, S., Cabrini, F., Tsukamoto, J., Durán, N., Alves, O. L. & Tasic, L. (2017) Antimicrobial textiles: Biogenic silver nanoparticles against Candida and Xanthomonas. *Materials Science and Engineering: C*, 75, 582-589.

Bannister, R. N. (2017) A review of operational methods of variational and ensemble-variational data assimilation. *Quarterly Journal of the Royal Meteorological Society*, 143(703), 607-633.

Baroutaji, A., Lenihan, S. & Bryan, K. (2019) Compaction analysis and optimisation of convex-faced pharmaceutical tablets using numerical techniques. *Particuology*, 47, 10-21.

Bastús, N. G., Merkoçi, F., Piella, J. & Puntes, V. (2014) Synthesis of Highly Monodisperse Citrate-Stabilized Silver Nanoparticles of up to 200 nm: Kinetic Control and Catalytic Properties. *Chemistry of Materials*, 26(9), 2836-2846.

Bellotti, R., Picotto, G. B. & Ribotta, L. (2022) AFM Measurements and Tip Characterization of Nanoparticles with Different Shapes. *Nanomanufacturing and Metrology*, 5(2), 127-138.

Bentea, L., Watzky, M. A. & Finke, R. G. (2017) Sigmoidal Nucleation and Growth Curves Across Nature Fit by the Finke–Watzky Model of Slow Continuous Nucleation and Autocatalytic Growth: Explicit Formulas for the Lag and Growth Times Plus Other Key Insights. *The Journal of Physical Chemistry C*, 121(9), 5302-5312.

Bhattacharya, P. K. & Burman, P. (2016) 11 - Linear Models, in Bhattacharya, P. K. & Burman, P. (eds), *Theory and Methods of Statistics*Academic Press, 309-382.

Bogireddy, N. K. R., Kiran Kumar, H. A. & Mandal, B. K. (2016) Biofabricated silver nanoparticles as green catalyst in the degradation of different textile dyes. *Journal of Environmental Chemical Engineering*, 4(1), 56-64.

Brook, M. A. (2023) Functional silicone oils and elastomers: new routes lead to new properties. *Chemical Communications*, 59(86), 12813-12829.

Calderón-Jiménez, B., Johnson, M. E., Montoro Bustos, A. R., Murphy, K. E., Winchester, M. R. & Vega Baudrit, J. R. (2017) Silver Nanoparticles: Technological Advances, Societal Impacts, and Metrological Challenges. *Frontiers in Chemistry*, 5(6).

Carrassi, A., Bocquet, M., Bertino, L. & Evensen, G. (2018) Data assimilation in the geosciences: An overview of methods, issues, and perspectives. *WIREs Climate Change*, 9(5), e535.

Chandhru, M., Logesh, R., Rani, S. K., Ahmed, N. & Vasimalai, N. (2019) One-pot green route synthesis of silver nanoparticles from jack fruit seeds and their antibacterial activities with escherichia coli and salmonella bacteria. *Biocatalysis and Agricultural Biotechnology*, 20, 101241.

Chen, X. & Lv, H. (2022) Intelligent control of nanoparticle synthesis on microfluidic chips with machine learning. *NPG Asia Materials*, 14(1), 69.

Chen, Y.-H. & Yeh, C.-S. (2002) Laser ablation method: use of surfactants to form the dispersed Ag nanoparticles. *Colloids and Surfaces A: Physicochemical and Engineering Aspects*, 197(1), 133-139.

Cheng, C. L., Shalabh & Garg, G. (2014) Coefficient of determination for multiple measurement error models. *Journal of Multivariate Analysis*, 126, 137-152.

Cheng, S., Jin, Y., Harrison, S. P., Quilodrán-Casas, C., Prentice, I. C., Yi-Ke, G. & Arcucci, R. (2022a) Parameter Flexible Wildfire Prediction Using Machine Learning Techniques: Forward and Inverse Modelling. *Remote Sensing*, 14(13), 3228.

Cheng, S., Prentice, I. C., Huang, Y., Jin, Y., Guo, Y.-K. & Arcucci, R. (2022b) Data-driven surrogate model with latent data assimilation: Application to wildfire forecasting. *Journal of computational physics*, 464, 111302.

Cheng, S., Quilodrán-Casas, C., Ouala, S., Farchi, A., Liu, C., Tandeo, P., Fablet, R., Lucor, D., Iooss, B., Brajard, J., Xiao, D., Janjic, T., Ding, W., Guo, Y., Carrassi, A., Bocquet, M. & Arcucci, R. (2023) Machine Learning With Data Assimilation and Uncertainty Quantification for Dynamical Systems: A Review. *IEEE/CAA Journal of Automatica Sinica*, 10(6), 1361-1387.

Chhabra, R. & Basavaraj, M. G. (eds) (2019) *Coulson and Richardson's Chemical Engineering, Volume 2A - Particulate Systems and Particle Technology (6th Edition)*Elsevier.

Chicco, D., Warrens, M. J. & Jurman, G. (2021) The coefficient of determination R-squared is more informative than SMAPE, MAE, MAPE, MSE and RMSE in regression analysis evaluation. *PeerJ Comput Sci*, 7, e623.

Chicea, D., Nicolae-Maranciuc, A., Doroshkevich, A. S., Chicea, L. M. & Ozkendir, O. M. (2023) Comparative Synthesis of Silver Nanoparticles: Evaluation of Chemical Reduction Procedures, AFM and DLS Size Analysis. *Materials (Basel)*, 16(15), 5244.

Cho, Y. K., Leite, F., Behzadan, A. & Wang, C. (2019) *Computing in Civil Engineering 2019: Data, Sensing, and Analytics*. Reston: Reston: American Society of Civil Engineers.

Chutrakulwong, F., Thamaphat, K., Tantipaibulvut, S. & Limsuwan, P. (2020) In Situ Deposition of Green Silver Nanoparticles on Urinary Catheters under Photo-Irradiation for Antibacterial Properties. *Processes*, 8(12), 1630.

Claeskens, G. & Hjort, N. L. (2008) *Model Selection and Model Averaging*. Cambridge: Cambridge University Press.

Cruz, D., Falé, P. L., Mourato, A., Vaz, P. D., Luisa Serralheiro, M. & Lino, A. R. L. (2010) Preparation and physicochemical characterization of Ag nanoparticles biosynthesized by Lippia citriodora (Lemon Verbena). *Colloids and Surfaces B: Biointerfaces*, 81(1), 67-73.

Curd, E. F., Railio, J., Gustavsson, J. A. N., Hogeling, J., Assad, M. E. H., Emilsen, J. A. N., Mazzacane, S. & Wiksten, R. (2001) 9 - AIR-HANDLING PROCESSES, in Goodfellow, H. & Tähti, E. (eds), *Industrial Ventilation Design Guidebook*. San Diego: Academic Press, 677-806.

Cushman-Roisin, B. & Beckers, J.-M. (2011) Chapter 22 - Data Assimilation, in Cushman-Roisin, B. & Beckers, J.-M. (eds), *International Geophysics*Academic Press, 725-760.

Dantas, K. N. M., Andrade, L. R., Lisboa, E., Santana, V. L., Santos, A. L. S., Mello, T. P., Sangenito, L. S., Lima, Á. S., Fricks, A. T., Begnami, A. F., Cano, A., Zielinska, A., Soares, C. M. F., Souto, E. B. & Severino, P. (2021) Antimycotic nail polish based on humic acid-coated silver nanoparticles for onychomycosis. *Journal of Chemical Technology & Biotechnology*, 96(8), 2208-2218.

Das, A. K. & Dewanjee, S. (2018) Chapter 3 - Optimization of Extraction Using Mathematical Models and Computation, in Sarker, S. D. & Nahar, L. (eds), *Computational Phytochemistry*Elsevier, 75-106.

Das, S., Bandyopadhyay, K. & Ghosh, M. M. (2021) Effect of stabilizer concentration on the size of silver nanoparticles synthesized through chemical route. *Inorganic Chemistry Communications*, 123, 108319.

Dash, R. & Dash, P. K. (2017) Chapter 25 - MDHS–LPNN: A Hybrid FOREX Predictor Model Using a Legendre Polynomial Neural Network with a Modified Differential Harmony

Search Technique, in Samui, P., Sekhar, S. & Balas, V. E. (eds), *Handbook of Neural Computation*Academic Press, 459-486.

De Leersnyder, I., De Gelder, L., Van Driessche, I. & Vermeir, P. (2019) Revealing the Importance of Aging, Environment, Size and Stabilization Mechanisms on the Stability of Metal Nanoparticles: A Case Study for Silver Nanoparticles in a Minimally Defined and Complex Undefined Bacterial Growth Medium. *Nanomaterials (Basel, Switzerland)*, 9(12), 1684.

Demchenko, V., Riabov, S., Kobylinskyi, S., Goncharenko, L., Rybalchenko, N., Kruk, A., Moskalenko, O. & Shut, M. (2020) Effect of the type of reducing agents of silver ions in interpolyelectrolyte-metal complexes on the structure, morphology and properties of silver-containing nanocomposites. *Scientific Reports*, 10(1), 7126.

Deshmukh, P. S. B. a. R. (2022) Microfluidic Devices Market Research, 2031. Available online: https://www.alliedmarketresearch.com/microfluidic-devices-market-A17085 [Accessed 19/07/2024].

Deutsch, J. L. & Deutsch, C. V. (2012) Latin hypercube sampling with multidimensional uniformity. *Journal of Statistical Planning and Inference*, 142(3), 763-772.

Dong, X.-Y., Gao, Z.-W., Yang, K.-F., Zhang, W.-Q. & Xu, L.-W. (2015) Nanosilver as a new generation of silver catalysts in organic transformations for efficient synthesis of fine chemicals. *Catalysis Science & Technology*, 5(5), 2554-2574.

Dong, X., Ji, X., Wu, H., Zhao, L., Li, J. & Yang, W. (2009) Shape Control of Silver Nanoparticles by Stepwise Citrate Reduction. *The Journal of Physical Chemistry C*, 113(16), 6573-6576.

Dung, C. T., Loc, n. Q., Huong, P. T., Duong, D. T. T., Hong, T. T., Quynh, L. M. & Nam, N. H. (2014) Combination of 4-ATP Coated Silver Nanoparticles and Magnetic Fe3O4 Nanoparticles by Inverse Emulsion Method. *VNU Journal of Science: Mathematics - Physics*, 30(2), 1-9.

Durakovic, B. (2017) Design of experiments application, concepts, examples: State of the art. *Periodicals of Engineering and Natural Sciences (PEN)*, 5(3), 421-439.

Echeverría, J. C., Moriones, P., Garrido, J. J., Ugarte, M. D., Cervera, L., Garaio, E., Gómez-Polo, C. & Pérez-Landazábal, J. I. (2021) Steering the synthesis of Fe3O4 nanoparticles under sonication by using a fractional factorial design. *Materials Chemistry and Physics*, 270, 124760.

Eckert, C. A. & Trinh, C. T. (2016) *Biotechnology for biofuel production and optimization / edited by Carrie Eckert, Cong Trinh* Amsterdam : Elsevier, 2016.

Eid, M. M. (2022) Characterization of Nanoparticles by FTIR and FTIR-Microscopy, in Mallakpour, S. & Hussain, C. M. (eds), *Handbook of Consumer Nanoproducts*. Singapore: Springer Nature Singapore, 645-673.

El-Khatib, A. M., Badawi, M. S., Ghatass, Z. F., Mohamed, M. M. & Elkhatib, M. (2018) Synthesize of Silver Nanoparticles by Arc Discharge Method Using Two Different Rotational Electrode Shapes. *Journal of Cluster Science*, 29(6), 1169-1175.

El Badawy, A. M., Scheckel, K. G., Suidan, M. & Tolaymat, T. (2012) The impact of stabilization mechanism on the aggregation kinetics of silver nanoparticles. *Science of The Total Environment*, 429, 325-331.

Elamawi, R. M., Al-Harbi, R. E. & Hendi, A. A. (2018) Biosynthesis and characterization of silver nanoparticles using Trichoderma longibrachiatum and their effect on phytopathogenic fungi. *Egyptian Journal of Biological Pest Control*, 28(1), 28.

Elechiguerra, J. L., Burt, J. L., Morones, J. R., Camacho-Bragado, A., Gao, X., Lara, H. H. & Yacaman, M. J. (2005) Interaction of silver nanoparticles with HIV-1. *Journal of Nanobiotechnology*, 3(1), 6.

Encina-Zelada, C. R., Cadavez, V., Teixeira, J. A. & Gonzales-Barron, U. (2019) Optimization of Quality Properties of Gluten-Free Bread by a Mixture Design of Xanthan, Guar, and Hydroxypropyl Methyl Cellulose Gums. *Foods*, 8(5), 156.

Epp, J. (2016) 4 - X-ray diffraction (XRD) techniques for materials characterization, in Hübschen, G., Altpeter, I., Tschuncky, R. & Herrmann, H.-G. (eds), *Materials Characterization Using Nondestructive Evaluation (NDE) Methods*Woodhead Publishing, 81-124.

Ezekiel, M. (1930) *Methods of correlation analysis*. Oxford, England: Wiley.

Feng, A., Hou, S., Yan, J., Wu, Q., Tang, Y., Yang, Y., Shi, J., Xiao, Z.-Y., Lambert, C. J., Zheng, N. & Hong, W. (2022) Conductance Growth of Single-Cluster Junctions with Increasing Sizes. *Journal of the American Chemical Society*, 144(34), 15680-15688.

Feng, X., Ruan, F., Hong, R., Ye, J., Hu, J., Hu, G. & Yang, Z. (2011) Synthetically Directed Self-Assembly and Enhanced Surface-Enhanced Raman Scattering Property of Twinned Crystalline Ag/Ag Homojunction Nanoparticles. *Langmuir*, 27(6), 2204-2210.

Fernández, J. G., Fernández-Baldo, M. A., Berni, E., Camí, G., Durán, N., Raba, J. & Sanz, M. I. (2016) Production of silver nanoparticles using yeasts and evaluation of their

antifungal activity against phytopathogenic fungi. *Process Biochemistry*, 51(9), 1306-1313.

Findlay, M. R., Freitas, D. N., Mobed-Miremadi, M. & Wheeler, K. E. (2018) Machine learning provides predictive analysis into silver nanoparticle protein corona formation from physicochemical properties. *Environmental Science: Nano*, 5(1), 64-71.

Fisher, M., Leutbecher, M. & Kelly, G. A. (2005) On the equivalence between Kalman smoothing and weak-constraint four-dimensional variational data assimilation. *Quarterly Journal of the Royal Meteorological Society*, 131(613), 3235-3246.

Fisher, R. A. (1922) The Goodness of Fit of Regression Formulae, and the Distribution of Regression Coefficients. *Journal of the Royal Statistical Society*, 85(4), 597-612.

Fissan, H., Ristig, S., Kaminski, H., Asbach, C. & Epple, M. (2014) Comparison of different characterization methods for nanoparticle dispersions before and after aerosolization. *Analytical Methods*, 6(18), 7324-7334.

Gao, Y. & Torrente-Murciano, L. (2020) Mechanistic insights of the reduction of gold salts in the Turkevich protocol. *Nanoscale*, 12(4), 2740-2751.

Ge, L., Li, Q., Wang, M., Ouyang, J., Li, X. & Xing, M. M. Q. (2014) Nanosilver particles in medical applications: synthesis, performance, and toxicity. *International journal of nanomedicine*, 9, 2399-2407.

Ghil, M. & Malanotte-Rizzoli, P. (1991) Data Assimilation in Meteorology and Oceanography, in Dmowska, R. & Saltzman, B. (eds), *Advances in Geophysics*Elsevier, 141-266.

Gilpin, L. H., Bau, D., Yuan, B. Z., Bajwa, A., Specter, M. & Kagal, L. (2018) Explaining Explanations: An Overview of Interpretability of Machine Learning, *2018 IEEE 5th*

International Conference on Data Science and Advanced Analytics (DSAA). 1-3 Oct. 2018.

Gioria, E., Signorini, C., Wisniewski, F. & Gutierrez, L. (2020) Green synthesis of time-stable palladium nanoparticles using microfluidic devices. *Journal of Environmental Chemical Engineering*, 8(5), 104096.

Glushko, V. N., Sadovskaya, N. Y., Usova, O. A., Blokhina, L. I. & Kozhukhov, V. I. (2015) Features of Obtaining Silver Nanoparticles in Non-Aqueos Media by Reduction of Silver Trifluoroacetate. *Oriental Journal of Chemistry*, 31(4), 2515-2520.

Gong, H., Cheng, S., Chen, Z., Li, Q., Quilodrán-Casas, C., Xiao, D. & Arcucci, R. (2022) An efficient digital twin based on machine learning SVD autoencoder and generalised latent assimilation for nuclear reactor physics. *Annals of nuclear energy*, 179, 109431.

Gong, H., Yu, Y., Li, Q. & Quan, C. (2020) An inverse-distance-based fitting term for 3D-Var data assimilation in nuclear core simulation. *Annals of nuclear energy*, 141, 107346.

Guerrini, L., Alvarez-Puebla, R. A. & Pazos-Perez, N. (2018) Surface Modifications of Nanoparticles for Stability in Biological Fluids. *Materials*, 11(7), 1154.

Halder, S., Ahmed, A. N., Gafur, M. A., Seong, G. & Hossain, M. Z. (2021) Size-Controlled Facile Synthesis of Silver Nanoparticles by Chemical Reduction Method and Analysis of Their Antibacterial Performance. *ChemistrySelect*, 6(36), 9714-9720.

Harada, M., Saijo, K., Sakamoto, N. & Ito, K. (2010) Characterization of water/AOT/benzene microemulsions during photoreduction to produce silver particles. *J Colloid Interface Sci*, 343(2), 423-32.

Harned, H. S. & Hildreth, C. L. (1951) The Diffusion Coefficient of Silver Nitrate in Dilute Aqueous Solution at 25°. *Journal of the American Chemical Society*, 73(7), 3292-3293.

Hassan, S. A. (2020) Artificial neural networks for the inverse design of nanoparticles with preferential nano-bio behaviors. *J Chem Phys*, 153(5), 054102.

He, Y., Wei, F., Ma, Z., Zhang, H., Yang, Q., Yao, B., Huang, Z., Li, J., Zeng, C. & Zhang, Q. (2017) Green synthesis of silver nanoparticles using seed extract of Alpinia katsumadai, and their antioxidant, cytotoxicity, and antibacterial activities. *RSC Advances*, 7(63), 39842-39851.

Henglein, A. (1993) Physicochemical properties of small metal particles in solution: "microelectrode" reactions, chemisorption, composite metal particles, and the atom-to-metal transition. *The Journal of Physical Chemistry*, 97(21), 5457-5471.

Henglein, A. & Giersig, M. (1999) Formation of Colloidal Silver Nanoparticles: Capping Action of Citrate. *The Journal of Physical Chemistry B*, 103(44), 9533-9539.

Ho, H. M. K., Craig, D. Q. M. & Day, R. M. (2022) Design of Experiment Approach to Modeling the Effects of Formulation and Drug Loading on the Structure and Properties of Therapeutic Nanogels. *Molecular Pharmaceutics*, 19(2), 602-615.

Hosseinpour-Mashkani, S. M. & Ramezani, M. (2014) Silver and silver oxide nanoparticles: Synthesis and characterization by thermal decomposition. *Materials Letters*, 130, 259-262.

Hrvat, F., Aleta, A., Džuho, A., Hasanić, O. & Spahić Bećirović, L. (2021) Artificial Intelligence in Nanotechnology: Recent Trends, Challenges and Future Perspectives, *CMBEBIH 2021*. Cham, 2021//. Springer International Publishing.

Huang, J., Li, Q., Sun, D., Lu, Y., Su, Y., Yang, X., Wang, H., Wang, Y., Shao, W., He, N., Hong, J. & Chen, C. (2007) Biosynthesis of silver and gold nanoparticles by novel sundriedCinnamomum camphoraleaf. *Nanotechnology*, 18(10), 105104.

Huberty, C. J. & Mourad, S. A. (1980) Estimation in Multiple Correlation/Prediction. *Educational and Psychological Measurement*, 40(1), 101-112.

Huff, C., Long, J. M. & Abdel-Fattah, T. M. (2020) Beta-Cyclodextrin-Assisted Synthesis of Silver Nanoparticle Network and Its Application in a Hydrogen Generation Reaction. *Catalysts*, 10(9), 1014.

Huntington, D. E. & Lyrintzis, C. S. (1998) Improvements to and limitations of Latin hypercube sampling. *Probabilistic Engineering Mechanics*, 13(4), 245-253.

Iashchishyn, I. A., Sulskis, D., Nguyen Ngoc, M., Smirnovas, V. & Morozova-Roche, L. A. (2017) Finke–Watzky Two-Step Nucleation–Autocatalysis Model of S100A9 Amyloid Formation: Protein Misfolding as “Nucleation” Event. *ACS Chemical Neuroscience*, 8(10), 2152-2158.

Inkson, B. J. (2016) 2 - Scanning electron microscopy (SEM) and transmission electron microscopy (TEM) for materials characterization, in Hübschen, G., Altpeter, I., Tschuncky, R. & Herrmann, H.-G. (eds), *Materials Characterization Using Nondestructive Evaluation (NDE) Methods*Woodhead Publishing, 17-43.

Iwamoto, M., Kuroda, K., Kanzow, J., Hayashi, S. & Faupel, F. (2005) Size evolution effect of the reduction rate on the synthesis of gold nanoparticles. *Advanced Powder Technology*, 16(2), 137-144.

Izak-Nau, E., Huk, A., Reidy, B., Uggerud, H., Vadset, M., Eiden, S., Voetz, M., Himly, M., Duschl, A., Dusinska, M. & Lynch, I. (2015) Impact of storage conditions and storage time on silver nanoparticles' physicochemical properties and implications for their biological effects. *RSC Advances*, 5(102), 84172-84185.

Jana, N. R. & Peng, X. (2003) Single-Phase and Gram-Scale Routes toward Nearly Monodisperse Au and Other Noble Metal Nanocrystals. *Journal of the American Chemical Society*, 125(47), 14280-14281.

Jebakumar Immanuel Edison, T. N. & Sethuraman, M. G. (2013) Electrocatalytic Reduction of Benzyl Chloride by Green Synthesized Silver Nanoparticles Using Pod Extract of Acacia nilotica. *ACS Sustainable Chemistry & Engineering*, 1(10), 1326-1332.

Jebril, S., Khanfir Ben Jenana, R. & Dridi, C. (2020) Green synthesis of silver nanoparticles using Melia azedarach leaf extract and their antifungal activities: In vitro and in vivo. *Materials Chemistry and Physics*, 248, 122898.

Jung, J. H., Cheol Oh, H., Soo Noh, H., Ji, J. H. & Soo Kim, S. (2006) Metal nanoparticle generation using a small ceramic heater with a local heating area. *Journal of Aerosol Science*, 37(12), 1662-1670.

Kania, D., Yunus, R., Omar, R., Abdul Rashid, S. & Mohamed Jan, B. (2021) Rheological investigation of synthetic-based drilling fluid containing non-ionic surfactant pentaerythritol ester using full factorial design. *Colloids and Surfaces A: Physicochemical and Engineering Aspects*, 625, 126700.

Kašpar, O., Koyuncu, A. H., Pittermannová, A., Ulbrich, P. & Tokárová, V. (2019) Governing factors for preparation of silver nanoparticles using droplet-based microfluidic device. *Biomedical Microdevices*, 21(4), 88.

Kathiravan, V., Ravi, S. & Ashokkumar, S. (2014) Synthesis of silver nanoparticles from Melia dubia leaf extract and their in vitro anticancer activity. *Spectrochim Acta A Mol Biomol Spectrosc*, 130, 116-21.

Kaviya, S., Santhanalakshmi, J., Viswanathan, B., Muthumary, J. & Srinivasan, K. (2011) Biosynthesis of silver nanoparticles using citrus sinensis peel extract and its antibacterial activity. *Spectrochimica Acta Part A: Molecular and Biomolecular Spectroscopy*, 79(3), 594-598.

Khan, S. A., Günther, A., Schmidt, M. A. & Jensen, K. F. (2004) Microfluidic Synthesis of Colloidal Silica. *Langmuir*, 20(20), 8604-8611.

Khan, Z., Al-Thabaiti, S. A., Obaid, A. Y. & Al-Youbi, A. O. (2011) Preparation and characterization of silver nanoparticles by chemical reduction method. *Colloids and Surfaces B: Biointerfaces*, 82(2), 513-517.

Khatoon, U. T., Nageswara Rao, G. V. S., Mohan, K. M., Ramanaviciene, A. & Ramanavicius, A. (2017) Antibacterial and antifungal activity of silver nanospheres synthesized by tri-sodium citrate assisted chemical approach. *Vacuum*, 146, 259-265.

Kim, D., Jeong, S. & Moon, J. (2006) Synthesis of silver nanoparticles using the polyol process and the influence of precursor injection. *Nanotechnology*, 17(16), 4019-4024.

Kim, Y., Lee Chung, B., Ma, M., Mulder, W. J., Fayad, Z. A., Farokhzad, O. C. & Langer, R. (2012) Mass production and size control of lipid-polymer hybrid nanoparticles through controlled microvortices. *Nano Lett*, 12(7), 3587-91.

King, B. M. (2010) Analysis of Variance, in Peterson, P., Baker, E. & McGaw, B. (eds), *International Encyclopedia of Education (Third Edition)*. Oxford: Elsevier, 32-36.

Kisyelova, T., Novruzova, A., Hajiyeva, F., Ramazanov, M. & Chianese, A. (2016) Effect of the reactor configuration on the production of silver nanoparticles. AIDIC Servizi S.r.l.

KoÇak Ç, C., Süleyman, K., KarabİberoĞlu, Ş. & Dursun, Z. (2020) Highly improved electrocatalytic oxidation of dimethylamine borane on silver nanoparticles modified polymer composite electrode. *Turk J Chem*, 44(1), 125-141.

Kora, A. J., Manjusha, R. & Arunachalam, J. (2009) Superior bactericidal activity of SDS capped silver nanoparticles: Synthesis and characterization. *Materials Science and Engineering: C*, 29(7), 2104-2109.

Kostigen Mumper, C., Ostermeyer, A.-K., Semprini, L. & Radniecki, T. S. (2013) Influence of ammonia on silver nanoparticle dissolution and toxicity to Nitrosomonas europaea. *Chemosphere*, 93(10), 2493-2498.

Kovalchuk, N. M., Roumpea, E., Nowak, E., Chinaud, M., Angeli, P. & Simmons, M. J. H. (2018) Effect of surfactant on emulsification in microchannels. *Chemical Engineering Science*, 176, 139-152.

Kovalchuk, N. M., Sagisaka, M., Steponavicius, K., Vigolo, D. & Simmons, M. J. H. (2019) Drop formation in microfluidic cross-junction: jetting to dripping to jetting transition. *Microfluidics and Nanofluidics*, 23(8), 103.

Krajczewski, J., Kołątaj, K. & Kudelski, A. (2017) Plasmonic nanoparticles in chemical analysis. *RSC Advances*, 7(28), 17559-17576.

Krishna, D. N. G. & Philip, J. (2022) Review on surface-characterization applications of X-ray photoelectron spectroscopy (XPS): Recent developments and challenges. *Applied Surface Science Advances*, 12, 100332.

Kumar, S. & Ganesan, S. (2017) Numerical simulation of nanocrystal synthesis in a microfluidic reactor. *Computers and Chemical Engineering*, 96, 128-138.

Kyrychenko, A., Pasko, D. A. & Kalugin, O. N. (2017) Poly(vinyl alcohol) as a water protecting agent for silver nanoparticles: the role of polymer size and structure. *Physical Chemistry Chemical Physics.*

Kytsya, A., Bazylyak, L., Hrynda, Y., Horechyy, A. & Medvedevdkikh, Y. (2015) The Kinetic Rate Law for the Autocatalytic Growth of Citrate-Stabilized Silver Nanoparticles. *International Journal of Chemical Kinetics*, 47(6), 351-360.

La Spina, R., Mehn, D., Fumagalli, F., Holland, M., Reniero, F., Rossi, F. & Gilliland, D. (2020) Synthesis of Citrate-Stabilized Silver Nanoparticles Modified by Thermal and pH Preconditioned Tannic Acid. *Nanomaterials*, 10(10), 2031.

LaMer, V. K. & Dinegar, R. H. (1950) Theory, Production and Mechanism of Formation of Monodispersed Hydrosols. *Journal of the American Chemical Society*, 72(11), 4847-4854.

Lane, T. P. & DuMouchel, W. H. (1994) Simultaneous Confidence Intervals in Multiple Regression. *The American Statistician*, 48(4), 315-321.

Lazarus, L. L., Riche, C. T., Marin, B. C., Gupta, M., Malmstadt, N. & Brutchey, R. L. (2012) Two-Phase Microfluidic Droplet Flows of Ionic Liquids for the Synthesis of Gold and Silver Nanoparticles. *ACS Applied Materials & Interfaces*, 4(6), 3077-3083.

LeCun, Y., Bengio, Y. & Hinton, G. (2015) Deep learning. *Nature*, 521(7553), 436-444.

Lee, K. J., Jun, B. H., Kim, T. H. & Joung, J. (2006) Direct synthesis and inkjetting of silver nanocrystals toward printed electronics. *Nanotechnology*, 17(9), 2424-2428.

Silver nanoparticles: Synthesis and application for nanomedicine 2019 MDPI AG.

Li, C.-Q. & Yang, W. (2023) 2 - Essential reliability methods, in Li, C.-Q. & Yang, W. (eds), *Time-Dependent Reliability Theory and Its Applications*Woodhead Publishing, 51-119.

Li, K., Jia, X., Tang, A., Zhu, X., Meng, H. & Wang, Y. (2012) Preparation of Spherical and Triangular Silver Nanoparticles by a Convenient Method. *Integrated Ferroelectrics*, 136(1), 9-14.

Liang, Y. & Wen, Z. (2014) 18 - Bio-based nutraceuticals from biorefining, in Waldron, K. (ed), *Advances in Biorefineries*Woodhead Publishing, 596-623.

Lifshitz, I. M. & Slyozov, V. V. (1961) The kinetics of precipitation from supersaturated solid solutions. *Journal of Physics and Chemistry of Solids*, 19(1), 35-50.

Lin, X. Z., Teng, X. & Yang, H. (2003) Direct Synthesis of Narrowly Dispersed Silver Nanoparticles Using a Single-Source Precursor. *Langmuir*, 19(24), 10081-10085.

Lin, X. Z., Terepka, A. D. & Yang, H. (2004) Synthesis of Silver Nanoparticles in a Continuous Flow Tubular Microreactor. *Nano Letters*, 4(11), 2227-2232.

Ling, F. W. M., Abdulbari, H. A. & Sim-Yee, C. (2022) Effect of residence time on the morphology of silica nanoparticles synthesized in a microfluidic reactor. *Journal of Flow Chemistry*, 12(1), 17-30.

Liu, F., Kozlovskaya, V., Zavgorodnya, O., Martinez-Lopez, C., Catledge, S. & Kharlampieva, E. (2014a) Encapsulation of anticancer drug by hydrogen-bonded multilayers of tannic acid. *Soft Matter*, 10(46), 9237-9247.

Liu, G., Ma, X., Sun, X., Jia, Y. & Wang, T. (2018a) Controllable Synthesis of Silver Nanoparticles Using Three-Phase Flow Pulsating Mixing Microfluidic Chip. *Advances in Materials Science and Engineering*, 2018, 14.

Liu, H., Li, J., Sun, D., Odoom-Wubah, T., Huang, J. & Li, Q. (2014b) Modeling of Silver Nanoparticle Formation in a Microreactor: Reaction Kinetics Coupled with Population Balance Model and Fluid Dynamics. *Industrial & Engineering Chemistry Research.*

Liu, H., Lu, M., Zhu, M., Zhang, H., Zhao, K., Wang, J. & Wei, J. (2018b) Continuous biosynthesis of silver nanoparticles in a hydrodynamic cavitation device and modeling of the process by numerical simulation strategy. *Journal of Nanoparticle Research*, 20(9), 8.

Liu, H., Zhang, H., Wang, J. & Wei, J. (2020) Effect of temperature on the size of biosynthesized silver nanoparticle: Deep insight into microscopic kinetics analysis. *Arabian Journal of Chemistry*, 13(1), 1011-1019.

Liu, L., Zhang, Z., Cao, L., Xiong, Z., Tang, Y. & Pan, Y. (2021) Cytotoxicity of phytosynthesized silver nanoparticles: A meta-analysis by machine learning algorithms. *Sustainable Chemistry and Pharmacy*, 21, 100425.

Loiseau, A., Asila, V., Boitel-Aullen, G., Lam, M., Salmain, M. & Boujday, S. (2019) Silver-Based Plasmonic Nanoparticles for and Their Use in Biosensing. *Biosensors (Basel)*, 9(2), 78.

Lu, H., Wang, H., Liu, Y., Wang, M., Hu, J. & Yang, Q. (2020) Substance transfer behavior controlled by droplet internal circulation. *Chemical Engineering Journal*, 393, 124657.

Lu, L., Sun, R. W., Chen, R., Hui, C. K., Ho, C. M., Luk, J. M., Lau, G. K. & Che, C. M. (2008) Silver nanoparticles inhibit hepatitis B virus replication. *Antivir Ther*, 13(2), 253-62.

Luty-Błocho, M., Wojnicki, M. & Fitzner, K. (2017) Gold Nanoparticles Formation via Au(III) Complex Ions Reduction with l-Ascorbic Acid. *International Journal of Chemical Kinetics*, 49(11), 789-797.

Ma, L., Hu, K., Wang, C., Yang, J. Y. & Liu, L. (2021) Prediction and Inverse Design of Structural Colors of Nanoparticle Systems via Deep Neural Network. *Nanomaterials (Basel)*, 11(12), 3339.

Ma, W., Cheng, F. & Liu, Y. (2018) Deep-Learning-Enabled On-Demand Design of Chiral Metamaterials. *ACS Nano*, 12(6), 6326-6334.

Madadelahi, M. & Shamloo, A. (2017) Droplet-based flows in serpentine microchannels: Chemical reactions and secondary flows. *International Journal of Multiphase Flow*, 97, 186-196.

Magdassi, S., Grouchko, M., Berezin, O. & Kamyshny, A. (2010) Triggering the Sintering of Silver Nanoparticles at Room Temperature. *ACS Nano*, 4(4), 1943-1948.

Magee, L. (1990) R² Measures Based on Wald and Likelihood Ratio Joint Significance Tests. *The American Statistician*, 44(3), 250-253.

Makgwane, P. R. & Ray, S. S. (2014) Synthesis of nanomaterials by continuous-flow microfluidics: a review. *J Nanosci Nanotechnol*, 14(2), 1338-63.

Manikprabhu, D. & Lingappa, K. (2013) Microwave Assisted Rapid and Green Synthesis of Silver Nanoparticles Using a Pigment Produced by Streptomyces coelicolor klmp33. *Bioinorganic Chemistry and Applications*, 2013, 341798.

Manojkumar, K., Sivaramakrishna, A. & Vijayakrishna, K. (2016) A short review on stable metal nanoparticles using ionic liquids, supported ionic liquids, and poly(ionic liquids). *Journal of Nanoparticle Research*, 18(4), 103.

Mansour, M., Thévenin, D., Nigam, K. D. P. & Zähringer, K. (2019) Generally-valid optimal Reynolds and Dean numbers for efficient liquid-liquid mixing in helical pipes. *Chemical Engineering Science*, 201, 382-385.

Mansouri, S. S. & Ghader, S. (2009) Experimental study on effect of different parameters on size and shape of triangular silver nanoparticles prepared by a simple and rapid method in aqueous solution. *Arabian Journal of Chemistry*, 2(1), 47-53.

Marciniak, L., Nowak, M., Trojanowska, A., Tylkowski, B. & Jastrzab, R. (2020) The Effect of pH on the Size of Silver Nanoparticles Obtained in the Reduction Reaction with Citric and Malic Acids. *Materials*, 13(23), 5444.

Martinez-Duarte, R. & Madou, M. (2010) SU-8 Photolithography and Its Impact on Microfluidics, *Microfluidics and Nanofluidics Handbook: Fabrication, Implementation and Applications*, 1st editionCRC PressEditors: Suman Chrakaborty, Sushanta K. Mitra, 231-268.

Mason, R. L., Gunst, R. F. & Hess, J. L. (2003) *Statistical design and analysis of experiments: with applications to engineering and science*, 2nd ed. edition. Wiley.

Masum, M. M. I., Siddiqa, M. M., Ali, K. A., Zhang, Y., Abdallah, Y., Ibrahim, E., Qiu, W., Yan, C. & Li, B. (2019) Biogenic Synthesis of Silver Nanoparticles Using Phyllanthus emblica Fruit Extract and Its Inhibitory Action Against the Pathogen Acidovorax oryzae Strain RS-2 of Rice Bacterial Brown Stripe. *Frontiers in Microbiology*, 10(820).

Mathews, P. G. (2005) *Design of Experiments with MINITAB* American Society for Quality (ASQ).

Mbanga, O., Cukrowska, E. & Gulumian, M. (2022) Dissolution kinetics of silver nanoparticles: Behaviour in simulated biological fluids and synthetic environmental media. *Toxicology Reports*, 9, 788-796.

McKay, M. D., Beckman, R. J. & Conover, W. J. (1979) Comparison of three methods for selecting values of input variables in the analysis of output from a computer code. *Technometrics*, 21(2), 239-245.

Mekki-Berrada, F., Ren, Z., Huang, T., Wong, W. K., Zheng, F., Xie, J., Tian, I. P. S., Jayavelu, S., Mahfoud, Z., Bash, D., Hippalgaonkar, K., Khan, S., Buonassisi, T., Li, Q. &

Wang, X. (2021) Two-step machine learning enables optimized nanoparticle synthesis. *npj Computational Materials*, 7(1), 55.

Milek, T. & Zahn, D. (2014) Molecular simulation of Ag nanoparticle nucleation from solution: Redox-reactions direct the evolution of shape and structure. *Nano Letters*, 14(8), 4913–4917.

Mondal, B., Pati, S. & Patowari, P. (2019) Analysis of mixing performances in microchannel with obstacles of different aspect ratios. *Proceedings of the Institution of Mechanical Engineers, Part E: Journal of Process Mechanical Engineering*, 233(5), 1045-1051.

Montgomery, D. C. (2013) *Design and analysis of experiments / Douglas C. Montgomery*, Eighth edition. edition. Hoboken, NJ : John Wiley and Sons, Incorporated, 2013.

Morales, M. C. & Zahn, J. D. (2010) Droplet enhanced microfluidic-based DNA purification from bacterial lysates via phenol extraction. *Microfluidics and Nanofluidics*, 9(6), 1041-1049.

Mozaffari, S., Li, W., Thompson, C., Ivanov, S., Seifert, S., Lee, B., Kovarik, L. & Karim, A. M. (2017) Colloidal nanoparticle size control: experimental and kinetic modeling investigation of the ligand–metal binding role in controlling the nucleation and growth kinetics. *Nanoscale*, 9(36), 13772-13785.

Mukherji, S., Bharti, S., Shukla, G. & Mukherji, S. (2019) Synthesis and characterization of size- and shape-controlled silver nanoparticles. *Physical Sciences Reviews*, 4(1), 82.

Myles, A. J., Feudale, R. N., Liu, Y., Woody, N. A. & Brown, S. D. (2004) An introduction to decision tree modeling. *Journal of Chemometrics*, 18(6), 275-285.

Nadagouda, M. N. & Varma, R. S. (2008) Green synthesis of silver and palladium nanoparticles at room temperature using coffee and tea extract. *Green Chemistry*, 10(8), 859-862.

Nagarajan, R. (2008) Nanoparticles: Building Blocks for Nanotechnology, *Nanoparticles: Synthesis, Stabilization, Passivation, and Functionalization*. ACS Symposium SeriesAmerican Chemical Society, 2-14.

Nakamura, T., Magara, H., Herbani, Y. & Sato, S. (2011) Fabrication of silver nanoparticles by highly intense laser irradiation of aqueous solution. *Applied Physics A: Materials Science & Processing*, 104, 1021-1024.

Nakano, M., Fujiwara, T. & Koga, N. (2016) Thermal Decomposition of Silver Acetate: Physico-Geometrical Kinetic Features and Formation of Silver Nanoparticles. *The Journal of Physical Chemistry C*, 120(16), 8841-8854.

Natekin, A. & Knoll, A. (2013) Gradient boosting machines, a tutorial. *Front Neurorobot*, 7, 21.

Nathanael, K., Cheng, S., Kovalchuk, N. M., Arcucci, R. & Simmons, M. J. H. (2023a) Optimization of microfluidic synthesis of silver nanoparticles: A generic approach using machine learning. *Chemical Engineering Research and Design*, 193, 65-74.

Nathanael, K., Galvanin, F., Kovalchuk, N. M. & Simmons, M. J. H. (2023b) Development of a predictive response surface model for size of silver nanoparticles synthesized in a T-junction microfluidic device. *Chemical Engineering Science*, 279, 118907.

Nathanael, K., Pico, P., Kovalchuk, N. M., Lavino, A. D., Simmons, M. J. H. & Matar, O. K. (2022) Computational modelling and microfluidics as emerging approaches to synthesis of silver nanoparticles – A review. *Chemical Engineering Journal*, 436, 135178.

Navaladian, S., Viswanathan, B., Viswanath, R. & Varadarajan, T. (2006) Thermal decomposition as route for silver nanoparticles. *Nanoscale Res Lett*, 2(1), 44-8.

Navlani, A., Fandango, A. & Idris, I. (2021) Python Data Analysis (3rd Edition). Packt Publishing.

Newswire, P. R. (2020) Silver Nanoparticles Market to Garner $4.1 Billion, Globally, By 2027 at 15.7% CAGR, Says Allied Market Research. *AlliedMarketResearch*. Available online: https://search.ebscohost.com/login.aspx?direct=true&db=bwh&AN=202010260940PR.NEWS.USPR.IO70096&site=ehost-live [Accessed 12/11/2021].

Ng, C. M., Chen, P. C. & Manickam, S. (2012) Green High-Gravitational Synthesis of Silver Nanoparticles Using a Rotating Packed Bed Reactor (RPBR). *Industrial & Engineering Chemistry Research*, 51(15), 5375-5381.

Niculescu, A. G., Chircov, C., Bîrcă, A. C. & Grumezescu, A. M. (2021) Fabrication and Applications of Microfluidic Devices: A Review. *Int J Mol Sci*, 22(4), 2011.

Nivedita, N., Ligrani, P. & Papautsky, I. (2017) Dean Flow Dynamics in Low-Aspect Ratio Spiral Microchannels. *Scientific Reports*, 7(1), 44072.

Njagi, E. C., Huang, H., Stafford, L., Genuino, H., Galindo, H. M., Collins, J. B., Hoag, G. E. & Suib, S. L. (2011) Biosynthesis of Iron and Silver Nanoparticles at Room Temperature Using Aqueous Sorghum Bran Extracts. *Langmuir*, 27(1), 264-271.

Noronha, V. T., Paula, A. J., Durán, G., Galembeck, A., Cogo-Müller, K., Franz-Montan, M. & Durán, N. (2017) Silver nanoparticles in dentistry. *Dent Mater*, 33(10), 1110-1126.

Nourafkan, E., Gao, H., Hu, Z. & Wen, D. (2017) Formulation optimization of reverse microemulsions using design of experiments for nanoparticles synthesis. *Chemical Engineering Research and Design*, 125, 367-384.

Ohgita, T., Namba, N., Kono, H., Shimanouchi, T. & Saito, H. (2022) Mechanisms of enhanced aggregation and fibril formation of Parkinson's disease-related variants of α-synuclein. *Scientific Reports (Nature Publisher Group)*, 12(1), 6770.

Orsavova, J., Misurcova, L., Ambrozova, J. V., Vicha, R. & Mlcek, J. (2015) Fatty Acids Composition of Vegetable Oils and Its Contribution to Dietary Energy Intake and Dependence of Cardiovascular Mortality on Dietary Intake of Fatty Acids. *International Journal of Molecular Sciences*, 16(6), 12871-12890. Available online: [Accessed.

Osawa, R. & Walsh, T. P. (1993) Effects of acidic and alkaline treatments on tannic acid and its binding property to protein. *Journal of Agricultural and Food Chemistry*, 41(5), 704-707.

Özkar, S. & Finke, R. G. (2017) Silver Nanoparticles Synthesized by Microwave Heating: A Kinetic and Mechanistic Re-Analysis and Re-Interpretation. *The Journal of Physical Chemistry C*, 121(49), 27643-27654.

Pandya, D., Vachharajani, B. & Srivastava, R. (2022) A review of data assimilation techniques: Applications in engineering and agriculture. *Materials Today: Proceedings*, 62, 7048-7052.

Parrey, S. H., Maseet, M., Ahmad, R. & Khan, A. B. (2021) Deciphering the Kinetic Study of Sodium Dodecyl Sulfate on Ag Nanoparticle Synthesis Using Cassia siamea Flower Extract as a Reducing Agent. *ACS Omega*, 6(18), 12155-12167.

Parveen, A., Kulkarni, N., Yalagatti, M., Abbaraju, V. & Deshpande, R. (2018) In vivo efficacy of biocompatible silver nanoparticles cream for empirical wound healing. *J Tissue Viability*, 27(4), 257-261.

Patil, G. A., Bari, M. L., Bhanvase, B. A., Ganvir, V., Mishra, S. & Sonawane, S. H. (2012) Continuous synthesis of functional silver nanoparticles using microreactor: Effect of surfactant and process parameters. *Chemical Engineering and Processing: Process Intensification*, 62, 69-77.

Paul, S., Basak, P., Majumder, R., Mukherjee, A., Ghosh, J., Patra, S. & Jana, N. K. (2020) Biochemical estimation of Moringa oleifera leaf extract for synthesis of silver nanoparticle mediated drug delivery system. *Journal of Plant Biochemistry and Biotechnology*, 29(1), 86-93.

Peard, W. J. & Pflaum, R. T. (1958) Interaction of Metal Ions with Heterocyclic Amines. Silver(I) Complexes. *Journal of the American Chemical Society*, 80(7), 1593-1596.

Pedregosa, F. (2011) Scikit-learn: Machine Learning in Python. *Journal of Machine Learning Research*, 12(10), 2825-2831.

Pelegrina, J. L. & Guillermet, A. F. (2018) The “critical limits for crystallinity” in nanoparticles of the elements: A combined thermodynamic and crystallographic critique. *Journal of Physics and Chemistry of Solids*, 114, 58-63.

Peng, H.-I., Krauss, T. D. & Miller, B. L. (2010) Aging induced Ag nanoparticle rearrangement under ambient atmosphere and consequences for nanoparticle-enhanced DNA biosensing. *Analytical chemistry*, 82(20), 8664-8670.

Perala, S. R. K. & Kumar, S. (2014) On the Two-Step Mechanism for Synthesis of Transition-Metal Nanoparticles. *Langmuir*, 30(42), 12703-12711.

Pestovsky, Y. S. & Srichana, T. (2022) Formation of Aggregate-Free Gold Nanoparticles in the Cyclodextrin-Tetrachloroaurate System Follows Finke–Watzky Kinetics. *Nanomaterials*, 12(4), 583.

Phan, H. T. & Haes, A. J. (2019) What Does Nanoparticle Stability Mean? *The Journal of Physical Chemistry C*, 123(27), 16495-16507.

Pico, P., Nathanael, K., Lavino, A. D., Kovalchuk, N. M., Simmons, M. J. H. & Matar, O. K. (2023) Silver nanoparticles synthesis in microfluidic and well-mixed reactors: A combined experimental and PBM-CFD study. *Chemical Engineering Journal*, 474, 145692.

Piwoński, I., Spilarewicz-Stanek, K., Kisielewska, A., Kądzioła, K., Cichomski, M. & Ginter, J. (2016) Examination of Ostwald ripening in the photocatalytic growth of silver nanoparticles on titanium dioxide coatings. *Applied Surface Science*, 373, 38-44.

Poling, B. E. (2001) The properties of gases and liquids / Bruce E. Poling, John M. Praausnitz, John P. O'Connell. *In:* O'Connell, J. P. & Prausnitz, J. M. (eds.) 5th ed. International ed. ed. London: London : McGraw-Hill Education.

Polte, J., Tuaev, X., Wuithschick, M., Fischer, A., Thuenemann, A. F., Rademann, K., Kraehnert, R. & Emmerling, F. (2012) Formation Mechanism of Colloidal Silver Nanoparticles: Analogies and Differences to the Growth of Gold Nanoparticles. *ACS Nano*, 6(7), 5791-5802.

Prema, P., Veeramanikandan, V., Rameshkumar, K., Gatasheh, M. K., Hatamleh, A. A., Balasubramani, R. & Balaji, P. (2022) Statistical optimization of silver nanoparticle synthesis by green tea extract and its efficacy on colorimetric detection of mercury from industrial waste water. *Environmental Research*, 204, 111915.

Profillidis, V. A. & Botzoris, G. N. (2019) Chapter 5 - Statistical Methods for Transport Demand Modeling, in Profillidis, V. A. & Botzoris, G. N. (eds), *Modeling of Transport Demand*Elsevier, 163-224.

Qin, Y., Ji, X., Jing, J., Liu, H., Wu, H. & Yang, W. (2010) Size control over spherical silver nanoparticles by ascorbic acid reduction. *Colloids and Surfaces A: Physicochemical and Engineering Aspects*, 372(1), 172-176.

Quintero-Quiroz, C., Acevedo, N., Zapata-Giraldo, J., Botero, L. E., Quintero, J., Zárate-Triviño, D., Saldarriaga, J. & Pérez, V. Z. (2019) Optimization of silver nanoparticle synthesis by chemical reduction and evaluation of its antimicrobial and toxic activity. *Biomaterials Research*, 23(1), 27.

Ramachandran, K. M. & Tsokos, C. P. (2021) Chapter 1 - Descriptive statistics, in Ramachandran, K. M. & Tsokos, C. P. (eds), *Mathematical Statistics with Applications in R (Third Edition)*Academic Press, 1-40.

Ranoszek-Soliwoda, K., Tomaszewska, E., Socha, E., Krzyczmonik, P., Ignaczak, A., Orlowski, P., Krzyzowska, M., Celichowski, G. & Grobelny, J. (2017) The role of tannic acid and sodium citrate in the synthesis of silver nanoparticles. *Journal of Nanoparticle Research*, 19(8), 273.

Rao, V. K., Abhinav, K. V., Karthik, P. S. and Singh, S. P. (2015) Conductive silver inks and their applications in printed and flexible electronics. *RSC Advances*, 5(95), 77760-77790.

Rashid, M. U., Bhuiyan, M. K. H. & Quayum, M. E. (2013) Synthesis of Silver Nano Particles (Ag-NPs) and their uses for Quantitative Analysis of Vitamin C Tablets. *Dhaka University Journal of Pharmaceutical Sciences*, 12, 29-33.

Ravi Kumar, D. V., Prasad, B. L. V. & Kulkarni, A. A. (2012) Segmented flow synthesis of Ag nanoparticles in spiral microreactor: Role of continuous and dispersed phase. *Chemical Engineering Journal*, 192, 357-368.

Reverberi, A. P., Vocciante, M., Salerno, M., Ferretti, M. & Fabiano, B. (2020) Green Synthesis of Silver Nanoparticles by Low-Energy Wet Bead Milling of Metal Spheres. *Materials*, 13(1), 63.

Rivero, P. J., Goicoechea, J., Urrutia, A. & Arregui, F. J. (2013) Effect of both protective and reducing agents in the synthesis of multicolor silver nanoparticles. *Nanoscale research letters*, 8(1), 101-101.

Rizwan, M. & Gwenin, C. (2021) Chapter 5 - Nanomaterials in renewable energy: UV-Visible spectroscopy characterization and applications, in Devasahayam, S. & Hussain, C. M. (eds), *Nano Tools and Devices for Enhanced Renewable Energy*Elsevier, 103-120.

Roldán, M. V., Pellegri, N. & de Sanctis, O. (2013) Electrochemical Method for Ag-PEG Nanoparticles Synthesis. *Journal of Nanoparticles*, 2013, 524150.

Ross Hallett, F. (1999) Scattering and Particle Sizing Applications*, in Lindon, J. C. (ed), *Encyclopedia of Spectroscopy and Spectrometry (Second Edition)*. Oxford: Academic Press, 2488-2494.

Roucoux, A., Schulz, J. & Patin, H. (2002) Reduced Transition Metal Colloids: A Novel Family of Reusable Catalysts? *Chemical Reviews*, 102(10), 3757-3778.

Sadeghi, R. & Ziamajidi, F. (2007) Apparent Molar Volume and Isentropic Compressibility of Trisodium Citrate in Water and in Aqueous Solutions of Polyvinylpyrrolidone at T = (283.15 to 308.15) K. *Journal of Chemical & Engineering Data*, 52(3), 1037-1044.

Sandoe, H. E., Watzky, M. A. & Diaz, S. A. (2019) Experimental probes of silver metal nanoparticle formation kinetics: Comparing indirect versus more direct methods. *International Journal of Chemical Kinetics*, 51(11), 861-871.

Santos, F. G., Fratelli, C., Muniz, D. G. & Capriles, V. D. (2018) Mixture Design Applied to the Development of Chickpea-Based Gluten-Free Bread with Attractive Technological, Sensory, and Nutritional Quality. *Journal of Food Science*, 83(1), 188-197.

Sarkar, M., Denrah, S., Das, M. & Das, M. (2021) Statistical optimization of bio-mediated silver nanoparticles synthesis for use in catalytic degradation of some azo dyes. *Chemical Physics Impact*, 3, 100053.

Sarrazin, F., Loubière, K., Prat, L., Gourdon, C., Bonometti, T. & Magnaudet, J. (2006) Experimental and numerical study of droplets hydrodynamics in MicroChannel. *AIChE Journal*, 52(12), 4061-4070.

Sattari, R. & Khayati, G. R. (2020) Prediction of the size of silver nanoparticles prepared via green synthesis: A gene expression programming approach. *Scientia Iranica*, 27(6), 3399-3411.

Schwarz, G. (1978) Estimating the Dimension of a Model. *The Annals of Statistics*, 6(2), 461-464.

Scott, S. M. & Ali, Z. (2021) Fabrication Methods for Microfluidic Devices: An Overview. *Micromachines (Basel)*, 12(3), 319.

Seemann, R., Brinkmann, M., Pfohl, T. & Herminghaus, S. (2012) Droplet based microfluidics. *Rep Prog Phys*, 75(1), 016601.

Sethuramiah, A. & Kumar, R. (2016) Chapter 6 - Statistics and Experimental Design in Perspective, in Sethuramiah, A. & Kumar, R. (eds), *Modeling of Chemical Wear*. Oxford: Elsevier, 129-159.

Shabanzadeh, P., Senu, N., Shameli, K. & Tabar, M. M. (2013) Artificial intelligence in numerical modeling of silver nanoparticles prepared in montmorillonite interlayer space. *Journal of Chemistry*, 2013, 1-8.

shafaei, A. & Khayati, G. R. (2020) A predictive model on size of silver nanoparticles prepared by green synthesis method using hybrid artificial neural network-particle swarm optimization algorithm. *Measurement.*

Shah, V., Bharatiya, B., Mishra, M. K., Ray, D. & Shah, D. O. (2019) Molecular insights into sodium dodecyl sulphate mediated control of size for silver nanoparticles. *Journal of Molecular Liquids*, 273, 222-230.

Shaikhaldein, H. O., Al-Qurainy, F., Nadeem, M., Khan, S., Tarroum, M. & Salih, A. M. (2020) Biosynthesis and characterization of silver nanoparticles using Ochradenus arabicus and their physiological effect on Maerua oblongifolia raised in vitro. *Sci Rep*, 10(1), 17569.

Shembekar, N., Chaipan, C., Utharala, R. & Merten, C. A. (2016) Droplet-based microfluidics in drug discovery, transcriptomics and high-throughput molecular genetics. *Lab on a Chip*, 16(8), 1314-1331.

Shen, F., LI, Y., LIU, Z.-M., CAO, R.-T. & WANG, G.-R. (2015) Advances in Micro-Droplets Coalescence Using Microfluidics. *Chinese Journal of Analytical Chemistry*, 43, 1942-1954.

Shukla, D., Joshi, A. A. & Mehra, A. (2009) Modeling of Formation of Nanoparticles in Reverse Micellar Systems: Ostwald Ripening of Silver Halide Particles. *Langmuir*, 25(6), 3786-3793.

Shutyaev, V., Zalesny, V., Agoshkov, V., Parmuzin, E. & Zakharova, N. (2023) Four-Dimensional Variational Data Assimilation and Sensitivity of Ocean Model State Variables to Observation Errors. *Journal of Marine Science and Engineering*, 11(6), 1253.

Siddiqi, K. S., Husen, A. & Rao, R. A. K. (2018) A review on biosynthesis of silver nanoparticles and their biocidal properties. *Journal of Nanobiotechnology*, 16(1), 14.

Singh, H., Du, J., Singh, P. & Yi, T. H. (2018) Extracellular synthesis of silver nanoparticles by Pseudomonas sp. THG-LS1.4 and their antimicrobial application. *Journal of Pharmaceutical Analysis*, 8(4), 258-264.

Sithole, N. T. & Ntuli, F. (2022) Evaluation of hydrazine, dimethylamine borane and glyoxylic acid as reducing agents in reductive precipitation. *South African Journal of Chemical Engineering*, 41, 17-25.

Sivaraman, S. K., Elango, I. S., Kumar, S. & Santhanam, V. (2009) A green protocol for room temperature synthesis of silver nanoparticles in seconds. *Current Science*, 97, 1055-1059.

Skrabalak, S. E., Wiley, B. J., Kim, M., Formo, E. V. & Xia, Y. (2008) On the Polyol Synthesis of Silver Nanostructures: Glycolaldehyde as a Reducing Agent. *Nano Letters*, 8(7), 2077-2081.

Sobczak-Kupiec, A., Malina, D., Wzorek, Z. & Zimowska, M. (2011) Influence of silver nitrate concentration on the properties of silver nanoparticles. *Micro & Nano Letters*, 6(8), 656-660.

Song, J., Wu, F., Wan, Y. & Ma, L. (2015) Colorimetric detection of melamine in pretreated milk using silver nanoparticles functionalized with sulfanilic acid. *Food Control*, 50, 356-361.

Song, Y. Y. & Lu, Y. (2015) Decision tree methods: applications for classification and prediction. *Shanghai Arch Psychiatry*, 27(2), 130-5.

Student (1908) The Probable Error of a Mean. *Biometrika*, 6(1), 1-25.

Sun, B., Fernandez, M. & Barnard, A. S. (2017) Machine Learning for Silver Nanoparticle Electron Transfer Property Prediction. *Journal of Chemical Information and Modeling*, 57(10), 2413-2423.

Szczepańska, E., Bielicka-Giełdoń, A., Niska, K., Strankowska, J., Żebrowska, J., Inkielewicz-Stępniak, I., Łubkowska, B., Swebocki, T., Skowron, P. & Grobelna, B. (2020) Synthesis of silver nanoparticles in context of their cytotoxicity, antibacterial activities, skin penetration and application in skincare products. *Supramolecular Chemistry*, 32(3), 207-221.

Tang, T., Yuan, Y., Yalikun, Y., Hosokawa, Y., Li, M. & Tanaka, Y. (2021) Glass based micro total analysis systems: Materials, fabrication methods, and applications. *Sensors and Actuators B: Chemical*, 339, 129859.

Tatarchuk, V. V., Sergievskaya, A. P., Korda, T. M., Druzhinina, I. A. & Zaikovsky, V. I. (2013) Kinetic Factors in the Synthesis of Silver Nanoparticles by Reduction of Ag+ with Hydrazine in Reverse Micelles of Triton N-42. *Chemistry of Materials*, 25(18), 3570-3579.

Tejamaya, M., Römer, I., Merrifield, R. C. & Lead, J. R. (2012) Stability of Citrate, PVP, and PEG Coated Silver Nanoparticles in Ecotoxicology Media. *Environmental Science & Technology*, 46(13), 7011-7017.

Thanh, N. T. K., Maclean, N. & Mahiddine, S. (2014) Mechanisms of Nucleation and Growth of Nanoparticles in Solution. *Chemical Reviews*, 114(15), 7610-7630.

Tsachouridis, K., Zhou, Y. & Anastasiou, A. D. (2024) Comparison of three droplet microreactors for the continuous production of nano and micro particles. *Chemical Engineering Science*, 293, 119956.

Tung, K. Y., Li, C. C. & Yang, J. T. (2009) Mixing and hydrodynamic analysis of a droplet in a planar serpentine micromixer. *Microfluidics and Nanofluidics*, 7, 545-557.

V. Goia, D. & Matijević, E. (1998) Preparation of monodispersed metal particles. *New Journal of Chemistry*, 22(11), 1203-1215.

Vallone, A., Estakhri, N. M. & Mohammadi Estakhri, N. (2023) Region-specified inverse design of absorption and scattering in nanoparticles by using machine learning. *Journal of Physics: Photonics*, 5(2), 024002.

Van Hyning, D. L. & Zukoski, C. F. (1998) Formation Mechanisms and Aggregation Behavior of Borohydride Reduced Silver Particles. *Langmuir*, 14(24), 7034-7046.

Vazquez-Muñoz, R., Meza-Villezcas, A., Fournier, P. G. J., Soria-Castro, E., Juarez-Moreno, K., Gallego-Hernández, A. L., Bogdanchikova, N., Vazquez-Duhalt, R. & Huerta-Saquero, A. (2019) Enhancement of antibiotics antimicrobial activity due to the silver nanoparticles impact on the cell membrane. *PLOS One*, 14(11), e0224904.

Velgosova, O., Čižmárová, E., Málek, J. & Kavuličova, J. (2017) Effect of storage conditions on long-term stability of Ag nanoparticles formed via green synthesis. *International Journal of Minerals, Metallurgy, and Materials*, 24(10), 1177-1182.

Vetra-Carvalho, S., van Leeuwen, P. J., Nerger, L., Barth, A., Altaf, M. U., Brasseur, P., Kirchgessner, P. & Beckers, J.-M. (2018) State-of-the-art stochastic data assimilation

methods for high-dimensional non-Gaussian problems. *Tellus A: Dynamic Meteorology and Oceanography*, 70(1), 1-43.

Wagner, C. (1961) Theorie der Alterung von Niederschlägen durch Umlösen (Ostwald-Reifung). *Zeitschrift für Elektrochemie, Berichte der Bunsengesellschaft für physikalische Chemie*, 65(7-8), 581-591.

Wagner, J. R., Mount, E. M. & Giles, H. F. (2014) 25 - Design of Experiments, in Wagner, J. R., Mount, E. M. & Giles, H. F. (eds), *Extrusion (Second Edition)*. Oxford: William Andrew Publishing, 291-308.

Wang, C. T. & Hu, Y. C. (2010) Mixing of Liquids Using Obstacles in Y-Type Microchannels. *Journal of Applied Science and Engineering*, 13(4), 385-394.

Wang, H., Qiao, X., Chen, J. & Ding, S. (2005) Preparation of silver nanoparticles by chemical reduction method. *Colloids and Surfaces A: Physicochemical and Engineering Aspects*, 256(2), 111-115.

Wang, J., Wang, J., Feng, L. & Lin, T. (2015) Fluid mixing in droplet-based microfluidics with a serpentine microchannel. *RSC Advances*, 5(126), 104138-104144.

Wang, M., Li, H., Li, Y., Mo, F., Li, Z., Chai, R. & Wang, H. (2020) Dispersibility and Size Control of Silver Nanoparticles with Anti-Algal Potential Based on Coupling Effects of Polyvinylpyrrolidone and Sodium Tripolyphosphate. *Nanomaterials (Basel)*, 10(6), 1042.

Wang, R., Liu, C., Wei, Y., Wu, P., Su, Y. & Zhang, Z. (2021) Inverse design of metal nanoparticles based on deep learning. *Results in Optics*, 5, 100134.

Wani, I. A., Khatoon, S., Ganguly, A., Ahmed, J. & Ahmad, T. (2013) Structural characterization and antimicrobial properties of silver nanoparticles prepared by inverse microemulsion method. *Colloids and Surfaces B: Biointerfaces*, 101, 243-250.

Watzky, M. A. & Finke, R. G. (1997) Transition Metal Nanocluster Formation Kinetic and Mechanistic Studies. A New Mechanism When Hydrogen Is the Reductant: Slow, Continuous Nucleation and Fast Autocatalytic Surface Growth. *Journal of the American Chemical Society*, 119(43), 10382-10400.

Wei, F., Zhao, X., Li, C. & Han, X. (2018) A novel strategy for water disinfection with a AgNPs/gelatin sponge filter. *Environmental Science and Pollution Research*, 25(20), 19480-19487.

Wojnicki, M., Fitzner, K. & Luty-Błocho, M. (2016) Kinetic studies of nucleation and growth of palladium nanoparticles. *Journal of Colloid and Interface Science*, 465, 190-199.

Wojnicki, M., Tokarski, T., Hessel, V., Fitzner, K. & Luty-Błocho, M. (2019) Continuous, monodisperse silver nanoparticles synthesis using microdroplets as a reactor. *Journal of Flow Chemistry*, 9(1), 1-7.

Wu, K. J., De Varine Bohan, G. M. & Torrente-Murciano, L. (2017) Synthesis of narrow sized silver nanoparticles in the absence of capping ligands in helical microreactors. *Reaction Chemistry and Engineering*, 2(2), 116-128.

Wu, Z., Zhou, W., Pang, C., Deng, W., Xu, C. & Wang, X. (2019) Multifunctional chitosan-based coating with liposomes containing laurel essential oils and nanosilver for pork preservation. *Food Chemistry*, 295, 16-25.

Wuithschick, M., Paul, B., Bienert, R., Sarfraz, A., Vainio, U., Sztucki, M., Kraehnert, R., Strasser, P., Rademann, K., Emmerling, F. & Polte, J. (2013) Size-Controlled Synthesis of Colloidal Silver Nanoparticles Based on Mechanistic Understanding. *Chemistry of Materials*, 25(23), 4679-4689.

Xie, Y., Ye, R. & Liu, H. (2006) Synthesis of silver nanoparticles in reverse micelles stabilized by natural biosurfactant. *Colloids and Surfaces A: Physicochemical and Engineering Aspects*, 279(1), 175-178.

Xu, L., Peng, J., Yan, M., Zhang, D. & Shen, A. Q. (2016a) Droplet synthesis of silver nanoparticles by a microfluidic device. *Chemical Engineering and Processing: Process Intensification*, 102, 186-193.

Xu, Z., Lu, C., Riordon, J., Sinton, D. & Moffitt, M. G. (2016b) Microfluidic Manufacturing of Polymeric Nanoparticles: Comparing Flow Control of Multiscale Structure in Single-Phase Staggered Herringbone and Two-Phase Reactors. *Langmuir*, 32(48), 12781-12789.

Yao, S., Yuan, Y., Xiao, C., Li, W., Kou, Y., Dyson, P. J., Yan, N., Asakura, H., Teramura, K. & Tanaka, T. (2012) Insights into the Formation Mechanism of Rhodium Nanocubes. *The Journal of Physical Chemistry C*, 116(28), 15076-15086.

Yaqoob, A. A., Umar, K. & Ibrahim, M. N. M. (2020) Silver nanoparticles: various methods of synthesis, size affecting factors and their potential applications–a review. *Applied Nanoscience*, 10(5), 1369-1378.

Yen, C. W., de Puig, H., Tam, J. O., Gómez-Márquez, J., Bosch, I., Hamad-Schifferli, K. & Gehrke, L. (2015) Multicolored silver nanoparticles for multiplexed disease diagnostics: distinguishing dengue, yellow fever, and Ebola viruses. *Lab Chip*, 15(7), 1638-41.

Yoneya, M. & Sugisawa, S. Y. (2019) Simulation of Colloidal Silver Nanoparticle Formation from a Precursor Complex. *Journal of Physical Chemistry C*, 123(17), 11257–11263.

Yoo, S., Nam, D. H., Singh, T. I., Leem, G. & Lee, S. (2022) Effect of reducing agents on the synthesis of anisotropic gold nanoparticles. *Nano Convergence*, 9(1), 5.

Yusuf, M. (2019) Silver Nanoparticles: Synthesis and Applications, in Martínez, L. M. T., Kharissova, O. V. & Kharisov, B. I. (eds), *Handbook of Ecomaterials*. Cham: Springer International Publishing, 2343-2356.

Zahoor, M., Nazir, N., Iftikhar, M., Naz, S., Zekker, I., Burlakovs, J., Uddin, F., Kamran, A. W., Kallistova, A., Pimenov, N. & Ali Khan, F. (2021) A Review on Silver Nanoparticles: Classification, Various Methods of Synthesis, and Their Potential Roles in Biomedical Applications and Water Treatment. *Water*, 13(16), 2216.

Zeng, Q., Jiang, X., Yu, A. & Lu, G. M. (2007) Growth mechanisms of silver nanoparticles: a molecular dynamics study. *Nanotechnology.*

Zhang, H. & Chiao, M. (2015) Anti-fouling Coatings of Poly(dimethylsiloxane) Devices for Biological and Biomedical Applications. *J Med Biol Eng*, 35(2), 143-155.

Zhang, P., Guo, Z., Ullah, S., Melagraki, G., Afantitis, A. & Lynch, I. (2021) Nanotechnology and artificial intelligence to enable sustainable and precision agriculture. *Nature Plants*, 7(7), 864-876.

Zhang, W., Qiao, X. & Chen, J. (2007) Synthesis of nanosilver colloidal particles in water/oil microemulsion. *Colloids and Surfaces A: Physicochemical and Engineering Aspects*, 299(1), 22-28.

Zhang, W., Qiao, X. & Chen, J. (2008) Formation of silver nanoparticles in SDS inverse microemulsions. *Materials Chemistry and Physics*, 109(2), 411-416.

Zhao, T., Sun, R., Yu, S., Zhang, Z., Zhou, L., Huang, H. & Du, R. (2010) Size-controlled preparation of silver nanoparticles by a modified polyol method. *Colloids and Surfaces A: Physicochemical and Engineering Aspects*, 366(1), 197-202.

Zhuang, Y., Cheng, S., Kovalchuk, N., Simmons, M., Matar, O. K., Guo, Y.-K. & Arcucci, R. (2022) Ensemble latent assimilation with deep learning surrogate model: application to drop interaction in a microfluidics device. *Lab on a Chip*, 22(17), 3187-3202.

Zwar, I. P., Trotta, C. d. V., Ziotti, A. B. S., Lima Neto, M., Araújo, W. L., de Melo, I. S., Ottoni, C. A. & de Souza, A. O. (2023) Biosynthesis of silver nanoparticles using actinomycetes, phytotoxicity on rice seeds, and potential application in the biocontrol of phytopathogens. *Journal of Basic Microbiology*, 63(1), 64-74.

APPENDIX A: STATISTICAL ANALYSIS

Sum of squares total (SST) Mathews (2005): The sum of squared differences between (y_i) individual experimental points and ($\bar{y}$) the mean of the response variable.

$$SST = \sum_{i=1}^{n}(y_i - \bar{y})^2 \quad \text{(A1)}$$

Sum of squares Regression (SSR) (Mathews, 2005): The sum of squared differences between ($\hat{y_i}$) predicted data points and ($\bar{y}$) the mean of the response variable.

$$SSR = \sum_{i=1}^{n}(\hat{y_i} - \bar{y})^2 \quad \text{(A2)}$$

Sum of squares error (SSE) (Mathews, 2005): The sum of squared differences between ($\hat{y_i}$) predicted data points and (y_i) observed data points.

$$SSE = \sum_{i=1}^{n}(\hat{y_i} - y_i)^2 \quad \text{(A3)}$$

R-squared (R^2) (Magee, 1990):

$$R^2 = 1 - \frac{SSE}{SST} \quad \text{(A4)}$$

R-squared adjusted ($R^2 adj.$)(Huberty & Mourad, 1980),(Ezekiel, 1930): In $R^2 adj.$ n is the number of observations and k is the number of terms containing variables in the regression.

$$R^2 adj. = 1 - \left(\frac{n-1}{n-k-1}\right)(1 - R^2) \quad \text{(A5)}$$

Mean squared (MS) (Mathews, 2005): The sum of squares of terms divided by the degrees of freedom (DFE), $DFE = p - 2$ where p is the number of experiments for each observation. For the regression term the DFE are equal to the number of predictors.

$$MS = \frac{SST}{DFE} \quad \text{(A6)}$$

Mean square error (MSE)(Mathews, 2005) : The sum of squares error divided by the $\mathrm{DFE}_{\mathrm{error}} = \mathrm{n} - \mathrm{k} - 1.$

$$\mathrm{MSE} = \frac{\mathrm{SSE}}{\mathrm{DFE}_{\mathrm{error}}} \tag{A7}$$

F-value (F)(Mathews, 2005):

$$\mathrm{F} = \frac{\mathrm{MS}}{\mathrm{MSE}} \tag{A8}$$

t-value(Mathews, 2005): The t-value is defined by the ratio of the estimated parameter (or coefficient) (β) to its standard error. A t-test is important to determine if a process has a significant effect on a population or whether the interested groups have differences from each other. In this research paper, t-statistics were used to build a pareto chart and identify the parameters that have the most significant effect on the response.

Hypothesis tests:

$$\mathrm{H_o}: \beta = 0$$

$$\mathrm{H_1}: \beta \neq 0$$

The hypothesis tests are performed with t-statistics (Student, 1908):

$$\mathrm{t} = \frac{\beta}{\text{standard error of } \beta} \tag{A9}$$

Confidence intervals (CI) (Lane & DuMouchel, 1994):

$$\mathrm{CI} = \widehat{y_1} \pm \mathrm{t}_{(1-\mathrm{a}/2\,,\mathrm{n}-\mathrm{k})} \times \sqrt{\mathrm{MSE}\,(\mathrm{X_o'}\,(\mathrm{X'X})^{-1}\mathrm{X_o}} \tag{A10}$$

Prediction intervals (PI) (Lane & DuMouchel, 1994):

$$\mathrm{PI} = \widehat{y_1} \pm \mathrm{t}_{(1-\mathrm{a}/2\,,\mathrm{n}-\mathrm{k})} \times \sqrt{\mathrm{MSE}\,(1 + \mathrm{X_o'}\,(\mathrm{X'X})^{-1}\mathrm{X_o}} \tag{A11}$$

In CI and PI, $\widehat{y_i}$ is the predicted response value, a is the level of significance, $t_{(1-a/2\,,n-k)}$ is the upper $(1-{}^{a}/_{2}$ Student t-critical value with $n-k$ degrees of freedom, n is the number of observations, k is the number of model parameters and MSE is the mean square error. For CI X is the design matrix while for PI X is the predictor matrix. The X_o is the vector or matrix of given predictor values (produced from the fitted values from design matrix or predictor matrix) and the X_o' is the transpose of the new vector or matrix of predictor values.

$$SSE = \sum_{i=1}^{n} (\widehat{y_i} - y_i)^2$$

Mean absolute error (MAE) (Chicco et al, 2021): In MAE, n is the number of data within training and testing data sets.

$$MAE = \frac{1}{n}\sum_{i=1}^{n}|\widehat{y_i} - y_i| \qquad \text{(A12)}$$

APPENDIX B: PARTICLES SIZES OF SILVER NANOPARTICLES AS A FUNCTION OF PH, CONCENTRATION OF TRISODIUM CITRATE, STORAGE TEMPERATURE, CURVATURE AND FLOW RATES

Table A1: Particles sizes of AgNPs at different conditions. The sizes were measured as a function of pH, storage temperature, concentration of TC, curvature, and flow rates.

pH	ST, ℃	[TC], mM	CR, dm^{-1}	FR, dm^3/min	Average size,nm
12	20	3.82	33.3	0.00004	21.59
7	0	3.82	0	0.00004	12.04
7	20	3.82	33.3	0.00004	10.63
12	0	3.82	0	0.00004	17.11
7	0	3.82	33.3	0.00004	6.55
12	20	3.82	0	0.00004	24.57
12	0	3.82	33.3	0.000001	21.04
7	20	3.82	0	0.000001	13.24
12	0	1.91	33.3	0.00004	3.92
7	20	2.87	0	0.00004	9.29
12	0	3.82	0	0.00001	18.47
7	0	1.91	0	0.00004	14.03
12	20	1.91	0	0.00004	4.70
7	20	3.82	33.3	0.00001	7.41
12	20	2.87	33.3	0.00004	8.50
12	0	2.87	0	0.00004	5.56
7	20	1.91	33.3	0.00004	9.04
7	0	3.82	0	0.000001	10.62
12	20	3.82	33.3	0.000001	23.69
12	20	3.82	0	0.00001	23.31
12	0	2.87	33.3	0.00001	8.97
7	20	2.87	0	0.00001	16.31
7	0	3.82	33.3	0.000001	8.61
7	20	1.91	33.3	0.000001	10.14
7	0	1.91	0	0.00001	13.31
12	20	2.87	0	0.000001	11.13
7	0	2.87	33.3	0.00001	6.22
7	20	1.91	0	0.000001	23.31

12	0	1.91	33.3	0.000001	5.16
12	0	3.82	33.3	0.00001	15.69
7	0	2.87	0	0.000001	11.48
12	20	1.91	0	0.00001	6.53
7	0	3.82	0	0.00001	11.31
12	20	3.82	0	0.000001	22.73
12	0	2.87	33.3	0.00004	8.50
7	20	2.87	33.3	0.000001	7.43
7	0	1.91	33.3	0.00001	5.46
12	20	2.87	33.3	0.00001	7.81
12	0	2.87	0	0.000001	8.02
7	20	1.91	33.3	0.00001	7.07
12	20	1.91	33.3	0.000001	6.23
7	0	2.87	0	0.00001	9.41
12	0	2.87	33.3	0.000001	5.79
12	20	2.87	0	0.00001	9.69
12	0	1.91	0	0.00001	5.18
7	0	1.91	33.3	0.000001	7.46
7	20	1.91	0	0.00004	17.73
7	0	1.91	0	0.000001	17.29
12	20	1.91	0	0.000001	7.27
7	20	2.87	33.3	0.00004	5.46
12	0	1.91	33.3	0.00001	4.21
7	0	2.87	0	0.00004	6.27
7	20	3.82	0	0.00001	12.76
7	20	2.87	33.3	0.00001	9.16

APPENDIX C: NUCLEATION AND GROWTH CONSTANTS OF SILVER NANOPARTICLES ALONG WITH PARTICLES SIZES IN A WELL-MIXED REACTOR FOR TWO SET OF CHEMICALS

Table A2: Particles sizes of AgNPs in a well-mixed reactor for two set of chemicals. The nucleation and growth constants are reported for both sets of chemicals as well. The first set of chemicals involve TA and TC and the second set of chemicals include DMAB and SDS.

Initial concentration of precursor (M)	Nucleation constant (min^{-1})	Growth constant ($\mathrm{M}^{-1}\mathrm{min}^{-1}$)	AgNPs size (1)	AgNPs size (2)	AgNPs size (3)
0.00008	0.014	831.25	3.84	3.42	4.19
0.00008	0.064	1120	2.87	2.95	2.93
0.00008	0.021	989.58	2.75	3.2	3.3
0.00008	0.125	1500	2.27	3.53	2.38
0.00092	0.0011	55.51	3.94	3.177	3.72
0.00092	0.0013	37.86	3.35	3.081333	3.67
0.00092	0.0015	44.81	3.052	3.013333	3.35
0.00092	0.1	77.97	0.73	0.735833	0.71
0.00092	0.012	13.66	1.32	1.255733	1.52
0.00092	0.0128	26.01	1.73	1.82	2.18
0.00041	0.002	92.52	3.09	4.69	2.28

APPENDIX D: PARTICLES SIZES OF SILVER NANOPARTICLES AS A FUNCTION OF NUCLEATION AND GROWTH CONSTANTS, STORAGE TEMPERATURE, REYNOLDS NUMBER AND DEAN NUMBER/REYNOLDS NUMBER FOR THE FIRST SET OF CHEMICALS

Table A3: Particles sizes of AgNPs at different conditions. The sizes were measured as a function of nucleation and growth constants, storage temperature, Reynolds number and Dean number/Reynolds number for the first set of chemicals.

Nucleation constant (min^{-1})	Growth constant ($\mathrm{M}^{-1}\mathrm{min}^{-1}$)	Storage temperature (℃)	Dean number / Reynolds number	Reynolds number	AgNPs size (1)	AgNPs size (2)	AgNPs size (3)
Original experiments							
0.0128	26.01	20	0.41	3.395	19.05	22.08	23.65
0.0015	44.81	0	0	3.395	11.1	13.03	12
0.0015	44.81	20	0.41	3.395	8.53	12.2	11.16
0.0128	26.01	0	0	3.395	17.62	16.71	16.99
0.0015	44.81	0	0.41	3.395	5.68	7.35	6.62
0.0128	26.01	20	0	3.395	23.38	25.52	24.8
0.0128	26.01	0	0.41	0.0849	19.83	19.81	23.49
0.0015	44.81	20	0	0.0849	12.64	13.54	13.54
0.1	77.97	0	0.41	3.395	4.39	3.58	3.79
0.0013	37.86	20	0	3.395	9.68	8.77	9.42
0.0128	26.01	0	0	0.849	19.77	17.39	18.24
0.0011	55.51	0	0	3.395	15.52	15.24	11.34
0.1	77.97	20	0	3.395	5.08	4.26	4.75
0.0015	44.81	20	0.41	0.849	6.73	7.54	7.95
0.012	13.66	20	0.41	3.395	9.53	7.28	8.68
0.012	13.66	0	0	3.395	5.3	6.097	5.29
0.0011	55.51	20	0.41	3.395	8.1	10.2	8.83
0.0015	44.81	0	0	0.0849	11.41	10.37	10.07
0.0128	26.01	20	0.41	0.0849	23.93	23.93	23.2
0.0128	26.01	20	0	0.849	21.52	22.95	25.47
Designed experiments based on decision tree							
0.0011	55.51	20	0.41	0.0849	8.932	10.141	11.35
0.0011	55.51	0	0	0.849	11.63	12.9	15.41

0.0128	26.01	0	0.41	0.849	15.7	14.28	17.1
0.0013	37.86	0	0	0.0849	12.19	11.34	10.91
0.0015	44.81	0	0	0.849	11.42	11.92	10.58
0.0128	26.01	20	0	0.0849	20.78	24.4	23.01
0.0013	37.86	20	0.41	0.0849	7.161	6.45	8.69
0.0011	55.51	20	0.41	0.849	7.87	7.074	6.27
0.0013	37.86	0	0	0.849	10.1	8.78	9.38
0.0011	55.51	20	0	3.395	18.52	16.47	18.2
Random experiments							
0.1	77.97	0	0.41	0.849	4.55	3.54	4.547
0.0013	37.86	0	0	3.395	6.414	6	6.4
0.0015	44.81	20	0	0.849	12.95	13.65	11.67
0.0013	37.86	20	0.41	0.849	9.034	8.58	9.88
0.1	77.97	0	0.41	1.698	3.98	3.68	4.38
0.012	13.66	0	0.41	1.698	6.996	7.38	6.996
0.1	77.97	20	0.41	1.698	5.22	5.27	4.94
0.0015	44.81	20	0	1.698	13.98	11.7	9.878
0.0011	55.51	0	0	1.698	16.2	15.65	16.11
0.0011	55.51	20	0	16.96	17.48	19.86	19.01
0.0011	55.51	20	0	5.662	15.45	20.416	18.1
0.0011	55.51	20	0.32	0.0849	14.05	13.87	13.25
0.0011	55.51	20	0.32	3.395	12.14	13.4	12.614
0.012	13.66	20	0.41	0.0849	9.91	10.29	11.31
0.012	13.66	0	0	0.849	7.45	8.7	6.1
0.012	13.66	20	0	3.395	9.24	11.6	9.7
0.012	13.66	0	0	1.698	7.73	6.45	6.28
0.0015	44.81	0	0	0.424	10.96	10.414	11.39
0.0015	44.81	0	0	1.698	12.48	10.78	10.95
0.0015	44.81	0	0	2.546	9.77	9.13	9.19
0.0013	37.86	0	0	0.424	16.84	14.7	15.67
0.0013	37.86	0	0	2.546	13.73	13.57	13.7
0.0013	37.86	0	0	1.698	15.6	13.14	13.36

APPENDIX E: TRANSMISSION ELECTRON MICROSCOPE IMAGES.

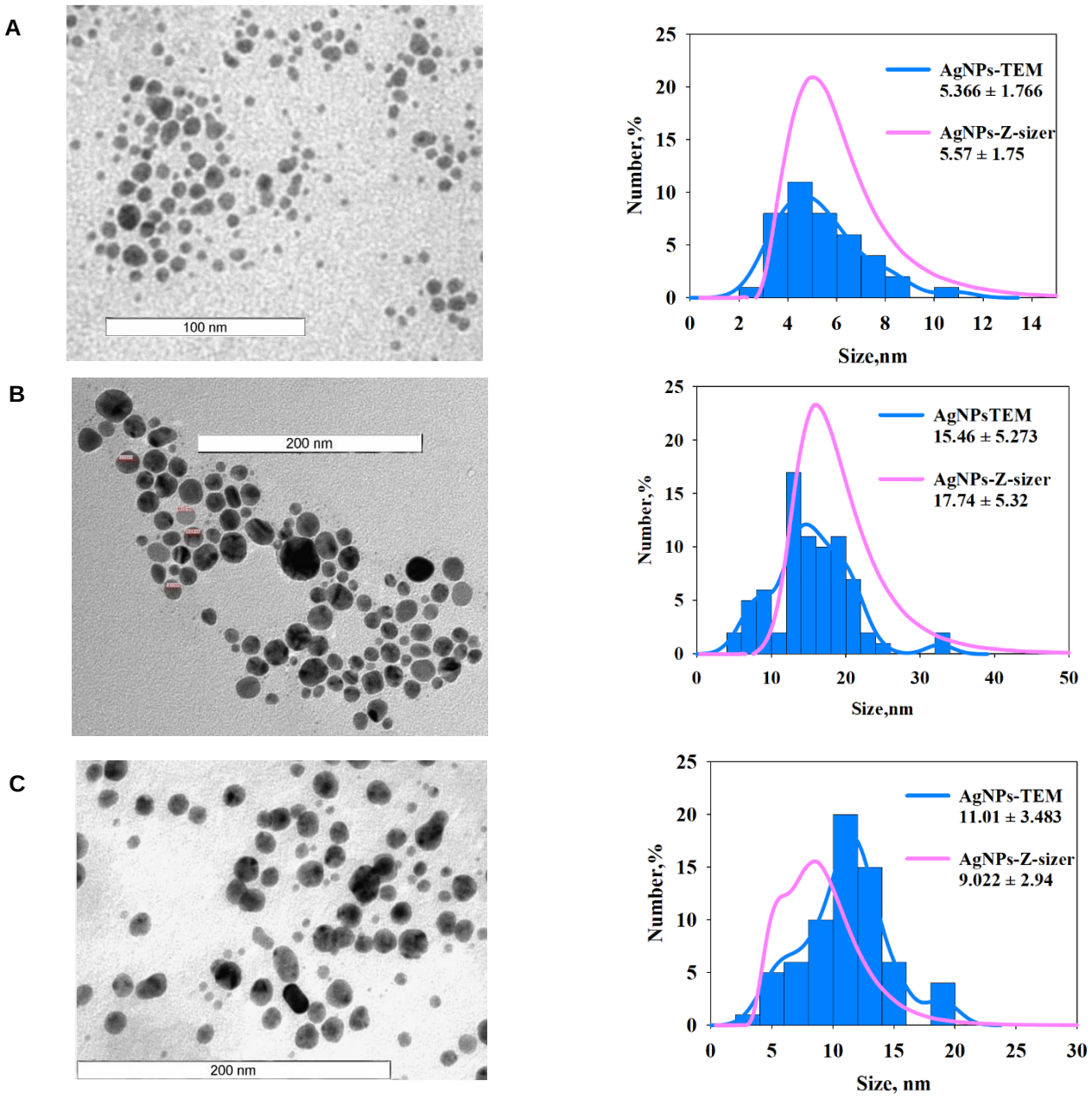


Figure A1: AgNPs size distribution from TEM and zeta-sizer. AgNPs at A) 4×10^{-5} dm^3/min, pH 12, TC 2.87 mM, and ST 0 ºC, B) 4×10^{-5} dm^3/min, pH 7 and TC 1.91 mM and ST 20 ºC and C) 4×10^{-5} dm^3/min, pH 7, TC 1.91 mM, CR 33.3 dm^{-1} and ST 20 ºC.

APPENDIX F: UV MEASUREMENTS FOR BOTH SET OF CHEMICALS.

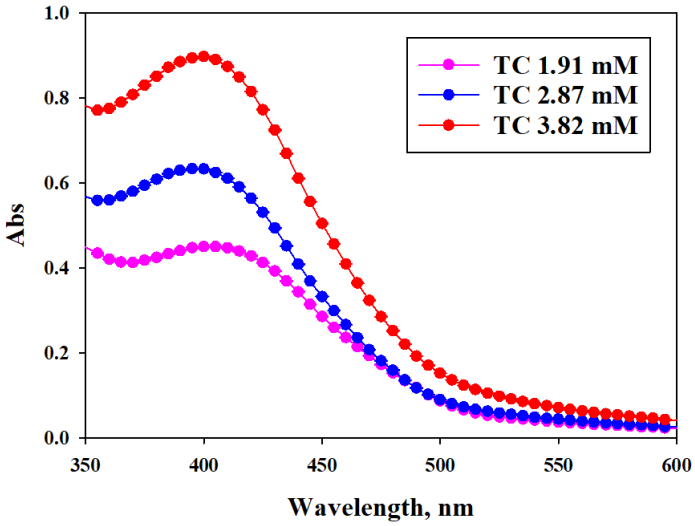


Figure A3: UV measurements of AgNPs obtained from the first set of chemicals at pH 7 for different concentrations of stabilising agent.

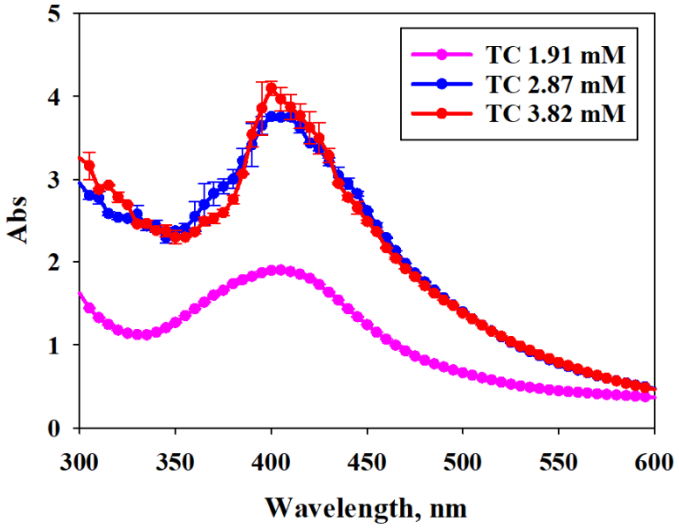


Figure A4: UV measurements of AgNPs obtained from the first set of chemicals at pH 12 for different concentrations of stabilising agent.

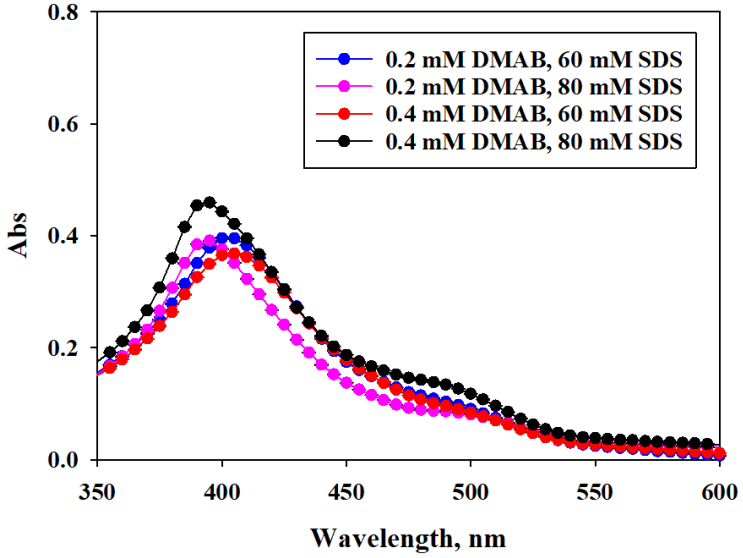


Figure A5: UV measurements of AgNPs obtained from the second set of chemicals at different investigated concentrations of reducing and stabilising agent.

APPENDIX G: PBM MODEL IN A WELL-MIXED REACTOR FOR 2ND SET OF CHEMICALS

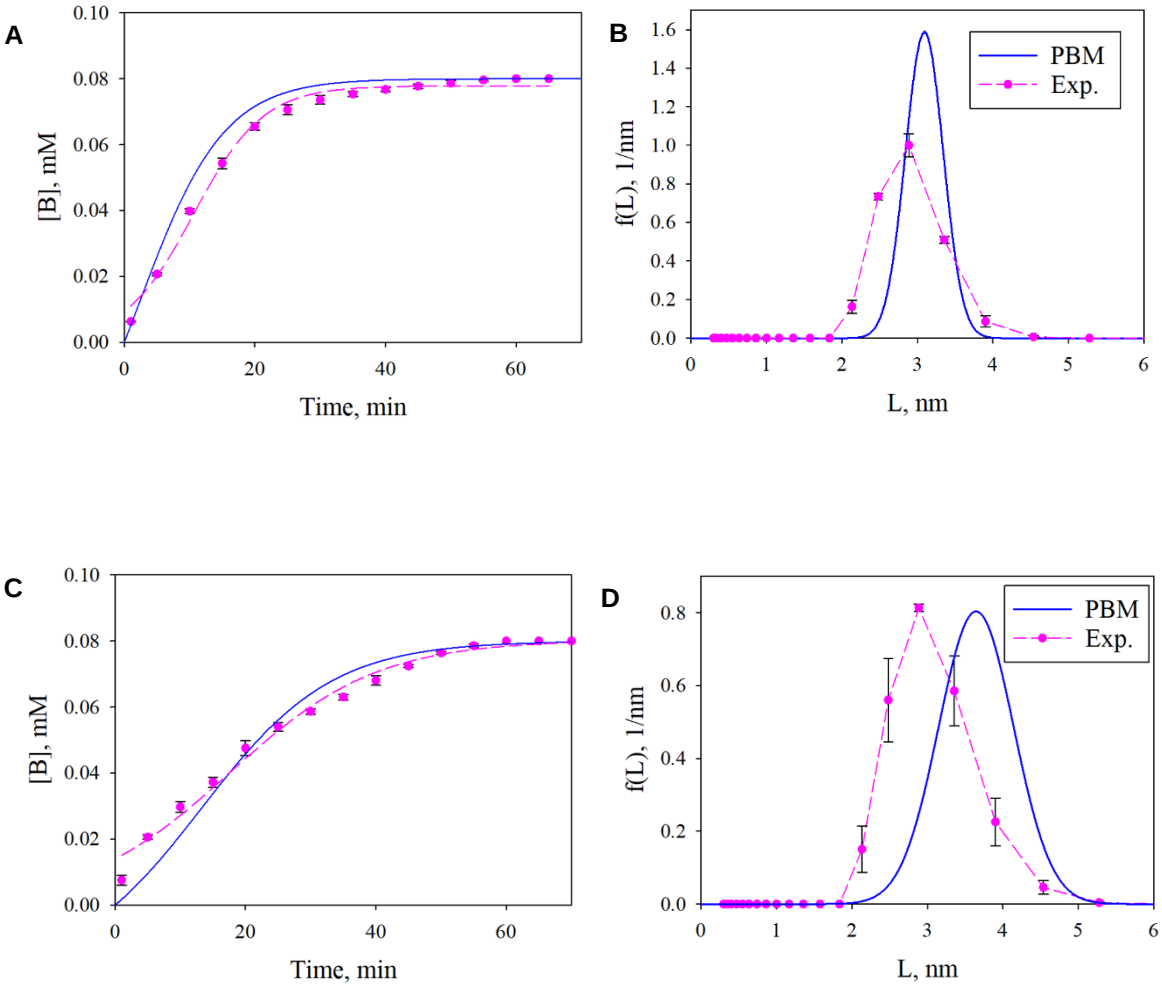


Figure A6: PBM model in a well-mixed reactor for 2nd set of chemicals. The graphs (A) and (C) show the temporal evolution of [B] between the experimental measurements (pink dots) and F-W based PBM predictions (blue line) while graphs (B) and (D) the PSD for AgNPs in a well-mixed reactor using 0.2 mM DMAB with 80 mM SDS and 0.4 mM DMAB with 60 mM SDS respectively. A length-based number density function assuming spherical particles was used. The function is given by

$G(L, y_i) = G(V, y_i)/3L^2$, where $G(V, y_j)$ is a volume-based growth rate. This expression assumes that particle growth in length (diameter) is proportional to particle size.

Table A4: Comparison of experimental measurements of d, σ and $PDI = (\sigma/d)^2$ with F-W based PBM predictions and normal distribution fitting for AgNPs in a well-mixed reactor under different concentrations of DMAB and SDS after full precursor consumption.

[DMAB], mM	[SDS], mM	k_1, min^{-1}	k_2, $M^{-1}min^{-1}$	$k_2 * A_o/k_1$	$d \pm \sigma$, nm (PDI)	
					PBM	Exp.
0.2	60	0.014	831.25	4.75	3.83 ± 0.57 (0.022)	3.82 ± 0.8 (0.05)
0.2	80	0.064	1120	1.40	3.09 ± 0.25 (0.007)	2.92 ± 0.5 (0.026)
0.4	60	0.021	989.58	3.77	3.65 ± 0.5 (0.019)	3.08 ± 0.56 (0.033)
0.4	80	0.125	1500	0.96	2.96 ± 0.19 (0.004)	2.73 ± 0.4 (0.021)

APPENDIX H: ALGORITHM 1 ITERATIVE MINIMISATION OF 3D-VAR COST FUNCTION VIA QUASI-NEWTON METHODS

Algorithm 1 Iterative Minimisation Of 3d-Var Cost Function Via Quasi-Newton Methods

Inputs : x_b,y,B,R,H

Parameters: k_{max} , ϵ

$x_0 = x_b$, $k = 0$

While $k < k_{max}$ and $||\nabla J(x_k)|| > \epsilon$ do:

$$J(x_k) = \frac{1}{2}||x_k - x_b||^2_{B^{-1}} + \frac{1}{2}||y - H(x)||^2_{R^{-1}}.$$

Linearize the H operator in the neighborhood of x_k:

$\nabla J(x_k) \approx 2B^{-1}(x_k - x_b) - 2H^T R^{-1}(y - H(x_k))$

Compute Hess ($J(x_k)$)

$xk+1 = xk - L3D\text{-}Var\ [Hess(J)(x_k)]^{-1}\nabla J(xk)$

$k = k+1$

end while

output: $x_a = x_k$